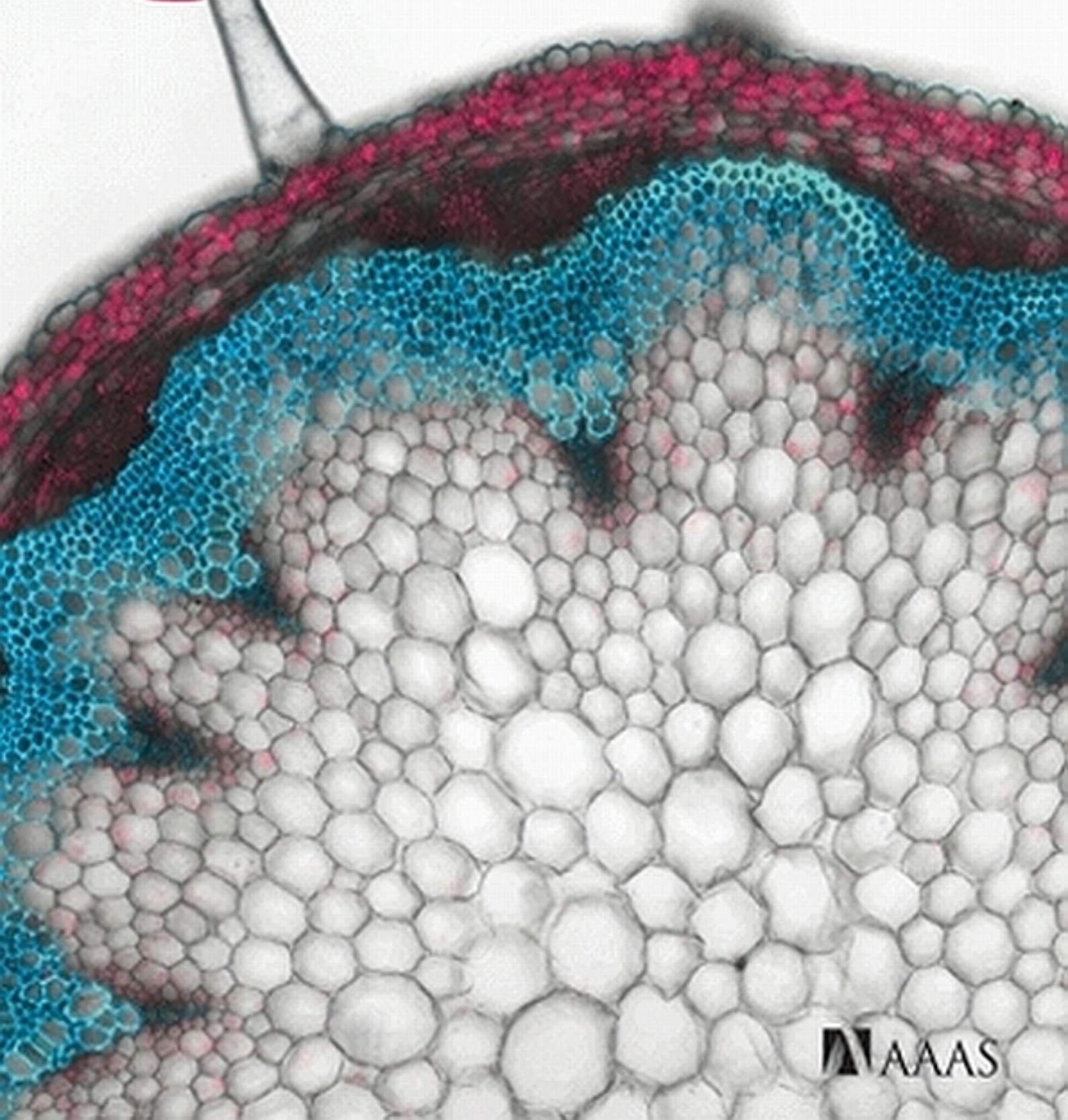


6 September 2013 | \$10

Science



AAAS

EDITORIAL

- 1043** Improving ERC Ethical Standards
Helga Nowotny and Pavel Exner

NEWS OF THE WEEK

- 1048** A roundup of the week's top stories

NEWS & ANALYSIS

- 1050** U.N. Taps Special Labs to Investigate Syrian Attack
As Syria Crisis Mounts, Scientist Looks Back at Last Major Chemical Attack
- 1052** Fluorine-Adding Bacteria May Transform Natural Product Medicines
Protein Designers Go Small
[>> Report p. 1089](#)
- 1053** Japan Gets Serious About Creating Its Own NIH
- 1055** Evolution Heresy? Epigenetics Underlies Heritable Plant Traits

NEWS FOCUS

- 1056** Boxed In
The Unruly Neutrino
- 1060** Sizing Up a Slumbering Giant
[>> Science Podcast](#)

LETTERS

- 1062** The Risky Road to Mars
V. E. Viola
Response
C. Zeitlin
Controversial Salt Report
Peppered with Uncertainty
D. M. Johns et al.

- 1064** CORRECTIONS AND CLARIFICATIONS

BOOKS ET AL.

- 1065** The Avian Migrant
J. H. Rappole, reviewed by F. Bairlein
- 1066** An Uncertain Glory
J. Drèze and A. Sen, reviewed by A. Robinson

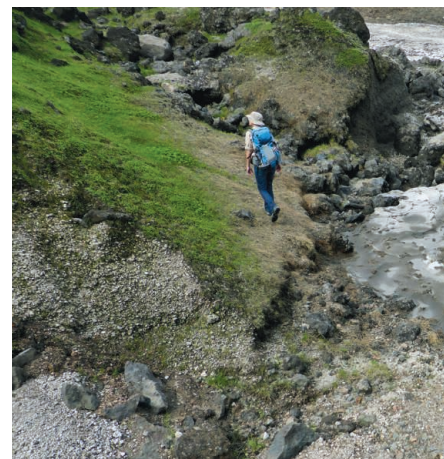
POLICY FORUM

- 1067** Certify Sustainable Aquaculture?
S. R. Bush et al.

PERSPECTIVES

- 1069** Fighting Obesity with Bacteria
A. W. Walker and J. Parkhill
[>> Research Article p. 1079](#)
- 1070** Reducing Earthquake Risk
B. E. Tucker
- 1072** Unraveling Charge Transport in Conjugated Polymers
R. A. Street
- 1073** Feedback on Galaxy Formation
B. R. McNamara
[>> Report p. 1082](#)
- 1075** A Hyperventilating Biosphere
I. Fung
[>> Report p. 1085](#)
- 1076** Uncloaking the Quantum Nature of Inelastic Molecular Collisions
P. Casavecchia and M. H. Alexander
[>> Report p. 1094](#)
- 1078** Retrospective: Tony Pawson (1952–2013)
T. Hunter

CONTENTS continued >>



page 1060



page 1065

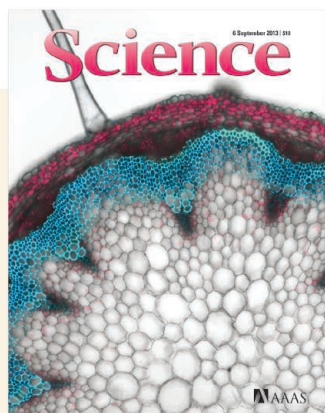
ON THE WEB THIS WEEK

>> Science Podcast

Listen to stories on failed stars, numerosity in the brain, monitoring a North Korean volcano, and more.

>> Find More Online

Check out *Science Express*, our podcast, videos, daily news, our research journals, and *Science Careers* at www.sciencemag.org.



COVER

Enhanced-color confocal microscopy image of a cross section of an *Arabidopsis* stem (diameter of full section: 2 millimeters; excluding the protruding epidermal hair cell). The cell walls in blue contain lignin, which provides strength to the walls. The magenta color in the cortex cells reflects the presence of chlorophyll. Caffeoyl shikimate esterase is an enzyme central to the biosynthesis of lignin, a major factor limiting biomass processing for biofuels. See page 1103.

Image: Lisa Sundin, Matyas Fendrych, and Daniel Van Damme/VIB, Belgium

DEPARTMENTS

- 1041** This Week in *Science*
1044 Editors' Choice
1046 *Science* Staff
1127 New Products
1128 *Science* Careers

RESEARCH ARTICLE

- 1079** Gut Microbiota from Twins Discordant for Obesity Modulate Metabolism in Mice
V. K. Ridaura et al.
Mice carrying gut bacteria from lean humans protect their cage mates from the effects of gut bacteria from fat humans.
Research Article Summary; for full text:
<http://dx.doi.org/10.1126/science.1241214>
>> *Perspective p. 1069*

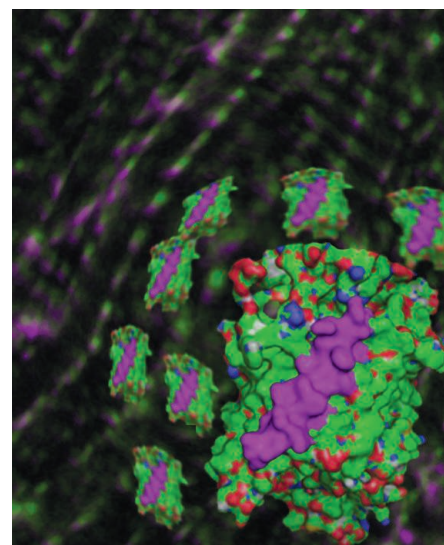
REPORTS

- 1080** Decades-Long Changes of the Interstellar Wind Through Our Solar System
P. C. Frisch et al.
Analysis of data collected by 10 different spacecraft indicates that our solar system's local environment may be changing.
- 1082** Radio Jets Clearing the Way Through a Galaxy: Watching Feedback in Action
R. Morganti et al.
High-resolution radio images of a galaxy reveal how a jet of relativistic particles is driving cold gas away from the center.
>> *Perspective p. 1073*
- 1085** Enhanced Seasonal Exchange of CO₂ by Northern Ecosystems Since 1960
H. D. Graven et al.
The amplitude of the seasonal cycle of carbon dioxide in high northern latitudes has increased by 50% since 1960.
>> *Perspective p. 1075*
- 1089** Expanding the Fluorine Chemistry of Living Systems Using Engineered Polyketide Synthase Pathways
M. C. Walker et al.
Biochemical pathways can be engineered to incorporate fluoroacetate into tri- and tetraketides in place of acetate.
>> *News story p. 1052*
- 1094** Observation of Partial Wave Resonances in Low-Energy O₂-H₂ Inelastic Collisions
S. Chefdeville et al.
Purely quantum mechanical effects are manifested in an experiment probing crossed molecular beams.
>> *Perspective p. 1076*
- 1096** Direct Determination of Absolute Molecular Stereochemistry in Gas Phase by Coulomb Explosion Imaging
M. Pitzer et al.
A simple molecule's three-dimensional structure can be ascertained from the fragment trajectories when it is blown apart.

- 1100** Achieving the Convention on Biological Diversity's Goals for Plant Conservation
L. N. Joppa et al.
Protecting 17% of the land surface and 60% of plant species is possible, but not at present.
- 1103** Caffeoyl Shikimate Esterase (CSE) Is an Enzyme in the Lignin Biosynthetic Pathway in *Arabidopsis*
R. Vanholme et al.
A key enzyme involved in lignin biosynthesis is identified and characterized in the model plant *Arabidopsis*.
- 1106** Epigenetic Regulation of Mouse Sex Determination by the Histone Demethylase Jmjd1a
S. Kuroki et al.
Histone modification controls mammalian sex determination.
- 1110** Single-Cell DNA-Methylation Analysis Reveals Epigenetic Chimerism in Preimplantation Embryos
C. Lorthongpanich et al.
Lethal epigenetic chimerism can be rescued by transfer of pronuclei.
- 1113** Neuroendocrine Control of *Drosophila* Larval Light Preference
N. Yamanaka et al.
The hormone that triggers the transition from larva to adult also induces the larvae to find a dark spot to do this safely.
- 1116** Conserved Regulation of Cardiac Calcium Uptake by Peptides Encoded in Small Open Reading Frames
E. G. Magny et al.
Small peptides regulate calcium transport and regular heart contraction in both flies and humans.
- 1120** A Causative Link Between Inner Ear Defects and Long-Term Striatal Dysfunction
M. W. Antoine et al.
In mutant mice, severe ear dysfunction is associated with motor hyperactivity.
- 1123** Topographic Representation of Numerosity in the Human Parietal Cortex
B. M. Harvey et al.
There is a map of numerical magnitude in the human brain.
>> *Science Podcast*



pages 1073 & 1082



page 1116

SCIENCE (ISSN 0036-8075) is published weekly on Friday, except the last week in December, by the American Association for the Advancement of Science, 1200 New York Avenue, NW, Washington, DC 20005. Periodicals Mail postage (publication No. 484460) paid at Washington, DC, and additional mailing offices. Copyright © 2013 by the American Association for the Advancement of Science. The title SCIENCE is a registered trademark of the AAAS. Domestic individual membership and subscription (51 issues): \$149 (\$74 allocated to subscription). Domestic institutional subscription (51 issues): \$990; Foreign postage extra: Mexico, Caribbean (surface mail) \$55; other countries (air assist delivery) \$85. First class, airmail, student, and emeritus rates on request. Canadian rates with GST available upon request, GST #1254 88122. Publications Mail Agreement Number 1069624. Printed in the U.S.A.

Change of address: Allow 4 weeks, giving old and new addresses and 8-digit account number. Postmaster: Send change of address to AAAS, P.O. Box 96178, Washington, DC 20090-6178. Single-copy sales: \$10.00 current issue, \$15.00 back issue prepaid includes surface postage; bulk rates on request. Authorization to photocopy material for internal or personal use under circumstances not falling within the fair use provisions of the Copyright Act is granted by AAAS to libraries and other users registered with the Copyright Clearance Center (CCC) Transactional Reporting Service, provided that \$30.00 per article is paid directly to CCC, 222 Rosewood Drive, Danvers, MA 01923. The identification code for Science is 0036-8075. Science is indexed in the Reader's Guide to Periodical Literature and in several specialized indexes.



Transforming Fat to Thin

How much does the microbiota influence the host's phenotype? **Ridaura *et al.*** (p. 1079; see the Perspective by **Walker and Parkhill**) obtained uncultured fecal microbiota from twin pairs discordant for body mass and transplanted them into adult germ-free mice. It was discovered that adiposity is transmissible from human to mouse and that it was associated with changes in serum levels of branched-chain amino acids. Moreover, obese-phenotype mice were invaded by members of the Bacteroidales from the lean mice, but, happily, the lean animals resisted invasion by the obese microbiota.

Pushy Black Hole

The giant black holes that sit at the centers of most galaxies influence the way galaxies evolve in poorly understood ways. **Morganti *et al.*** (p. 1082; see the Perspective by **McNamara**) have acquired high-resolution radio images of a galaxy with an actively accreting black hole from which a jet of relativistic particles emanates. The observations show that a cloud of neutral hydrogen gas is being driven outward, possibly contributing to star formation and galaxy growth.

Downs and Ups

Every spring, the concentration of CO₂ in the atmosphere of the Northern Hemisphere decreases as terrestrial vegetation grows, and every fall, CO₂ rises as vegetation dies and rots. Climate change has destabilized the seasonal cycle of atmospheric CO₂ such that **Graven *et al.*** (p. 1085, published online 8 August; see the Perspective by **Fung**) have found that the amplitude of the seasonal cycle has exceeded 50% at some latitudes. The only way to explain this increase is if extratropical land ecosystems are growing and shrinking more than they did half a century ago, as a result of changes in the structure and composition of northern ecosystems.

Lignin Biosynthesis Complications

Lignin is a polymer that lends its sturdy properties to wood and makes plant cell walls tougher, which creates problems for chemists converting cellulosic plant biomass into biofuels.

Vanholme *et al.* (p. 1103, published online 15 August; see the cover) have identified a new step in the biosynthetic pathway of lignin in *Arabidopsis* in which caffeoyl shikimate esterase catalyzes synthesis of caffeate. Cellulose from mutant plants, which had reduced amounts of lignin, was more efficiently processed into glucose.

Fatal Chimeras

Impaired DNA-methylation maintenance during early embryonic development may cause imprinting-related diseases. **Lorthongpanich *et al.*** (p. 1110) have devised a sensitive assay to probe multiple imprinted gene loci for their DNA-methylation state at the single-cell level. Blastomeres with defective imprinting showed complex, epigenetic chimeras developed with fatal defects. Pronuclear transfer restored normal mouse development, offering a therapeutic strategy to overcome epigenetic defects caused by maternal insufficiencies.

Looking for the Dark

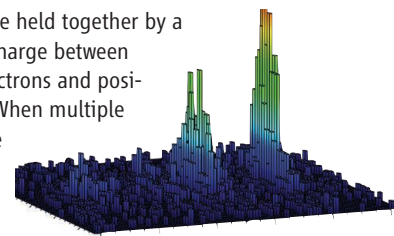
Mature *Drosophila* larvae wander away from food and seek a dark site for pupation. While investigating this phenomenon **Yamanaka *et al.*** (p. 1113) found that four prothoracicotrophic hormone (PTTH)-producing neurons mediate light preference in the central brain. PTTH circulates in the hemolymph and signals via its receptor, Torso, to two light sensors, sensitizing them for light detection. The larvae can then transform from wandering larvae into immobile pupae hidden from light and predatory eyes.

Deafness and Misbehavior

Behavioral problems accompanied by hyperactivity often occur in children with severe hearing loss and vestibular impairment. Explanations have focused on socioenvironmental factors, but **Antoine *et al.*** (p. 1120) found that inner ear defects can cause dysfunction in the striatum, which leads to abnormal behavior—especially hyperactivity—mediated by dopamine and glutamate signals, in an area of the striatum that is instrumental in controlling motor output. The abnormal behavior can be reversed by injection of an extracellular signal-regulated kinase inhibitor, which provides a novel target pathway for the treatment of behavioral disorders.

Absolute Images

Molecules are held together by a balance of charge between negative electrons and positive nuclei. When multiple electrons are expelled by laser irradiation, the remaining, mutually repulsive nuclei fly apart in a Coulomb explosion. Instead of traditional x-ray diffraction methods that require crystalline samples, **Pitzer *et al.*** (p. 1096) show that by tracking the fragment trajectories from laser-induced Coulomb explosions of relatively simple gas phase molecules, they can determine the absolute stereochemical configuration of enantiomers (mirror-image isomers).



Additional summaries

Wind of Change

The flow of interstellar gas and dust through the solar system was thought to be unvarying, but **Frisch *et al.*** (p. 1080) show that there has been a significant variation of the direction of the flow of interstellar helium through the solar system over the past 40 years. The data, collected by 10 different spacecraft over much of the space age, hint of changes rather than constancy in the solar system's galactic environment.

Quantum Collision Course

Our experience of a world apparently governed by classical physics is a consequence of the fact that quantum mechanical effects average out in size regimes much larger than nanometers. Even at the molecular level, the quantized nature of rotational energy distributions is often obscured by averaging effects. **Chefdeville *et al.*** (p. 1094; see the Perspective by **Casavecchia and Alexander**) have observed a striking manifestation of quantized rotation in the scattering trajectories of colliding H₂ and O₂ molecular beams. The experimentally resolved partial wave resonances show essentially complete agreement with theoretical calculations and deviate starkly from classical collision paradigms.

Stitching in Fluoroacetate

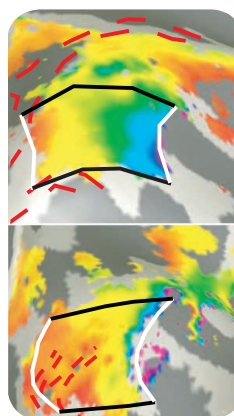
Polyketide synthase enzymes stitch together an impressively diverse series of organic compounds from simple acetate and propionate building blocks. **Walker *et al.*** (p. 1089) now show that these biochemical pathways can be engineered to incorporate fluoroacetate—a primary product of the only known native enzymatic fluorination route—into tri- and tetraketides. In *Escherichia coli* cells, this process shows potential as a

versatile means of inserting fluorine substituents into a range of complex molecules for use in pharmaceutical and agrochemical research.

Number Sense

Numerosity perception resembles primary sensory perception and, indeed, it has been called the number sense. As all primary senses are organized topographically in the cortex, **Harvey *et al.*** (p. 1123)

tested the hypothesis that numerosity is also organized topographically. Applying ultrahigh-field functional brain scanning and using custom-designed analysis, they confirmed that a topographical numerosity map occurs in the human parietal cortex, which displays conventional characteristics, such as a systematic relationship between the cortical location's preferred numerosity and cortical magnification and tuning width.



Plant Protection

The Convention on Biological Diversity's 20 Aichi Targets, agreed in October 2010, extend to 2020 an international commitment to halt the loss of biodiversity. Using data from "The Plant List" (www.theplantlist.org), **Joppa *et al.*** (p. 1100), show that ~65% of plant species are endemic to 17% of the terrestrial land surface

and include many islands, with mainland contributions concentrated heavily in central and southern America and Asia. These regions include 75% of all plant species. These regions are also important for terrestrial vertebrates—containing most of all—bird, mammal, and amphibian species, but less than one-sixth of this land surface is under protection.

More Determined Sex

Although several transcription factors participate in mammalian sex determination, the contribution from specific epigenetic regulation is just being revealed. **Kuroki *et al.*** (p. 1106) show that a JmjC domain-containing protein, Jmjd1a, catalyzes H3K9 demethylation of the Y-linked sex-determining gene *Sry* in mice to enable its expression above the required threshold level. Ablation of Jmjd1a function results in mouse male-to-female sex reversal, hence not only revealing a mechanism of *Sry* regulation but also the pivotal role of epigenetic regulation in mammalian sex determination.

smORFing for Calcium

Genomes contain thousands of small open reading frames (smORFs), short DNA sequences coding for peptides of less than 100 amino acids. **Magny *et al.*** (p. 1116, published on 22 August) describe two smORF-encoded peptides of less than 30 amino acids regulating calcium transport and, hence, regular heart contraction, in the fruit fly *Drosophila*. These peptides seem to have been conserved for more than 550 million years in a range of species from flies to humans, where they have been implicated in severe heart diseases. Such conservation suggests that smORFs might be an ancient part of our functional genome.



Helga Nowotny is president of the ERC.



Pavel Exner is vice-president of the ERC and chair of the ERC Scientific Council Standing Committee on Conflict of Interest, Scientific Misconduct and Ethics.

Improving ERC Ethical Standards

IMAGINE SITTING OVER A PILE OF APPLICATIONS SUBMITTED TO ONE OF THE MOST PRESTIGIOUS FUNDING agencies. Suddenly, what you read appears familiar—not only the idea, but its terminology and the methods proposed. You recognize entire sentences because you wrote them. This scenario must have been an utter surprise for one of the European Research Council's (ERC's) evaluation panel members who, last year, stumbled across the most bizarre case of scientific misconduct that the organization has witnessed so far. The proposal, submitted some years earlier to a funding agency on a different continent, was copied by one of the reviewers, a highly recognized scientist, and then submitted to the ERC. It was pure chance that the former applicant detected the fraud.

The anecdote illustrates not only the difficulties of detecting scientific fraud, which any funding agency in the world faces, but also the problems that the ERC is trying to fight. Since its beginning in 2007, the ERC Scientific Council established a strict set of rules for how to deal with fraud, conflicts of interest, and scientific misconduct. However, the larger legal framework of the European Commission (EC) under which the ERC operates links “fraud” only to financial aspects. The ERC is then obliged to report any (accomplished or attempted) misbehavior to OLAF, the European antifraud police. Financial fraud, however, causes the least headaches. In the above case, the ERC was unable to take action against the mischievous applicant.

The EC rules require funding agencies to avoid institutional conflicts of interest. A research proposal cannot be evaluated by a person from the same host institution as the applicant. In the case of a single legal entity, such as the Centre National de la Recherche Scientifique (CNRS) in France, this would seriously limit the function of reviewing panels. In 2012, the ERC achieved an exemption from this constraint. To fill the gap between the general legal rules and the desired system of high ethical standards, the ERC Scientific Council established in 2009 a standing committee to deal with ethical issues. So far, the ERC has evaluated more than 30,000 proposals, and the number of colleagues serving on its review panels approaches 3000. During the same time, the number of detected cases of misbehavior was under 30. But the temptation to be dishonest remains for some, as ERC grants represent exceptional prestige and money.

In 2011, an applicant from a respected European university forged a document. The researcher's university was told, but reacted only after the person reapplied and forged another document. The ERC lacks the legal means to exclude such an applicant from future funding competitions. It therefore urges host institutions to be more proactive and follow up in cases of suspected misconduct of researchers they employ. This includes imposing sanctions when the facts warrant it.

The ERC has strict policies on conflict of interest. To avoid bias in the evaluation procedure, the ERC requires any evaluator with an institutional connection to the applicant to leave the room when the application is discussed, as this is considered a disqualifying conflict. However, for close personal relationships, such as spouse, parent, and child, or other close personal bonds, this is not sufficient. Such a relationship is considered a strongly disqualifying conflict of interest, and the evaluator is required to withdraw from the call for proposals entirely.

The ERC is constantly learning, improving its rules as it moves forward. With the vigilance of its panel members, reviewers, and scientific officers and stronger cooperation from host institutions, it will succeed in not accepting anything less than the highest standards.

— Helga Nowotny and Pavel Exner

10.1126/science.1244098





EDUCATION

Self-Efficacy Is the Key

The natural response to the shift toward inquiry-based science education is an increase in faculty-mentored undergraduate research experiences (UREs). Large amounts of data describe the impact of UREs on student gains in performing research-related procedures, thinking and working like a scientist, and interest in graduate school. Much less is known about the processes through which student gains are achieved and the organization and dynamics of specific URE programs. Adedokun *et al.* used structural equation modeling to explore a URE program with a specific focus on exploring the relationships among three key outcomes: research skills, research self-efficacy, and aspiration for research careers. A post-participation survey was given to 156 students who typically spent 4 to 10 hours per week in their faculty mentor's laboratory and attended a seminar class on research conduct. Modeling data showed significant direct relationships between research skills and research self-efficacy, and between research skills and aspirations. Additionally, positive relationships between self-efficacy and aspirations and an indirect effect of research skills on aspirations via self-efficacy were shown. Research self-efficacy thus partially mediates the relationship between research skills and student aspirations for research careers. — MM

J. Res. Sci. Teach. 10.1002/tea.21102 (2013).

NEUROSCIENCE

Stroke Recovery

Astrocytes are the most numerous cells in the mammalian brain, providing metabolic support for neurons and modulating synaptic transmission. They can also help to repair neuronal injuries, replacing central nervous system cells that cannot regenerate. Because they are believed to protect neurons from injury and death, there is interest in exploring their therapeutic potential, in particular to promote recovery after stroke. Although astroglia have been derived in vitro from human embryonic stem cells, it is not clear whether a subpopulation of astroglia might better promote repair. Jiang *et al.* generated highly pure populations of astroglia progenitors from human embryonic stem cells and observed that those expressing the transcription factor Olig2 showed strong neuroprotective effects against oxidative stress and glutamate toxicity in vitro. Further, rats that received hippocampal transplants of human Olig2⁺ astroglia soon after being subjected to global cerebral ischemia showed increased synaptogenesis and improved learning and memory in water maze trials. The observed differential expression of growth factors, neurotrophic factors, cytokines, and chemokines related to synaptic function may account

for differences in the ability of this astroglia population to promote recovery. — LDC

Nat. Comm. 4, 10.1038/ncomms3196 (2013).

CANCER

Highway Deconstruction

Because most cancer patients die of metastatic disease, there is substantial interest in understanding—and pharmacologically thwarting—the molecular events that drive or facilitate metastasis. Early in the process within the primary tumor, cells attach to and migrate along collagen networks, which take them to blood vessels that carry them to distant organs they ultimately colonize. A new study suggests that these collagen highways are particularly important for an aggressive soft-tissue sarcoma that frequently and fatally metastasizes to the lung. Using mouse models, Eisinger-Mathason *et al.* show that when primary sarcomas become deprived of oxygen, a transcription factor called HIF1 α (hypoxia-inducible factor 1 α) is induced, which in turn enhances the expression of PLOD2 (procollagen-lysinase, 2-oxoglutarate 5-dioxygenase 2), an enzyme that creates dense and highly disorganized networks of collagen by adding hydroxyl groups to collagen monomers. Sarcomas in mice treated with a drug known to inhibit PLOD2 expression

(minoxidil, which is commonly used for hair restoration) exhibited more-organized patterns of collagen and had a reduced propensity to metastasize to the lung. — PAK

Cancer Discov. 3, 10.1158/2159-8290.CD-13-0118 (2013).

NEUROSCIENCE

Finding Parallels

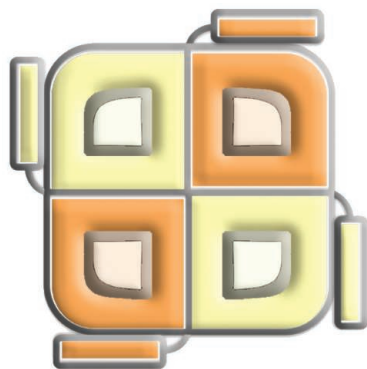
The transcription factor nuclear factor I-A (NFIA) controls genetic programs implicated in cellular metabolism and the migration of normal glial cells. NFIA is overexpressed in some gliomas: tumors of the central nervous system that contain cells resembling glial cells. In the hematopoietic system, NFIA is regulated by the microRNA miR-223. Glasgow *et al.* now document a similar relationship of NFIA and miR-223 in glial cells and in gliomas. Their results show that during normal development, miR-223 represses NFIA and blocks the proliferation of glial precursors; the cells are then left to switch into differentiation pathways. In gliomas, miR-223, which may be expressed in only some gliomas, can repress NFIA and thus suppress glioma cell growth. These results pave the way to understanding what is and is not parallel between normal development and cancer. — PJH

J. Neurosci. 33, 13560 (2013).

BIOCHEMISTRY

Four Closure

The Ca^{2+} -binding protein calmodulin (CaM) is involved in the regulation of many membrane channels, but how it modulates permeability remains unclear. Reichow *et al.* have combined electron microscopy, structural modeling, molecular dynamics, and mutagenesis to study the interaction of the aquaporin AQP0 and CaM. Each monomer in the tetrameric AQP0 contains a water-conducting pore. Fitting crystal structures of the AQP0 tetramer and CaM into a 25 Å electron microscopic reconstruction revealed that CaM bound to the C-terminal helices of adjacent AQP0 monomers. Initially, CaM binds to one helix, and its proximity to the neighboring monomer then allows it to capture the second one. Molecular dynamics simulations suggested that, although it only links two monomers, CaM restricts the dynamics of all four



monomers in the tetramer. The constriction site CSII at the cytoplasmic vestibule of the channel has been proposed to gate access. Interestingly, the AQP0 residues that were stabilized most by CaM mapped to the C-terminal helices, the base of the last transmembrane helix, and residues that form CSII. In AQP0, tetramerization is not required for water permeability; however, these results show that its quaternary structure facilitates cooperative regulation, and the regulation of other membrane channels by CaM may rely on similar mechanisms. — VV
Nat. Struct. Mol. Biol. **20**, 10.1038/nsmb.2630 (2013).

MATERIALS SCIENCE

Making Mg Magnificent

When crystalline materials are stressed, defects in the crystal planes become mobile once a critical stress is reached. The stress required for movement of these dislocations along different slip planes can vary considerably, leading to poor ductility. Magnesium is an example of

a material with an extreme anisotropy: The critical stress required for deformation along nonbasal planes is 100 times larger than along basal ones. Yu *et al.* postulated that even though materials are known to be stronger when they are smaller, there are upper bounds to this enhancement, so that the critical anisotropy should decrease. They tested single-crystal Mg samples ranging from 850 to 80 nm in size inside a quantitative electron microscope. At sizes between 200 and 400 nm, significant strengthening of the samples was seen, but the ductility remained poor. Below 100 nm, there was a shift in the deformation behavior. As the local flow stresses approached 2 GPa, there was increasing activation of the nonbasal planes, leading to a large amount of plastic deformation. These size effects could be employed to

make better use of other high plastically anisotropic materials. The use of grain boundaries could allow for larger overall samples, because the boundaries will act as stress concentrators and preferred sources for the nucleation and emission of

dislocations, which is important during plastic deformation of a sample. — MSL

Proc. Natl. Acad. Sci. U.S.A. **110**, 13289 (2013).

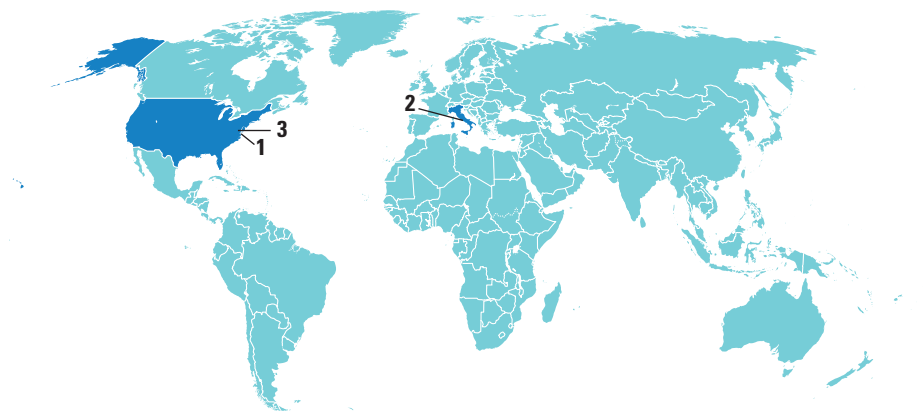
APPLIED PHYSICS

Slowly Does It

The rise and fall of pitch of a passing police siren gives a familiar example of the Doppler effect. In such a case, the speed of the moving object is appreciable compared to the speed of sound, with fast-moving objects relatively easy to detect. The situation is somewhat more difficult for slow-moving objects, where the frequency shift can be very small. Detection typically requires complex interferometry. Bortolozzo *et al.* show that a slow light medium can be used to accentuate and detect tiny frequency shifts associated with slow-moving objects. Obviating the need for complex optics, they use a balanced detection scheme where they simply split a laser beam in two and measure the intensity difference between the two beams once they pass through the slow light medium. They can detect frequency shifts down to 1 μHz and suggest that the simple setup should allow for remote sensing of slow-moving objects. — ISO

Opt. Lett. **38**, 3107 (2013).

AROUND THE WORLD



U.S. East Coast 1

Virus Culprit in Dolphin Deaths

A measleslike virus appears to be the chief cause of the droves of dead dolphins that washed ashore along the U.S. East Coast this summer, researchers announced on 28 August. Since 1 July, 333 bottlenose dolphins have been recovered from beaches between New York and North Carolina—10 times the number usually recovered at this time of year.

In early August, the National Oceanic and Atmospheric Administration (NOAA)



Beached. A measleslike virus killed hundreds of dolphins this summer.

declared an Unusual Mortality Event, freeing up federal funding for NOAA's Marine Mammal Health and Stranding Response Program (MMHSRP) to retrieve and assess the mammals' remains. The team used molecular techniques to probe for the virus as well as traditional examinations of the dead animals' lungs, brains, and lymph systems. The culprit appears to be a type of morbillivirus, a group

that includes viruses that cause measles in humans and distemper in dogs.

Morbillivirus was also responsible for a 1987 die-off that killed more than 700 dolphins. Wild dolphins exposed during that epidemic likely developed immunity to the virus, but animals born since 1987 are probably susceptible, says MMHSRP head Teri Rowles. The epidemic will continue until the number of susceptible animals dwindles, researchers predict.

<http://scim.ag/dolphinmeasles>

Rome 2

Scientists Named *Senatore a Vita*

Two well-known Italian scientists have been appointed "senator for life" by President Giorgio Napolitano to honor their contributions to society. Physicist Carlo Rubbia, 79, and brain stem cell biologist Elena Cattaneo, 50, received the honor along with conductor Claudio Abbado and architect Renzo Piano on 30 August. Senators for life—of which there are now six—have the same voting rights as the 315 elected members of the Italian Senate.

Rubbia shared the 1984 Nobel Prize in physics with Simon van der Meer and is still active at CERN in Geneva, Switzerland. In addition to her research, Cattaneo is active in outreach and in public debates, including an ongoing fight against an unproven stem cell therapy in Italy (<http://scim.ag/stemdebate>).

The Italian scientific community is cheering the announcement. "The appointment of senators for life makes us proud as researchers and confirms the attention of the President of the Republic for the world of scientific research," said Italian National Research Council President Luigi Nicolais in a press release.

Washington, D.C. 3

Consent Rules at Issue After Premie Controversy

In the wake of a controversial study involving premature infants, the U.S. government is considering changing how biomedical researchers inform patients about the risks of clinical experiments. The controversy—which put some neonatal research on hold for several months—was the subject of a 28 August hearing held by the U.S. Department of Health and Human Services.



No go? Premie therapies may get new consent rules.

The U.S. Office for Human Research Protections threatened to sanction 23 universities for failing to adequately disclose the risks of death and blindness posed by the so-called SUPPORT trial, which compared oxygen therapies provided to 1316 premature infants (*Science*, 19 April, p. 254). But it backed off following complaints from researchers, saying the issue needed more discussion (*Science*, 14 June, p. 1270). At the meeting, bioethicists argued that researchers should be able to waive some consent requirements if a study—such as SUPPORT—involves providing patients with standard care they might receive anyway. But a number of parents involved in the trial said they never would have agreed if they'd been told about all the risks. <http://scim.ag/premieconsent>

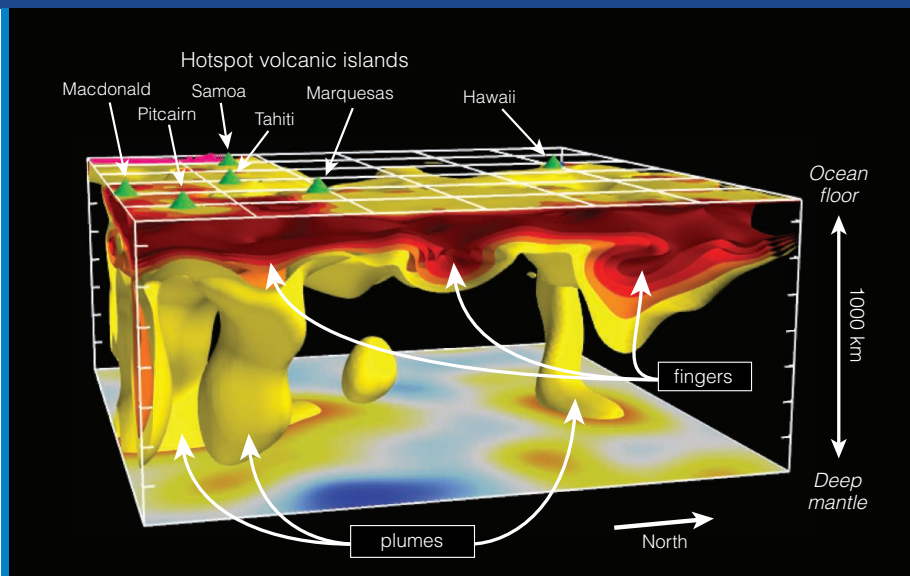
NEWSMAKERS

Science Wins Keck Prize

Science magazine has won one of four 2013 Communication Awards from the National Academy of Sciences, National Academy of Engineering, and Institute of Medicine. The annual awards, supported by the W. M. Keck Foundation, recognize excellence in reporting and communicating science, engineering, and medicine to the general public. Each award comes with a \$20,000 prize.

Science was honored in the magazine/newspaper category for four articles from

CREDITS (TOP TO BOTTOM): GETTY IMAGES/HEMERA/ISTOCKPHOTO.COM; AKIRA SUWA/PHILADELPHIA INQUIRER/MCT/LANDOV



Sharper View Reveals Earth's Innards

By probing thousands of kilometers of solid rock with seismic waves, seismologists have found a new kind of deep-Earth feature. The hottest rock—such as the plume rising through the mantle beneath Hawaii—has been particularly hard to image, driving a decades-long debate over how deep the sources of such hot spot plumes actually are.

Thanks to powerful computers, however, seismologists can now spot new features using hot rock's effect on the wiggles of seismic waves—not just the waves' speed, as in earlier seismic imaging. Seismologist Scott French of the University of California, Berkeley, and colleagues report online in *Science* this week that by using this “full-waveform inversion” technique, they have traced the Hawaiian plume (yellow) to a depth of at least 1000 kilometers. That suggests plumes span the entire 2900-kilometer-thick mantle, not just its uppermost layer as many scientists have contended.

The new imaging also reveals long “fingers” streaked across the Pacific 250 kilometers to 400 kilometers down (red)—apparently hot rock from the plumes flowing perpendicular to midocean ridges, where new ocean tectonic plates form.

Although all three consented to the procedure, the investigations, which began in 2011, found that, among other infractions, the physicians violated university policy by taking steps to patent the treatment without proper approval—crossing a line between “innovative care,” which allows for untested treatments in dire circumstances, and more strictly regulated medical research. The surgeons maintain they were acting in the interests of the patients, expected to live no longer than 15 months without treatment.

FINDINGS

A Cap on Mammal Virus Numbers

There are at least 320,000 viruses in mammals still waiting to be discovered, report scientists who have studied flying foxes in Bangladesh. From 2006 to 2010, the researchers caught hundreds of the big bats and collected urine and fecal samples as well as throat swabs before letting them go again. They then fished out all the viral sequences they could find belonging to nine virus families, including coronaviruses, herpesviruses, and influenza A viruses.

They found 55 viruses in all, 50 of which had never been seen before. Using statistical methods, they found that three viruses were likely missed, for a total of 58. Extrapolating to the 5486 other mammal species, that means about 320,000 viruses in total, the team reports this week in *mBio*.

The research cost approximately \$1.2 million, the authors calculate, and identifying all 320,000 mammal viruses in the wild would cost about \$6.3 billion. Peter Daszak, president of EcoHealth Alliance and one of the authors, says that identifying all viruses would help in combating future outbreaks. “It would be the beginning of the end for pandemics.” <http://scim.ag/mammvir>

NOTED

>The chairman of the U.S. House of Representatives science committee says that the Environmental Protection Agency (EPA) isn't giving him the health and air pollution data he demanded in a controversial 1 August subpoena (*Science*, 9 August, p. 604), and that **the agency now stands in default**. “You did not provide ... anything new,” Representative Lamar Smith (R-TX) wrote on 3 September to EPA chief Gina McCarthy. Smith set a new deadline of 30 September.

a special issue on human conflict (18 May 2012). The writers are **Eliot Marshall**, for “Parsing Terrorism”; **Elizabeth Culotta**, for “Roots of Racism”; **Ann Gibbons**, for “The Ultimate Sacrifice”; and **Greg Miller**, for “Drone Wars.” The awards committee described the collection of stories as “an articulate, wide-ranging examination of what social scientists have learned about human violence, conflict, and terrorism.”

The other 2013 winners are: David George Haskell, for his book, *The Forest Unseen*; Joanne Silberner, David Baron, and PRI's The World, for four radio pieces on “the hidden toll cancer takes in impoverished nations”; and an online series in *USA TODAY* on the toxic legacy of abandoned lead factories.

UC Davis Neurosurgeons Resign

Two University of California, Davis, neurosurgeons who tried to treat three people with terminal brain cancer by inserting gas-

trointestinal bacteria into their brains have resigned after internal investigations found that they failed to follow ethical guidelines governing medical research.



Muizelaar

Paul Muizelaar, former head of the neurosurgery department, retired and left the university in June; colleague **Rudolph J. Schrot** announced his resignation this summer, effective 31 August.

In 2010 and 2011, Muizelaar and Schrot applied live bacteria to the patients' open head wounds, based on observations that postoperation infection can prolong life in patients with glioblastoma, the most common and deadly form of brain tumor. One individual survived for a year; the other two developed sepsis and died within weeks of surgery.

CHEMICAL WEAPONS

U.N. Taps Special Labs To Investigate Syrian Attack

On the last day of August, a German airplane landed at Rotterdam airport in the Netherlands. It carried the U.N. inspectors who investigated the alleged chemical attack in Syria, along with samples—probably hundreds of them, scientists say, from soil, water, blood, clothes, and hair—carefully labeled and jealously guarded to ensure their integrity. Two days later, the samples continued their journey to specialized chemical laboratories in Europe. In the coming days, those labs will deliver the official verdict on whether chemical weapons were used in the 21 August attack near Damascus, which killed hundreds of men, women, and children—and if so, which ones.

For the labs, which the United Nations has declined to identify, the exercise is an extremely rare opportunity to apply skills honed in decades of research, spurred by Saddam Hussein's use of chemical weapons in Iraq in the late 1980s and a Japanese cult's 1995 sarin attack on riders of Tokyo's subway system. The work has led to vast improvements in the detection of minute quantities of chemical weapons or their breakdown products, says Maarten Nieuwenhuizen, a consultant at TNO, a research organization in Rijswijk, the Netherlands, that works for the Dutch ministry of defense.

Among the key improvements are new methods to detect nerve gases attached to long-lived blood proteins that have “dramatically extended” the period in which scientists can find evidence after an attack, says Ralf Trapp, an independent consultant on chemical weapons living in France. Whereas investigators often had just a few days, they can now come in 3 or 4 weeks after an attack and find evidence. That difference could prove crucial in Syria, where 5 days elapsed before the U.N. inspection team moved in.

Some experts have concluded from the

horrific footage from Syria—which showed victims suffering from paralysis and muscle spasms—that the most likely culprit was sarin or a related nerve gas. And some countries say the evidence is already in. On 4 June, French foreign minister Laurent Fabius announced that a military lab had discovered the fingerprints of sarin in blood, urine, and hair samples from victims of earlier attacks, collected by Syrian doctors and smuggled out of the country by a reporter at *Le Monde*. Last Sunday, U.S. Secretary of State John Kerry added that a U.S. analysis of blood and hair samples from Syrian emergency workers also

samples may have been tampered with,” says Alastair Hay, an environmental toxicologist at the University of Leeds in the United Kingdom. The U.N.-led investigation, in which custody is assured from beginning to end, “provides legitimacy,” Hay says.

Although the United Nations is formally in charge, it has entrusted most of the work to the Organisation for the Prohibition of Chemical Weapons (OPCW) in The Hague, established in 1997 to verify adherence to a 1993 global agreement banning chemical arms. (Syria is one of the few countries that has not signed.) OPCW, which has never before undertaken an investigation, has a network of 21 designated, highly specialized institutions, including TNO, in 17 countries. To shield the labs—many of them military establishments—from media attention or other types of unwanted pressure, OPCW hasn't revealed which ones it picked to help in the Syria investigation, but a U.N. spokesperson says that all are in Europe.

Scientists at the labs have various ways of demonstrating the use of chemical weapons, many of which break down quickly after being deployed. They can look for the agents themselves, or their degradation products, in environmental samples such as soil, water, victims' hair and clothes, or shrapnel. Sometimes, these can provide very specific clues: A compound called isopropyl methylphosphonic acid, for instance, is a unique breakdown product of sarin.

Environmental samples can occasionally provide evidence long after the fact. In 1992, Hay was part of a team that found evidence of the use of sarin and mustard gas at a site in Iraq where Hussein was suspected to have used chemical weapons 4 years earlier. “We were very lucky,” Hay says, because the compounds

had been buried at high concentrations inside the craters created by rockets.

In general, however, environmental evidence is hard to detect after just a few days, says TNO analytical chemist Marcel van der Schans. In contrast, “the clock ticks more slowly” for biomedical samples, such as urine, blood, or tissue, he says. These samples can also prove that an attack actually harmed



Race against time. In the case of a sarin attack, scientists can find evidence in many types of samples; so-called protein adducts in blood and tissue last longest.

fingered sarin in the Damascus attack.

But intelligence from any single country “doesn't hold power in the international law arena,” says Raymond Zilinskas, a chemical and biological weapons specialist at the Monterey Institute of International Studies in California, especially if it's unclear who collected the samples or had access to them. “There's always going to be suspicions that

people, Nieuwenhuizen says: “You add the human side of the story.”

Blood, in particular, is now a valuable source of information. Organophosphate nerve gases like sarin do their horrific job by binding to an enzyme called acetylcholinesterase, which plays a key role in muscle control. But they cling to other proteins in blood as well, forming so-called protein adducts that are detectable even weeks after exposure. In weapons investigations, analytical chemists usually focus on an abundant blood protein called butyrylcholinesterase. New techniques make it possible either to dislodge the nerve gas from the protein and measure the

agent using gas chromatography, or to break down the proteins and measure the fragment modified by the poison.

The techniques, based on basic research at TNO's own laboratory, can't always discriminate between so-called G-agents, including sarin, and V-agents, such as VX, because the agents lose a chemical group that distinguishes them as they bind to human proteins. But that may not matter for the purpose of the investigation, Van der Schans says.

Normally, the labs have 2 weeks to submit a report on their investigation, but U.N. Secretary-General Ban Ki-moon has asked OPCW to expedite its analysis if scientifically

possible. The report may not show whether the Syrian government is responsible for the attacks, as the United States and France maintain, or whether the rebels launched them, as Syria and its allies say. Some clues—such as impurities, traces of stabilizing chemicals, or characteristics of shrapnel—could shed light on the culprit, and OPCW protocols stipulate that labs can report such information. But they are expected to stick to the scientific facts, Trapp says. “They will put all of the evidence together and paint a picture that makes it possible for others to draw conclusions.”

—MARTIN ENSERINK

With reporting by Jocelyn Kaiser.

As Syria Crisis Mounts, Scientist Looks Back at Last Major Chemical Attack

Before the alleged nerve gassing 2 weeks ago in Syria, the worst such chemical weapons attack against civilians in history was the March 1988 bombing of Kurds in the village of Halabja in northern Iraq by Saddam Hussein. At least 3200 people are thought to have died from a combination of nerve agents and mustard gas. Iran and the Kurds invited the nonprofit organization Doctors Without Borders to investigate.

The team arrived a week after the attacks and stayed for 5 days. It included Dirk Dons, a young assistant in a toxicology laboratory at the State University of Ghent in Belgium (now Ghent University). Dons spoke with *Science* about his experiences. (Although Dons now works for the Belgium military, he spoke as a private citizen.) For a longer version of this interview, see <http://scim.ag/DirkDons>.

—JOCELYN KAISER

Q: Can you describe your visit?

D.D.: I went with two doctors to Halabja. That was the 25th of March, so only 8 days later. We saw a lot of dead bodies. We did an estimation of the dead. We counted the streets, we counted bodies in some area, and then you made a calculation. We had a good estimation of the area because with a chopper [helicopter] we went over the area. We calculated 5000. Iran said 5500; Human Rights Watch estimated 3500.

We took samples from soil, vegetation, we took little dead animals, we took a lot of pictures. We took blank samples, too. Because we were following our own [Ghent] lab's standard operating procedures. At that moment there were no procedures from the Organisation for the Prohibition of Chemical Weapons or from the United Nations. There was no accepted chain of custody protocol.

The only thing that we took as detection equipment was a chemical agent monitor, a handheld ion mobility spectrometer. We could make a distinction between vesicants [blistering agents such as mustard gas] and neurotoxins [such as sarin].

Q: The bodies had not been moved yet?

D.D.: It was not possible. It was a fighting area. When we were there, jets were flying over. We had a time slot of 2 hours and during this 2 hours we had to do everything on that spot. It's very difficult to do the job as an inspector. You don't know the place and you've got to get a quick impression and start.



Seeking justice. Iraqi Kurds carry photos of victims of the 1988 mustard and nerve gas bombing of Halabja.

Q: Did you also visit survivors?

D.D.: We took blood and urine samples from survivors in refugee camps and from people in the region who were in hospitals. Another part of the investigation was interviews. We went to hospitals where we could interview some victims if they were able to answer our questions. It was always with interpreters. You lose a lot of things during these interviews.

We also talked to first responders and especially first responders with a lot of experience. In Tehran we spoke with [toxicologists and physicians who] treated patients. They had a lot of experience with the treatment.

Q: What was it like seeing victims of the attacks?

D.D.: I was rather young, I was in my 20s. It was shocking. It was one of the most awful things that I have seen in my life. But I was accompanied by Dr. Reginald Moreels, president of [Doctors Without Borders] Belgium, who was a surgeon with a lot of experience in war regions. He calmed me down. He said, “You’ve got to think, ‘You’ve got a job to do.’” At that moment you try to become rational. The empathy for the things you see stops. Then you only think, I’ve got to do this job collecting samples, make an estimation of the dead people. You stop looking at the children and the women who are the victims.

Q: What happened after your visit?

D.D.: We made our report from the visit. We tried to keep to the facts. That's one thing I learned during that mission. You can't say who is responsible when you only do interviews and you only take samples.

SYNTHETIC BIOLOGY

Fluorine-Adding Bacteria May Transform Natural Product Medicines

The element fluorine is highly reactive, toxic in many compounds, and almost entirely irrelevant in biology. But chemists who make medicines adore it. In 2012, three of the top 10 best-selling drugs, with sales of more than \$20 billion, contained the element. By adding a touch of fluorine, chemists can fine-tune the properties of would-be drugs, helping them selectively latch on to their targets, avoid destruction by enzymes, and wade through the fatty membranes surrounding cells. The trick works best with small molecules; when chemists add fluorine to very large ones, such as the antibiotic erythromycin and other large compounds made by living things, it usually destroys the function of the molecule.

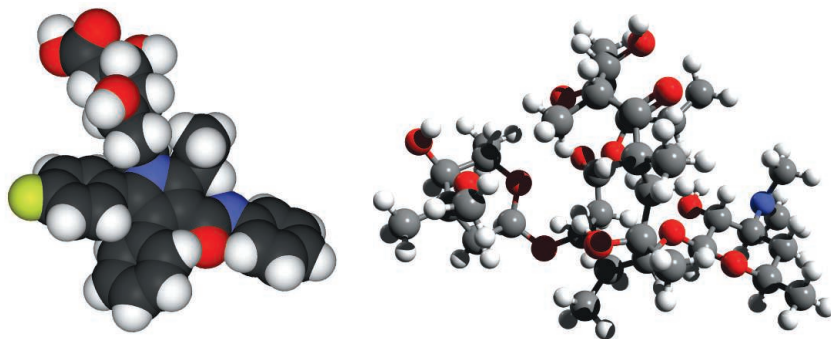
Natural products chemists may soon gain a new level of control—by enlisting biology itself to add the fluorine. On page 1089, researchers at the University of California, Berkeley, and Stanford University in Palo Alto, California, report that they've engineered bacteria to make key fluorine-containing starting materials and then

incorporate them into compounds called polyketides, a diverse class of some 20,000 known molecules that contains some of medicine's most powerful antibiotics, antifungals, and insecticides.

"It's exciting," says Wilfred van der Donk, a chemist at the University of Illinois, Urbana-Champaign. "Fluorine plays a really important role in medicinal chemistry." Many complex natural products are

potential drugs but have problems with toxicity, being cleared by the body too quickly, and other concerns, van der Donk notes. Chemists would love to have the power of natural products yet be able to tailor them like small molecules. "Now you have the best of both worlds if you can do this efficiently," van der Donk says.

Fluorine's medicinal prowess stems from its eagerness to snag an electron from another atom, forming a very tight bond. Because bonds between fluorine and carbon are so hard to disrupt, they make organic compounds less susceptible to degradation by enzymes called P450s that normally break down small drug molecules quickly.

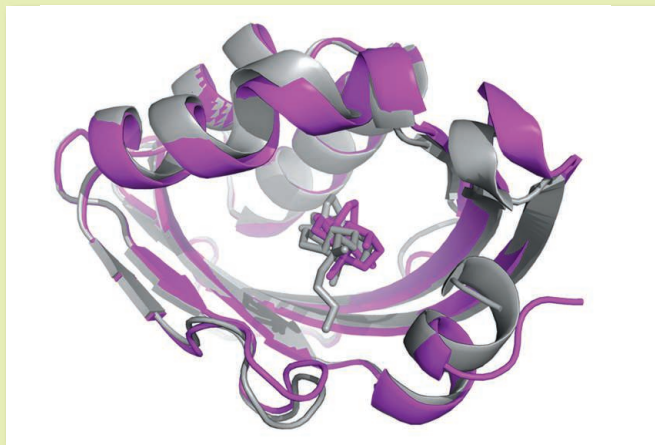


Key atom. Drugs, such as the anticholesterol medication atorvastatin (*left*), use fluorine (green) to improve their properties. Chemists can now do the same for large molecules, such as erythromycin (*right*).

Protein Designers Go Small

For living things, the task is a cinch: Make proteins that can bind tightly and specifically to small molecules, such as the neurotransmitter nitric oxide. Protein engineers would love to mimic the feat to create new drugs and diagnostics. In the past, their best efforts at computer-aided protein design fell short, because small molecules have few chemical handles for proteins to latch onto.

No longer. This week in *Nature*, researchers led by computational



Tight fit. An atomic scale x-ray structure (magenta) of a protein bound to a small molecule reveals a close match to the computer prediction (gray).

protein designer David Baker at the University of Washington, Seattle, and structural biologist Barry Stoddard of the Fred Hutchinson Cancer Research Center in Seattle report that they've designed a protein to tightly grab a heart drug steroid called digoxigenin, while excluding similar steroids such as digitoxigenin (even the name is almost indistinguishable) and progesterone.

"It's a very impressive result," says Brian Kuhlman, a biochemist at the University of North Carolina, Chapel Hill. And it is long-awaited. Ten years ago, for example, Duke University researchers published two papers claiming that they had created a protein tailored to a specific small molecule, only to have a former postdoctoral assistant from the same lab challenge the results in 2009.

Baker and his group succeeded using a multipronged approach. Among the most important considerations, Baker says, they designed their algorithm to pay special attention to weak hydrogen bonds and van der Waals interactions between particular amino acids in the protein and water-loving "polar" portions of the molecule. They also designed the binding pocket that grabs digoxigenin to be fairly rigid, which makes the protein more selective for the compound.

The new work holds out hope that protein designers will be able to use similar techniques to design novel therapeutics that sop up unwanted small molecules in the body, as well as diagnostics that can find similarly small targets. But more than that, Kuhlman says, the work restores protein engineers' confidence that they can solve one of their greatest challenges. "It's a very powerful example that in some cases we can do this."

—ROBERT F. SERVICE

Fluorine's small size also allows medicinal chemists to swap it into molecules in place of tiny hydrogen atoms or small methyl groups (a carbon atom bound to three hydrogens) without changing the shape of the molecule. The change often increases the overall electronic stability of the compound and typically makes it easier for it to associate with lipids and thus cross the fatty lipid-rich cell membranes.

In developing small-molecule drugs, chemists can add fluorine at specific positions on a molecule. But in large drug compounds, it is hard to control where fluorine atoms will end up. To get around this problem, researchers led by Michelle Chang, a chemist at Berkeley, and Chaitan Khosla, a biochemist at Stanford, reengineered two key changes into *Escherichia coli* bacteria that had previously been engineered to make polyketides. First, they equipped the bacteria to process a cheap fluorinated compound called fluoroacetate, a substance that they normally shun. To do so, the California team inserted a gene for a protein that enables the microbes to convert fluoroacetate into a fluorinated version of a key polyketide building block called malonyl-coenzyme A (malonyl-CoA).

Normally in *E. coli*, the enzymes that take up malonyl-CoA would ignore its fluorinated relative. So Chang's team mutated the native malonyl uptake gene to inactivate it, and then replaced it with one that produces a protein more tolerant of the fluorinated building block. Their strategy worked. By further tailoring the genes of *E. coli*, they not only got the microbes to incorporate fluoromalonyl-CoA into polyketides, but also were able to control at which position on the molecule the fluorine was incorporated. "Having the blueprint to do this inside an organism is really exciting," van der Donk says.

That doesn't mean the work is done. Polyketides that serve as medicines are typically far more complex than the paired ring structures produced by these *E. coli*. But Chang notes that microbes build that complexity by repeatedly adding the building blocks that the team worked with, and then refining the structure. "We're definitely happy that these results are a stepping stone into making some useful compounds," Chang says.

Not just useful. Finding a way to selectively add fluorine to large drug molecules could revolutionize natural product medicines much as it has already done for the blockbuster drugs that people rely on every day.

—ROBERT F. SERVICE

2014 BUDGET

Japan Gets Serious About Creating Its Own NIH

TOKYO—As Japan tries to spend its way out of economic stagnation, its scientists are poised to share in the bounty. Government agencies unveiled their 2014 budget requests last week; the Ministry of Education is seeking a 20% increase, to \$12 billion, for S&T funding. But one government initiative is ruffling feathers in the scientific community: A new Cabinet-level team is calling for a collection of biomedical research projects intended to form the nucleus of a Japanese version of the U.S. National Institutes of Health (NIH).

While the U.S. agency ranges across basic, translational, and clinical research, Japan's will stress outcomes. "Many

tion team, comprising the entire Cabinet, to oversee planning.

Compared with the U.S. NIH, which has an annual budget of \$30 billion and a sprawling research portfolio, Japan's version will start out small and goal-driven. On 30 August, the promotion team announced a plan to spend \$1.4 billion—a 37% increase over comparable spending this year—on nine major research initiatives (see table). The team also set targets: The cancer initiative, for example, should have 10 or more new therapies in clinical trials by 2020.

An official with the Cabinet's Health Policy Office says the initiatives grew out of research efforts at three relevant ministries—education, health, and economy. Agencies typically negotiate individually with the finance ministry to finalize amounts that are bundled into a governmental budget that goes to the legislature in December and takes effect in April. For the health and medical strategy, the promotion team will coordinate plans among the three ministries and craft a unified budget item. The ministries will be responsible for distributing and managing the funds.

The health and medical strategy team, with input from expert advisers, also plans to hammer out a detailed plan for the Japan NIH by January and gain passage of authorizing legislation by March. The team will have to wrestle with questions such as whether the Japan NIH will have its own campus and directly manage research institutes, and what will happen to the education ministry's investigator-initiated grants, known in Japan as grants-in-aid for scientific research.

Many in the scientific community feel they have been left in the dark as the plans took shape. "Scientists really do not want to see that NIH plan undermine the grants-in-aid," says Yoshiko Takahashi, a developmental biologist at Kyoto University who serves on an education ministry advisory committee.

At least at first, the education ministry will continue to manage the grants-in-aid program separately from the health and medical strategy. But while the government is pumping money into Japan's NIH, the education ministry is seeking a mere 1% increase, to \$2.38 billion, for those grants.

—DENNIS NORMILE

Major Research Initiatives Under Japan's Health and Medical Strategy*

Cancer:	\$215 million
Neuroscience:	\$100 million
Infectious diseases:	\$61 million
Incurable diseases:	\$96 million
Medical technologies:	\$167 million
Regenerative medicine:	\$164 million
Genomic medicine:	\$130 million
Drug discovery:	\$310 million
Medical devices:	\$167 million

*proposed 2014 spending

researchers agree on the need to better connect basic [biomedical] research and clinical research," says Takashi Onishi, an engineer who is president of the Science Council of Japan, the nation's largest grouping of researchers. But he says the scientific community has had little input into the planning process so far, leading to fears that basic research could suffer.

Prime Minister Shinzo Abe started calling for a Japan NIH to be part of his economic growth strategy last spring. In endorsing the concept in June, the administration's Industrial Competitiveness Council noted that a Japan NIH could "strongly support the commercialization of innovative medical technologies" (*Science*, 21 June, p. 1384). Last month, Abe established a health and medical strategy promo-

PLANT BIOLOGY

Evolution Heresy? Epigenetics Underlies Heritable Plant Traits

LISBON—For some evolutionary biologists, just hearing the term epigenetics raises hackles. They balk at suggestions that something other than changes in DNA sequences—such as the chemical addition of methyl groups to DNA or other so-called epigenetic modifications—has a role in evolution. All of which guarantees that a provocative study presented at an evolutionary biology meeting* here last month will get close scrutiny. It found that heritable changes in plant flowering time and other traits were the result of epigenetics alone, unaided by any sequence changes.

The result could be a milestone in the debate, says Oliver Bosssdorf, a plant evolutionary ecologist from the University of Tübingen in Germany. “I expect this will become a landmark paper.” At the very least, it will stoke one of the hottest topics in evolutionary biology. Nontraditional mechanisms of inheritance were the focus of three symposia at the meeting, two with standing room only attendance. “It’s an exploding field,” says Etienne Danchin, an evolutionary biologist at CNRS, the French national research agency, in Toulouse.

For 50 years, changes in an organism’s DNA sequence have been considered the sole currency of evolution. Epigenetic mechanisms—methylation and other chemical modifications that do not alter the sequence of DNA bases—can also influence a trait, by suppressing or promoting a gene’s activity. But those changes were thought to be too ephemeral to affect evolution. Although a few researchers have shown that epigenetic modifications can persist through several generations, critics would point out that these studies couldn’t rule out undiscovered genetic variation might really be in play. “The burden of proof is on the epigeneticist,” Bosssdorf says.

Now, quantitative geneticist Frank Johannes of the University of Groningen in the Netherlands has tried to provide it. At the meeting, he described how he and colleagues tied DNA methylation patterns to heritable variation in flowering time and root length in different strains of the model plant *Arabidopsis thaliana*. The team was able to home in on differentially methylated DNA regions that were responsible for the variation—and

to show that DNA sequences near and far from those sites were almost identical in all the lines.

The origins of Johannes’s analysis lie in work by Vincent Colot from the Institut de Biologie de l’Ecole Normale Supérieure in Paris and Philippe Guerche and Frédéric Hospital, colleagues from the



Epi-evolution? Hundreds of specially bred lines of *Arabidopsis* (bottom) reveal that epigenetic modifications underlie heritable variation in flowering time.

French agricultural research agency, INRA. Seven years ago, they crossed two nearly genetically identical *Arabidopsis* strains, one normal and the other lacking a gene whose protein helped maintain methylation. Through further breeding, the researchers created 500 *Arabidopsis* strains with distinct patterns of low and high methylation sites in their genomes—a catalog of epigenetic variation that researchers could then study for links to physical traits in the plant

lines. “To create these lines was really brilliant,” Bosssdorf says.

In 2009, Johannes and his colleagues reported that some methylation patterns in these lines were stable over the eight generations tested. They also noticed differences in the plants’ flowering times and heights. Since then, Colot, Johannes, and their colleagues managed to pinpoint a few regions on the plant chromosomes that control flowering time and root length—and established those same sites had differences in methylation among the various plant lines.

Colot and his collaborators sequenced the genomes of 80 of the *Arabidopsis* lines studied, and with Johannes, have found almost no differences in the DNA at those same sites. The researchers also ruled out that the trait changes were caused by transposable elements, rogue DNA that’s typically held in check by methylation. “So the heritable basis [of the traits] had to be due to differential methylation,” Johannes concluded.

The study is “a huge step forward in showing that [methylation] has an impact in phenotype and matters in natural variation,” says Christina Richards, an evolutionary ecologist from the University of South Florida in Tampa.

Yet she and others note the work has limitations. “The source of variation was very artificial” in the lab-made strains, Richards notes, and *Arabidopsis*, with its unusually small plant genome, may not reflect what happens in other plants. “We still need more evidence that these are true effects and that this is something that influences evolution in natural populations,” adds Jon Ågren, an evolutionary ecologist at Uppsala University in Sweden.

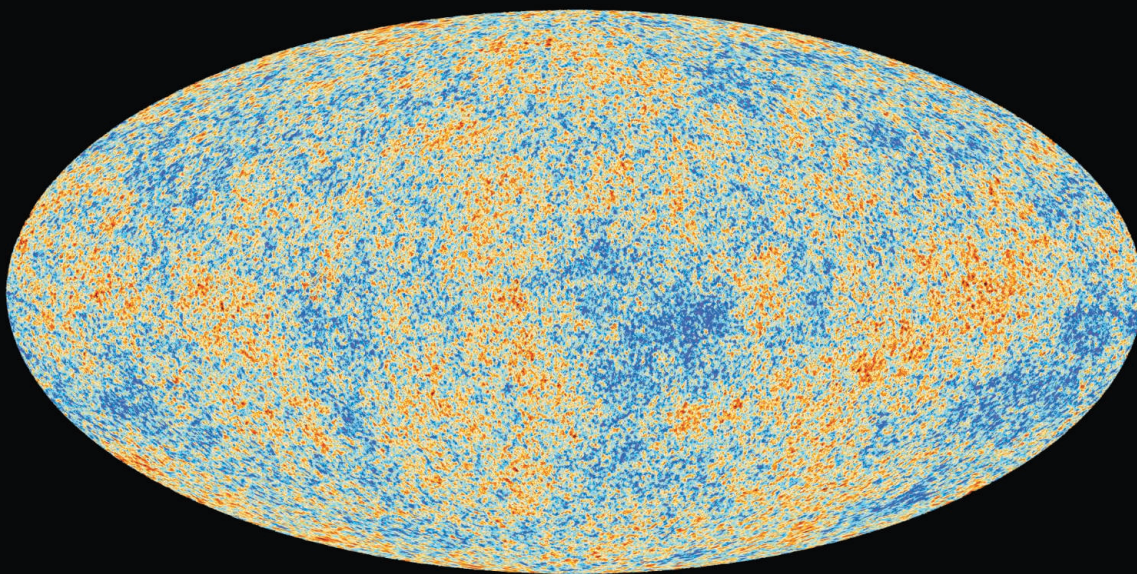
Johannes says his team found similar connections between methylation and flowering time in natural strains of this plant, indicating that the laboratory study has some relevance to wild populations. But the experiment doesn’t address the most controversial aspect of epigenetics and evolution—whether an environmental stress can alter an organism’s epigenetic markings and lead to a permanent trait change that’s acted upon by natural selection—a notion that, to some, sounds suspiciously like Lamarckism.

“A lot more hard evidence is necessary before one can claim that epigenetics plays a very important role in evolution,” says ecological geneticist Koen Verhoeven at the Netherlands Institute of Ecology in Wageningen. And, Richards adds, “people are really stubborn about accepting that that’s possible.”

—ELIZABETH PENNISI

CREDIT: VINCENT COLOT(2)

*The XIV Congress of the European Society for Evolutionary Biology was held 19–24 August.



Boxed In

In a year of triumphs for their reigning models, cosmologists and particle physicists yearn for something new that they can't explain

FOR COSMOLOGISTS, IT WAS THE MOST eagerly awaited result in a decade—and to some, an enormous letdown. This March, scientists working with the European Space Agency's Planck spacecraft presented the best study yet of the afterglow of the big bang, the so-called cosmic microwave background (CMB). Since the 1990s, measurements of the microwaves had confirmed that the cosmos burst into existence instantaneously and revealed how much matter and energy it contains. Cosmologists hoped Planck would provide even deeper insights.

Planck did everything it was supposed to do. Launched in 2009, it measured tiny variations in the temperature of the CMB across the sky with exquisite precision. The results were a near-perfect fit to what theory predicted. And that was the problem: "There's no evidence that there's new physics required beyond what we knew before," says George Efstathiou, a cosmologist at the University of Cambridge in the United Kingdom and member of the Planck team.

Cosmologists aren't alone in feeling stymied. For decades, particle physicists have struggled in vain to find something their own standard model cannot explain—with one notable exception (see sidebar, p. 1058). Last year, physicists discovered a particle called the Higgs boson, the last miss-

ing piece in that master theory, and this year they confirmed that the Higgs has the basic properties predicted by the standard model. Many would be happier if it didn't. "Everybody would say, 'Yay!'" says Robert Plunkett of Fermi National Accelerator Laboratory (Fermilab) in Batavia, Illinois.

Cosmologists and particle physicists haven't explained everything. Neither of their standard models, for example, sheds any light on origins of the mysterious dark matter whose gravity binds the galaxies or the bizarre dark energy that's accelerating the expansion of the universe. Still, what the models do explain, they explain so well that scientists find themselves explicitly struggling to poke holes in their own theories. "We know that they're incomplete," Efstathiou says. "So you just have to push until the models crack—and they will crack."

But where? Theorists have dreamed up all sorts of wild theories beyond the standard models. But, practically speaking, experimenters point to a handful of most-promising spots in which to dig for something new—although none guarantees a treasure.

The Higgs and what else?

For particle physicists, the question is simple: Can they find something new besides the Higgs boson? If so, it is most likely to appear

in the birthplace of the Higgs itself: the 27-kilometer-long Large Hadron Collider (LHC) at CERN, near Geneva, Switzerland. Since it started taking data in 2010, the LHC has collected only 1% of the total expected by 2030. And some physicists say the discovery of the Higgs itself suggests other new particles will turn up in the 99% to come.

The argument stems from the role of the Higgs. Ordinary matter consists of a handful of particles: the up quarks and down quarks that form the protons and neutrons in atomic nuclei, the electrons that flesh out the atom, and the neutrinos that emerge in nuclear decay called beta decay. These particles have two sets of heavier cousins that can be blasted into fleeting existence with atom smashers. The standard model describes how such particles interact through three forces: the electromagnetic force, which creates light; the strong force, which binds quarks; and the weak force, which causes beta decay. (The theory doesn't include gravity.)

But there's a catch: Assigning masses to the particles spoils the mathematical symmetries on which the whole theoretical construct depends. So somehow the particles must create their own mass by interacting with one another.

That's where the Higgs comes in. Physicists assume the vacuum contains a field a bit

CREDIT: ESA/PLANCK COLLABORATION

Picture perfect. Standard cosmology accounts for every ripple in the cosmic microwave background.

like an electric field. Particles interact with that “Higgs field” to gain energy and, thanks to the equation $E = mc^2$, mass. Just as an electric field consists of quantum particles called photons, the Higgs field consists of Higgs bosons lurking “virtually” in the vacuum. When physicists blasted the Higgs out of hiding, they proved nature uses this scheme.

That feat also suggests more particles await discovery. In a bit of feedback, particles popping in and out of the vacuum should affect the Higgs, and standard model particles should make its mass soar a quadrillion times higher than is observed. Either that or a certain parameter must be fine-tuned to 23-digit precision to cancel out the excess. Such a coincidence is far-fetched, physicists argue. Instead, they say, new particles should exist that would counteract the effect in a more “natural” way.

In particular, something must exist to counteract the one standard model particle that interacts with the Higgs most powerfully, the weighty top quark. “The argument is really ‘We’ve got to find a partner to the top quark,’” says Joseph Incandela of the University of California (UC), Santa Barbara, spokesperson for the team working with the CMS particle detector at the LHC, which spotted the Higgs. Such particles should be within the LHC’s reach, says Beate Heinemann of UC Berkeley, a deputy spokesperson for the team working with the ATLAS detector, which also spotted the Higgs. “If they’re not light enough so that we can see them, then they’re also so heavy that they won’t help with the problem,” she says.

Some physicists say that this naturalness argument has had its day. Decades ago, they note, the same argument spawned a concept called supersymmetry, which posits for each known particle a massive “superpartner.” Yet collider experiments haven’t turned up a single superpartner, says Guido Altarelli, a theorist at the University of Rome (Roma Tre), so the whole idea needs a rethink. “If you ask me whether there will be new physics at the LHC, I don’t know,” Altarelli says. “However, based on what we have already seen, I strongly suspect the answer is no.”

Physicists should know in a few years. The LHC is undergoing repairs that should nearly double its energy when it comes back on in 2015. A couple of years’ worth of data should then tell physicists if there’s anything within the collider’s reach.

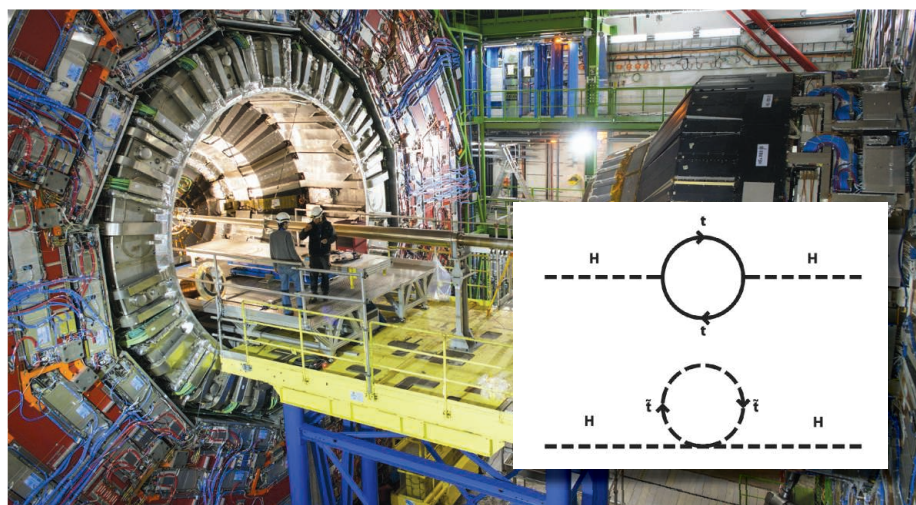
If nothing turns up, researchers may have to seek new physics in more precise mea-

surements of familiar particles. For example, the LHC feeds a smaller detector called LHCb that studies particles called B mesons, which contain a hefty bottom quark and a lighter antiquark. Those particles’ properties are affected by other particles popping in and out of existence within them. So if they stray too far from the standard model predictions, the discrepancies could be a sign of new particles at work—possibly ones too heavy to be produced by the LHC.

“You have at least an equal chance to see new physics in these precision experiments as you do directly at the LHC, maybe even

Ordinary matter settled into the clumps to form the galaxies.

Λ CDM fits the data—including the latest results from Planck—with breathtaking precision, but as a theory many find it wanting. It assumes only generic definitions of ingredients such as dark matter and dark energy (for example, dark matter is matter that doesn’t interact with radiation) and doesn’t say what they really are. “It’s not a theory, it’s math,” says Adam Riess, a cosmologist at the Space Telescope Science Institute in Baltimore, Maryland. “I don’t find it that satisfying that the math is simple.”



Weight check. A Higgs boson should gain mass by turning into a top quark and an anti-top quark and back into a Higgs (*inset, top*). Physicists at the LHC (*pictured*) suspect a new particle counters that effect (*inset, bottom*).

more,” says Hassan Jawahery, an LHCb member from the University of Maryland, College Park. Figuring out what you’ve found may be harder, however.

Filling in the known unknowns

An equally fruitful place to hunt for new physics is the universe at large. Some cosmologists, too, feel they have reached a stalemate with their own standard model—but unlike the standard model of particle physics, theirs is tantalizingly incomplete.

Known as Λ CDM (pronounced “lambda CDM”), the model gives a simple recipe for the cosmos: 5% ordinary matter, 27% cold dark matter (the CDM), and 68% dark energy. (The “ Λ ” stands for the simplest version of dark energy.) Within the first 10^{-32} seconds, it holds, the universe doubled and redoubled its size 60 times in a faster-than-light growth spurt called “inflation,” which pulled space geometrically “flat” like a taut bedsheet. Inflation also hugely magnified tiny quantum fluctuations in the universe’s density, into which dark matter gravitated to form a “cosmic web” of vast filaments and clumps.

The gaps may open an opportunity. For example, inflation is essentially a useful “just-so story” that explains the flatness and near-uniformity of the universe. But close study of the CMB could help reveal what drove inflation—and the answer could point to physics beyond our current understanding.

The microwaves in the CMB are polarized, like light reflecting off a lake. And gravity waves rippling through the universe during inflation should have left swirls known as “B modes” in the pattern of polarization across the sky. The strength of the swirls should reveal the energy density of the universe during inflation and give theorists their first solid data on the quantum process that caused the blowup. A half-dozen teams, including Planck’s, are racing to spot such “primordial” B modes.

Others hope to decipher dark energy, perhaps the biggest mystery in all of physics. Cosmologists discovered it 15 years ago when they used stellar explosions called type Ia supernovae to trace the history of the universe’s expansion. In shocking contrast to expectations, they found that the expansion is

The Unruly Neutrino

One clan of particles shamelessly flouts the rules of physicists' standard model: neutrinos. The theory says that they shouldn't have mass. Yet they do, and from the perspective of the theory, they misbehave wildly. "In neutrino physics there are places where you could have 10, 20, or 50% deviations from the standard model," says Patrick Huber, a theorist at the Virginia Polytechnic Institute and State University in Blacksburg. For those seeking new physics, "that makes it a worthwhile place to look."

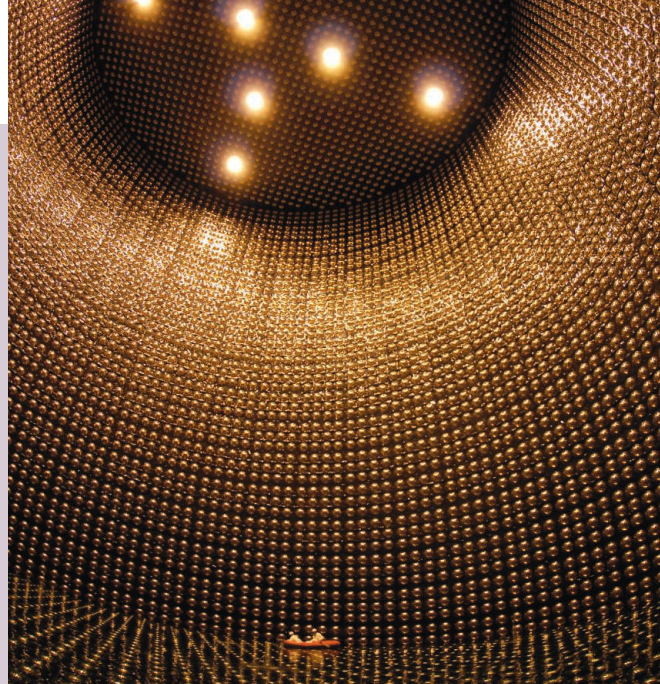
Born of a type of nuclear decay, neutrinos interact with matter so weakly that they can easily zip through a light-year of lead. They come in different "flavors," and in 1998, physicists working with the Super-Kamiokande detector in a mine near Hida, Japan, showed that neutrinos generated when cosmic rays strike the atmosphere change flavor in flight. That morphing proves that neutrinos have mass, though just a trace—less than a billionth as much as an electron. Were neutrinos massless, then according to Einstein's theory of relativity, they would have to travel at light speed. In that case, time would stand still for them and change would be impossible.

For all their unruliness, "you're absolutely allowed to say that there is an emerging picture" of neutrinos, says André de Gouvêa, a theorist at Northwestern University in Evanston, Illinois. Their three flavors—electron, muon, and tau—blend into one another in "oscillations" that are described by just six parameters: the three differences in the masses, which determine the speeds of the oscillations, and three abstract mixing angles, which determine how much different flavors mix. In just the past 18 months that model has come in to much sharper focus.

In March 2012, physicists with the Daya Bay Reactor Neutrino Experiment in China measured the last unknown mixing angle and found that it was bigger than many had assumed. All three mixing angles are now known to be bigger than zero, and that result implies that neutrinos and antineutrinos could oscillate differently—an asymmetry called CP violation that could help explain how the universe generated so much more matter than antimatter. The Daya Bay result in particular suggests that CP violation could be relatively easy to spot—if it's there—says Robert Plunkett of Fermi National Accelerator Laboratory (Fermilab) in Batavia, Illinois: "Things that were thought to be very difficult are within striking distance."

The emerging model grew even crisper this March, when cosmologists with the European Space Agency's Planck spacecraft released their study of the cosmic microwave background. The analysis probes the number of neutrino flavors and casts doubt on previous hints that a fourth, "sterile" neutrino might exist. "The vanilla cosmology with three neutrinos works great," de Gouvêa says. "That's sad but true."

Physicists plan to put their understanding to the acid test in ever larger experiments that shoot neutrinos hundreds of kilometers through Earth, allowing them to change flavors along the way. In the United States, the proposed Long-Baseline Neutrino Experiment would fire neutrinos 1300 kilometers from Fermilab to a detector in an abandoned



Elusive. To detect even a few neutrinos, physicists need huge detectors such as Japan's Super-Kamiokande, which holds 50,000 tonnes of water.

mine in South Dakota. In Japan, the planned Hyper-Kamiokande Experiment would shoot neutrinos 295 kilometers to a detector 20 times the size of Super-Kamiokande.

Physicists hope that by taking enough different kinds of measurements, they may uncover discrepancies that challenge their current neutrino model. "If we try measuring neutrino mixing in many different ways, will surprises emerge?" asks Mary Bishai, a physicist at Brookhaven National Laboratory in Upton, New York. "Will the three-flavor model start to break down?"

Physicists would also like to know how neutrinos get their mass in the first place. Like other particles in the standard model, they could acquire it from interactions with the Higgs field. Or, more tantalizingly, they might get their mass through a so-called seesaw mechanism, which would relate the neutrino's tiny mass to physics at an energy scale far higher than any particle accelerator could ever reach. But for this to happen, the neutrino must have one odd property: It must be its own antiparticle.

To find out if it is, physicists are using underground detectors to look for a new type of nuclear decay called neutrinoless double beta decay, which can occur only if the neutrino is its own antiparticle. So far, no clear sightings have turned up. In July, the GERDA experiment in Italy's subterranean Gran Sasso National Laboratory showed that a previously claimed observation in the isotope germanium-76 was spurious. If the decay exists, many researchers suspect it will take far bigger detectors, weighing a tonne or more, to spot it. Or it could be immeasurably small.

Still, neutrino physics is the one place researchers have peeked beyond the standard model, giving these elusive particles a powerful allure. **—A. C.**

speeding up, as if powered by some form of space-stretching energy.

The key question is whether that dark energy is a property of space itself—a "cosmological constant," which Einstein denoted Λ —or something in space. To tell the difference, cosmologists want to know how the density of dark energy has changed over cosmic time. If dark energy is part of space, then its density should have remained constant. If it's something in space, then its

density may have fallen as space expanded. The difference is captured in a single parameter, w , which should be -1 for a cosmological constant and something like -0.9 for something else. "Our fondest hope is that we can give one more clue to the theorists," Riess says. "What if w isn't equal to -1 ? That would be pointing in a direction."

Planck may have already done a little pointing, Riess says. Its data yields a value for the expansion rate of the uni-

verse that differs slightly from the value measured directly by studying relatively nearby stars and galaxies. That could be a clue that dark energy has changed and isn't a cosmological constant, he says, although the discrepancy is too small to stake a claim on.

Other cosmologists are probing dark energy by looking at how structures such as galaxy clusters grew over time—a process slowed by dark energy's space-stretching

effect. They are eager to see how the results fit with those from other methods such as supernovae, says Marcelle Soares-Santos, a Fermilab physicist working on the Dark Energy Survey, a 5-year study using the 4-meter Blanco telescope at the Cerro Tololo Inter-American Observatory in Chile. If dark-energy measurements from supernovae and from structure growth disagree, then gravity might behave differently on different scales, and dark energy could be an illusion produced by scientist's misunderstanding of gravity.

Common ground: stalking dark matter

Perhaps the most fertile place to advance both particle physics and cosmology is in the area where the fields explicitly overlap: the search for dark matter. For 80 years, astronomers and cosmologists have seen its gravitational fingerprints. Now, physicists hope to spot particles of the stuff floating about.

Dark matter could consist of so-called weakly interacting massive particles, or WIMPs: hypothetical beefy bits of matter that interact with ordinary matter only through the feeble weak force. The idea of WIMPs was born in 1980s, when theorists noted that if the infant universe spawned such particles, then just enough of them should linger now to provide the dark matter—provided they weigh between about 10 and 1000 times as much as a proton. Known as the “WIMP miracle,” that coincidence helped make WIMPs the leading dark-matter candidate.

Scientists hope to detect WIMPs in several ways. Perhaps the LHC will blast them into existence—although it hasn't yet. Or astrophysicists hope to spot them colliding in space and annihilating one another to produce other particles. In 2008, physicists with an Italian satellite experiment called PAMELA observed an excess of high-energy positrons that could come from such annihilations—although the positrons could also be coming from a more mundane source, such as a pulsar.

Most directly, physicists hope to see passing WIMPs as they ping off atomic nuclei in sensitive particle detectors. “I’m biased, but I still believe that the direct search for dark matter is one of the most promising ways we can look for how the standard model is broken,” says Richard Gaitskell, a physicist at Brown University who works on a detector called LUX at the Sanford Underground Research Facility in Lead, South Dakota.

Teams have been leap-frogging one another in building bigger and more sensitive detectors deep underground, where they're shielded from ordinary radiation. Researchers with the Cryogenic Dark Matter Search (CDMS) are running a detector filled with 10 kilograms of germanium in the

but the Higgs exchange regime remains. “That’s right where we are,” Weiner says. “That’s the regime that the current experiments are probing.”

In April, the CDMS team reported three events that could be signs of WIMPs a few times as massive as a proton. And for more than a decade, researchers with the DAMA experiment in Gran Sasso have claimed a signal of such light WIMPs. But those results remain to be confirmed, and the most likely mass range is still a few hundred times the mass of a proton, says Blas Cabrera, a CDMS team member from Stanford University in Palo Alto, California. The tonne-scale detectors now being planned should be sensitive to those masses, Cabrera says. “Probably 5 years from now is when we will have some more clarity,” he says.

The unexpected

Particle physicists and cosmologists have no assurances that any of the possibilities will come to pass. If nothing pans out, some acknowledge, they could find themselves simply verifying their prevailing theories over and over again. “It could easily happen that we come up against the limit of our understanding,” says Saul Perlmutter, a cosmologist at Lawrence Berkeley National Laboratory in California.

Still, Perlmutter says he’s optimistic that more breakthroughs will come in unexpected ways—as one did 15 years ago, when he and others

first detected dark energy. “Pushing to see new regimes of the universe has been one of the most productive games we’ve played,” he says, “and not because you get the results you’re after, but because you find things you didn’t expect.”

Daniel Eisenstein, a cosmologist at Harvard University who is studying the large-scale structure of the universe, agrees. “I guess the question is, will we be asking the same questions 20 years from now?” he says. “And I think there is every possibility that we’ll be on to some significantly different threads.”

—ADRIAN CHO

THE STANDARD MODELS

	PARTICLE PHYSICS	COSMOLOGY
What it is	A quantum-mechanical theory of the fundamental building blocks of matter and three of the four forces of nature	A theory of the content and evolution of the universe
Ingredients	The roster of known fundamental particles and a mathematical clockwork that explains the origins of the weak, strong, and electromagnetic forces in terms of mathematical symmetries	Generic definitions of dark matter and dark energy, Einstein's theory of gravity, and the concept of inflation—the notion that the infant universe ballooned at greater-than-light speed
Accomplishments	Accounts for everything seen with atom-smashers so far	Through computer simulations, reproduces statistically the properties of the cosmic microwave background, the distribution of the galaxies, etc.
Shortcomings	Doesn't include gravity, dark matter, or dark energy. Doesn't account for neutrino mass. Possesses curious, arbitrary structure	Doesn't explain what dark matter or dark energy are, or how inflation happened

Soudan mine in Minnesota. The LUX detector contains 370 kilograms of liquid xenon and should soon start taking data. Next year, the XENON team will turn on its new 1-tonne detector in Italy's subterranean Gran Sasso National Laboratory. Bigger devices are in the works.

That race is entering an intriguing phase, says Neal Weiner, a theorist at New York University in New York City. WIMPs ought to interact with ordinary matter primarily in one of two ways: either by exchanging a quantum particle called a Z boson or by exchanging a Higgs boson. Experiments have ruled out the stronger Z boson process,



NORTH KOREA

Sizing Up a Slumbering Giant

A thousand years ago, Mount Paektu unleashed one of the biggest eruptions in recent history. An unusual collaboration aims to learn why the volcano is so potent

People in the hamlet of Sin Mu Song in northwestern North Korea had never laid eyes on a Westerner before James Hammond set to work in a nearby potato field last month. With North Korean colleagues, the seismologist from Imperial College London installed a broadband seismometer in an underground concrete shelter. Afterward, he sampled the local tobacco, rolled in a piece of Korean newspaper. “It was really smooth,” he says, like “a pretty nice cigar.”

Hammond had reason to celebrate. He and two U.K.-based colleagues had just completed the first season of a trailblazing project to assess the eruption history, underlying

structure, and potential for future unrest at Mount Paektu, a volcano straddling the border between the Democratic People’s Republic of Korea (DPRK) and China. “We felt very privileged,” says Clive Oppenheimer, a volcanologist at the University of Cambridge in the United Kingdom.

Paektu is quiet now, but it has a fearsome past. In the middle of the 10th century C.E., the volcano, called Changbai in China, uncorked the Millennium Eruption, one of the largest of the past 10,000 years. A decade ago, swarms of small tremors at the volcano set Chinese and Korean authorities on edge, prompting both nations to step up monitoring.

The geological spasms subsided, but concerns that Paektu may be poised to blow again have opened the door to one of the first substantive scientific collaborations between DPRK and the West.

Getting the remarkable enterprise off the ground wasn’t easy. It took 2 years to win permissions from the U.K. and U.S. governments to ship crucial instruments to North Korea and the last-minute intervention

of the United Kingdom’s Royal Society to sign agreements with DPRK organizations that allowed fieldwork to proceed. But as Martyn Poliakoff, foreign secretary of the Royal Society, puts it, “We felt it was something that is well worth doing.”

A scarred land

The week of fieldwork “really was spectacular,” says Hammond, who installed six broadband seismometers on a line running east from the volcano. The instruments will listen for any stirring beneath Paektu. They will also register seismic waves from across the globe as they ripple through Paektu’s plumbing, allowing Hammond and company to image its magma chamber and surrounding rock.

While Hammond set to work, Oppenheimer and his graduate student, Kayla Iacovino, a U.S. citizen, collected samples, mostly pumice, that should reveal new details about the sequence of events during the Millennium Eruption and recent, smaller eruptions.

The scars from the ancient explosion are still visible. The blast heaped ash and pumice on 33,000 square kilometers of northeast China and Korea, charring and entombing a thick forest and creating a barren landscape that to this day is largely treeless. Gargantuan pyroclastic flows—avalanches of superheated gas and debris—seared whole valleys and lined their walls with otherworldly ignimbrite rock tubes. In recent history, only the 1815 Tambora eruption in Indonesia—responsible for the “year without a summer”—has rivaled it.

Paektu’s ferocity is an enigma. It lies hundreds of kilometers west of the Ring of



Wasteland. Geologist Kim Ju Song (*foreground*) and a colleague examine Millennium Eruption deposits on Paektu’s eastern flank.

CREDITS (TOP TO BOTTOM): CLIVE OPPENHEIMER; KOSIMA WEBER-LIU

On the prowl. Researchers on last month's expedition searched for rocks that could shed light on past eruptions.

Fire, where colliding tectonic plates along the edge of the Pacific Basin fuel many of the world's most powerful volcanoes. One possible explanation for its potency is water squeezed from minerals in the subducting Pacific Plate, 600 kilometers below the volcano. Adding water to hot mantle rock can cause it to melt, creating a magma supply.

But the chemistry of Paektu's pumice and other data cast doubt on that explanation, says James Gill, a volcanologist at the University of California, Santa Cruz, who has conducted fieldwork on the Chinese side of the volcano since 1990.

Gill sees signs that the volcano is instead stoked by a mantle plume—a deep-rooted conduit that carries magma from the lower mantle to the surface. Backing that idea are unpublished data from a seismic array in China showing a “hole” in the subduction slab under Paektu. But other mantle processes may also be at play, and research on the volcano's Chinese flanks has failed to settle the question.

That's why Oppenheimer and Hammond seized an opportunity that arose 2 years ago (*Science*, 4 November 2011, p. 584). The Pyongyang International Information Center on New Technology and Economy, or PIINTEC, a nongovernment organization, had reached out to Oppenheimer, a specialist on volcanic gases and author of a popular textbook, proposing a collaborative project. He roped in Hammond, a comrade in arms from a volcanological project in the blazing hot back-of-Eritrea.

North Korea offered different challenges. The first was funding. Hammond got the big-ticket items for free: The U.K. Natural Environment Research Council's Geophysical Equipment Facility loaned the seismometers. The Korean Earthquake Bureau (KEB) in Pyongyang, which is operating the array, agreed to periodically download data onto hard disks and send them to the Environmental Education Media Project, a nonprofit organization in Beijing that serves as a liaison between North Korea and the West. It will forward the data to Hammond.

To house the seismometers, KEB staff members in recent months erected concrete huts at three of their field stations, including one beside the picturesque caldera lake, Lake Chon. Farther out from Paektu, KEB built

bunkers for instruments in three villages, including one in the potato field at Sin Mu Song, where residents have promised to keep an eye on the equipment to deter vandals.

Funding for station construction, maintenance, and logistics came from the Richard Lounsbery Foundation in Washington, D.C., via a grant to AAAS, *Science*'s publisher. Both organizations are assiduously reaching out to scientists in nations having difficult relations with the United States. The project is off to a great start, says Norman Neureiter, senior adviser to AAAS's Center for Science Diplomacy. “Cooperation based on a real desire to get the job done has been excellent on both sides,” he says.

U.N. and U.S. export controls and sanctions on North Korea posed a tougher challenge. They prohibit a long list of instruments and devices, including ones as simple as thumb drives and cameras, from being shipped or carried into the country, even for temporary, personal use. AAAS spent months working with the U.S. State Department and the Commerce Department to land an export license for the project. The U.K. government's review of a separate license application took even longer, with approval coming just days before the seismometers had to be put on a plane for Pyongyang. “Everybody behaved sensibly and didn't get into a panic,” Poliakov says.

Another challenge was fulfilling the North Koreans' desire for legal documents spelling out the research plan and each party's responsibilities. It was too complicated for KEB and PIINTEC to sign such a document with a U.S. organization, but the Royal Society came to the rescue.

Delving deeper

Once in North Korea, Oppenheimer and Iacovino spent several days collecting samples at favorite outcrops of senior KEB geologist Kim Ju Song and his colleagues in the bureau and the DPRK Academy of Sciences. A highlight was excavating at the base of a 10-meter-thick blanket of pumice from the Millennium Eruption. “It's always interesting to see what was on the ground immediately before a big eruption,” Oppenheimer says. Pollen, for instance, can reveal the season that the ash fell. And deposits at the bottom of the heap show how the eruption began to unfold—information that could help researchers assess the hazards of a modern-day Millennium-scale eruption.

Oppenheimer and Iacovino also plan to study volatiles trapped within crystals in the pumice, which can hold clues to the types and amounts of gases released. Such details

could explain why the Millennium Eruption, unlike other eruptions on that scale, did not cool Earth's climate—a curious fact that volcanologist Xu Jiandong of the China Earthquake Administration in Beijing and his colleagues reported in January in *Geophysical Research Letters*.

The black pumice at the top of the pile presents its own mystery: Was it deposited by pyroclastic flows during the Millennium Eruption, or by one of a handful of later blasts known from historical records? Characterizing these eruptions, including the most recent in 1903, can reveal how Paektu's plumbing has changed since the Millennium Eruption. Oppenheimer and Iacovino also took a motor-



boat out on Lake Chon to observe volcanic gases bubbling to the surface. They intend to return next summer to collect and analyze the gases, which could hold clues to the viscosity of the magma. More viscous magma would take higher pressure to eject, raising the odds of a more powerful eruption.

In future expeditions, the team hopes to image the volcano's magma chambers with magnetotelluric sensors, which map subsurface variations in conductivity. They also hope to host Korean colleagues in the United Kingdom, for training in volcano monitoring and to collaborate on analyses of rock samples and data interpretation. Publications arising from the fieldwork will surely have DPRK co-authors, Oppenheimer says. Hammond envisions a more extensive seismometer array. But a full picture of the mountain's insides will also require data from stations across the border in China, Gill says—which means more science diplomacy.

Still, by simply beating the odds and nurturing mutual respect, last month's expedition has revealed possibilities for scientific cooperation hitherto unimaginable—reason enough for the scientists and their backers to break out the cigars.

—RICHARD STONE

Online

sciencemag.org



Podcast interview
with author
Richard Stone ([http://
scim.ag/pod_6150](http://scim.ag/pod_6150)).

LETTERS

edited by Jennifer Sills

The Risky Road to Mars

IN THEIR REPORT “MEASUREMENTS OF energetic particle radiation in transit to Mars on the Mars Science Laboratory” (31 May, p. 1080), C. Zeitlin *et al.* try to assess the radiation risks to astronauts from exposure to galactic cosmic rays and solar flares during a manned expedition to Mars. They conclude that astronauts will receive about two-thirds of the lifetime exposure limit for humans during the round trip. I believe the dose could be even higher.

Zeitlin *et al.* did not consider the secondary effects of radiation-induced nuclear reactions in the human body. Nuclear reactions of protons and alpha particles with carbon, nitrogen, and oxygen nuclei lead to formation of lithium, beryllium, and boron nuclei. These reactions are most likely to happen for incident protons and alphas with energies between 5 and 100 MeV, particularly those between 10 and 50 MeV (1).



Astronaut on Mars (artist's conception)

The lithium, beryllium, and boron nuclei produced in such reactions are low in energy and much more heavily ionizing (i.e., more dangerous) than higher-energy protons or alphas. Thus, this type of radiation, below 100 MeV, is most likely to produce significant damage in human tissue. This radiation comes not only from the primary flare and galactic cosmic ray fluxes studied by Zeitlin *et al.*, but also from the secondary flux of protons and alphas originating in the space capsule shielding, as well as from nuclear reactions. In the event of a significant solar flare event while an astronaut is outside the space capsule, the radiation effects would be further magnified, because the reaction probabilities are highest at energies corresponding to the solar flare spectrum.

V. E. VIOLA

Golden, CO 80401, USA. E-mail: viola@indiana.edu

Reference

1. S. M. Read, V. E. Viola, *Atomic Data and Nuclear Data Tables* **31**, 359 (1984).

Response

IT IS TRUE THAT LOW-ENERGY LITHIUM, BERYLLIUM, and boron are produced in interactions between energetic protons and other ions with target carbon, nitrogen, and oxygen nuclei. As Viola describes, these nuclear fragments are low in energy and can have linear energy transfers of hundreds of keV/μm in water. However, such particles typically have very short ranges, traveling just tens or hundreds of micrometers in water before coming to rest. Thus, they produce very large, but highly localized, energy depositions in tissue. The biological effects of these types of energy depositions are not well known. According to the widely used International Commission on Radiological Protection Publication 60 (1), the quality factor—the factor by which a dose of radiation must be multiplied to estimate

the associated biological damage—for this type of energy deposition reaches a peak at 100 keV/μm, then falls with increasing linear energy transfer due to the “overkill” effect, in which more energy is deposited locally than is required to kill cells (2). Many or most of the lithium, beryllium, and boron fragments in this category have linear energy transfers in the overkill region.

Our measurements during the Curiosity rover's transit to Mars are reported as point values of dose and dose equivalent—that is, they are the values that would be received at skin depth and not deeper in the body were an astronaut to be placed in the same radiation field. Extrapolation to points inside the body requires use of a radiation transport model, and properly constructed models (3, 4) take account of all nuclear interaction products,

including the low-energy light ions mentioned by Viola. Thus, transport model calculations based on our measurements can accurately include this contribution to the physical dose. How these and other contributions with high linear energy transfers should be weighted in terms of their biological effects is an open question, one that is the subject of much current research.

CARY ZEITLIN

Southwest Research Institute, Boulder, CO 80302, USA.
E-mail: zeitlin@boulder.swri.edu

References

1. ICRP, “1990 Recommendations of the International Commission on Radiological Protection” [ICRP Publication 60, Ann. ICRP 21 (1-3), 1991]; www.icrp.org/publication.asp?id=ICRP%20Publication%2060.
2. J. Kiefer, *Int. J. Radiat. Biol.* **48**, 873 (1985).
3. T. C. Slaba *et al.*, *J. Comput. Phys.* **229**, 9397 (2010).
4. S. Agostinelli *et al.*, *Nucl. Instr. Meth. A* **506**, 250 (2003).

Controversial Salt Report Peppered with Uncertainty

A RECENT INSTITUTE OF MEDICINE (IOM) assessment (1) provoked controversy by concluding that there is a lack of evidence for health benefits of reducing sodium intake to the very low levels recommended by some authoritative groups (“Report reignites battle over low-salt diets,” K. Kupferschmidt, *News & Analysis*, 24 May, p. 908). The IOM report was remarkable not only for its cautious analysis of the evidence—the authors said they could not define a “healthy” sodium intake range—but for its acknowledgment that salt’s contribution to disease had been controversial for four decades. By contrast, in 2010, when the IOM issued “Strategies to reduce sodium intake in the United States,” the committee chair stated, “For 40 years we have known about the relationship between sodium and the development of...life threatening diseases” (2). The new report shattered that sense of certitude. Unfortunately, instead of embracing the IOM analysis as an opportunity to pause to consider new evidence and retarget recommendations, authorities involved in the salt issue have largely dismissed, ignored, or explained away the report.

The American Heart Association (AHA) used the most aggressive message management strategy: It forcefully questioned the IOM committee’s interpretation of the science (3). Advocacy groups and scientists associated with the campaign to reduce salt consumption adopted another tactic: They asserted that the IOM’s nuanced analysis had been misrepresented in media reports that had emphasized disagreement over an issue of marginal importance—the evidentiary basis for recommending that at-risk groups totaling half the U.S. population reduce their sodium intake to 1500 mg per day, a level achieved by few consumers. They then claimed that such media reports distracted from the central message upon which everyone agreed: that excessive salt intake was perilous for health (4).

Those affiliated with the report itself also sought to temper the impression that the IOM had muddied the scientific waters on salt. In an unusual 3 June letter to U.S. Secretary of Health and Human Services Kathleen Sebelius, Harvey Fineberg, President of the IOM, lamented that some press outlets had “misstated” the report’s conclusions and emphasized that the Centers for Disease Control and Prevention (CDC), IOM, AHA, and other authorities were “congruent” in supporting a population-wide reduction in sodium intake (5). Three days later, a com-

mentary by three members of the IOM salt committee likewise stressed that the Dietary Guidelines for Americans (DGA), IOM, AHA, and the World Health Organization (WHO) were “congruent” in the belief that excess sodium intake should be reduced (6).

Other key players essentially ignored the IOM study. The New York City Health Department, which leads a coalition of health organizations in a partnership with industry to reduce sodium in restaurant and packaged foods, and the CDC—the agency that commissioned the report—both took this approach. Global health leaders also disregarded the IOM analysis: Two weeks after the report’s release, representatives from some 200 nations at the 66th World Health Assembly adopted a resolution to combat noncommunicable diseases that included a plan to cut salt intake 30% by 2025 in an effort to achieve the WHO’s sodium target of less than 2000 mg daily—a level at which the IOM said there was no evidence of health benefit (7).

At this moment, the mixed scientific picture of salt that now bears the imprimatur of the prestigious IOM may well be addressed by a period of self-imposed silence. But in the next year, when new U.S. Dietary Guidelines must be drafted, it is certain that opponents of strict salt regulation will use the IOM’s findings to support their demands that policy recommendations be grounded in evidence of the highest caliber—a standard that those concerned with the hazards of salt assert would be almost impossible to meet.

This latest chapter in the salt saga underscores a fundamental challenge faced by policy-makers responsible for confronting morbidity and mortality at the population level: What should be done when the evidence appears to be uncertain or more complex than desirable from the perspective of public health messaging (8)? However challenging, we propose that a reflective policy approach, flexible enough to accommodate changing evidence, would serve the public well and reinforce the public trust in evidence-informed public health policy.

DAVID MERRITT JOHNS,^{1*} RONALD BAYER,¹
SANDRO GALEA²

¹Department of Sociomedical Sciences, Mailman School of Public Health, Columbia University, New York, NY 10032, USA. ²Department of Epidemiology, Mailman School of Public Health, Columbia University, New York, NY 10032, USA.

*Corresponding author. E-mail: dmj2119@columbia.edu

References

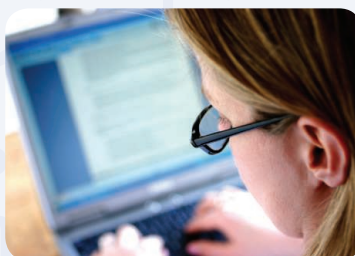
1. IOM, “Sodium intake in populations: Assessment of Evidence” (National Academies Press, Washington, DC, 2013).
2. IOM, “FDA should set standards for salt added to processed foods, prepared meals”

How do you engage?

AAAS Early Career Award for Public Engagement with Science

Nominations are now open. For eligibility information and instructions, visit aaas.org/go/PESaward.

Deadline October 15



ADVANCING SCIENCE, SERVING SOCIETY

LETTERS

(<http://www8.nationalacademies.org/onpinews/newsitem.aspx?RecordID=12818>).

3. American Heart Association, "New IOM report an incomplete review of sodium's impact, says American Heart Association" (<http://newsroom.heart.org/news/new-iom-report-an-incomplete-review-of-sodiums-impact-says-american-heart-association>).
4. Center for Science in the Public Interest, Letter to Mdmes. Kolata, Strauch, and Sullivan and Messrs. Boffey and Rosenthal (http://cspinet.org/new/pdf/scientists_letter_to_nyt_about_iom_sodium_study_-_5-24-13.pdf).
5. H. Fineberg, Letter to the Honorable Kathleen Sebelius (http://cspinet.org/new/pdf/iom_fineberg_letter_to_sibelius06032013.pdf).
6. B. L. Strom, C. M. Anderson, J. H. Ix, *JAMA* **310**, 31 (2013).
7. 66th World Health Assembly, "Follow-up to the political declaration of the high-level meeting of the General Assembly on the prevention and control of non-communicable diseases" (http://ncdalliance.org/sites/default/files/rfiles/Final%20OR%20with%20GAP_A66_R10-en.pdf).
8. R. Bayer, D. M. Johns, S. Galea, *Health Affairs* **31**, 2738 (2012).

CORRECTIONS AND CLARIFICATIONS

News Focus: "Discovery of a new titi monkey" by A. Regalado (2 August, p. 451). The name of the conservation group created by Javier García was incorrectly given as Herencia Nacional; the correct name is Herencia Natural (Natural Heritage). The HTML and PDF versions online have been corrected.

Perspectives: "Y weigh in again on modern humans" by R. L. Cann (2 August, p. 465). In the figure, Denisovians should have been spelled Denisovans. The HTML and PDF versions online have been corrected.

Editors' Choice: "Unintended consequences" (26 July, p. 319). The units for the cited concentrations of particulates should have been $\mu\text{g}/\text{m}^3$, not mg/m^3 . The HTML and PDF versions online have been corrected.

News & Analysis: "Fragile wetland will test Turkey's resolve in protecting biodiversity" by J. Bohannon (26 July, p. 332). In the final paragraph, State Hydraulic Works, not the Ministry of Development, should be named as the granter of dam contracts. The HTML and PDF versions online have been corrected.

News Focus: "Indispensable outsider" by A. Finkbeiner (26 July, p. 334). In the timeline, "Brokers fast Fourier transform algorithm development" was placed in the year 1973. Garwin brokered the fast Fourier transform in 1963. The HTML version online has been corrected.

Reports: "Nuclear PTEN controls DNA repair and sensitivity to genotoxic stress" by C. Bassi *et al.* (26 July, p. 395). Ref. 15 should have been the following: C. Lee *et al.*, *Cancer Res.* **64**, 6906 (2004). The HTML and PDF versions online have been corrected.

Letters to the Editor

Letters (~300 words) discuss material published in *Science* in the past 3 months or matters of general interest. Letters are not acknowledged upon receipt. Whether published in full or in part, Letters are subject to editing for clarity and space. Letters submitted, published, or posted elsewhere, in print or online, will be disqualified. To submit a Letter, go to www.submit2science.org.

ANIMAL BEHAVIOR

Mysterious Travelers Revisited

Franz Bairlein

Each northern fall, billions of birds, from tiny hummingbirds to large swans, leave their breeding and natal sites, moving to mostly southern and often very distant places for wintering. Some traverse continents [e.g., peregrines (*Falco peregrinus*) travel from Greenland to northern Argentina]. Others cross oceans [e.g., 25-g northern wheatears (*Oenanthe oenanthe*) fly from Arctic Canada over the northern Atlantic to northwestern Europe and then turn south for another 3000 km to western Africa]. All confront numerous challenges. Thus it is unsurprising that avian migration has long fascinated people, including authors. So what can another book add beyond the many already available [e.g., (1–3)]?

Aware of that question, avian ecologist John Rappole (Smithsonian Conservation Biology Institute) offers his “‘reflective inquiry’ ... on what a migrant is and how it came to be.” Focusing on New World passerines (“songbirds”), he takes readers through the annual cycle of an avian migrant. His account highlights field observations, many of which he gathered over four decades of experience and pioneering research on the nonbreeding ecology of Neotropical migrants. Rather than compiling “various aspects of bird migration,” Rappole presents “a synthesis and consideration of the larger picture” intended to deepen our understanding. His personal, selective survey of the ecology and evolution of bird migration emphasizes comparisons between migrants’ and residents’ evolutionary, ecological, and behavioral traits.

Therefore, despite the subtitle and the more than 1300 literature references, the book is neither a review of state-of-the-art knowledge nor a textbook on bird migration. But it is not important that Rappole’s treatments of various aspects of migratory birds (such as orientation and navigation, physiology, stopover ecology, tracking methodology, climate change, and conservation) are rather cursory and fail to reflect the latest available research.

The reviewer is at the Institute of Avian Research, An der Vogelwarte 21, 26386 Wilhelmshaven, Germany. E-mail: franz.bairlein@ifv-vogelwarte.de

The author’s way of thinking, critically addressing existing hypotheses and theories, and formulating alternative hypotheses (often rather conflicting and provocative) makes the book readable, inspiring, and stimulating if challenging as well.

Innate, genetic dispositions have been demonstrated for various migratory traits. These include the onset of first-fall migration, amount of migratory activity (*Zugunruhe*, or migratory restlessness), and directional preferences in naïve hatch-year birds. Since their discovery, the migration route hypothesis—that young birds on their initial migration without parental or social guidance simply fly in an innate direction for an innate, particular amount of time, thus leading them to the wintering range—has become widely accepted.

But Rappole prefers a “destination” hypothesis, that juvenile migrants possess “a genetic program enabling them to home to the ancestral area from which the parent population was derived (often the wintering area).” It seems clear that many current migrants, especially passerines, derived from resident ancestral populations in the tropics. Nevertheless, evidence of the existence of such a homing program is weak, and we don’t know anything about how young birds recognize or locate their winter home. When A. C. Perdeck (4) displaced first-fall migrant European starlings (*Sturnis vulgaris*) 600 km perpendicu-

lar to their normal, population-specific route, the birds continued in the direction of their normal course. In contrast, simultaneously displaced adult birds compensated for their displacement and navigated back to their population-specific wintering area. If the young would have known home, they should have compensated as well. This example does not, however, entirely negate Rappole’s hypothesis. We may need to consider the temporal scale of the evolution of migration. The destination hypothesis may fit the early

evolution of migration and tropical migrants, whereas many current migration systems are largely of much younger evolutionary age. For example, human-induced changes in distribution of migrants (as illustrated by the consequences of land clearance from the European colonization of North America) can radically change migration patterns in a rather short time. Such relatively rapid changes are not simply behavioral responses (flexibility) but build on a strong micro-evolutionary component (5).

The disproportional decline of many northern migrants (especially long-distance tropical migrants) as compared to short-distance migrants or residents is of global

Northern wheatear.



concern. The different trends indicate that population sizes are shaped not simply by aspects of breeding areas or by the migratory behavior but also by factors particular to long-distance migration. The energetic demands of flying make long-distance migrants especially dependent on proper fueling prior to and during migration. Stopover sites that provide sufficient food are required for successful migration as well as successful subsequent breeding. Environmental conditions in wintering areas also affect subsequent breeding success, thus the importance of halting habitat destruction and even recreating habitats on the nonbreeding grounds of migrants. The conservation of migration systems also requires a better understanding of carry-over effects from nonbreeding into breeding and related population change. Therefore, I like that the book devotes so much attention to population ecology and population regulation. It includes two appendices by Alan Pine that introduce the mathematics of population dynamics of periodic breeders. Although unexpected in a book on migration, such an extended excursus into population dynamics is worthwhile.

The Avian Migrant The Biology of Bird Migration

by John H. Rappole
Columbia University Press,
New York, 2013. 457 pp. \$80,
£55. ISBN 9780231146784.

Hopefully, *The Avian Migrant* will stimulate future research in linking migration and breeding. There is much to be gained by looking at migration as part of the entire annual life cycle rather than a separate, though fascinating, behavior.

References

1. P. Berthold, E. Gwinner, E. Sonnenschein, Eds., *Avian Migration* (Springer, Berlin, 2003).
2. R. Greenberg, P. P. Mara, Eds., *Birds of Two Worlds: The Ecology and Evolution of Migration* (Johns Hopkins Univ. Press, Baltimore, 2005).
3. I. Newton, *The Migration Ecology of Birds* (Academic Press, Amsterdam, 2008).
4. A. C. Perdeck, *Ardea* **46**, 1 (1958).
5. P. Berthold, A. J. Helbig, G. Mohr, U. Querner, *Nature* **360**, 668 (1992).

10.1126/science.1242577

SOCIAL SCIENCE

A Too-Soft Critique of India's Growth

Andrew Robinson

In 1927, American journalist Katherine Mayo published *Mother India* (1), a notorious polemic against India and Indians that gave satisfaction to British colonialists and American racists while naturally infuriating most Indians. Mahatma Gandhi famously commented that the book was “cleverly and powerfully written” but seemed like “the report of a drain inspector” who concludes with some triumph: “the drains are India.”

Although *Mother India* is largely forgotten (except by older Indians), its ghost seems to inhibit *An Uncertain Glory*, an indictment of the Indian state by economists Jean Drèze (Allahabad University) and Nobel laureate Amartya Sen (Harvard University). After three decades of trawling the data compiled by central and state governments, Indian nongovernmental organizations, and international bodies, these long-time collaborators (2) know—possibly better than any other commentators—how Indian governments since the 1980s have failed the vast majority of Indians, especially in health care, education, poverty reduction, and the justice system. They bluntly acknowledge in the preface, “The history of world devel-

The reviewer is the author of the forthcoming *India: A Short History*. E-mail: andrew.robinson33@virgin.net



opment offers few other examples, if any, of an economy growing so fast for so long with such limited results in terms of reducing human deprivations.” As they are at pains to demonstrate, the benefits of economic growth have been more widely shared even in India’s neighbor Bangladesh, let alone in rapidly growing China.

Here are a few of their many shocking facts: According to the 2011 Indian census, fully 50 percent of households lack toilets. Among the 132 countries for which comparable data are available, air pollution in India ranks highest. Due to teacher indifference and absenteeism among teachers and students, the teaching time in north Indian rural government schools is about 50 days per year. Although the celebrated Nalanda University was established six centuries before Europe’s oldest universities, no Indian university is among the world’s top 200. In 2009–10, 30% of the Indian population (350 million people) were living below the official (very low) poverty line. Meanwhile, 30% of the members of Parliament in 2009 had criminal charges, including murder, pending against them.

The authors, Indian citizens, belong to the relatively small group that has benefited from India’s impressive economic growth of the past two decades. Seemingly in order not to challenge this wealthy group’s interests or offend its sensitivities, the book as a whole shies away from trenchant criticism. Instead, it pulls most of its punches and too often takes refuge in academic equivocation and statistical manipulation, thereby forfeiting much of its undoubted potential influence.

For example, the chapter “Accountability and Corruption” avoids mentioning any corrupt politician, government official, businessman, or institution by name—despite the legion of well-established cases (a handful of which have ended in jail). Not even the

Coverage critique. Anusha Rizvi’s black comedy *Peepli Live* satirizes media and political responses to farmer suicides.

Bofors arms scandal of the late 1980s that undermined and sank the Congress government led by Rajiv Gandhi—a scandal as resonant for India as Watergate is for the United States—rates a mention. Nor does the anticorruption campaigner Anna Hazare, who transfixed the Indian government

and media through much of 2011–12 with his Gandhi-style public fasts (whether effectively or not remains to be determined). And it is surely peculiar to discuss “Poverty and Social Support” without mentioning India’s well-publicized farmer suicides. Between 1995 and 2012, over a quarter-million Indian farmers (according to conservative official figures) committed suicide in despair at their indebtedness created by the drive toward corporate farming: “the largest wave of suicides in history” (3), notes P. Sainath, an award-winning journalist admired by Sen. Also absent in an interesting chapter on caste and its continuing dominance, “The Grip of Inequality,” is the controversial Mayawati, former chief minister of the key northern state of Uttar Pradesh, who in the 1990s transformed Indian electoral politics as a leader of the low-caste Dalits (former Untouchables).

As for the contradictions of Indian science and technology, they too are neglected. In particular, many excellent Indian scientists openly acknowledge that they can successfully conduct original research in Europe and the United States but not in their home country, largely because of political interference and hierarchical attitudes. Of the four Nobel prizes awarded to Indian-born scientists, only one—that given to physicist C. V. Raman, in colonial times—was for research done in India. Sen himself felt obliged to leave 1950s India and work in western universities in order to achieve success and recognition. This hoary Indian intellectual phenomenon, ignored in *An Uncertain Glory*, is among the most debilitating problems that bedevil the subcontinent’s social and cultural—rather than merely economic—development that Drèze and Sen earnestly desire.

References

1. K. Mayo, *Mother India* (Harcourt, Brace, New York, 1927).
2. J. Drèze, A. Sen, *India: Economic Development and Social Opportunity* (Oxford Univ. Press, Delhi, 1995).
3. www.counterpunch.org/2009/02/12/the-largest-wave-of-suicides-in-history.

10.1126/science.1243165

CREDIT: PEEPLI LIVE/COURTESY UTI MOTION PICTURES AND AKPL

GLOBAL FOOD SUPPLY

Certify Sustainable Aquaculture?

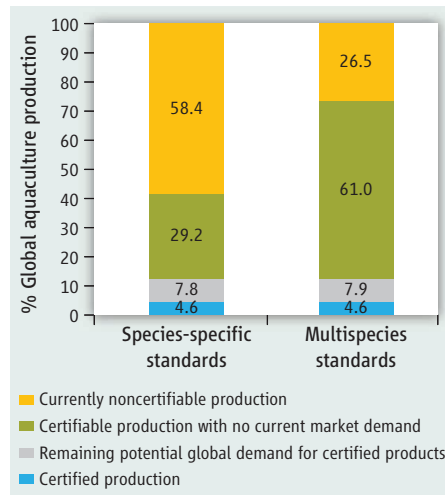
S. R. Bush,^{1*} B. Belton,² D. Hall,³ P. Vandergeest,⁴ F. J. Murray,⁵ S. Ponte,⁶ P. Oosterveer,¹ M. S. Islam,⁷ A. P. J. Mol,¹ M. Hatanaka,⁸ F. Kruijssen,⁹ T. T. T. Ha,¹⁰ D. C. Little,⁵ R. Kusumawati¹

Aquaculture, the farming of aquatic organisms, provides close to 50% of the world's supply of seafood, with a value of U.S. \$125 billion. It makes up 13% of the world's animal-source protein (excluding eggs and dairy) and employs an estimated 24 million people (1). With capture (i.e., wild) fisheries production stagnating, aquaculture may help close the forecast global deficit in fish protein by 2020 (2). This so-called “blue revolution” requires addressing a range of environmental and social problems, including water pollution, degradation of ecosystems, and violation of labor standards.

One response to these problems has been the rise of sustainability certification. Reflecting on the launch of the Aquaculture Stewardship Council (ASC) to oversee sustainability standards, we argue that, although certification makes a contribution, it also has significant limits and should be considered one approach among many for steering aquaculture toward sustainable production.

Sustainability certification is a market-based system involving (i) setting standards for ecological and social interactions, (ii) auditing compliance with these standards, (iii) attaching labels to products and enterprises that meet the standards, and (iv) creating institutions to perform these functions (3). Although these can be carried out by public bodies, certification systems largely run by private organizations, such as firms and/or nongovernmental organizations (NGOs), are gaining prominence.

Certification has emerged in sectors where governance has shifted away from state regulation. Activists frustrated with slow and inadequate government responses to environmental threats and private sector actors seeking to avoid increased production costs and damage to their reputations



Global potential of certified aquaculture production. The left bar reflects standards adopted by the ASC. The right bar reflects standards adopted by GLOBALG.A.P. and ACC (see SM for details).

have contributed to the rise of certification (4, 5). The goals of certification include increasing consumer trust, providing legitimacy to producers, and reducing liability by ensuring compliance with safety and quality standards (4). These goals also motivate seafood sustainability certification, including both aquaculture and capture fisheries, which has expanded in recent years to include more than 30 standards and information schemes (6).

Markets for Sustainability Certification

The greatest demand for certified aquaculture products comes from North America and Europe, where large supermarket and restaurant chains have committed to selling only certified sustainable seafood by 2015 (7). Global and regional buyers are turning to certified seafood in response to NGO campaigns that threaten their brands by associating them with “bad” environmental and labor practices.

Only a small proportion of world aquaculture production (4.6%) is currently certified (see the chart). The approach to date, now exemplified by the ASC, has been to develop “species-specific” standards for each of the 13 species groups with the highest demand in global export markets. These account for 41.6% of worldwide aquacul-

Certification's limited contribution to sustainable aquaculture should complement public and private governance.

ture production by weight, which leaves 58.4% not covered and, therefore, “non-certifiable” (see the chart). Recent introduction of generic multispecies standards (that apply across more than one species group) by two ASC competitors, the Aquaculture Certification Council (ACC) and the Good Agricultural Practices organization GLOBALG.A.P., has expanded the potentially certifiable volume of global production to 73.5% (see the chart). Despite covering nearly twice as much production, the multispecies standards represent an increase of only 0.1% in likely demand over the species-specific standards, because much of what is potentially certifiable is produced and sold in countries (notably China) with little demand for sustainability certification (8) [see supplementary materials (SM)].

Certification schemes cover a range of criteria from organic to responsible to sustainable aquaculture, representing demand for different product qualities. Schemes compete for suppliers, which must comply with one or more standards to access specific (northern) markets. They compete for buyers by attempting to convince retailers and branded agro-food processors to distribute aquaculture products carrying their label. They compete for approval from—and form alliances with—influential NGOs.

Producers have to make strategic decisions about which standards to adopt and, thus, which processors to use and international markets to access. These choices also influence the support that local governments, NGOs, and donors offer (e.g., by underwriting on-farm improvements or management of common resources, such as water).

Narrow Take on Sustainability

The unit of certification largely determines what is included in and excluded from definitions of sustainability. Fisheries and forestry certification schemes take zonal or sectoral approaches and involve resource managers (e.g., boards and government departments). Certification in aquaculture, as in organic agriculture, takes an enterprise-level approach. Because private production units (farms or value chains) are certified, the cumulative impacts of multiple farms in a particular location (9) or the

¹Wageningen University, Wageningen 6708 LX, Netherlands. ²WorldFish, Dhaka 1213, Bangladesh. ³Wilfrid Laurier University, Waterloo, Ontario N2L 3C5, Canada. ⁴York University, Toronto, Ontario M3J 1P3, Canada. ⁵University of Stirling, Stirling FK9 4LA, UK. ⁶Copenhagen Business School, Frederiksberg, DK-2000 Denmark. ⁷Nanyang Technological University, Singapore 639798. ⁸Sam Houston State University, Huntsville, TX 77340, USA. ⁹WorldFish, General Post Office 10670, Penang, Malaysia. ¹⁰Vietnam Forestry University, Ha Noi, Vietnam.

*Corresponding author. E-mail: simon.bush@wur.nl

impact of aquaculture on surrounding agriculture or mangrove conservation is rarely effectively considered (10). Farm-level certification systems, such as ASC, pay some attention to effects from inputs, such as seed and feed, but do not include those resulting from processing [e.g., (11)]. The impact of nonmarine feed inputs, such as soy and wheat, is not considered. None of the main aquaculture certification schemes consider environmental costs of distribution and transportation.

These narrow definitions of sustainability reflect the structure of standard-setting institutions and the feasibility of measurement and regulation using technical parameters. Even multistakeholder processes used to develop ASC standards, including public input through forums and online review, have been criticized for adopting a technical focus that reflects interests and values of the most powerful actors to the exclusion of others (9). Many stakeholders, especially producers in the Global South, are unable to participate for reasons of language, access, cost, time, or resources; others disagree with the whole approach. Even when such stakeholders participate, they are often unable to meaningfully influence outcomes (9).

This suggests that certification is substantially a strategy for buyers to avoid adverse publicity by outsourcing reputational risk, whereas costs are imposed on suppliers. The leverage of powerful actors, including environmental activists and northern buyers, in defining standards for aquaculture has left little room for local understandings of agroecology and social dimensions of equity and justice (12).

Although the ASC has incorporated social standards, the codification of complex, context-dependent social issues, especially those beyond the farm, remains problematic. Working conditions and worker rights are a key issue with shrimp and salmon produced in the Global South. Certification may produce enclaves with improved working conditions and may raise the profile of labor issues with state regulatory agencies. But certification alone cannot improve poor working conditions in the broader aquaculture sector.

Inclusion and Exclusion

Certification is complex and expensive and assumes a level of managerial capability that most aquaculture producers in the Global South do not have. Without external support (e.g., from a collective or co-op, donor-funded project, processor or buyer, government, or NGO), smallholders are often excluded

from markets that require certification. Compliance is easier for larger-scale, better-capitalized production units that can deal with record-keeping and administrative requirements; certification tends to strengthen trends toward consolidation in export-oriented sectors (13). Not only producers are excluded, but also up- and downstream supply chain actors, e.g., collectors, small-scale traders, brokers, and input suppliers.

Variants of certification systems (such as group certification) that cater to problems of smallholders can mitigate these exclusions. However, although niche schemes (e.g., organic and fair trade) confer premiums that can protect smaller enterprises, schemes that target mainstream northern markets, such as the ASC, do not. A failure to tailor certification to smallholder needs usually results in their exclusion from these markets (14). Smallholders already forced to comply with advanced national food safety and traceability systems [e.g., those in Thailand, see (15)] are better positioned to meet stringent organic or sustainability certification requirements than those in countries where state enforcement is weaker.

The addition of carp to new multispecies standards appears to mark an expansion of coverage but highlights a point of exclusion. Because of differing cuisines and the consumption of a relatively small range of species in northern markets (carp is predominantly grown and consumed in the Global South), widespread certification of carp is unlikely. Even if carp is certified, consumer interest in emerging middle-class markets focuses on food safety, and sustainability or social qualities remain niche concerns (8). Nevertheless, emergence of domestic standards demonstrates that concern over sustainability may increase; certifiers should explore complementarities given projected future dominance of these markets.

Beyond Limits to Certification

Comparative advantages and potential synergies of certification should be explored vis-à-vis a mix of other private governance strategies (e.g., ethical supply chain management) and state regulation. Although private sustainability certification was born in part out of fear of underregulation by states, it is now blamed for being inflexible, divisive, and restrictive (5). The assumption that countries in the Global South are incapable of regulating aquaculture no longer holds true everywhere. Countries that have dealt with mandatory international food-safety requirements demonstrate a capacity to better govern sustainability and represent some

of the most important domestic markets in the Global South for aquaculture products.

Northern-led certification need no longer be imposed in lieu of state regulation or in isolation from local standards development but should be institutionalized as part of a broader array of approaches, including state and private regulation in the Global South. Successful certification schemes often build on what the state has already done, through food safety, traceability, or state-led voluntary better-management practices (12, 16). The question remains as to whether improved public and private engagement in the South would result in less exclusionary outcomes for producers. But as limitations of international sustainability certification become apparent, there is a need to explore new hybrid forms of environmental governance that draw on the strengths of states, the private sector, and institutions such as ASC.

References and Notes

1. Food and Agriculture Organization of the United Nations (FAO), "The State of World Fisheries and Aquaculture" (FAO Fisheries and Aquaculture Department, FAO, Rome, 2012).
2. S. J. Hall, A. Delaporte, M. J. Phillips, M. Beveridge, M. O'Keefe, *Blue Frontiers: Managing the Environmental Costs of Aquaculture* (The WorldFish Center, Penang, Malaysia, 2011).
3. T. Mutersbaugh, D. Klooster, M.-C. Renard, P. Taylor, *J. Rural Stud.* **21**, 381–388 (2005).
4. M. Hatanaka, C. Bain, L. Busch, *Food Policy* **30**, 354–369 (2005).
5. C. Béné, *Dev. Policy Rev.* **23**, 585–614 (2005).
6. G. Parkes *et al.*, *Rev. Fish. Sci.* **18**, 344–356 (2010).
7. F. Asche, R. E. Dahl, D. V. Gordon, T. Trollvik, P. Aandahl, *Mar. Resour. Econ.* **26**, 255–265 (2011).
8. P. Xu, Y. Zeng, Q. Fong, T. Lone, Y. Liu, *Food Contr.* **28**, 74–82 (2012).
9. B. Belton, F. Murray, J. Young, T. Telfer, D. C. Little, *Ambio* **39**, 2–13 (2010).
10. S. R. Bush *et al.*, *Ecol. Soc.* **15**, 15 (2010).
11. R. Bosma, P. Anh, J. Potting, *Int. J. Life Cycle Assess.* **16**, 903–915 (2011).
12. P. Vandergeest, *World Dev.* **35**, 1152–1171 (2007).
13. L. Lebel, P. Lebel, P. Garden, D. H. Giap, S. Khurutmuang, S. Nakayama, *Globalizations* **5**, 211–226 (2008).
14. M. Maertens, J. F. M. Swinnen, *World Dev.* **37**, 161–178 (2009).
15. M. M. Dey, M. A. Rab, K. M. Jahan, A. Nisapa, A. Kumar, M. Ahmed, *Econ. Manag.* **9**, 217–236 (2005).
16. T. T. T. Ha, S. R. Bush, *Environ. Plann. C Gov. Policy* **28**, 1101–1119 (2010).

Acknowledgments: The authors acknowledge support from Interdisciplinary Research and Education Fund RESCOPAR program (Wageningen University), Social Sciences and Humanities Research Council of Canada standard grant Privatizing Environmental Governance, Framework Programme 7–European Union–funded Sustaining Ethical Aquaculture Trade project (no. 222889), CGIAR Research Program on Aquatic Agricultural Systems. D.C.L. is director of Nam Sai Farms and adviser to Global Aquaculture Alliance. Thanks also go to J. Hall, J. Clapp, M. Bailey, and L. M. Mai.

Supplementary Materials

www.sciencemag.org/cgi/content/full/341/6150/1067/DC1

10.1126/science.1237314

MICROBIOLOGY

Fighting Obesity with Bacteria

Alan W. Walker and Julian Parkhill

The human large intestine harbors a complex community of microorganisms (microbiota) that affect many aspects of our physiology and health (1). Numerous lines of evidence, particularly from rodent models, have suggested that the intestinal microbiota may play a role in the development of obesity. On page 1079 of this issue, Ridaura *et al.* (2) demonstrate that the microbiota from lean or obese humans induces similar phenotypes in mice and, more remarkably, that the microbiota from lean donors can invade and reduce adiposity gain in the obese-recipient mice if the mice are fed an appropriate diet.

Ridaura *et al.* recruited four human female twin pairs discordant for obesity and transferred the intestinal microbiota in fecal samples from each of them into the intestines of germ-free mice. Animals receiving a transplant from the obese (Ob) twin donors developed increased adiposity compared to those receiving transplants from lean (Ln) twin donors. Differences in mouse adiposity could also be reproduced after inoculation of germ-free mice with collections of cultured bacteria grown from twin-pair fecal samples. Cohousing of mice harboring cultured bacteria from an obese twin (Ob^{ch}) with mice harboring cultured bacteria from a lean twin (Ln^{ch}) prevented the development of increased adiposity in the Ob^{ch} mice. This occurred in tandem with successful colonization of Ob^{ch} intestines by bacteria from the Ln^{ch} mice. By contrast, Ob^{ch} microbes did not transmit to Ln^{ch} mice, and these animals remained lean. This indicated that transmissibility of intestinal microbes and adiposity phenotype were tightly linked.

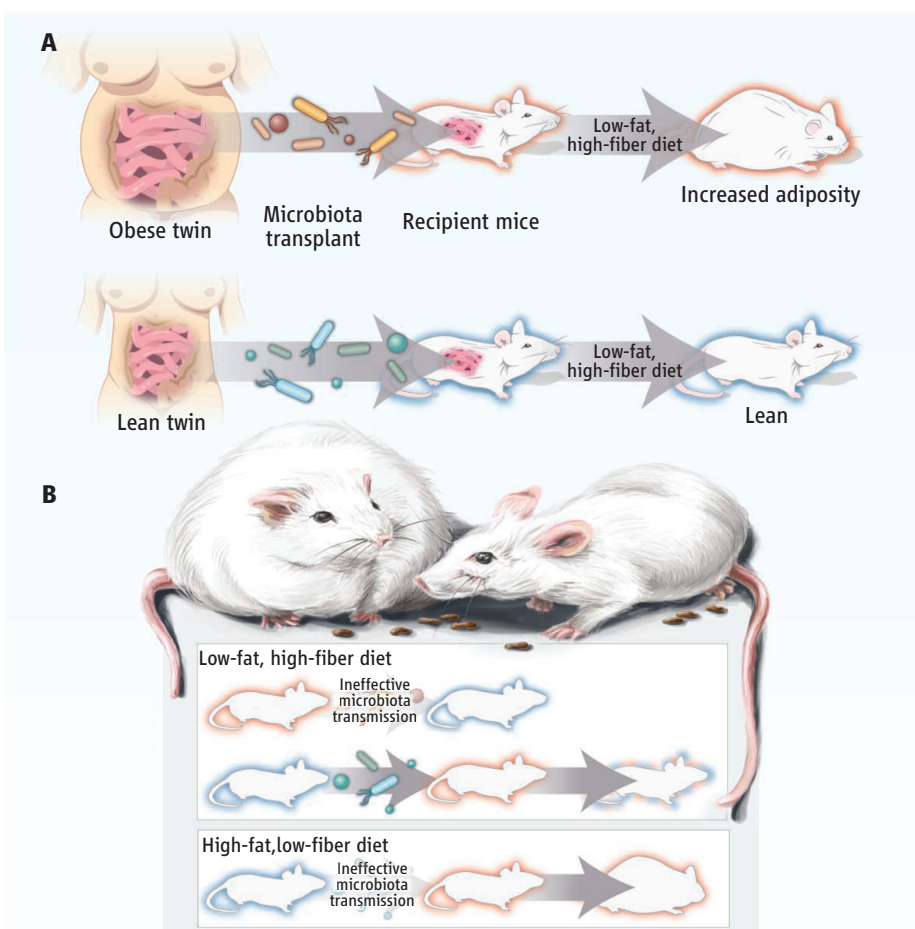
Analysis of the bacterial communities showed that members of the Bacteroidetes phylum, particularly *Bacteroides* spp., could pass from the Ln^{ch} mice and colonize the Ob^{ch} mice, suggesting that these bacteria were largely responsible for protection against increased adiposity. However, cohousing of Ob^{ch} mice with lean mice inoculated with a relatively simple mix of just 39 defined bacterial strains, including many of the *Bacteroides* species that were previously correlated

with reduced adiposity, did not reduce adiposity in the Ob^{ch} mice. This indicates that more complex bacterial interactions underlie protection against increased body mass and associated metabolic disturbance.

Ridaura *et al.* also identified diet as an important factor in the transmission of microbiota and associated host phenotype. Lean twin-derived bacterial strains effectively colonized and ameliorated excess adiposity in Ob^{ch} mice when the recipients were fed a low-fat, high-fiber diet. This was not the case when the mice were fed a diet that was high in saturated fat but low in fiber.

Intestinal bacteria from lean humans can confer protection against fat gain in experimental mice.

The findings support some emerging hypotheses regarding potential mechanisms by which the microbiota can affect host weight gain. One of the main activities of the intestinal microbiota is to break down and ferment dietary fibers into short-chain fatty acids (SCFAs) such as acetate, propionate, and butyrate. The host absorbs these acids, and humans obtain perhaps 5 to 10% of daily energy requirements from them (3). Ridaura *et al.* show that the microbiota in Ln mice produces greater amounts of SCFAs, particularly propionate and butyrate, and digests more of the plant fiber present in the mouse's



Please pass the microbiota. (A) Germ-free mice inoculated with microbiota from obese or lean human twins take on the microbiota characteristics of the donor. Those receiving the obese microbiota (red outline) had an increase in adiposity, whereas those receiving the lean microbiota (blue outline) remained lean. (B) If fed an appropriate diet, mice harboring the obese microbiota, when cohoused with mice harboring the lean microbiota, are invaded by the lean microbiota and do not develop increased adiposity (blue and red outline). By contrast, the obese microbiota does not effectively colonize mice harboring the lean microbiota, and these mice remain lean.

CREDIT: V. AITOUNIAN/SCIENCE

Pathogen Genomics Group, Wellcome Trust Sanger Institute, Wellcome Trust Genome Campus, Hinxton CB10 1SA, UK. E-mail: parkhill@sanger.ac.uk

diet than the microbiota of Ob mice. Thus, increased weight gain in Ob mice does not result from increased energy harvest. Rather, the finding supports previous studies showing that although SCFAs are a source of energy, they promote leanness by inhibiting fat accumulation in adipose tissue, raising energy expenditure, and enhancing production of hormones associated with feelings of satiety (4–6). Other putative mechanisms include a role for the microbiota in metabolizing bile acids, branched-chain amino acids, and acylcarnitines, which have all been linked to either insulin resistance or obesity in humans and mice.

A key question is the translatability of the findings to a human clinical context. *Bacteroides* species, correlated with reduced adiposity by Ridaura *et al.*, have repeatedly been implicated in protection against obesity in mice (7). However, evidence from human studies is mixed (8). Indeed, *Bacteroides*, and the propionate that they produce, can be more abundant in overweight and obese individuals than in lean counterparts (9). Furthermore, *Bacteroides* have been associated with diets high in animal protein and saturated fats (10) and are notably reduced in lean African

individuals consuming diets high in fiber compared to Europeans consuming typical Western diets (11). Given these potential discrepancies, it will be important to verify in humans the activity of bacteria that are beneficial in mouse models.

Perhaps the most intriguing finding of Ridaura *et al.* is that microbial protection from increased adiposity is only possible against the backdrop of a suitable host diet. It may be that future microbiota-based therapies for an obese individual will require an alteration in diet to aid colonization by beneficial microbes. This offers a potentially synergistic approach, whereby reduced caloric intake and increased fiber consumption not only have a positive impact on energy balance but might also promote transplanted microbial communities that are associated with leanness.

Fecal transplants in humans have been used to beneficially alter the microbiota in a variety of ailments (12). Notably, a recent study showed that fecal transplants from lean individuals into obese counterparts improved insulin sensitivity in some obese recipients (13). The procedure is not risk free, however, with the potential for introducing pathogens

to the recipient. The mouse model presented by Ridaura *et al.* is therefore timely, as it offers the potential to test human-derived bacterial strains, and accompanying dietary regimens, within a controlled mammalian host environment. The study is a step toward the ultimate goal of developing relatively simple mixtures of bacteria for testing as anti-obesity therapeutics.

References

1. A. W. Walker, T. D. Lawley, *Pharmacol. Res.* **69**, 75 (2013).
2. V. K. Ridaura *et al.*, *Science* **341**, 1241214 (2013); DOI: 10.1126/science.1241214.
3. L. V. Hooper, T. Midtvedt, J. I. Gordon, *Annu. Rev. Nutr.* **22**, 283 (2002).
4. I. Kimura *et al.*, *Nat. Commun.* **4**, 1829 (2013).
5. Z. Gao *et al.*, *Diabetes* **58**, 1509 (2009).
6. M. J. Keenan *et al.*, *Obesity (Silver Spring)* **14**, 1523 (2006).
7. P. J. Turnbaugh *et al.*, *Nature* **444**, 1027 (2006).
8. S. H. Duncan *et al.*, *Int. J. Obes.* **32**, 1720 (2008).
9. A. Schwirtz *et al.*, *Obesity (Silver Spring)* **18**, 190 (2010).
10. G. D. Wu *et al.*, *Science* **334**, 105 (2011).
11. C. De Filippo *et al.*, *Proc. Natl. Acad. Sci. U.S.A.* **107**, 14691 (2010).
12. E. van Nood *et al.*, *N. Engl. J. Med.* **368**, 407 (2013).
13. A. Vrieze *et al.*, *Gastroenterology* **143**, 913, e7 (2012).

10.1126/science.1243787

GEOPHYSICS

Reducing Earthquake Risk

Brian E. Tucker

The preceding Perspectives in this series (1–4) provide snapshots of the earthquake and tsunami risks, hazard monitoring and risk mitigation activities, and current research questions concerning some of the world's seismic hot spots—South Central Asia, the Caribbean, Turkey, Tokyo, and Santiago. The image that emerges is one of considerable progress in reducing losses due to earthquakes and tsunamis in some places but of growing and evolving risks in others.

In the past two decades, the prevailing approach to reducing the consequences of earthquakes and tsunamis has emphasized raising awareness of these hazards, promoting methods of reducing their associated risk,

and incorporating the results of Earth science and earthquake engineering research into post-earthquake reconstruction. The United Nations (UN) International Strategies for

Disaster Reduction serves as a platform to coordinate these efforts and, through its Hyogo Framework for Action, has declared the goal “to substantially reduce disaster losses by

2015 by building the resilience of nations and communities to disasters” (5).

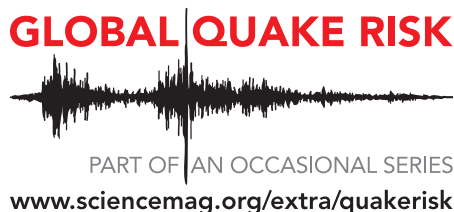
Despite these diverse and sustained efforts, human and economic losses due to earthquakes are increasing and are projected to continue to rise in the future (6, 7). The past decade (2001 to 2012) saw more than three times as many earthquake-related deaths as the preceding two decades (1981 to 2000) (8). These losses are increasingly concentrated in developing countries because of

How can a higher level of earthquake preparedness be achieved, particularly in developing nations?

differences in urban population growth (see the figure) and the quality of seismic-resistant construction (9–11). Why is progress so frustratingly slow?

The Importance of Being Prepared

One reason is that historically, far fewer resources have been invested in pre-earthquake preparedness and risk reduction than in post-earthquake response, reconstruction, and recovery; this is particularly true in developing countries. One study (12) suggests that of all international aid for humanitarian assistance, less than 10% is directed to disaster prevention; a more recent study (13) estimates that this figure is only 1%. Post-disaster activities are important and reliably garner generous support among individuals, governments, and nonprofit organizations, appealing to the human impulse to help those in need. Yet a comparison of the consequences of recent earthquakes in developing countries, where preparedness is rare, and industrialized countries, where it is much more common, sug-



diet than the microbiota of Ob mice. Thus, increased weight gain in Ob mice does not result from increased energy harvest. Rather, the finding supports previous studies showing that although SCFAs are a source of energy, they promote leanness by inhibiting fat accumulation in adipose tissue, raising energy expenditure, and enhancing production of hormones associated with feelings of satiety (4–6). Other putative mechanisms include a role for the microbiota in metabolizing bile acids, branched-chain amino acids, and acylcarnitines, which have all been linked to either insulin resistance or obesity in humans and mice.

A key question is the translatability of the findings to a human clinical context. *Bacteroides* species, correlated with reduced adiposity by Ridaura *et al.*, have repeatedly been implicated in protection against obesity in mice (7). However, evidence from human studies is mixed (8). Indeed, *Bacteroides*, and the propionate that they produce, can be more abundant in overweight and obese individuals than in lean counterparts (9). Furthermore, *Bacteroides* have been associated with diets high in animal protein and saturated fats (10) and are notably reduced in lean African

individuals consuming diets high in fiber compared to Europeans consuming typical Western diets (11). Given these potential discrepancies, it will be important to verify in humans the activity of bacteria that are beneficial in mouse models.

Perhaps the most intriguing finding of Ridaura *et al.* is that microbial protection from increased adiposity is only possible against the backdrop of a suitable host diet. It may be that future microbiota-based therapies for an obese individual will require an alteration in diet to aid colonization by beneficial microbes. This offers a potentially synergistic approach, whereby reduced caloric intake and increased fiber consumption not only have a positive impact on energy balance but might also promote transplanted microbial communities that are associated with leanness.

Fecal transplants in humans have been used to beneficially alter the microbiota in a variety of ailments (12). Notably, a recent study showed that fecal transplants from lean individuals into obese counterparts improved insulin sensitivity in some obese recipients (13). The procedure is not risk free, however, with the potential for introducing pathogens

to the recipient. The mouse model presented by Ridaura *et al.* is therefore timely, as it offers the potential to test human-derived bacterial strains, and accompanying dietary regimens, within a controlled mammalian host environment. The study is a step toward the ultimate goal of developing relatively simple mixtures of bacteria for testing as anti-obesity therapeutics.

References

1. A. W. Walker, T. D. Lawley, *Pharmacol. Res.* **69**, 75 (2013).
2. V. K. Ridaura *et al.*, *Science* **341**, 1241214 (2013); DOI: 10.1126/science.1241214.
3. L. V. Hooper, T. Midtvedt, J. I. Gordon, *Annu. Rev. Nutr.* **22**, 283 (2002).
4. I. Kimura *et al.*, *Nat. Commun.* **4**, 1829 (2013).
5. Z. Gao *et al.*, *Diabetes* **58**, 1509 (2009).
6. M. J. Keenan *et al.*, *Obesity (Silver Spring)* **14**, 1523 (2006).
7. P. J. Turnbaugh *et al.*, *Nature* **444**, 1027 (2006).
8. S. H. Duncan *et al.*, *Int. J. Obes.* **32**, 1720 (2008).
9. A. Schwierz *et al.*, *Obesity (Silver Spring)* **18**, 190 (2010).
10. G. D. Wu *et al.*, *Science* **334**, 105 (2011).
11. C. De Filippo *et al.*, *Proc. Natl. Acad. Sci. U.S.A.* **107**, 14691 (2010).
12. E. van Nood *et al.*, *N. Engl. J. Med.* **368**, 407 (2013).
13. A. Vrieze *et al.*, *Gastroenterology* **143**, 913, e7 (2012).

10.1126/science.1243787

GEOPHYSICS

Reducing Earthquake Risk

Brian E. Tucker

The preceding Perspectives in this series (1–4) provide snapshots of the earthquake and tsunami risks, hazard monitoring and risk mitigation activities, and current research questions concerning some of the world's seismic hot spots—South Central Asia, the Caribbean, Turkey, Tokyo, and Santiago. The image that emerges is one of considerable progress in reducing losses due to earthquakes and tsunamis in some places but of growing and evolving risks in others.

In the past two decades, the prevailing approach to reducing the consequences of earthquakes and tsunamis has emphasized raising awareness of these hazards, promoting methods of reducing their associated risk,

and incorporating the results of Earth science and earthquake engineering research into post-earthquake reconstruction. The United Nations (UN) International Strategies for

GLOBAL QUAKE RISK



PART OF AN OCCASIONAL SERIES

www.sciencemag.org/extra/quakerisk

Disaster Reduction serves as a platform to coordinate these efforts and, through its Hyogo Framework for Action, has declared the goal “to substantially reduce disaster losses by

2015 by building the resilience of nations and communities to disasters” (5).

Despite these diverse and sustained efforts, human and economic losses due to earthquakes are increasing and are projected to continue to rise in the future (6, 7). The past decade (2001 to 2012) saw more than three times as many earthquake-related deaths as the preceding two decades (1981 to 2000) (8). These losses are increasingly concentrated in developing countries because of

How can a higher level of earthquake preparedness be achieved, particularly in developing nations?

differences in urban population growth (see the figure) and the quality of seismic-resistant construction (9–11). Why is progress so frustratingly slow?

The Importance of Being Prepared

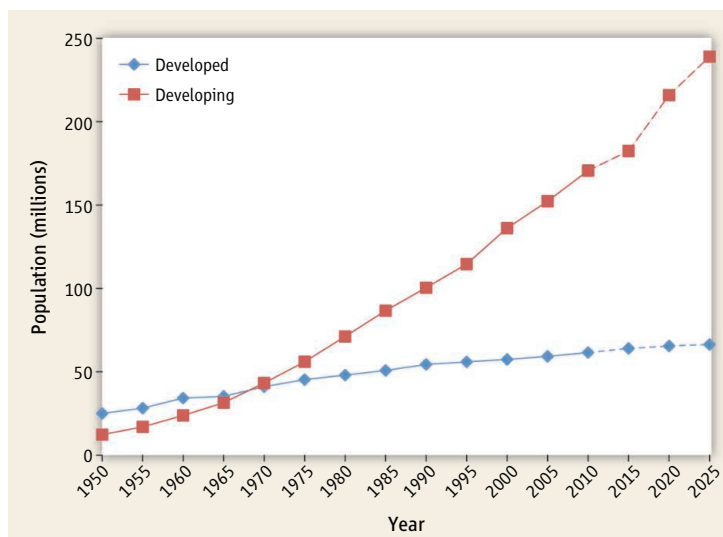
One reason is that historically, far fewer resources have been invested in pre-earthquake preparedness and risk reduction than in post-earthquake response, reconstruction, and recovery; this is particularly true in developing countries. One study (12) suggests that of all international aid for humanitarian assistance, less than 10% is directed to disaster prevention; a more recent study (13) estimates that this figure is only 1%. Post-disaster activities are important and reliably garner generous support among individuals, governments, and nonprofit organizations, appealing to the human impulse to help those in need. Yet a comparison of the consequences of recent earthquakes in developing countries, where preparedness is rare, and industrialized countries, where it is much more common, sug-

gests the large potential benefits of increasing investments in mitigation and preparedness.

After its magnitude (M) 9.5 earthquake of 1960, Chile embarked on a robust earthquake safety program, which, as Stein and Toda describe (3), included developing and enforcing a modern building code. During that same time period, Haiti, lulled by more than two centuries of seismic quiescence and hampered by poverty and political turbulence, largely disregarded its earthquake risk. In the first 2 months of 2010, large earthquakes struck both countries. How did the resulting losses compare? Modeling by the U.S. Geological Survey (USGS) (14) indicates that in the 27 February 2010 Chile M 8.8 earthquake, 0.1% of Chileans who experienced severe shaking died, compared with 11% of Haitians who were subjected to the same strength of shaking in the 12 January 2010 M 7.0 Haiti earthquake. In other words, Haitian buildings appear to be 100 times as lethal as Chilean buildings.

The disproportionate impact of the 2010 earthquakes in Haiti and Chile is not the only evidence suggesting the effectiveness of earthquake risk mitigation. In 1988, a M 6.9 earthquake struck Armenia, killing at least 25,000 people in building collapses, whereas in 1994, a M 6.7 earthquake in Los Angeles, California—where earthquake risk reduction measures had been applied for decades—killed only 60. Using the USGS earthquake catalog (8), I compared the lethality of all moderate-sized (M 6.0 to 7.9) earthquakes (excluding the outliers of the 1976 Tangshan and 1994 Kobe events) that occurred from 1970 through 2012 and found that the average number of deaths per earthquake in each of the 10 most earthquake-prone developing countries was about 90 times as high as the average number of deaths per earthquake in California, Japan, and Chile. Although the number of earthquakes in this data set is not sufficient to allow a statistically robust conclusion, this ratio also suggests the positive effect of risk mitigation and preparedness.

The lives lost in the 2011 Tohoku tsunami numbered [thanks in part to an early tsunami warning system similar to that described for the Caribbean by von Hillebrandt-Andrade (4)] fewer than 19,000; this toll represented only about 5% of the population that was



Increasing urban earthquake risk. The plot shows the total population since 1950 of “developing” and “developed” cities [selected from the world’s 50 most populous cities (20)] that are located within 100 km of a fault capable of generating an earthquake with $M \geq 7$. Over the past 60 years, the number of people exposed to strong earthquake shaking in cities in developing countries has grown by about a factor of 7 more than in developed countries. Accounting for changes in both population and the quality of seismic-resistant construction suggests that over this period, the relative earthquake risk of cities in developing countries, compared to that of cities in developed countries, has increased by 2 to 3 orders of magnitude.

occupying land inundated by the tsunami (15). In contrast, if a tsunami were to strike Padang, West Sumatra, it is anticipated to kill several hundred thousand people of that city’s total population of 900,000 (16). Were it not for the failure of the Fukushima nuclear power plants, the Tohoku earthquake and tsunami might now be famous for showing the benefits of preparedness and mitigation.

Learning from Public Health Campaigns

Why have the science, engineering, and public policies that have substantially reduced earthquake losses in California, Japan, and Chile over the past century not been applied more widely? Why did it take, as described by Erdik (2), two M 7 earthquakes occurring 3 months apart just 80 km from Istanbul to motivate that technologically competent, economically sound, and highly seismically active country to initiate the much-needed risk reduction activities now under way? Why are existing building codes often unenforced in developing countries, as discussed by Bilham and Gaur (1)? Increased cost, unawareness of risk and mitigation options, lack of trained craftsmen, poor construction materials, and corruption are mentioned as possible reasons. But another has been largely ignored: human psychology.

For example, Gilbert (17) has argued that threats that capture human attention are personalized, imminent, or rapidly increas-

ing; recently, Gawande (18) described how these same characteristics can explain the dramatically different speeds with which surgeons adopted anesthetics (fast) and antiseptics (slow). The threat of an earthquake seems remote to most people. To be successful, earthquake and tsunami risk reduction efforts must do more than “build back better,” raise awareness, deploy early warning systems, and promote enforcement of building codes. They must overcome the psychological remoteness of rare earthquakes by providing tangible social and economic incentives.

Public health advocates have achieved some success addressing similar challenges in campaigns such as those to use seat belts, prevent unsafe sex, and stop smoking. Publishing statistics on the

increasing occurrence of lung cancer and auto fatalities was not sufficient; nor were photos of black, leathery lungs on cigarette packages or photos in driver education movies of gory accident scenes. Taxes, fines, and opprobrium were used. And painstaking, sustained one-on-one work with community leaders and opinion-shapers was necessary. The earthquake risk reduction community might find effective lessons, models, and tactics from studying those public health campaigns.

Incentives to enforce modern building codes and increase earthquake preparedness could come in many forms. International corporations, UN agencies, multilateral development banks, and international corporations could insist on purchasing and renting only buildings designed and constructed according to modern building codes. Local governments could reduce the property tax rate on such buildings. Tourist travel guides could identify those hotels located in areas of high earthquake or tsunami risk that have trained their staff in emergency response.

Additionally, regional associations of governments, and even the UN, could develop guidelines on how member countries could reduce their risks and then publicize those that follow those guidelines. For example, in 2005, the Organisation for Economic Cooperation and Development (OECD) adopted guidelines for effective school earthquake safety programs, and its Council passed a

recommendation that its members establish such programs (19); the OECD could now publish a list of which countries have done so. In addition, development banks could offer loan guarantees to construction companies that incorporate seismic-resistant features into new buildings.

More of the Same Is Not Enough

The approach followed over the past two decades to reduce earthquake risk will not allow the UN to meet its goal of substantially reducing losses by 2015 (5). Nor will it do so by 2020. Risk creation is outpacing risk reduction. Investments in earthquake preparedness and mitigation must be materially increased. The task of reducing earthquake risk must be viewed not as just an engineering and scientific challenge but also as a sociological and psychological one. It is time to reassess our methods, look for solutions outside the fields of earthquake

engineering and Earth science, and refocus our efforts.

References and Notes

1. R. Bilham, V. Gaur, *Science* **341**, 618 (2013).
2. M. Erdik, *Science* **341**, 724 (2013).
3. R. S. Stein, S. Toda, *Science* **341**, 850 (2013).
4. C. von Hillebrandt-Andrade, *Science* **341**, 966 (2013).
5. United Nations Office for Disaster Reduction, Hyogo Framework for Action; www.unisdr.org/we/coordinate/hfa
6. R. Bilham, *Bull. Earthquake Eng.* **2009**, 1 (2009).
7. T. L. Holzer, J. C. Savage, *Earthq. Spectra* **29**, 155 (2013).
8. USGS, Significant earthquakes of the world; <http://earthquake.usgs.gov/earthquakes/eqarchives/significant>
9. B. E. Tucker, J. Trumbull, S. Wyss, in *Issues in Urban Earthquake Risk*, B. E. Tucker, M. Erdik, C. Hwang, Eds. (Kluwer, Dordrecht/Boston/ London, 1994), pp. 1–10.
10. Geohazards International, Vulnerable communities; www.geohaz.org/risk/vulnerable.html.
11. M. Wyss, *Nat. Hazards* **34**, 305 (2005).
12. S. La Trobe, S. P. Venton, *Natural Disaster Risk Reduction: The Policy and Practice of Selected Institutional Donors* (Tearfund Research Project, Teddington, Middlesex, UK, July 2003).
13. Global Humanitarian Assistance, GHA Report 2011; www.globalhumanitarianassistance.org/wp-content/uploads/2011/07/gha-report-2011.pdf.
14. USGS, Earthquake Hazards Program PAGER: Prompt Assessment of Global Earthquakes for Response; <http://earthquake.usgs.gov/pager>.
15. Earthquake Engineering Research Institute, *Learning from Earthquakes: The Japan Tohoku Tsunami of March 11, 2011* (EERI Special Earthquake Report, Oakland, CA, November 2011).
16. M. Di Mauro, K. Megawati, V. Cedillos, B. Tucker, *Nat. Hazards* **10.1007/s11069-013-0632-z** (2013).
17. D. Gilbert, *Stumbling on Happiness* (Knopf, New York, 2006).
18. A. Gawande, *New Yorker* 29 www.newyorker.com/reporting/2013/07/29/130729fa_fact_gawande (2013).
19. OECD, Recommendation of the Council Concerning Guidelines on Earthquake Safety in Schools, 21 July 2005; <http://webnet.oecd.org/OECD/ACTS/Instruments/ShowInstrumentView.aspx?InstrumentID=143&InstrumentPID=139&Lang=en&Book=False>.
20. UN Department of Economic and Social Affairs, World Urbanization Prospects, the 2011 Revision; <http://esa.un.org/unup>.

Acknowledgments: The ideas expressed in this article were developed in discussions with R. Bilham, T. Brennan, A. Chakos, L. Dengler, S. Fraser, T. Holzer, K. Kishore, C. Konold, B. Runser, J. Savage, G. Trumbull, D. Wald, and K. Yawitz.

10.1126/science.1239236

MATERIALS SCIENCE

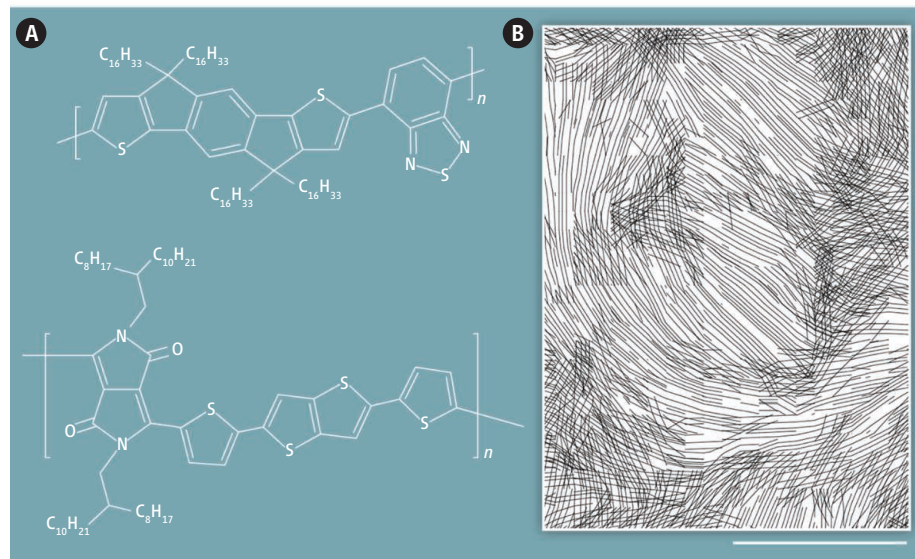
Unraveling Charge Transport in Conjugated Polymers

R. A. Street

Polymer semiconductors have picked up the pace in the constant search for new and better electronic materials. High carrier mobility is an essential figure-of-merit for their applications as thin-film transistors (TFTs), solar cells, and light-emitting diodes. Polymers are disordered materials with partial crystallinity, and disorder introduces localized electronic states at the band edges—the so-called band tail—that trap electrons and reduce mobility. Reaching a mobility of $1 \text{ cm}^2 \text{ V}^{-1} \text{ s}^{-1}$ was the result of engineering polymers with increased crystallinity to reduce the effect of band tail states. Reported mobilities have recently surged to between about 5 and $10 \text{ cm}^2 \text{ V}^{-1} \text{ s}^{-1}$ (1), but the polymers are less ordered, according to some structural measurements. Two recent papers help resolve this puzzle. Zhang *et al.* (2) use a combination of structural probes to show that the high-mobility polymers gain longer-range structural order, if not high crystallinity, by having a more rigid backbone. Noriega *et al.* (3) provide

a careful analysis of the role of disorder in charge transport for the specific case of polymers, and conclude that high crystallinity is not essential for high mobility.

The relation between structure and electronic conduction in polymers is complex. These highly anisotropic molecules have high conductivity along the backbone chain,



High-mobility polymers. (A) Examples of repeat units are shown for two of the new polymers with high carrier mobility (1, 2). (B) A reconstruction from an electron-microscopy image reveals the long-range orientation of a high-mobility polymer (4). Scale bar: 250 nm.

Palo Alto Research Center, Palo Alto, CA 94304, USA.
E-mail: street@parc.com

moderate conductivity between chains when the backbone rings are aligned face-to-face, and very little conductivity between the widely spaced lamellar planes. High crystallinity optimizes the face-to-face alignment and so gives good conduction in a two-dimensional lamellar. However, the grain boundaries between crystallites limit conduction, and with a typical grain size on the order of 10 nm, there are plenty of disordered grain boundaries. The new polymers, designed to have a more rigid backbone, may have lower local crystallinity, but the polymer chains are aligned over longer distances (see the figure). Chabynyc and colleagues have mapped out the alignment and found that it extends for up to 1 μm (4, 5). More conduction occurs along the favorable backbone direction, with less need for face-to-face conduction, and fewer large-angle grain boundaries to impede conduction. The long-range orientation of the rigid backbone polymers evidently more than compensates for the lower local crystallinity.

The disorder effects are also not simple. Noriega *et al.* point out that amorphous regions of the polymer have a larger band gap than the more ordered regions and should be excluded from the conduction process because carriers cannot reach them. Hence, a small crystallite surrounded by an amorphous grain boundary region creates a barrier impeding conduction to the next grain. Long-range orientation of the polymer allows the carriers to bypass the highly disordered regions without being affected and only move through the more ordered regions. The mechanism is analogous to the conduction of nanowire mats (6). Very-low-density mats of carbon or silver nanowires are highly conductive because their length allows them to intersect many other wires, and the empty spaces between wires do not impede the conduction. Such rodlike percolation may be a suitable model for the polymers. What matters is not whether the polymer is uniformly conducting, only that there are sufficient continuous conducting paths.

A mobility of 5 to 10 $\text{cm}^2 \text{V}^{-1} \text{s}^{-1}$ has important technological consequences for flat-panel displays because it is the threshold needed by the TFTs that drives an organic light-emitting diode (OLED) display. The incumbent polycrystalline silicon technology has both cost and technological drawbacks that make it vulnerable to competition. It would be a nice vindication of organic semiconductor research if future displays have both organic TFTs and emitting diodes. However, there is tough competition from amorphous metal oxide TFTs

(7) because their mobility of 10 to 20 $\text{cm}^2 \text{V}^{-1} \text{s}^{-1}$ also puts them in the OLED range. Their development raised a similar question of how an amorphous semiconductor can have such a high mobility. The explanation is that amorphous metal oxides have large s-orbitals that are spherically symmetric and insensitive to disorder in the bond angles, so that band tail states are few and shallow. The argument for the high-mobility polymers is also insensitivity to disorder but for a very different reason.

Single crystals of small conjugated organic molecules can have room-temperature mobilities up to 20 to 30 $\text{cm}^2 \text{V}^{-1} \text{s}^{-1}$ (8), and theoretical calculations indicate that this value is about the upper limit for a polymer (9). It is not known how much

closer a solution-deposited polymer can approach this limit. The gains in polymer mobility have come from trying new ideas for molecular designs, learning what works, and refining the design, and there is no reason to suppose that chemists will run out of ideas any time soon.

References

1. J. Li *et al.*, *Sci. Rep.* **2**, 754 (2012).
2. X. Zhang *et al.*, *Nat. Commun.* **4**, 2238 (2013).
3. R. Noriega *et al.*, *Nat. Mater.* **10**, 1038/nmat3722 (2013).
4. C. J. Takacs *et al.*, *Nano Lett.* **13**, 2522 (2013).
5. B. A. Collins *et al.*, *Nat. Mater.* **11**, 536 (2012).
6. S. De *et al.*, *ACS Nano* **3**, 1767 (2009).
7. K. Nomura *et al.*, *Science* **300**, 1269 (2003).
8. V. Podzorov *et al.*, *Phys. Rev. Lett.* **93**, 086602 (2004).
9. J. E. Northrup, *Phys. Rev. B* **76**, 245202 (2007).

10.1126/science.1242935

ASTRONOMY

Feedback on Galaxy Formation

B. R. McNamara^{1,2}

High-resolution radio images reveal how jets of relativistic particles can drive the dynamics of galaxy evolution.

The rate of star formation in galaxies peaked about 10 billion years ago when the universe was just over 3 billion years old. It has been in decline ever since. Whereas spiral galaxies, like the Milky Way, slowly churn disks of cold gas clouds into young blue stars, giant elliptical galaxies today are dormant. Despite having developed atmospheres of tenuous, 10-million-degree gas waiting to cool and fuel star formation, most are “red and dead” (see the figure). Why they remain so is one of the great mysteries of galaxy formation. On page 1082 of this issue, Morganti *et al.* (1) reveal part of the answer.

Research into galaxy formation has largely focused on environmental factors. For example, galaxies confined to dense regions in groups and clusters experience collisions and other gravitational interactions that tend to remove gas that would otherwise form stars (2). In more isolated regions of space, the opposite can occur. Strong galaxy interactions and collisions stir and compress the gas, inducing star formation and triggering quasar activity (3). Although external forces

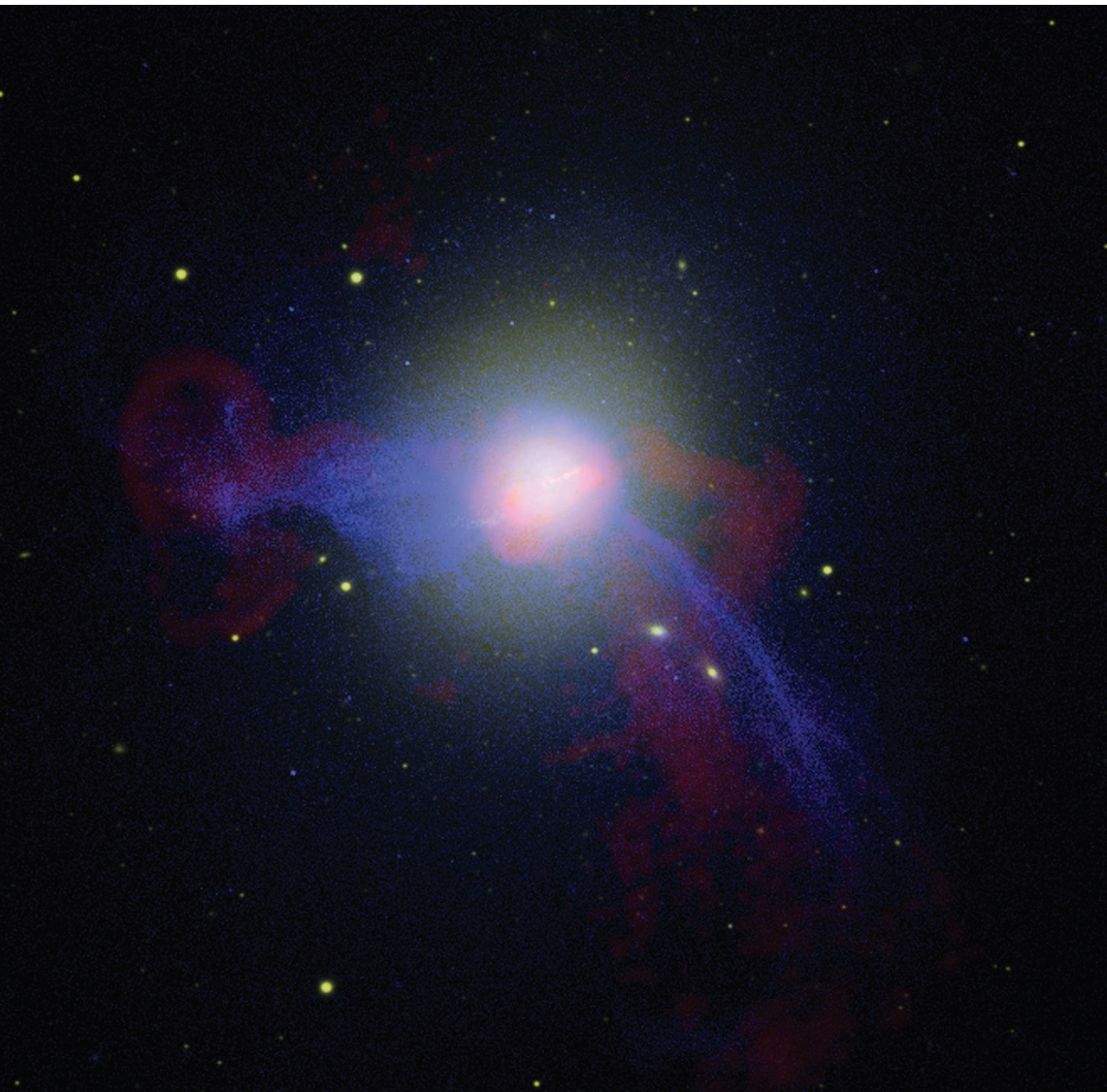
certainly help shape galaxies, they are not the whole story.

Over the past 20 years, it has become clear that most galaxies harbor central black holes with masses between 10^6 and $10^{10} M_{\odot}$ (solar masses) (4). The ratio of a galaxy's mass to its central black hole mass today is surprisingly constant at a value of roughly 1000:1, regardless of the galaxy's mass (5, 6). This has led many to suggest that so-called supermassive black holes coevolve with the galaxies (3) and perhaps even regulate their growth (3, 4, 7, 8).

How can a black hole with an event horizon smaller than the size of the solar system shape the structure of an entire galaxy? As matter falls into the growing black hole, its enormous gravitational energy is released in the forms of radiation and relativistic jets. The radiation and jets interact with the surrounding gas, driving it away from the black hole and out of the galaxy, thus preventing it from forming stars (7). This process, known as active galactic nucleus feedback, may be able to regulate the growth of the galaxy and the black hole itself (7, 8).

4C12.50 is an archetype in a class of burgeoning galaxies known as ultraluminous infrared galaxies (ULIRGs), the infrared luminosity exceeding 1 trillion times that of the Sun (9). Most of its infrared radiation is

¹Department of Physics and Astronomy, University of Waterloo, 200 University Avenue West, Waterloo, Ontario N2L 5M3, Canada. ²Perimeter Institute for Theoretical Physics, 31 Caroline Street, Waterloo, Ontario N2L 2Y5, Canada. E-mail: mcnamara@uwaterloo.ca



Red and dead. Messier 87 is located 16 Mpc away in the Virgo cluster of galaxies. It is a nearby example of a “red and dead” giant elliptical galaxy harboring a $(4 \text{ to } 6) \times 10^9 M_{\odot}$ nuclear black hole. Stars are in white, x-ray atmosphere is in blue, and radio synchrotron emission is in red. M87 is an archetypal example of a giant elliptical galaxy experiencing radio mode feedback (11).

reprocessed ultraviolet light emitted by hot young stars and the accreting black hole. An ULIRG is enshrouded in cold (30 to 100 K) clouds and dust that are so thick that most of the ultraviolet light is unable to escape. Instead, it is absorbed by dust that then shines in infrared light. The cold molecular clouds and accompanying star formation in 4C12.50 are thought to have arrived in a catastrophic merger of two spiral galaxies. (The Milky Way’s star-formation rate is only a few solar masses per year, whereas star formation is proceeding at hundreds of solar masses per year in 4C12.50.) Most of the gas will be consumed by star formation. However, some will be expelled in winds driven by radiation pressure, supernova explosions (9), and by its powerful radio jets

(1). Objects like 4C12.50 may eventually emerge as elliptical galaxies.

Relativistic radio jets are streams of plasma traveling near light speed, launched from the vicinity of supermassive black holes. Composed of charged particles and magnetic fields, they carry enormous energy and momentum flux. Their impact is clearly seen in x-ray images of elliptical galaxies and galaxy clusters. As radio jets push through the hot atmosphere surrounding the host galaxy, they inflate vast cavities that rise buoyantly (7). The bubbles and their associated shock fronts transfer the kinetic energy of the jet into the hot atmospheres, preventing them from cooling into cold molecular clouds. This process, in part, keeps elliptical galaxies from forming stars (7, 8, 10).

Apparently, this is only part of the picture. Morganti *et al.* show, using a clever technique, that radio jets interact not only with tenuous hot atmospheres, but also with cold, dense gas. The authors took advantage of situations where the synchrotron emission from the jet itself illuminates gas clouds from behind. The clouds then cast a radio shadow, a slight dimming of the radio flux, at a radio frequency that depends on the speed of the clouds along the line of sight. By combining signals from radio telescopes located around the world, the positions of the clouds can be pinpointed on the sky to a tiny fraction of an arc second. As long as the radio source is bright and the clouds are big enough and dense enough to absorb most of the radio flux striking them, they can be detected in galaxies at nearly any distance. Unfortunately, the technique is sensitive only to gas lying along the line of sight to the radio source. Therefore, the gas mass can only be estimated using the strength of the absorption feature. It cannot be measured directly.

Morganti *et al.* found cold clouds traveling toward us at about 1000 km s^{-1} and at a rate of roughly 20 solar masses per year. The clouds will surely be driven away from the sites of star formation in 4C12.50 before they collapse into stars. Some

may escape the galaxy entirely. Uncertainties in the outflowing mass make it difficult to determine the immediate impact on the star-formation history of 4C12.50 itself. Nevertheless, this result has broad consequences. It demonstrates that radio jets, which are common to all elliptical galaxies, can couple to dense gas and accelerate it to high speeds. Research using the new Atacama Large Millimeter Array is showing that radio bubbles can indeed drive outflows of molecular gas at rates of hundreds of solar masses per year. This process, known as radio-mechanical feedback, or radio mode feedback (10), was thought to operate only on the hot, tenuous atmospheres of galaxies and clusters. It now seems that radio mode feedback

CREDIT: (X-RAY) NASA/CXC/CFAW. FORMAN ET AL.; (RADIO) NRAO/AUI/NSF/W. COTTON; (OPTICAL) NASA/ESA/HUBBLE HERITAGE TEAM (STSC/AURA), AND R. GENDLER

operates on both the hot and cold gas in galaxies. Because of this and the fact that radio jets are a common and recurrent phenomenon in galaxies, radio mode feedback could be a key process that governs the growth of elliptical galaxies and the supermassive black holes lurking at their centers.

References

1. R. Morganti *et al.*, *Science* **341**, 1082 (2013).
2. F. Combes, *Int. Astron. Union Symp.* **217**, 440 (2004).
3. J. Kormendy, L. C. Ho, *Annu. Rev. Astron. Astrophys.* **51**, 511 (2013).
4. D. M. Alexander, R. C. Hickox, *New Astron. Rev.* **56**, 93 (2012).
5. L. Ferrarese, D. Merritt, *Astrophys. J.* **539**, L9 (2000).
6. K. Gebhardt *et al.*, *Astrophys. J.* **539**, L13 (2000).
7. B. R. McNamara, P. E. J. Nulsen, *Annu. Rev. Astron. Astrophys.* **45**, 117 (2007).
8. A. C. Fabian, *Annu. Rev. Astron. Astrophys.* **50**, 455 (2012).
9. S. Veilleux, G. Cecil, J. Bland-Hawthorne, *Annu. Rev. Astron. Astrophys.* **43**, 769 (2005).
10. D. J. Croton, *Mon. Not. R. Astron. Soc.* **365**, 11 (2006).
11. W. R. Forman *et al.*, *Astrophys. J.* **665**, 1057 (2007).

10.1126/science.1243114

ATMOSPHERIC SCIENCE

A Hyperventilating Biosphere

Inez Fung

In the Northern Hemisphere, CO₂ concentrations in the atmosphere oscillate regularly over the course of each year (see the figure). This “breathing” occurs because CO₂ declines in the atmosphere during the growing season, when CO₂ uptake via photosynthesis exceeds the release from microbial respiration, and increases during the rest of the year, when release exceeds uptake. On page 1085 of this issue, Graven *et al.* (1) present evidence that the breathing rate has accelerated greatly over the past 50 years.

The depth of the breathing is captured by the net ecosystem production (NEP), the integrated net uptake over the months when CO₂ uptake exceeds release (see the figure, panel A). NEP would equal the net release integrated over the rest of the year if the biosphere were at equilibrium, with growth balancing mortality and decay. NEP is greatest at high latitudes, where the growing season is short, and smallest in the tropics, where the monthly fluxes into and out of the atmosphere nearly cancel throughout the year.

Long-term increases in the amplitude of the annual CO₂ cycles were first noted by Pearman and Hyson in 1981 (2) and have

since been established with increasing confidence. They have been attributed to increasing photosynthetic uptake, an earlier growing season, and increasing decomposition in response to changes in climate and atmospheric composition. Even so, the CO₂ monitoring stations are sparse and are located in remote marine locations, and it is not clear how widespread the biosphere response has been.

Graven *et al.*, in a masterful stroke, have stitched together separate pieces of aircraft CO₂ records over the North Pacific (see the figure, panels B to D) to estimate the CO₂ amplitude trends in the middle troposphere, about 3 to 6 km above Earth’s surface. They find that the 50-year amplitude trends in the mid-troposphere resemble those at the few monitoring sites at the surface. The trends are huge: ~10% per decade at high latitudes and ~5% per decade over the mid-latitudes. Winds mix CO₂ throughout the atmosphere, albeit incompletely. The mid-tropospheric amplitude trends therefore signify an increasing NEP over a wide swath of the biosphere, with the increase fastest at high latitudes.

The question arises, what is causing the Northern Hemisphere land biosphere, especially at high latitudes, to go into hyperdrive? Surely, the biosphere must be enjoying the

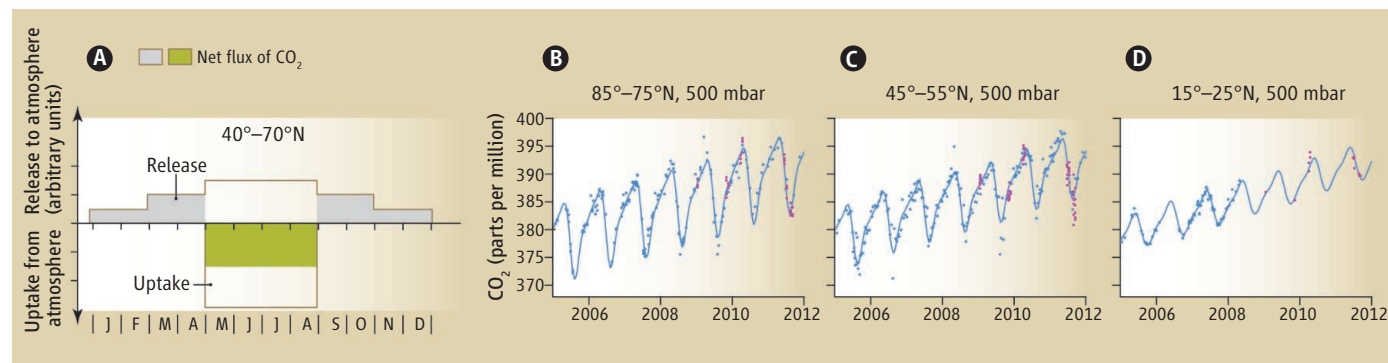
Seasonal carbon dioxide uptake and release patterns are changing as a result of global warming.

warming. Satellite observations show that from 1982 to 2011, the photosynthetic season has been lengthening over the past three decades: On average, the onset of greening of northern ecosystems (>45°N) has advanced by 1 day per decade in the spring, and the seasonally integrated photosynthesis has increased, consistent with the warming and thawing (3). However, enhanced photosynthesis alone is not enough to explain the large increase in CO₂ amplitude seen by Graven *et al.* The authors hypothesize that observed changes in the structure of the biosphere—for example, northward migration of the tree line, increased shrub cover in the Arctic, and reestablishment of forests after fires—have enhanced carbon uptake to the extent necessary to explain the amplitude trend.

The satellite data show that the photosynthetic season of northern ecosystems does

Deeper breathing. The net ecosystem productivity (green) captures the seasonal uptake of carbon dioxide by the biosphere (A). Graven *et al.* have used aircraft data to determine how carbon dioxide concentrations have oscillated in the troposphere over recent decades. The seasonal oscillations are largest at high latitudes (B) than at mid- (C) and low-latitudes (D). The amplitude of this “breathing” is increasing, especially at high latitudes. [Panels B to D adapted from fig. S4 in (1)]

University of California, Berkeley, Berkeley, CA 94720–4767, USA. E-mail: ifung@berkeley.edu



not extend as far into autumn as the warming and thawing seasons and ends earlier, by ~ 0.9 days per decade (3).

The longer decomposition season, coupled with greater amounts of detritus from enhanced photosynthesis and faster decomposition rates, would contribute to a higher atmospheric CO_2 buildup and hence a larger CO_2 amplitude (4). Microbes, the agents of decomposition, are having a feast not only in the melting permafrost, but in the entire Northern Hemisphere (5–7). The microbial feast would in turn supply nutrients to enhance photosynthetic uptake and support the poleward march of ecosystems.

Graven *et al.* show that the CO_2 amplitude trend is not well simulated by the current generation of global Earth system models. These models include the life cycles of ecosystems, with photosynthetic uptake sensitive to atmospheric CO_2 and ambient climate; and litter decomposition (and concomitant microbial respiration) vary-

ing with temperature and soil moisture. In some models, vegetation structure changes with fires and changing climate. So what is missing?

Permafrost carbon dynamics is just beginning to be incorporated into the next-generation models (8). Still, understanding of the transient carbon dynamics of a thawing Arctic is rudimentary. The Carbon in Arctic Reservoirs Vulnerability Experiment (CARVE), a NASA mission, has observed episodic bursts of high CO_2 and CH_4 throughout the thaw season (9), not the slow, steady release predicted by the models. The U.S. Department of Energy's Next Generation Ecosystem Experiments in the Arctic (NGEE-Arctic) (10), NASA's Arctic-Boreal Vulnerability Experiment (ABOVE) (11), and the European Union's PAGE21 project (12) all promise to deliver new insights that will advance the modeling.

The biosphere is changing, and changing rapidly. Currently it is a sink for a quarter

of the anthropogenic CO_2 emissions. Will it continue to act as a sink for fossil fuel-derived CO_2 ? Current results, including those reported by Graven *et al.*, suggest that it will do so until microbial respiration overtakes photosynthetic uptake. The race is on.

References

1. H. D. Graven *et al.*, *Science* **341**, 1085 (2013); 10.1126/science.1239207.
2. G. P. Pearman, P. Hyson, *J. Geophys. Res.* **86**, 9839 (1981).
3. J. Barichivich *et al.*, *Glob. Change Biol.* 10.1111/gcb.12283 (2013).
4. S. Piao *et al.*, *Nature* **451**, 49 (2008).
5. M. L. Goulden *et al.*, *Science* **279**, 214 (1998).
6. E. A. G. Schuur *et al.*, *Bioscience* **58**, 701 (2008).
7. B. Bond-Lamberty, A. Thomson, *Nature* **464**, 579 (2010).
8. C. D. Koven *et al.*, *Proc. Natl. Acad. Sci. U.S.A.* **108**, 14769 (2011).
9. C. E. Miller, S. J. Dinardo, Aerospace Conference, 2012 IEEE; 10.1109/AERO.2012.6187026.10.1109/AERO.2012.6187026.
10. <http://ngee-arctic.ornl.gov>
11. <http://above.nasa.gov>
12. <http://page21.eu>

10.1126/science.1242004

CHEMISTRY

Uncloaking the Quantum Nature of Inelastic Molecular Collisions

Piergiorgio Casavecchia¹ and Millard H. Alexander²

Collisions between molecules can be reactive, resulting in a change in their chemical identity, or inelastic, resulting in a change in only their internal energy or orientation. On page 1094 of this issue, Chefdeville *et al.* (1) report on the predominant contribution of quantum-mechanical resonances to the inelastic scattering and excitation of molecular oxygen (O_2) by molecular hydrogen (H_2).

A crucial quantity as two partners approach, collide, and then recede is the “orbital” angular momentum l . This quantity is the product of their initial relative velocity, their reduced mass, and the impact parameter b , which is the offset off-axis as the two molecules approach one another (see the figure, panel A; b is zero for a head-on collision). In quantum mechanics, l can take on only integer values, in units of Planck's constant. The overall, or integral, cross section (the effectiveness of reaction or energy transfer) is the

weighted sum of the contributions from collisions at separate values of l . To connect these values to chemical kinetics, the thermal rate coefficient is calculated as the average of the integral cross section over a distribution of relative velocities of the colliding molecules. Strictly speaking, the summation is really over all values of the total angular momentum J , which is the vector sum of l , N (the nuclear rotational angular momentum), and S (the total electronic spin angular momentum).

In the experiments of Chefdeville *et al.*, the collision energies are low enough, the mass of the H_2 collision partner small enough, and the resolution in collision energy high enough to allow a clean resolution of the contribution of individual partial waves—individual values of J —to the integral inelastic cross section. In scanning the collision energy, they observe sharp peaks in the measured cross sections, which they attribute to resonances associated with low values of J . [A resonance is a metastable, short-lived state that is accessed and then decays during the course of a collision (2).]

In O_2 , the spins of the two outermost electrons are not paired up, so that $S = 1$. The O_2

Experiment and theory combine to reveal quantum resonances when hydrogen molecules hit and excite oxygen molecules.

molecule has a permanent magnetic moment that lies in the same direction as S , even in the absence of an external magnetic field. Symmetry considerations restrict N to only odd integer values. In the lowest rotational state of O_2 , N and S are antiparallel so that the total molecular angular momentum j is zero.

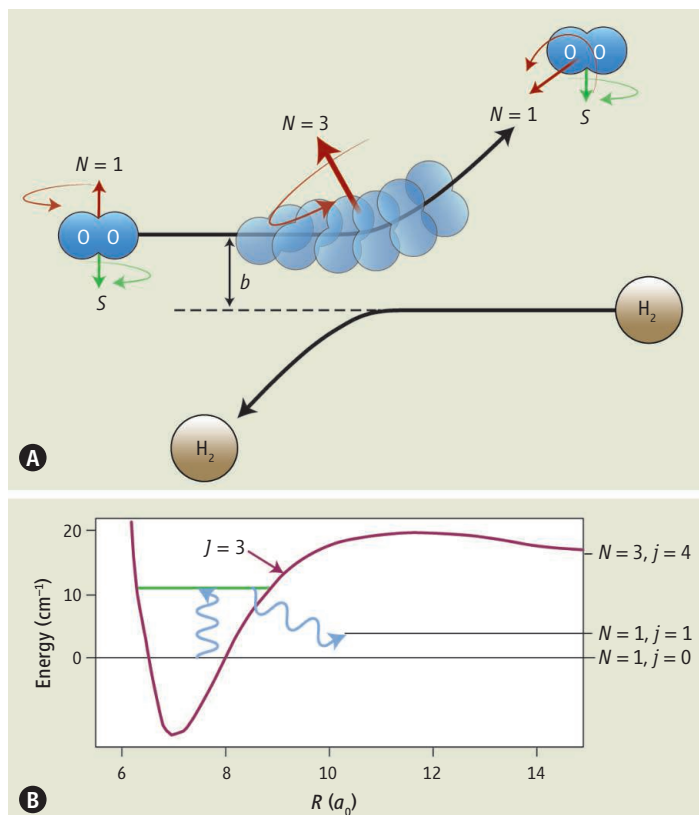
In the sophisticated experiment of Chefdeville *et al.*, a collimated, energy-resolved beam of O_2 formed predominantly in its ground state ($N = 1, j = 0$) collided with a beam of H_2 in its singlet ground state ($S = 0$). The H_2 beam was cooled into its lowest possible rotational state ($N = 0$), which corresponds to the *para* nuclear spin modification and is nearly spherical.

In their experiments, O_2 was scattered inelastically into a higher ($N = 1, j = 1$) spin-rotation level, where S and N are perpendicular. The ($N = 1, j = 1$) state lies $\sim 4 \text{ cm}^{-1}$ (0.5 meV) higher in energy than the ground state (3), a consequence of the weak interaction between the spin magnetic moment and the “end-over-end” rotation of the O_2 . As the collision energy increased from 4 to 20 cm^{-1} , the probability of excitation to the $N = 1, j = 1$ level showed three well-resolved peaks.

¹Dipartimento di Chimica, Università degli Studi di Perugia, 06123 Perugia, Italy. ²Department of Chemistry and Biochemistry and Institute for Physical Science and Technology, University of Maryland, College Park, MD 20742–2021, USA. E-mail: piero@dyn.unipg.it, mha@umd.edu

A highly resolved molecular collision.

(A) The O_2 molecule initially in its lowest spin-rotation level ($N = S = 1, j = 0$) collides with H_2 at impact parameter b . The rotational angular momentum N (red arrow) and the electronic spin S (green arrow) are opposite in direction so that the total molecular angular momentum j is 0. The purely electrostatic interaction of O_2 with H_2 cannot change the direction or magnitude of S . The H_2 molecule in its lowest ($N = 0$) level behaves as a spherical particle. (B) Illustration of the adiabatic O_2 - H_2 interaction potential for the $J = 3$ partial wave, in which distance is given in units of the Bohr radius a_0 . The green line indicates the energy of the quasibound complex in which O_2 is excited to the $N = 3$ level. At collision energies near this value, the inelastic scattering is greatly enhanced. At this energy, when the collision partners approach to closer than $9a_0$, the O_2 partner can ephemerally access (shown by the vertical wiggly arrow) the $N = 3$ state, which is energetically allowed inside this distance. As the collision partners recede, the ephemeral rotationally excited state of O_2 (a Feshbach resonance) must relax to the lower $N = 1$ state. As this occurs, there is a substantial probability that N will end up reoriented. Subsequently, the angular momenta N and S recouple, which leaves the O_2 molecule in the ($N = 1, j = 1$) spin-rotation state (in which N is oriented perpendicular to S).



In general, collisions are direct processes and can be modeled well by classical mechanics. For $l > 0$, there is a small barrier in the interaction potential at long-range due to the repulsive centrifugal interaction between the collision partners. (At nonzero impact parameter, the relative kinetic energy is partially transformed into rotation.) Quantum mechanics allows the partners to tunnel inside the centrifugal barrier, a process for which there is no classical analog. At certain collision energies, the probability of tunneling is greatly enhanced, and the collision partners become temporarily trapped together inside the centrifugal barrier. This is called a shape resonance because the energy at which the trapping occurs is determined by the shape of the centrifugal barrier.

The interaction between H_2 and O_2 is sufficiently attractive that a complex can be formed between H_2 and rotationally excited O_2 , even when there is not enough energy to permit the O_2 to escape in a rotationally excited state. These ephemeral states, which exist only for particular values of the energy, are called Feshbach resonances.

At collision energies where either shape or Feshbach resonances occur, the “lifetime” of the collision will be substantially longer. This trapping greatly amplifies the probability of inelastic scattering, in comparison with collisions at energies off resonance, as illus-

trated in the figure, for the resonance that Chefdeville *et al.* labeled “b.” The energies of the trapped states are extremely sensitive to the underlying H_2 - O_2 interaction potential and to the centrifugal potential. Thus, for each partial wave, the resonances occur at slightly different collision energies.

Chefdeville *et al.* also report a quantum-chemical calculation of the O_2 - H_2 interaction potential, followed by an accurate solution of the Schrödinger equation for the scattering. These simulations permit a convincing attribution of the three observed peaks to shape resonances associated with the $J = 2$ partial wave and to Feshbach resonances associated with the $J = 2, 3$, and 4 partial waves. The calculations also reveal that the observed spin-rotation inelasticity is due almost entirely to these resonances. Off resonance, the predicted inelasticity is much smaller.

Previous experimental studies of the reactive scattering of fluorine atoms and hydrogen ($F + HD \rightarrow FH + D$) revealed similar single partial-wave resonances that were corroborated by quantum scattering calculations (4). The possible appearance of shape and Feshbach resonances in the inelastic scattering of the OH radical has been discussed but not yet confirmed experimentally (5). Recently, Chefdeville *et al.* (6) interpreted oscillations in the energy dependence of experimentally determined cross sections

for the inelastic scattering of CO by H_2 as evidence of partial-wave resonances. Because there was substantial overlap between these features, it is the present O_2 - H_2 study that provides a more convincing assignment of these dramatic quantum effects.

Radio astronomy has identified a multitude of molecules in interstellar gas clouds (7). Many of these clouds are cold, with temperatures ranging from 10 to 100 K (corresponding to energies from 7 to 70 cm^{-1}). Understanding the efficiencies of collisional excitation and deexcitation is key to developing kinetic models to explain the formation and abundance of these molecules (8). Because the element H makes up

about three-quarters of the mass of the universe (9), by far the most common collision partner in cold clouds is molecular hydrogen (H_2). The remarkable accuracy of the theoretical predictions of the quantum features of the scattering of O_2 by H_2 seen by Chefdeville *et al.* confirms that similar calculations can provide accurate data for modeling in astrophysical environments the concentration and population distribution of O_2 , as well as other systems not accessible in the laboratory.

References and Notes

1. S. Chefdeville *et al.*, *Science* **341**, 1094 (2013).
2. G. C. Schatz, *Science* **288**, 1599 (2000).
3. W. M. Welch, M. Mizushima, *Phys. Rev. A* **5**, 2692 (1972).
4. W. Dong *et al.*, *Science* **327**, 1501 (2010).
5. K. B. Gubbels *et al.*, *J. Chem. Phys.* **136**, 144308 (2012).
6. S. Chefdeville *et al.*, *Phys. Rev. Lett.* **109**, 023201 (2012).
7. Wikipedia, List of interstellar and circumstellar molecules; http://en.wikipedia.org/wiki/List_of_molecules_in_interstellar_space.
8. J. Woodall, M. Agúndez, A. J. Markwick-Kemper, T. J. Millar, *Astron. Astrophys.* **466**, 1197 (2007).
9. Wikipedia, Abundance of the chemical elements; http://en.wikipedia.org/wiki/Abundance_of_the_chemical_elements.

Acknowledgments: This work was supported by the Italian Ministero dell’Istruzione, dell’Università e della Ricerca (PRIN 2010–2011, grant 2010ERFKXL) (P.C.); the U.S. National Science Foundation (grant CHE–1213332); and the U. S. Department of Energy (grant DE50002323) (M.H.A.).

10.1126/science.1244109

RETROSPECTIVE

Tony Pawson (1952–2013)

Tony Hunter

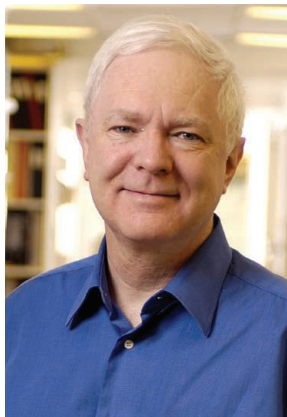
On 7 August 2013, the scientific community lost Tony Pawson, a pioneer in elucidating the mechanistic principles of intracellular signal transduction. His enduring legacy will be the discovery that the Src homology 2 (SH2) domain in one protein interacts with a phosphorylated tyrosine residue in another protein. This insight was the basis for his enormously influential idea that eukaryotic signaling systems comprise modular interaction domains that are used in combinations to propagate signals throughout the cell.

Tony was born in Kent, England, in 1952, and educated at Winchester College and the University of Cambridge, graduating in 1973. He received his Ph.D. in 1976 working at the Imperial Cancer Research Fund (ICRF) where he studied the proteins encoded by the Rous sarcoma virus (RSV) genome under Alan Smith. At the University of California, Berkeley, he worked with Steven Martin, who had established that transformation of normal cells to cancer cells requires an RSV protein. In 1979, the viral Src (v-Src) transforming protein was found to have the unprecedented ability to phosphorylate tyrosine. This sparked Tony's interest, and he quickly showed that the v-Fps transforming protein of Fujinami sarcoma virus (FSV) had the same activity, establishing tyrosine phosphorylation as a general mechanism of viral transformation.

In 1981, Tony became an assistant professor at the University of British Columbia in Vancouver. In collaboration with Michael Smith, he scanned the FSV transforming gene and discovered nontransforming insertions in a noncatalytic region of v-Fps, homologous to that lying immediately upstream of the v-Src kinase domain. Based on the homology and consequences of these insertions, he concluded that this noncatalytic domain had an important function and called it SH2. In a key advance, he showed that isolated SH2s bind to phosphorylated tyrosines in other proteins.

This established a new paradigm of signaling in which induced protein-protein interaction transduces the signal.

With SH2 as the prototype, Tony delineated how modular interaction domains could assemble signaling complexes to propagate an extracellular stimulus through intracellular signals. It soon became clear that SH2 domain-containing proteins were involved downstream of many types of cell surface receptors and were elements in proteins with distinct functions, including adaptors, enzymes, and transcription factors. Tony characterized other modular domains that interact with proteins either constitutively or inducibly. He quickly became the champion of modular protein inter-



action domains, and wrote a series of influential reviews.

In his talks, given in characteristic style, Tony stressed how modular domains could be exploited to build new signaling modules and pathways during evolution. For example, once they evolved, SH2 domains could link an existing signaling pathway to a new type of receptor system that used tyrosine phosphorylation. He validated this concept by altering the specificity of SH2 domains and creating new interaction domain combinations that rewired signaling pathways. One of his most recent discoveries was the importance of modular domain ligand affinities in dictating signal strength.

In 1985, Tony joined the Samuel Lunenfeld Research Institute (SLRI) of Mount Sinai Hospital (now the Lunenfeld-Tanenbaum Research Institute) in Toronto as a senior scientist. Over the next 25 years, he had a huge influence on science in the region, as a professor at the University of Toronto and as director of research at the SLRI from 2000 to 2005. He recruited outstanding scientists to the institute, promoted proteomics as a key technology for studying signaling networks, and founded MDS Proteomics, a proteomics-based drug discovery company. He received numerous prestigious Canadian awards, and in 2006 he was awarded the Companion of Honor by the Queen. His many international

A "titan of signaling" who established principles of protein-protein interactions that influenced our understanding of cellular signal transduction.

prizes included the Gairdner Award, the Wolf Prize, and the Kyoto Prize. He had been widely tipped to win the Nobel Prize.

I first met Tony in 1974 while he was a student at ICRF, through our common interest in using in vitro translation systems to study the products of viral genomes. We could not have known it at the time, but our paths were to cross innumerable times in the subsequent nearly 40 years. Shortly after he moved to Berkeley in 1976, I invited him to speak at the Salk Institute. Our last interaction was at the 2013 FASEB Meeting on Protein Kinases and Protein Phosphorylation where he gave the keynote talk. We organized many conferences together and collaborated on several projects, right up until his death. Each of us trained a graduate student who did postdoctoral work in the other's lab.

Our upbringing had many things in common. We were born less than 20 miles apart in Kent, attended "public" schools in England before graduating from the University of Cambridge, and ended up in North America. We also shared a love for rivers. Tony was an avid fly fisherman, and whenever at a meeting near mountains, he took an afternoon off to fish. His father, Tony Pawson Sr., was world fly fishing champion, and Tony often said that he went to North America to get away from his father's fame in the UK as a cricketer and soccer player. My wife and I had many enjoyable outings with Tony and his wife Maggie in different parts of the world. Maggie died of lung cancer in 2011, and Tony really never got over her loss.

Soon after his sudden passing, I went rafting on the Middle Fork of the Salmon River in Idaho, giving me time to reflect on my friend's life and contributions. He influenced the next generation of scientists not only by his seminal findings, but through his interactions at meetings, where he was known for his enthusiasm and approachability and the encouragement that he gave to younger scientists. "The other Tony" will be sorely missed by his three children, his friends, by all those in the scientific community who knew him, and by everyone whose science was influenced by his work. His latest research was going better than ever, and it is tragic that we will never know what other new principles of signal transduction he might have uncovered.

10.1126/science.1244986

Salk Institute, 10010 North Torrey Pines Road, La Jolla, CA 92037, USA. E-mail: hunter@salk.edu

CREDIT: MOUNT SINAI HOSPITAL

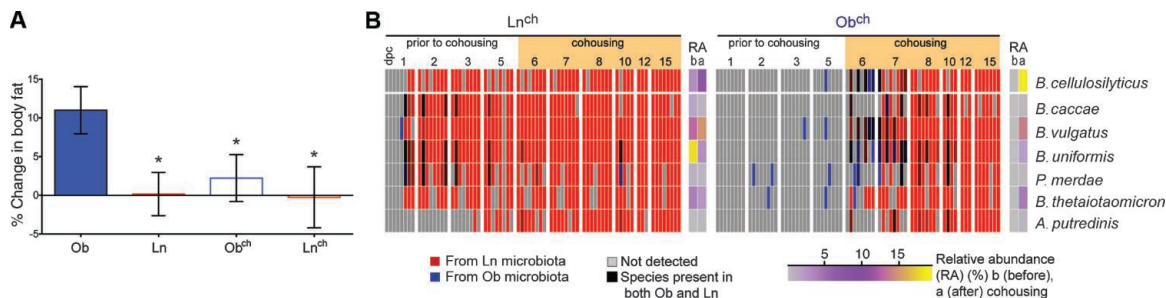
Gut Microbiota from Twins Discordant for Obesity Modulate Metabolism in Mice

Vanessa K. Ridaura, Jeremiah J. Faith, Federico E. Rey, Jiye Cheng, Alexis E. Duncan, Andrew L. Kau, Nicholas W. Griffin, Vincent Lombard, Bernard Henrissat, James R. Bain, Michael J. Muehlbauer, Olga Ilkayeva, Clay F. Semenkovich, Katsuhiko Funai, David K. Hayashi, Barbara J. Lyle, Margaret C. Martini, Luke K. Ursell, Jose C. Clemente, William Van Treuren, William A. Walters, Rob Knight, Christopher B. Newgard, Andrew C. Heath, Jeffrey I. Gordon*

Introduction: Establishing whether specific structural and functional configurations of a human gut microbiota are causally related to a given physiologic or disease phenotype is challenging. Twins discordant for obesity provide an opportunity to examine interrelations between obesity and its associated metabolic disorders, diet, and the gut microbiota. Transplanting the intact uncultured or cultured human fecal microbiota from each member of a discordant twin pair into separate groups of recipient germ-free mice permits the donors' communities to be replicated, differences between their properties to be identified, the impact of these differences on body composition and metabolic phenotypes to be discerned, and the effects of diet-by-microbiota interactions to be analyzed. In addition, cohousing coprophagic mice harboring transplanted microbiota from discordant pairs provides an opportunity to determine which bacterial taxa invade the gut communities of cage mates, how invasion correlates with host phenotypes, and how invasion and microbial niche are affected by human diets.

Methods: Separate groups of germ-free mice were colonized with uncultured fecal microbiota from each member of four twin pairs discordant for obesity, or with culture collections from an obese (Ob) or lean (Ln) co-twin. Animals were fed a mouse chow low in fat and rich in plant polysaccharides (LF-HPP) or one of two diets reflecting the upper or lower (Hi or Lo) tertiles of consumption of saturated fats (SF) and fruits and vegetables (FV) based on the U.S. National Health and Nutrition Examination Survey (NHANES). Ln or Ob mice were cohoused 5 days after colonization. Body composition changes were defined by quantitative magnetic resonance. Microbiota or microbiome structure, gene expression, and metabolism were assayed by 16S ribosomal RNA profiling, whole-community shotgun sequencing, RNA-sequencing, and mass spectrometry. Host gene expression and metabolism were also characterized.

Results and Discussion: The intact uncultured and culturable bacterial component of Ob co-twins' fecal microbiota conveyed significantly greater increases in body mass and adiposity than those of Ln communities. Differences in body composition were correlated with differences in fermentation of short-chain fatty acids (increased in Ln), metabolism of branched-chain amino acids (increased in Ob), and microbial transformation of bile acid species (increased in Ln and correlated with down-regulation of host farnesoid X receptor signaling). Cohousing Ln and Ob mice prevented development of increased adiposity and body mass in Ob cage mates and transformed their microbiota's metabolic profile to a leanlike state. Transformation correlated with invasion of members of Bacteroidales from Ln into Ob microbiota. Invasion and phenotypic rescue were diet-dependent and occurred with the diet representing the lower tertile of U.S. consumption of saturated fats and upper tertile of fruits and vegetables but not with the diet representing the upper tertile of saturated fats and lower tertile of fruit and vegetable consumption. These results reveal that transmissible and modifiable interactions between diet and microbiota influence host biology.



Cohousing Ln and Ob mice prevents adiposity phenotype in Ob cage mates (Ob^{ch}). (A) The adiposity change after 10 days of cohousing. **P* < 0.05 versus Ob controls (Student's *t* test). (B) Bacteroidales from Ln^{ch} microbiota invade the Ob^{ch} microbiota. Columns show individual mice.

READ THE FULL ARTICLE ONLINE
<http://dx.doi.org/10.1126/science.1241214>

Cite this article as V. K. Ridaura *et al.*, *Science* **341**, 1241214 (2013).
 DOI: 10.1126/science.1241214

FIGURES IN THE FULL ARTICLE

Fig. 1. Reliable replication of human donor microbiota in gnotobiotic mice.

Fig. 2. Cohousing Ob^{ch} and Ln^{ch} mice transforms the adiposity phenotype of cage mates harboring the obese co-twin's culture collection to a leanlike state.

Fig. 3. Effect of cohousing on metabolic profiles in mice consuming the LF-HPP diet.

Fig. 4. Effects of NHANES-based LoSF-HiFV and HiSF-LoFV diets on bacterial invasion, body mass, and metabolic phenotypes.

Fig. 5. Invasion analysis of species-level taxa in Ob^{ch} or Ln^{ch} mice fed the NHANES-based LoSF-HiFV diet.

Fig. 6. Acylcarnitine profile in the skeletal muscle of mice colonized with the Ob or Ln culture collections from dizygotic twin pair 1 and fed the LoSF-HiFV diet.

SUPPLEMENTARY MATERIALS

Materials and Methods
 Supplementary Text
 Figs. S1 to S17
 Tables S1 to S17
 References and Notes

RELATED ITEMS IN SCIENCE

A. W. Walker, J. Parkhill, Fighting obesity with bacteria. *Science* **341**, 1069–1070 (2013).
 DOI: 10.1126/science.1243787

The list of author affiliations is available in the full article online.

*Corresponding author. E-mail: jgordon@wustl.edu

Gut Microbiota from Twins Discordant for Obesity Modulate Metabolism in Mice

Vanessa K. Ridaura,¹ Jeremiah J. Faith,¹ Federico E. Rey,¹ Jiye Cheng,¹ Alexis E. Duncan,^{2,3} Andrew L. Kau,¹ Nicholas W. Griffin,¹ Vincent Lombard,⁴ Bernard Henrissat,^{4,5} James R. Bain,^{6,7,8} Michael J. Muehlbauer,⁶ Olga Ilkayeva,⁶ Clay F. Semenkovich,⁹ Katsuhiko Funai,⁹ David K. Hayashi,¹⁰ Barbara J. Lyle,¹¹ Margaret C. Martini,¹¹ Luke K. Ursell,¹² Jose C. Clemente,¹² William Van Treuren,¹² William A. Walters,¹³ Rob Knight,^{12,14,15} Christopher B. Newgard,^{6,7,8} Andrew C. Heath,² Jeffrey I. Gordon^{1*}

The role of specific gut microbes in shaping body composition remains unclear. We transplanted fecal microbiota from adult female twin pairs discordant for obesity into germ-free mice fed low-fat mouse chow, as well as diets representing different levels of saturated fat and fruit and vegetable consumption typical of the U.S. diet. Increased total body and fat mass, as well as obesity-associated metabolic phenotypes, were transmissible with uncultured fecal communities and with their corresponding fecal bacterial culture collections. Cohousing mice harboring an obese twin's microbiota (Ob) with mice containing the lean co-twin's microbiota (Ln) prevented the development of increased body mass and obesity-associated metabolic phenotypes in Ob cage mates. Rescue correlated with invasion of specific members of Bacteroidetes from the Ln microbiota into Ob microbiota and was diet-dependent. These findings reveal transmissible, rapid, and modifiable effects of diet-by-microbiota interactions.

Microbial community configurations vary substantially between unrelated individuals (1–9), which creates a challenge in designing surveys of sufficient power to determine whether observed differences between disease-associated and healthy communities differ significantly from normal interpersonal variation. This challenge is especially great if, for a given disease state, there are many associated states of the microbial species (microbiota) or microbial gene repertoire (microbiome), each shared by relatively few individuals. Microbiota configurations

are influenced by early environmental exposures and are generally more similar among family members (2, 7, 10, 11).

There have been conflicting reports about the relation between interpersonal differences in the structure of the gut microbiota and host body mass index (BMI). Taxonomic profiles for obese and lean individuals may have distinct patterns between human populations, but technical issues related to how gut samples are processed and community members are identified by 16S ribosomal RNA (rRNA) gene sequencing may also play a role in observed differences. The relative contributions of the microbiota and dietary components to obesity and obesity-related metabolic phenotypes are unclear and likely multifaceted (2, 12–17). Transplants of fecal microbiota from healthy donors to recipients with metabolic syndrome have provided evidence that the microbiota can ameliorate insulin-resistance, although the underlying mechanisms remain unclear (18).

Monozygotic (MZ) or dizygotic (DZ) twins discordant for obesity (19, 20) provide an attractive model for studying the interrelations between obesity, its associated dietary and lifestyle risk factors, and the gut microbiota/microbiome. In the case of same-sex twins discordant for a disease phenotype, the healthy co-twin provides a valuable reference control to contrast with the co-twin's disease-associated gut community. However, this comparison is fundamentally descriptive and cannot establish causality. Transplanting a fecal sample obtained from each twin in a discordant pair into separate groups of recipient germ-free mice provides an opportunity to (i) identify structural and functional

differences between their gut communities; (ii) generate and test hypotheses about the impact of these differences on host biology, including body composition and metabolism; and (iii) determine the effects of diet-by-microbiota interactions through manipulation of the diets fed to these “humanized” animals and/or the representation of microbial taxa in their gut communities.

Reproducibility of Microbiota Transplants from Discordant Twins

We surveyed data collected from 21- to 32-year-old female twin pairs ($n = 1539$) enrolled in the Missouri Adolescent Female Twin Study [MOAFTS; (21, 22); for further details, see ref. (23)]. We recruited four twin pairs, discordant for obesity (obese twin BMI > 30 kg/m²) with a sustained multiyear BMI difference of ≥ 5.5 kg/m² ($n = 1$ MZ and 3 DZ pairs) (Fig. 1A). Fecal samples were collected from each twin, frozen immediately after they were produced, and stored at -80°C . Each fecal sample was introduced, via a single oral gavage, into a group of 8- to 9-week-old adult male germ-free C57BL/6J mice (one gnotobiotic isolator per microbiota sample; each recipient mouse was individually caged within the isolator; $n = 3$ to 4 mice per donor microbiota sample per experiment; $n = 1$ to 5 independent experiments per microbiota). All recipient mice were fed, ad libitum, a commercial, sterilized mouse chow that was low in fat (4% by weight) and high in plant polysaccharides (LF-HPP) (23). Fecal pellets were obtained from each mouse 1, 3, 7, 10, and 15 days post colonization (dpc) and, for more prolonged experiments, on days 17, 22, 24, 29, and 35.

Unweighted UniFrac-based comparisons of bacterial 16S rRNA data sets generated from the input human donor microbiota, from fecal samples collected from gnotobiotic mice and from different locations along the length of the mouse gut at the time they were killed (table S1A), plus comparisons of the representation of genes with assignable enzyme commission numbers (ECs) in human fecal and mouse cecal microbiomes (defined by shotgun sequencing), disclosed that transplant recipients efficiently and reproducibly captured the taxonomic features of their human donor's microbiota and the functions encoded by the donor's microbiome (see Fig. 1B; fig. S1, A to E; fig. S2; table S1B; and table S2, A to D) (23). The 16S rRNA data sets allowed us to identify bacterial taxa that differentiate gnotobiotic mice harboring gut communities transplanted from all lean versus all obese co-twins [analysis of variance (ANOVA) using Benjamini-Hochberg correction for multiple hypotheses] [table S3; see (23) for details].

Reproducible Transmission of Donor Body Composition Phenotypes

Quantitative magnetic resonance (QMR) analysis was used to assess the body composition of transplant recipients 1 day, 15 days, and, in

¹Center for Genome Sciences and Systems Biology, Washington University School of Medicine, St. Louis, MO 63108, USA.

²Department of Psychiatry, Washington University School of Medicine, St. Louis, MO 63110, USA. ³George Warren Brown School of Social Work, Washington University, St. Louis, MO 63130, USA. ⁴Architecture et Fonction des Macromolécules Biologiques, CNRS and Aix Marseille Université, CNRS UMR 7257, 13288 Marseille, France. ⁵Department of Cellular and Molecular Medicine, Faculty of Health and Medical Sciences, University of Copenhagen, DK-2200, Copenhagen, Denmark. ⁶Sarah W. Stedman Nutrition and Metabolism Center, Duke University Medical Center, Durham, NC 27710, USA. ⁷Department of Medicine, Duke University Medical Center, Durham, NC 27710, USA. ⁸Department of Pharmacology and Cancer Biology, Duke University Medical Center, Durham, NC 27710, USA. ⁹Department of Medicine, Washington University School of Medicine, St. Louis, MO 63110, USA. ¹⁰Mondelez International, Glenview, IL 60025, USA. ¹¹Kraft Foods Group, Glenview, IL 60025, USA. ¹²Department of Chemistry and Biochemistry, University of Colorado, Boulder, CO 80309, USA. ¹³Molecular, Cellular and Developmental Biology, University of Colorado, Boulder, CO 80309, USA. ¹⁴BioFrontiers Institute, University of Colorado, Boulder, CO 80309, USA. ¹⁵Howard Hughes Medical Institute, University of Colorado, Boulder, CO 80309, USA.

*To whom correspondence should be sent. E-mail: jgordon@wustl.edu

the case of longer experiments, 8, 22, 29, and 35 days after transplantation. The increased adiposity phenotype of each obese twin in a discordant twin pair was transmissible: The change in adipose mass of mice that received an obese co-twin's fecal microbiota was significantly greater than the change in animals receiving her lean twin's gut community within a given experiment and was reproducible across experiments ($P \leq 0.001$, one-tailed unpaired Student's t test; $n = 103$ mice phenotyped) (Fig. 1, C to E). Epididymal fat pad weights (normalized to total body weight) were also significantly higher in mice colonized with gut communities from obese twins ($P \leq 0.05$, one-tailed unpaired Student's t test). These differences in adiposity were not associated with statistically significant differences in daily chow consumption (measured on days 1, 8, and 15 after gavage and weekly thereafter for longer experiments) or with appreciably greater inflammatory responses in recipients of obese compared with lean co-twin fecal microbiota as judged by fluorescence-activated cell sorting (FACS) analysis of the CD4⁺ and CD8⁺ T cell compartments in spleen, mesenteric lymph nodes, small intestine, or colon [see (23) for details].

Functional Differences Between Transplanted Microbial Communities

Fecal samples collected from gnotobiotic mice were used to prepare RNA for microbial RNA sequencing (RNA-Seq) of the transplanted microbial communities' meta-transcriptomes (table S1C). Transcripts were mapped to a database of sequenced human gut bacterial genomes and assigned to *Kyoto Encyclopedia of Genes and Genomes* (KEGG) Enzyme Commission numbers (EC numbers) [see ref. (23)]. Significant differences and distinguishing characteristics were defined using ShotgunFunctionalizeR, which is based on a Poisson model (24) (see table S4 and table S5 for ECs and KEGG level 2 pathways, respectively). Transcripts encoding 305 KEGG ECs were differentially expressed between mice harboring microbiomes transplanted from lean or obese donors [ShotgunFunctionalizeR, Akaike's information criterion (AIC) < 5000; $P \leq 10^{-30}$].

Mice harboring the transplanted microbiomes from the obese twins exhibited higher expression of microbial genes involved in detoxification and stress responses; in biosynthesis of cobalamin; metabolism of essential amino acids (phenylalanine, lysine, valine, leucine, and isoleucine)

and nonessential amino acids (arginine, cysteine, and tyrosine); and in the pentose phosphate pathway (fig. S3, A and B; table S4, B to G; and table S5). Follow-up targeted tandem mass spectrometry (MS/MS)-based analysis of amino acids in sera obtained at the time mice were killed demonstrated significant increases in branched-chain amino acids (BCAA: Val and Leu/Ile), as well as other amino acids (Met, Ser, and Gly), plus trends to increase (Phe, Tyr, and Ala), in recipients of microbiota from obese compared with lean co-twins in discordant twin pairs DZ1 and MZ4 (tables S1D and S6A). These specific amino acids, as well as the magnitude of their differences, are remarkably similar to elevations in BCAA and related amino acids reported in obese and insulin-resistant versus lean and insulin-sensitive humans (25). This finding suggested that the gut microbiota from obese subjects could influence metabolites that characterize the obese state.

In contrast, the transplanted microbiomes from lean co-twins exhibited higher expression of genes involved in (i) digestion of plant-derived polysaccharides [e.g., α -glucuronidase (EC 3.2.1.139), α -L-arabinofuranosidase (EC 3.2.1.55)]; (ii) fermen-

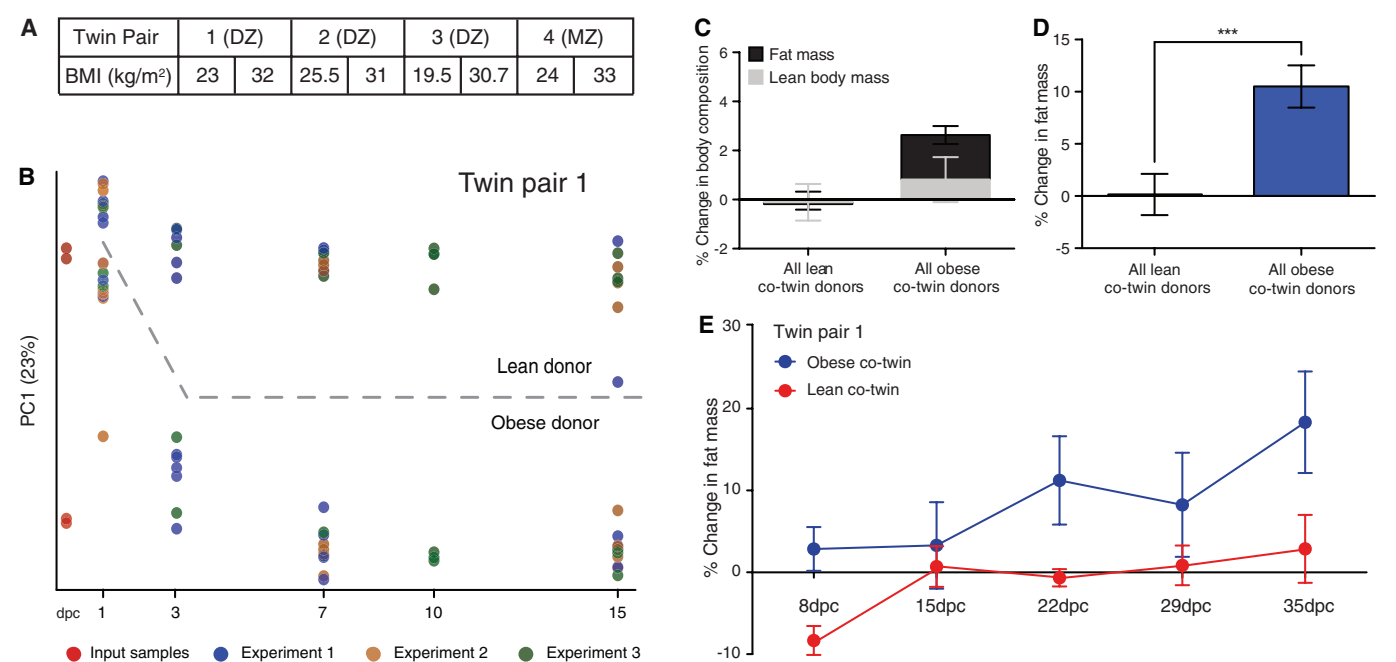


Fig. 1. Reliable replication of human donor microbiota in gnotobiotic mice. (A) Features of the four discordant twin pairs. (B) Assembly of bacterial communities in mice that had received intact and uncultured fecal microbiota transplants from the obese and lean co-twins in DZ pair 1. Principal coordinates analysis plot of principal coordinate 1 (PC1) based on an unweighted UniFrac distance matrix and 97%OTUs present in sampled fecal communities. Circles correspond to a single fecal sample obtained at a given time point from a given mouse and are colored according to the experiment ($n = 3$ independent experiments). Note that assembly is reproducible within members of a group of mice that have received a given microbiota, as well as between experiments. (C) Body composition, defined by QMR, was performed 1 day and 15 dpc of each mouse in each recipient group. Mean values (\pm SEM) are plotted for the percent increase in fat mass and lean body mass at 15 dpc for all recipient mice of each of the four obese co-twins' or lean co-twins' fecal microbiota, normalized to the

initial body mass of each recipient mouse. A two-way ANOVA indicated that there was a significant donor effect ($P \leq 0.05$), driven by a significant difference in adiposity and total body mass between mice colonized with a lean or obese co-twin donor's fecal microbiota (adjusted $P \leq 0.05$; Šidák's multiple comparison test). (D) Mean values (\pm SEM) are plotted for the percent change in fat mass at 15 dpc for all recipient mice of each of the four obese co-twins' or lean co-twins' fecal microbiota. Data are normalized to initial fat mass ($n = 3$ to 12 animals per donor microbiota; 51 to 52 mice per BMI bin; total of 103 mice). *** $P \leq 0.001$, as judged by a one-tailed unpaired Student's t test. (E) More prolonged time course study for recipients of fecal microbiota from co-twins in discordant DZ pair 1 (mean values \pm SEM plotted; $n = 4$ mice per donor microbiota). The difference between the gain in adiposity calculated relative to initial fat mass (1 dpc) between the two recipient groups of mice is statistically significant ($P \leq 0.001$, two-way ANOVA).

tation to butyrate [acetyl-CoA C-acetyltransferase (EC 2.3.1.9), 3-hydroxybutyryl-CoA dehydrogenase (EC 1.1.1.157), 3-hydroxybutyryl-CoA dehydratase (EC 4.2.1.55), butyryl-CoA dehydrogenase (EC 1.3.8.1)] (fig. S3, C and D); and (iii) fermentation to propionate [succinate dehydrogenase (EC 1.3.99.1), phosphoenolpyruvate carboxykinase (EC 4.1.1.32), methylmalonyl-CoA mutase (EC 5.4.99.2)] (table S4A). Follow-up gas chromatography–mass spectrometry (GC-MS) of cecal contents confirmed that levels of butyrate and propionate were significantly increased and that levels of several mono- and disaccharides significantly decreased in animals colonized with lean compared with obese co-twin gut communities ($P \leq 0.05$, unpaired Student's t test) (fig. S4, A and B, and table S6B). Procrustes analysis, using a Hellinger distance matrix (26), revealed significant correlations between taxonomic structure [97% identity (97%ID) threshold for defining distinct operational taxonomic units (OTU) in fecal samples], transcriptional profiles (enzyme representation in fecal mRNA populations), and metabolic profiles (GC-MS of cecal samples), with separation of groups based on donor microbiota and BMI (Mantel test, $P \leq 0.001$) (fig. S5).

These results suggest that, in this diet context, transplanted microbiota from lean co-twins had a greater capacity to breakdown and ferment polysaccharides than the microbiota of their obese co-twins. Previous reports have shown that increased microbial fermentation of nondigestible starches is associated with decreased body weight and decreased adiposity in conventionally raised mice that harbor a mouse microbiota [e.g., refs. (27–29)].

Phenotypes Produced by Bacterial Culture Collections

We followed up these studies of transplanted, intact, and uncultured donor communities with a set of experiments involving culture collections produced from the fecal microbiota of one of the discordant twin pairs. Our goal was to determine whether cultured bacterial members of the co-twins' microbiota could transmit the discordant adiposity phenotypes and distinctive microbiota-associated metabolic profiles when transplanted into gnotobiotic mouse recipients that received the LF-HPP chow diet.

Collections of cultured anaerobic bacteria were generated from each co-twin in DZ pair 1 and subsequently introduced into separate groups of 8-week-old germ-free male C57BL/6J mice ($n = 5$ independent experiments; $n = 4$ to 6 recipient mice per culture collection per experiment). The culture collections stabilized in the guts of recipient mice within 3 days after their introduction [see (23); fig. S6, A to E; and table S7 for documentation of the efficient and reproducible capture of cultured taxa and their encoded gene functions between groups of recipient mice].

As in the case of uncultured communities, we observed a significantly greater increase in adiposity in recipients of the obese twin's culture collection compared with the lean co-twin's culture collection ($P \leq 0.02$, one-tailed unpaired Student's t test) (Fig. 2, A and B). Nontargeted GC-MS showed

that the metabolic profiles generated by the transplanted culture collections clustered with the profiles produced by the corresponding intact uncultured communities (fig. S6E). In addition, the fecal biomass of recipients of the culture collection from the lean twin was significantly greater than the fecal biomass of mice receiving the culture collection from her obese sibling; these differences were manifest within 7 days ($P \leq 0.0001$, two-way ANOVA) (fig. S7A).

Cohousing Ob and Ln Animals Prevents an Increased Adiposity Phenotype

Because mice are coprophagic, the potential for transfer of gut microbiota through the fecal-oral route is high. Therefore, we used cohousing to determine whether exposure of a mouse harboring a culture collection from the lean twin could prevent development of the increased adiposity phenotype and microbiome-associated metabolic profile of a cage mate colonized with the culture collection from her obese co-twin or vice versa. Five days after gavage, when each of the inoculated microbial consortia had stabilized in the guts of recipient animals, a mouse with the lean co-twin's culture collection was cohoused with a mouse with the obese co-twin's culture collection (abbreviated Ln^{ch} and Ob^{ch}, respectively). Control groups consisted of cages of dually housed recipients of the lean twin culture collection and dually housed recipients of the obese co-twin's culture collection ($n = 3$ to 5 cages per housing configuration per experiment; $n = 4$ independent experiments; each housing configuration in each experiment was placed in a separate gnotobiotic isolator) (Fig. 2A). All mice were 8-week-old C57BL/6J males. All were fed the same LF-HPP chow ad libitum that was used for transplants involving the corresponding uncultured communities. Bedding was changed before initiation of cohousing. Fecal samples were collected from all recipients 1, 2, 3, 5, 6, 7, 8, 10, and 15 days after gavage. Body composition was measured by QMR 1 and 5 days after gavage, and after 10 days of cohousing.

Ob^{ch} mice exhibited a significantly lower increase in adiposity compared with control Ob animals that had never been exposed to mice harboring the lean co-twin's culture collection ($P \leq 0.05$, one-tailed unpaired Student's t test). Moreover, the adiposity of these Ob^{ch} animals was not significantly different from Ln controls ($P > 0.05$, one-tailed unpaired Student's t test) (Fig. 2B). In addition, exposure to Ob^{ch} animals did not produce a significant effect on the adiposity of Ln^{ch} mice: Their adiposity phenotypes and fecal biomass were indistinguishable from dually housed Ln controls (Fig. 2B; and fig. S7, B and C). Cohousing caused the cecal metabolic profile of Ob^{ch} mice to assume features of Ln^{ch} and control Ln animals, including higher levels (compared with dually housed Ob controls) of propionate and butyrate and lower levels of cecal mono- and disaccharides, as well as BCAA and aromatic amino acids (Fig. 2, C and D, and fig. S8).

Principal coordinates analysis of unweighted UniFrac distances revealed that the fecal micro-

biota of Ob^{ch} mice were reconfigured so that they came to resemble the microbiota of Ln^{ch} cage mates. In contrast, the microbiota of the Ln^{ch} cage mates remained stable (fig. S9, A to C). We performed a follow-up analysis to identify species-level taxa that had infiltrated into and/or had been displaced from the guts of mice harboring the Ln and Ob culture collections. We did so by characterizing the direction and success of invasion. Microbial SourceTracker estimates, for every species-level taxon or 97%ID OTU, the Bayesian probability (P) of its being derived from each of a set of source communities (30). The fecal microbiota of Ln or Ob controls sampled 5 days after colonization were used as source communities to determine the direction of invasion. The fecal communities belonging to each Ln^{ch} and Ob^{ch} mouse were then traced to these sources. We defined the direction of invasion for these bacterial taxa, by calculating the log odds ratio of the probability of a Ln origin (PLn) or an Ob origin (POb) for each species-level taxon or 97%ID OTU, i , as follows:

$$\log_2 (PLn_i / POB_i)$$

A positive log odds ratio indicated that a species or 97%ID OTU was derived from a Ln source; a negative log odds ratio indicated an Ob source. An invasion score was calculated to quantify the success of invasion of each species or 97%ID OTU, i , into each cohousing group, j , as follows:

$$\text{Invasion Score}_{ij} = \log_2 \left(\frac{\overline{A}_{ij}}{\overline{B}_j} \right)$$

where \overline{A}_{ij} is the average relative abundance of taxon i in all fecal samples collected from group j after cohousing, and \overline{B}_j is its relative abundance in all samples taken from that group before cohousing.

The observed mean of the distribution of invasion scores for Ob^{ch} animals was significantly higher than that for dually housed Ob-Ob controls ($P \leq 0.0005$, Welch's two-sample t test) (fig. S10A). This was not the case for Ln^{ch} animals when compared with dually housed Ln-Ln controls ($P > 0.05$), which suggested that there was significant invasion of components of the Ln^{ch} microbiota into the microbiota of Ob^{ch} cage mates, but not vice versa. To quantify invasion further, we used the mean and standard deviation of the null distribution of invasion scores (defined as the scores from recipients of the Ln or Ob microbiota that had never been cohoused with each other) to calculate a z value and a Benjamini-Hochberg adjusted P value for the invasion score of each species in Ln^{ch} and Ob^{ch} mice. We conservatively defined a taxon as a successful invader if it (i) had a Benjamini-Hochberg adjusted $P \leq 0.05$, (ii) was represented in $\geq 75\%$ of Ob^{ch} or Ln^{ch} mice when sampled 7 and 10 days after initiation of cohousing, and (iii) had a relative abundance of $\leq 0.05\%$ before cohousing and $\geq 0.5\%$ in the fecal microbiota at the time mice were killed. We defined a taxon that was displaced from an animal's microbiota upon cohousing as having a relative

abundance $\geq 1\%$ in Ln^{ch} or Ob^{ch} mice before they were cohoused and a relative abundance $< 0.5\%$ after cohousing.

The direction and success of invasion are shown in Fig. 2E and table S8A. The most successful Ln^{ch} invaders of the Ob^{ch} microbiota were

members of the Bacteroidetes (rank order of their invasion scores: *Bacteroides cellulosilyticus*, *B. uniformis*, *B. vulgatus*, *B. thetaiotaomicron*,

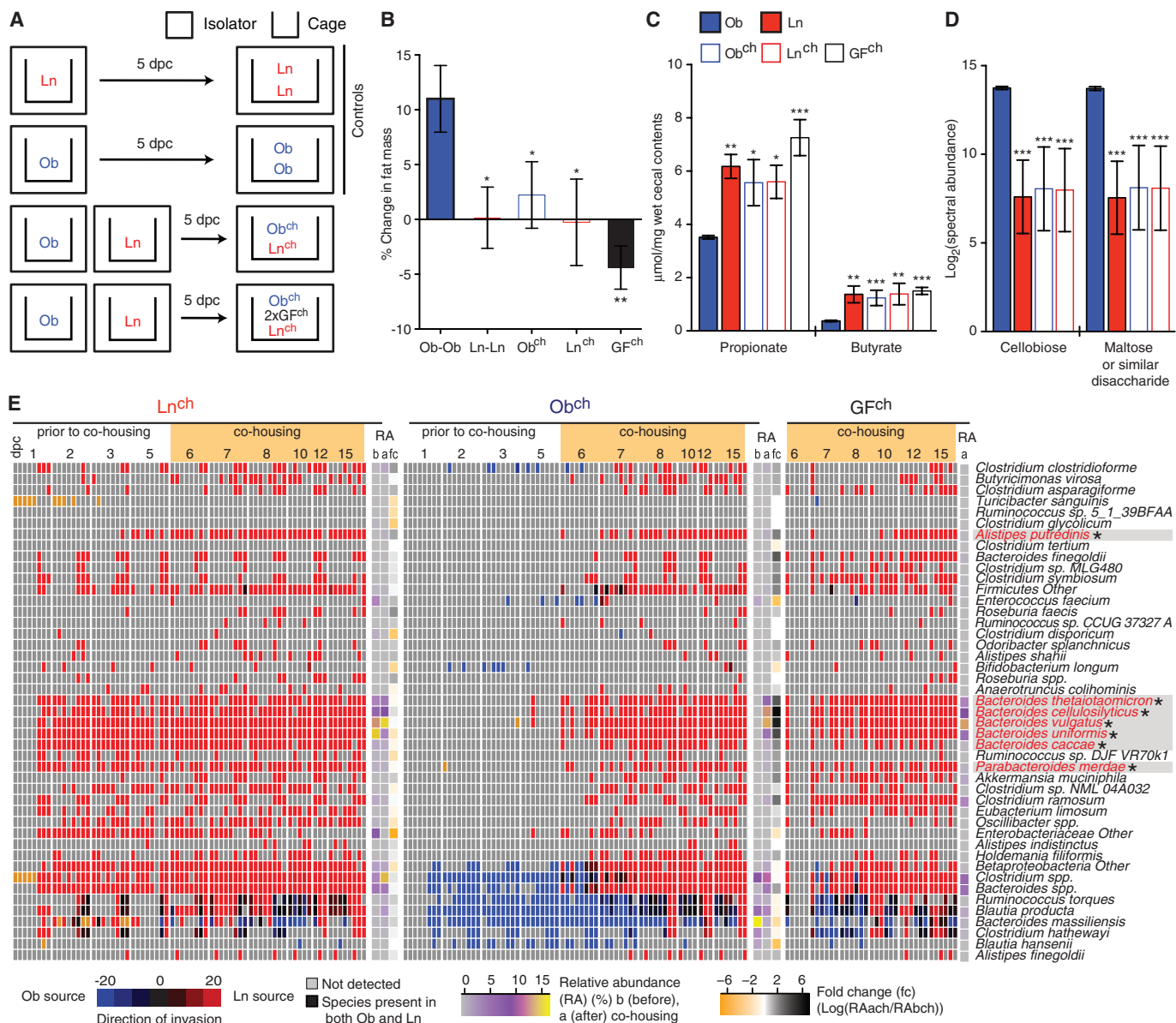


Fig. 2. Cohousing Ob^{ch} and Ln^{ch} mice transforms the adiposity phenotype of cage mates harboring the obese co-twin's culture collection to a lean-like state. (A) Design of cohousing experiment: 8-week-old, male, germ-free C57BL/6J mice received culture collections from the lean (Ln) twin or the obese (Ob) co-twin in DZ twin pair 1. Five days after colonization, mice were cohoused in one of three configurations: Control groups consisted of dually housed Ob-Ob or Ln-Ln cage mates; the experimental group consisted of dually housed Ob^{ch}-Ln^{ch} cage mates (data shown from five cages per experiment; two independent experiments) or Ob^{ch}-Ln^{ch}-GF^{ch}-GF^{ch} cage mates (*n* = 3 cages per experiment). All mice were fed a LF-HPP diet. (B) Effects of cohousing on fat mass. Changes from the first day after cohousing to 10 days after cohousing were defined using whole-body QMR. **P* ≤ 0.05, ***P* ≤ 0.01 compared with Ob-Ob controls, as defined by one-tailed unpaired Student's *t* test. (C) Targeted GC-MS analysis of cecal short-chain fatty acids. Compared with Ob-Ob controls, the concentrations of propionate and butyrate were significantly higher in the ceca of Ob^{ch}, Ln-Ln, Ln^{ch}, and GF^{ch} mice. (D) Nontargeted GC-MS analysis of cecal levels of cellobiose and "maltose or a similar disaccharide." **P* ≤ 0.05; ***P* ≤ 0.01; ****P* ≤ 0.005. (E) Evidence that bacterial species from the Ln^{ch}

microbiota invade the Ob^{ch} microbiota. Shown are SourceTracker-based estimates of the proportion of bacterial taxa in a given community sampled from a cage mate. For Ob^{ch}-Ln^{ch} cohousing experiments, Ob^{ch} and Ln^{ch} microbiota were designated as sink communities, whereas the gut microbiota of Ob-Ob and Ln-Ln controls (at 5 dpc) were considered source communities. Red indicates species derived from the Ln^{ch} gut microbial community. Blue denotes species derived from the Ob^{ch} microbiota. Black denotes unspecified source (i.e., both communities have this species), whereas orange indicates an uncertain classification by the SourceTracker algorithm. "Other" after a genus name means unclassified. An asterisk placed next to a species indicates that it is a successful invader as defined in the text. Average relative abundance (RA) in the fecal microbiota is shown before cohousing (b, at 5 dpc) and after cohousing (a, at 15 dpc). The average fold-change (fc) in relative abundance for a given taxon, for all time points before and after cohousing is shown (excluding the first 2 days immediately after gavage of the microbiota and immediately after initiation of cohousing). Note that only taxa with significant changes in relative abundance between samples collected before and samples collected after cohousing are shown. For a full accounting of all taxa, see table S8A.

B. caccae, *Alistipes putredinis*, and *Parabacteroides merdae*). Invasiveness exhibited specificity at the 97%ID OTU level (fig. S11). In contrast, cohousing did not result in significant invasion of Ln^{ch} intestines with members of the Ob^{ch} microbiota.

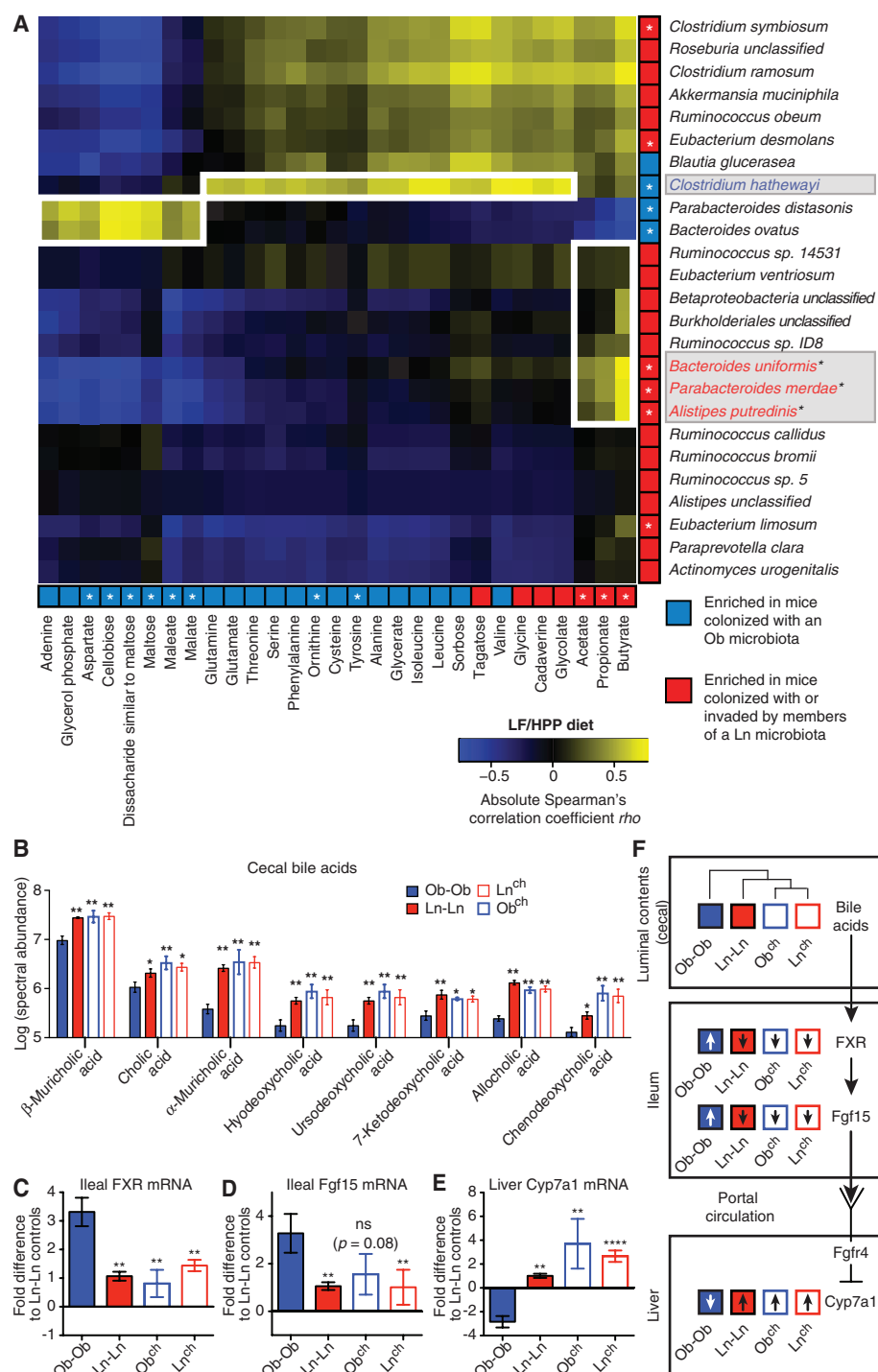
In macroecosystems, successful invaders are often more likely to become established if they are from divergent taxa that do not share a niche with members of the native entrenched community (31, 32). We used the Net Relatedness Index [NRI (33)] to show that Ln and Ob communities

have different phylogenetic structures and that the patterns of phylogenetic clustering and dispersion of Ob, but not Ln microbiota, change as a consequence of cohousing. Specifically fecal Ln, Ln^{ch} , and Ob^{ch} communities had a negative NRI, which indicates that the community is more phylogenetically dispersed than Ob controls. Furthermore, the fecal communities of Ln^{ch} and Ob^{ch} animals had significantly more shared branch length with each other after cohousing compared with before cohousing [for a description of calculations and interpretation, see (23), fig. S9E,

and fig. S12]. Together, these patterns of phylogenetic overdispersion and increased shared branch length in cohoused Ln^{ch} and Ob^{ch} animals led us to hypothesize that Bacteroides in the Ln^{ch} community were efficient invaders of Ob^{ch} communities because they were able to occupy unoccupied niches in Ob^{ch} intestines. Note that increased representation of Bacteroidetes has been documented in several independent studies of the gut microbiota of conventionally raised lean mice compared with mice having genetic- or diet-induced obesity (34, 35).

Fig. 3. Effect of cohousing on metabolic profiles in mice consuming the LF-HPP diet.

(A) Spearman's correlation analysis of cecal metabolites and cecal bacterial species-level taxa in samples collected from Ob^{ch} , Ln^{ch} , GF^{ch} , $\text{Ln}^{39\text{ch}}$, and $\text{Ob}^{\text{ch/Ln}^{39}}$ cage mates and from Ob-Ob and Ln-Ln controls (correlations with $P \leq 0.0001$ are shown). Taxonomic assignments were made using a modified taxonomy from the National Center for Biotechnology Information (of the U.S. National Institutes of Health) (23). Bacterial species and cecal metabolites enriched in animals colonized with either the Ln or Ob culture collections are colored red and blue, respectively. An asterisk in the colored box indicates that a taxon or metabolite is significantly enriched in mice colonized with Ln (red) or Ob (blue) culture collections. Bacterial species colored red denote significant invaders from Ln^{ch} mice into the gut microbiota of Ob^{ch} cage mates. (B) Cecal bile acids measured by UPLC-MS. Note that levels are plotted as log-transformed spectral abundances. Significance of differences relative to Ob-Ob controls were defined using a two-way ANOVA with Holm-Šidák's correction for multiple hypotheses; $*P \leq 0.05$; $**P \leq 0.01$. (C and D) QPCR assays of FXR and Fgf15 mRNA levels in the distal ileum. Data are normalized to Ln-Ln controls. (E) QPCR of hepatic Cyp7a1 mRNA, normalized to Ln-Ln controls. $*P \leq 0.05$; $**P \leq 0.01$; $****P \leq 0.001$ (defined by one-tailed, unpaired Student's *t* test using Ob-Ob mice as reference controls). (F) Correlating cecal bile acid profiles with the FXR-Fgf15-Cyp7A signaling pathway in the different groups of mice. (Top) The dendrogram highlights the differences in the profiles of 37 bile acid species between Ob-Ob controls and the other three treatment groups (table S11). The dendrogram was calculated using the Bray-Curtis dissimilarity index and the average relative abundance of each bile acid species among all mice belonging to a given treatment group.



Control experiments involving cohousing a germ-free (GF^{ch}) mouse with an Ob mouse 5 days after transplantation of the complete culture collection from the obese co-twin demonstrated effective transmission of the Ob adiposity phenotype to the GF cage mate (defined by epididymal fat pad weight as a percentage of total body weight; $P > 0.05$, comparing GF^{ch}-Ob and Ob^{ch}-GF cage mates with a two-tailed unpaired Student's t test). The adiposity (epididymal fat pad weights) of the GF^{ch}-Ob cage mate was significantly greater compared with GF-GF controls [$1.4 \pm 0.1\%$ of body weight (Ob^{ch}-GF); $1.4 \pm 0.05\%$ (GF^{ch}-Ob); $1.5 \pm 0.05\%$ (Ob-Ob controls) versus $0.8 \pm 0.06\%$ (GF-GF controls); $P < 10^{-4}$, two-tailed unpaired Student's t test between GF^{ch}-Ob and GF-GF controls; $n = 6$ GF-GF, 8 Ob-Ob, and 10 GF^{ch}-Ob-Ob^{ch}-GF)].

In separate experiments, we cohoused two GF animals together with one Ln and one Ob animal, 5 days after colonization of Ln and Ob mice (repeated in three separate cages, each cage in a separate isolator). As with previous experiments, bedding was changed before initiation of cohousing. The GF “bystanders” did not develop increased adiposity phenotypes and manifested cecal metabolic profiles and fecal biomass characteristics of their Ln^{ch} cage mates and Ln controls (Fig. 2, B to E, and fig. S7F). In the initial phase of cohousing (days 1 to 2), the microbiota of GF^{ch} mice in each cage resembled that of noncohoused Ob-Ob controls (fig. S9D). By the next day, the

microbiota of each ex-GF^{ch} animal had undergone a dramatic change in composition, with $94.8 \pm 0.4\%$ of taxa now derived from their Ln^{ch} cage mate (defined by SourceTracker; see table S8A for log odds ratio scores). The most prominent invaders were the same prominent invaders from the Ln^{ch} microbiota described above (i.e., all of the Bacteroidales) (Fig. 2E). We concluded that these Ln-derived taxa had greater fitness in the guts of C57BL/6J mice consuming this diet, and had a “dominant-negative” effect on host adiposity.

Changes in the Cecal Metatranscriptome and Metabolome of Ob^{ch} Animals

Cecal samples collected at the time mice were killed from Ln^{ch}, Ob^{ch}, and control Ob and Ln animals were subjected to microbial RNA-Seq. Reads were assigned to ECs as above, and Euclidean distances were calculated from the EC matrix. The results revealed that the metatranscriptomes of Ob^{ch} animals were significantly more similar to those of their Ln^{ch} cage mates and Ln controls than to Ob controls, consistent with a functional transformation of the Ob^{ch} microbiota to a leanlike state as a consequence of invasion of the Ln taxa ($P \leq 0.0001$ as measured by a one-way ANOVA, with Holm-Šidák's correction for multiple hypotheses) (fig. S13). The majority (55.9%) of ECs that were enriched in the cecal metatranscriptomes of Ob^{ch} mice, compared with dually housed Ob-Ob controls, were also significantly

enriched in dually housed Ln-Ln versus Ob-Ob controls, including ECs that participate in carbohydrate metabolism and protein degradation. The latter encompassed five enzymes involved in the KEGG pathway for degradation of the BCAA valine, leucine, and isoleucine (transcripts encoding EC 1.2.4.4; EC 2.6.1.42; EC 5.1.99.1, and EC 6.4.1.3, which map to the genomes of invading members of the *Bacteroides*, and EC 4.2.1.17, which maps to members of Clostridiaceae) (table S9). The increased expression of genes involved in BCAA degradation is consistent with the reduced cecal levels of BCAA observed in Ln-Ln, Ln^{ch} and Ob^{ch} animals versus Ob-Ob controls (fig. S8). These results are consistent with the notion that invasion by *Bacteroides* increases the efficiency of BCAA degradation in the gut, reducing production of BCAA and related metabolites by the microbiome and contributing to decreased circulating levels of BCAA in the host. As with transplanted, intact, and uncultured microbiota from the discordant twin pairs, targeted MS/MS analysis confirmed that Ob-Ob controls had a global increase in serum levels of BCAAs, as well as higher levels of Met, Ser, Gly, Phe, Tyr, and Ala compared with Ln-Ln controls ($P \leq 0.05$, matched one-way ANOVA) (table S10). However, after 10 days of cohousing, Ob^{ch} animals did not exhibit a statistically significant reduction in serum BCAA levels compared with Ob-Ob controls, although levels in Ln^{ch} cage mates were signifi-

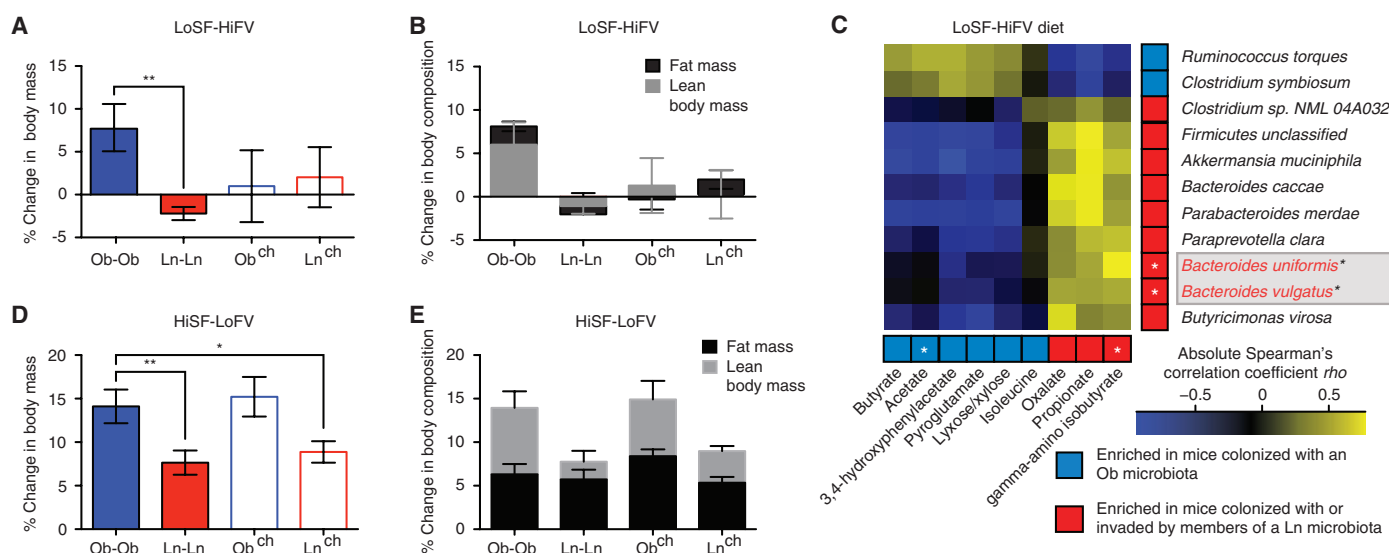


Fig. 4. Effects of NHANES-based LoSF-HiFV and HiSF-LoFV diets on bacterial invasion, body mass and metabolic phenotypes. (A and B) Mean \pm SEM percent changes in total body mass (A) and body composition [fat and lean body mass, normalized to initial body mass on day 4 after gavage (B)] occurring between 4 and 14 days after colonization with culture collections from the Ln or Ob co-twin in DZ pair 1. Cohousing Ln and Ob mice prevents an increased body mass phenotype in Ob^{ch} cage mates fed the representative LoSF-HiFV human diet ($n = 3$ to 5 cages per treatment group; 26 animals in total). $**P \leq 0.01$, based on a one-way ANOVA after Fisher's least significant difference test (also see table S14 for statistics). (C) Spearman's correlation analysis between bacterial species-level taxa and metabolites in cecal samples collected from mice colonized with culture collections from DZ twin pair 1 Ln and Ob co-twins and fed a LoSF-HiFV diet. Red and blue squares indicate metabolites or

taxa that are significantly enriched in samples collected from dually housed Ln-Ln or Ob-Ob controls respectively. An asterisk in the colored box indicates that a taxon or metabolite is significantly enriched in mice colonized with Ln (red) or Ob (blue) culture collections. (D and E) Mean \pm SEM of changes in body mass and body composition in mice colonized with intact uncultured microbiota from DZ twin pair 2 and fed the representative HiSF-LoFV human diet. Ob-Ob controls have greater total and lean body mass than Ln-Ln controls, but this phenotype is not rescued in Ob^{ch} animals (see table S14 for statistics). $*P < 0.05$, $**P \leq 0.01$ based on a one-way ANOVA. Note that the HiSF-LoFV diet produces a significantly greater increase in body mass, specifically fat mass, in mice harboring the lean co-twins microbiota (Ln-Ln and Ln^{ch}) than when they are fed the LoSF-HiFV diet [see (A) versus (D), and (B) versus (E); two-way ANOVA with Holm-Šidák's correction for multiple hypotheses].

cantly lower than in Ob-Ob controls and not different from Ln controls (table S10). More complete understanding of the contributions of the gut microbial community to Ob-associated metabolic phenotypes will require detailed, long-term, time-series studies of microbial and host transcriptomes and metabolomes.

Significant correlations between cecal metabolite levels and bacterial species represented in the microbiota of Ob-Ob, Ln-Ln, Ln^{ch}, Ob^{ch} and GF^{ch} mice consuming the LF-HPP diet are summarized in Fig. 3A (defined by asymptotic *P* values for all Spearman's correlations, corrected for multiple hypotheses using the Benjamini-Hochberg procedure). For example, BCAA and the products of amino acid metabolism were positively correlated with *Clostridium hathewayi* (Fig. 3A). This member of the Firmicutes represented an average of 2.54% of the Ob fecal microbiota before cohousing; its relative abundance was significantly reduced in Ob^{ch} animals, and it was not able to successfully invade the microbiota of Ln^{ch} cage mates (Figs. 2E and 3A and table S8A).

Three members of the Bacteroidetes, *B. uniformis*, *Parabacteroides merdae*, and *A. putredinis*, which were prominent invaders of the Ob^{ch} gut, positively correlated with cecal acetate, propionate, and butyrate levels. Whereas members of these species generate acetate

and propionate, their ability to produce butyrate has not been reported. Their positive association with butyrate levels could be due to interspecies acetate cross-feeding with butyrate-producing taxa (36, 37). The negative correlation between adiposity and cecal butyrate and propionate concentrations in Ln^{ch}, Ob^{ch}, and GF^{ch} microbiota ($r = -0.49$ and -0.45 , respectively, $P \leq 0.05$) is consistent with previous studies claiming a role for these short-chain fatty acids in influencing host energy balance (38, 39).

The gut microbiota affects the composition and relative abundance of bile acids species through a variety of metabolic transformations (40, 41). Ultra-performance liquid chromatography-mass spectrometry (UPLC-MS) analysis of 37 bile acid species in cecal samples obtained from Ln-Ln, Ob-Ob, Ob^{ch}, and Ln^{ch} mice revealed significantly lower levels of eight bile acids in Ob-Ob compared with Ln-Ln controls (Fig. 3B). Cohousing rescued these differences, with Ob^{ch} mice having bile acid profiles that were more similar to Ln-Ln than to Ob-Ob controls and not significantly different from Ln^{ch} cage mates ($n = 5$ to 6 mice per group; see table S11 for all bile acids measured that exhibit significant differences between Ob-Ob and Ln-Ln controls).

Bile acids can have direct metabolic effects on the host via the nuclear farnesoid X receptor (FXR)

(42). Intestinal FXR mediates intestinal fibroblast growth factor 15 (Fgf15) production. Fgf15, secreted by the gut epithelium and delivered to hepatocytes via the portal circulation, acts through fibroblast growth factor receptor 4 (*Fgfr4*) to inhibit expression of the rate-limiting enzyme in bile acid biosynthesis, cholesterol 7- α -hydroxylase (*Cyp7a1*) (Fig. 3, C to F) (43). Engineered FXR deficiency in leptin-deficient mice protects against obesity and improves insulin sensitivity (42). Overexpression of *Cyp7a1* in the livers of transgenic mice also prevents diet-induced obesity and insulin resistance (44). Sequestering bile acids with the drug colestevam lowers blood sugar in humans with type 2 diabetes (45). Quantitative reverse transcription polymerase chain reaction (qRT-PCR) analysis disclosed that, compared with Ln-Ln animals, Ob-Ob mice have increased FXR and Fgf15 mRNA levels in their distal small intestine (ileum) and decreased hepatic *Cyp7a1* expression. Ob^{ch} mice have expression profiles that are not significantly different from Ln-Ln controls (or Ln^{ch}) (Fig. 3, C to E). Differences in bile acid metabolism, in addition to the documented differences in carbohydrate fermentation by Ob compared with Ln microbial communities highlight some of the mechanisms that could contribute to the observed microbiota-mediated effects on body composition.

LoSF-HiFV

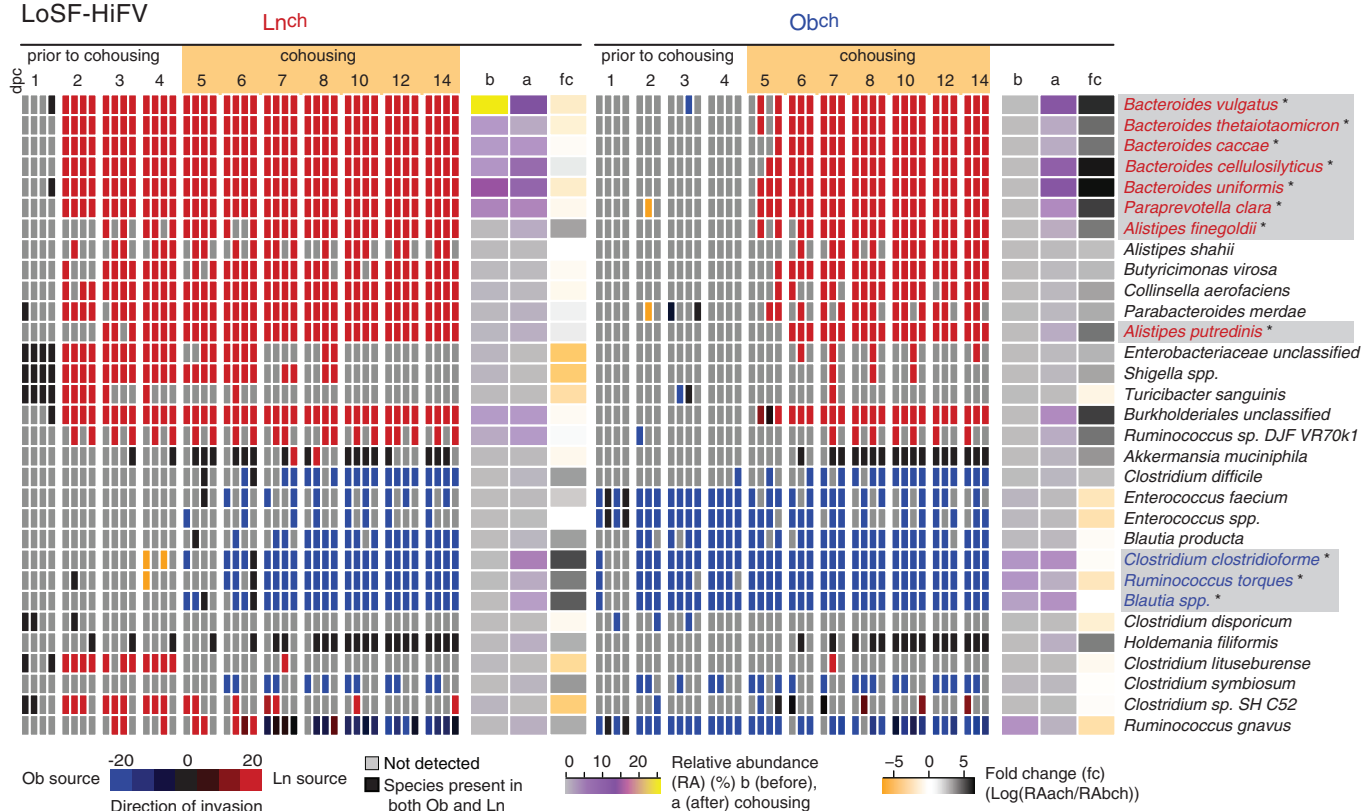


Fig. 5. Invasion analysis of species-level taxa in Ob^{ch} or Ln^{ch} mice fed the NHANES-based LoSF-HiFV diet. Red indicates species derived from the Ln^{ch} gut microbial community. Blue denotes species derived from the Ob^{ch} microbiota. The mean relative abundance of each species-level taxon before

(b: 3 and 4 dpc) and after (a: 8, 10 and 14 dpc) cohousing is noted. Average fold-change (fc) in relative abundance of taxa before and after colonization was defined as in the legend to Fig. 2E. An asterisk (*) denotes bacterial species that satisfy our criteria for classification as successful invaders (see text).

Taxa-Specific Effects on Body Composition and Metabotype

We subsequently colonized GF mice with a consortium of 39 sequenced taxa (97%ID OTUs) from the lean co-twin's culture collection; 22 OTUs from *Bacteroides*, including *B. cellulosilyticus*, *B. vulgatus*, *B. thetaiotaomicron*, *B. caccae*, *B. ovatus*; 11 OTUs from *Ruminococcaceae* (one of the four family-level taxa that discriminate lean from obese), and six strains of *Collinsella aerofaciens* (richly endowed with genes involved in the acquisition and fermentation of diverse dietary carbohydrates) (see table S12 for features of the 39 sequenced genomes). Five days after colonization with the 39 taxa, these Ln39 mice were cohoused with Ob mice. Control groups consisted of dually housed Ln-Ln and dually housed Ob-Ob animals (fig. S14A) ($n = 5$ cages of cohoused animals per group; two independent experiments). Mice harboring the 39-member consortium (Ln39^{ch}), when cohoused with Ob (Ob^{ch}Ln39^{ch}) animals, remained lean (fig. S14, A and B). However, Ln39^{ch} animals were not able to confer protection against an increase in adiposity of their Ob^{ch} cage mates, nor did they exhibit a significant increase in their cecal butyrate levels (figs. S14, B and C and S7, D and E). Even though some species like *B. cellulosilyticus* and *B. vulgatus* from the Ln39^{ch} microbiota exhibited significant invasion into the microbiota of Ob^{ch}Ln39^{ch} cage mates, there was an overall decrease in invasion efficiency for members of the Ln39 consortia compared with those in the complete Ln culture collection [the mean of the distribution of invasion scores for the Ob^{ch}Ln39^{ch} microbiota was not significantly different from Ob-Ob controls ($P > 0.05$, Welch's two-sample t test)] (fig. S10B, table S8B). These findings illustrate how invasiveness and adiposity are dependent on community context.

Diet-Specific Effects

To define the effects of diet on Ln and Ob microbiota-mediated transmission of body composition and metabolic phenotypes, we constructed a diet made with foods that characterize diets representing the lower tertile of consumption of saturated fats and the upper tertile of consumption of fruits and vegetables reported in 1-day recalls by participants in the U.S. National Health and Nutrition Examination Survey (NHANES) during the period 2003–2008 [table S13 (23)]. Mice fed this low-saturated fat, high fruits and vegetables (LoSF-HiFV, ~33% kcal of fat per 100 g) NHANES-based diet were colonized with either the Ln or Ob human culture collections and subsequently cohoused. Dually housed Ln-Ln and Ob-Ob animals served as reference controls ($n = 3$ to 5 cages per housing configuration; two independent experiments). Ob-Ob cage mates consuming the LoSF-HiFV diet had significantly increased body mass compared with Ln-Ln cage mates, which reflected a significant increase in both adipose and lean body mass (one-way unpaired Student's t test; $P \leq 0.001$) (Fig. 4, A and B, and table S14).

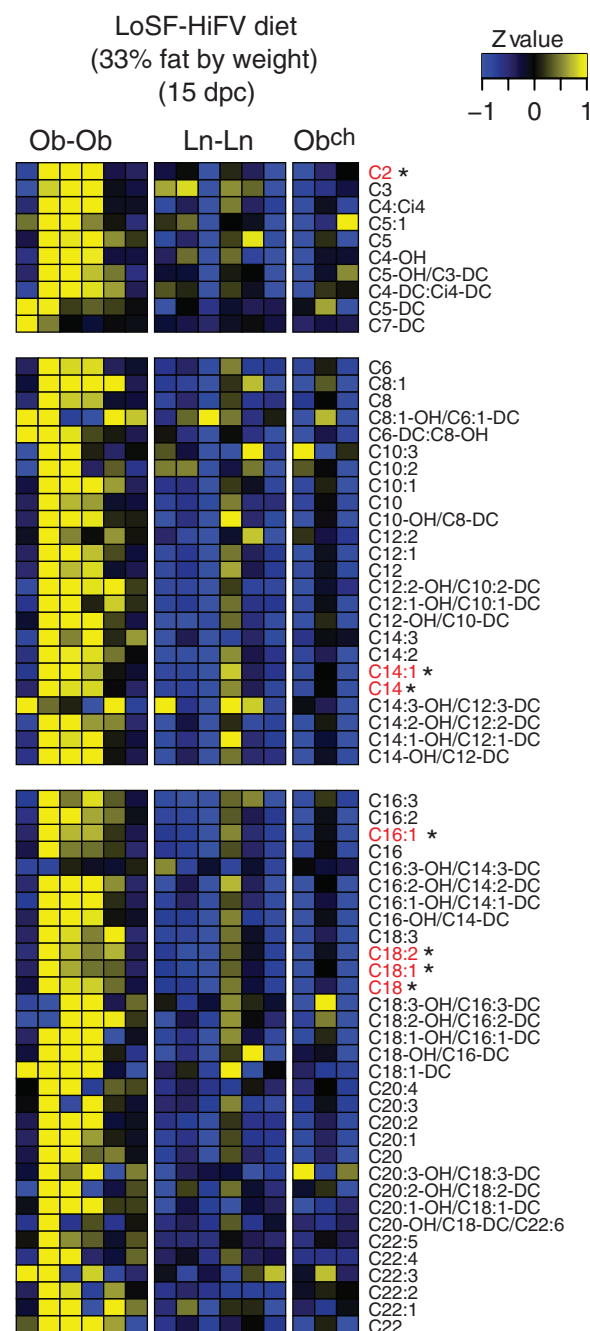
Cohousing prevented development of an Ob body composition phenotype in Ob^{ch} animals (Fig. 4, A and B).

We used 16S rRNA analysis of fecal samples collected on days 1 to 8, 10, 12, and 14 after gavage of the culture collections, and it revealed that this rescue was accompanied by invasion of taxa from Ln^{ch} to Ob^{ch} cage mates ($P \leq 10^{-6}$; Welch's two sample t test comparing the mean of the distributions of invasion scores between Ob-Ob controls and Ob^{ch} animals) with the most invasive species being members of *Bacteroides* (i.e., *B. uniformis*, *B. vulgatus*, and *B. cellulosilyticus*) (Fig. 5; fig. S15, A to C; and fig. S10C). These species were also successful invaders in mice fed the LF-HPP

diet (Fig. 2E). As was the case with the LF-HPP mouse chow, fecal samples collected from Ln-Ln controls and from Ln^{ch} and Ob^{ch} animals fed the human (NHANES-based) LoSF-HiFV diet had significantly greater microbial biomass compared with Ob-Ob controls (two-way ANOVA, $P \leq 0.001$ after Holm-Sidak's correction for multiple hypothesis). Moreover, fecal microbial biomass in Ob^{ch} and Ln^{ch} animals was not significantly different (not shown).

Significant correlations between cecal metabolites and cecal bacterial taxa in mice fed a LoSF-HiFV diet are summarized in Fig. 4C. As in mice fed a LF-HPP diet, the invasive species *B. uniformis* and *B. vulgatus* were significantly and positively

Fig. 6. Acylcarnitine profile in the skeletal muscle of mice colonized with the Ob or Ln culture collections from DZ twin pair 1 and fed the LoSF-HiFV diet. Each column represents a different animal and each row a different acylcarnitine. The identities and levels of these acylcarnitines were determined by targeted MS/MS (see table S15 for mean values \pm SEM for each treatment group). A two-way ANOVA with Holm-Sidak's correction was used to calculate whether the level of each acylcarnitine was significantly different between Ob-Ob and Ln-Ln, Ln^{ch}, or Ob^{ch} animals. * $P \leq 0.05$.



correlated with increased cecal propionate levels in Ln-Ln, Ob^{ch}, and Ln^{ch} animals compared with Ob-Ob controls.

Obesity-related insulin resistance has been associated with broad-scale accumulation of acylcarnitines in skeletal muscle (46, 47). Maneuvers that resolve the acylcarnitine accumulation in muscle, including knockout of the malonylCoA decarboxylase gene (*Mlycd*) or overexpression of carnitine acyltransferase (*Crat*), also resolve the insulin-resistance phenotype in mice (47, 48). Therefore, we used targeted MS/MS to measure 60 acylcarnitine species (C2 to C22) in liver, skeletal muscle, and serum (table S15, A to C). With the LF-HPP mouse chow (4% fat by weight), Ob-Ob animals had significantly higher levels of hepatic short-chain acylcarnitines (C2, C4:C4i, and C4-OH) compared with Ln-Ln mice (fig. S16; two-way ANOVA after Holm-Šidák's correction). The differences in short-chain acylcarnitines were rescued in Ob^{ch} animals, which resembled Ln-Ln controls ($n = 5$ animals per treatment group).

Ob-Ob controls fed the LoSF-HiFV diet (33% fat by weight) also had clear increases in accumulation of a group of even-, long-chain acylcarnitines (C14, C14:1, C16, C16:1, C18, C18:1, and C18:2) in their liver and skeletal muscle compared with Ln-Ln controls [multivariate ANOVA (MANOVA), $P \leq 0.001$; $n = 3$ to 6 animals per treatment group]. Cohousing Ln and Ob animals rescued this metabolic phenotype in the skeletal muscle and liver (and cecum) of Ob^{ch} mice (i.e., there was no statistically significant difference compared with Ln-Ln controls) (Fig. 6, fig. S16, and table S15). There were no significant differences in accumulation of these acylcarnitines in the plasma of Ob-Ob, Ln-Ln, and cohoused animals (table S15, B and C). Together, these results suggest that the gut microbiome influences systemic lipid metabolism.

Because these findings raised the possibility that the Ob microbiome is capable of conferring muscle insulin resistance at least in the context of a human (LoSF-HiFV) diet, we subjected Ob-Ob and Ln-Ln animals to a glucose tolerance test 15 days after colonization with their human donor's gut culture collections. An increase in serum glucose concentration was observed 15 min after intraperitoneal injection of glucose in Ob-Ob animals (means \pm SEM: 338.5 ± 11.07 mg/dl in Ob-Ob animals versus 304.6 ± 17.78 mg/dl in Ln-Ln animals; $P = 0.06$, unpaired Student's *t* test; $n = 10$ to 11 animals per group). No significant differences in serum insulin concentrations between these groups were documented at 30 min after glucose was administered, nor did we observe significant differences in insulin signaling in liver and skeletal muscle, defined by levels of immunoreactive Akt phosphorylated at Thr³⁰⁸ and the Akt substrate AS160 phosphorylated at Thr⁶⁴² measured 3 min after an insulin bolus (23). We concluded that the elevation in skeletal muscle long-chain acylcarnitines observed in mice colonized for just 15 days with an Ob culture collection and consuming the LoSF-HiFV diet is associated with mild glucose intolerance and may be an early

manifestation of the pathobiologic effects of obese microbiota on host physiology and metabolism. More complete time-course studies will be required to test if this lesion in glucose homeostasis will evolve into full-fledged insulin resistance with longer exposure to Ob microbiota.

To determine whether the effects exerted by diet on the invasive potential of members from the Ln microbiota were specific to the culture collections prepared from members of discordant twin pair 1 or robust to other Ln co-twin microbiota, we fed the LoSF-HiFV diet to mice colonized with intact uncultured fecal microbiota from members of discordant twin pair 2. Cohousing experiments performed using the same experimental design described above revealed invasion of the communities of Ob^{ch} animals by bacterial species from their Ln^{ch} cage mates, most notably members of the Bacteroidetes (figs. S10D and S17A, see table S8D for invasion scores).

In follow-up experiments, separate groups of germ-free mice colonized with intact uncultured microbiota from discordant twin-pair 2 were fed a second NHANES-based diet made with foods that characterize U.S. diets representing the upper, rather than lower, tertile of consumption of saturated fats and the lower, rather than upper, tertile of consumption of fruits and vegetables (abbreviated HiSF-LoFV; 44% fat by weight). Significant differences in body composition were documented between Ob-Ob and Ln-Ln mice fed this diet. However, cohousing of Ln and Ob mice failed to attenuate or block development of an increased body mass phenotype in Ob^{ch} cage mates ($n = 5$ to 11 animals per housing configuration) (Fig. 4, D and E). Remarkably, there was a lack of significant invasion of members of the Ln^{ch} microbiota into the guts of Ob^{ch} cage mates (figs. S10E and S17B and table S8E). If biased fecal pellet consumption was the underlying mechanism leading to invasion of members of the Ln microbiota into the guts of Ob^{ch} mice in the cohousing experiments, it would have to be diet- and microbiota-dependent. Together, these results emphasize the strong microbiota-by-diet interactions that underlie invasion and illustrate how a diet high in saturated fats and low in fruits and vegetables can select against human gut bacterial taxa associated with leanness.

Prospectus

The findings described above provide a starting point for future studies that systematically test the effects of specified diet ingredients on microbiota-associated body composition and metabolic phenotypes (e.g., components that when added or subtracted restore invasiveness of specific members of the microbiota in the context of the HiSF-LoFV diet). A benefit of using the approach described in this report is that the target human population embodying a phenotype of interest is integrated into the animal model through selection of gut microbiota representative of that population and diets representative of their patterns of food consumption. Our finding that cul-

ture collections generated from human microbiota samples can transmit donor phenotypes of interest (body composition and metabolites) has a number of implications. If these derived culture collections can transmit a phenotype, the stage is set for studies designed to determine which culturable components of a given person's gut community are responsible. These tests can take the form of experiments where mice containing culture collections from donors with different phenotypes are cohoused and used to determine whether invasion by components of one community into another transforms the cage mate's phenotype and, correspondingly, the properties of the human microbial communities they harbor. Sequenced culture collections generated from human gut microbiota donors also provide an opportunity to model and further address basic issues such as the determinants of invasiveness including the mechanisms by which invasion is impacted by diet composition, as well as the mechanisms by which invading components affect microbial and host metabolism. This issue is important for identifying next-generation probiotics, prebiotics, or a combination of the two (synbiotics). Moreover, the ability to generate a culture collection, from an individual—whose composition is resolved to the gene level, whose properties can be validated in preclinical models, and whose “manufacture” is reproducible—may provide a safer and more sustainable alternative to fecal transplants for microbiome-directed therapeutics (18, 49).

References and Notes

1. P. B. Eckburg *et al.*, Diversity of the human intestinal microbial flora. *Science* **308**, 1635–1638 (2005). doi: [10.1126/science.1110591](https://doi.org/10.1126/science.1110591); pmid: [15831718](https://pubmed.ncbi.nlm.nih.gov/15831718/)
2. P. J. Turnbaugh *et al.*, A core gut microbiome in obese and lean twins. *Nature* **457**, 480–484 (2009). doi: [10.1038/nature07540](https://doi.org/10.1038/nature07540); pmid: [19043404](https://pubmed.ncbi.nlm.nih.gov/19043404/)
3. E. K. Costello *et al.*, Bacterial community variation in human body habitats across space and time. *Science* **326**, 1694–1697 (2009). doi: [10.1126/science.1177486](https://doi.org/10.1126/science.1177486); pmid: [19892944](https://pubmed.ncbi.nlm.nih.gov/19892944/)
4. J. Qin *et al.*, A human gut microbial gene catalogue established by metagenomic sequencing. *Nature* **464**, 59–65 (2010). doi: [10.1038/nature08821](https://doi.org/10.1038/nature08821); pmid: [20203603](https://pubmed.ncbi.nlm.nih.gov/20203603/)
5. J. Ravel *et al.*, Vaginal microbiome of reproductive-age women. *Proc. Natl. Acad. Sci. U.S.A.* **108** (Suppl. 1), 4680–4687 (2011). doi: [10.1073/pnas.1002611107](https://doi.org/10.1073/pnas.1002611107); pmid: [20534435](https://pubmed.ncbi.nlm.nih.gov/20534435/)
6. P. Gajer *et al.*, Temporal dynamics of the human vaginal microbiota. *Sci. Transl. Med.* **4**, 132ra52 (2012). doi: [10.1126/scitranslmed.3003605](https://doi.org/10.1126/scitranslmed.3003605)
7. T. Yatsunenko *et al.*, Human gut microbiome viewed across age and geography. *Nature* **486**, 222–227 (2012). pmid: [22699611](https://pubmed.ncbi.nlm.nih.gov/22699611/)
8. C. Huttenhower *et al.*, Structure, function and diversity of the healthy human microbiome. *Nature* **486**, 207–214 (2012). doi: [10.1038/nature11234](https://doi.org/10.1038/nature11234); pmid: [22699609](https://pubmed.ncbi.nlm.nih.gov/22699609/)
9. K. Faust *et al.*, Microbial co-occurrence relationships in the human microbiome. *PLoS Comput. Biol.* **8**, e1002606 (2012). doi: [10.1371/journal.pcbi.1002606](https://doi.org/10.1371/journal.pcbi.1002606); pmid: [22807668](https://pubmed.ncbi.nlm.nih.gov/22807668/)
10. M. G. Dominguez-Bello *et al.*, Delivery mode shapes the acquisition and structure of the initial microbiota across multiple body habitats in newborns. *Proc. Natl. Acad. Sci. U.S.A.* **107**, 11971–11975 (2010). doi: [10.1073/pnas.1002601107](https://doi.org/10.1073/pnas.1002601107); pmid: [20566857](https://pubmed.ncbi.nlm.nih.gov/20566857/)

11. J. J. Faith *et al.*, Succession of microbial consortia in the developing infant gut microbiome. *Science* **341**, 1237439 (2013).
12. S. Greenblum, P. J. Turnbaugh, E. Borenstein, Metagenomic systems biology of the human gut microbiome reveals topological shifts associated with obesity and inflammatory bowel disease. *Proc. Natl. Acad. Sci. U.S.A.* **109**, 594–599 (2012). doi: [10.1073/pnas.1116053109](#); pmid: [22184244](#)
13. M. L. Zupancic *et al.*, Analysis of the gut microbiota in the old order Amish and its relation to the metabolic syndrome. *PLoS ONE* **7**, e43052 (2012). doi: [10.1371/journal.pone.0043052](#); pmid: [22905200](#)
14. S. H. Duncan *et al.*, Human colonic microbiota associated with diet, obesity and weight loss. *Int. J. Obes. (London)* **32**, 1720–1724 (2008). doi: [10.1038/ijo.2008.155](#); pmid: [18779823](#)
15. A. Schwierdt *et al.*, Microbiota and SCFA in lean and overweight healthy subjects. *Obesity (Silver Spring)* **18**, 190–195 (2010). doi: [10.1038/oby.2009.167](#); pmid: [19498350](#)
16. A. Santacruz *et al.*, Gut microbiota composition is associated with body weight, weight gain and biochemical parameters in pregnant women. *Br. J. Nutr.* **104**, 83–92 (2010). doi: [10.1017/S0007114510000176](#); pmid: [20205964](#)
17. R. Jumpertz *et al.*, Energy-balance studies reveal associations between gut microbes, caloric load, and nutrient absorption in humans. *Am. J. Clin. Nutr.* **94**, 58–65 (2011). doi: [10.3945/ajcn.110.010132](#); pmid: [21543530](#)
18. A. Vrieze *et al.*, Transfer of intestinal microbiota from lean donors increases insulin sensitivity in individuals with metabolic syndrome. *Gastroenterology* **143**, 913, e7 (2012). doi: [10.1053/j.gastro.2012.06.031](#); pmid: [22728514](#)
19. P. Hakala, A. Rissanen, M. Koskenvuo, J. Kaprio, T. Rönneaa, Environmental factors in the development of obesity in identical twins. *Int. J. Obes. Relat. Metab. Disord.* **23**, 746–753 (1999). doi: [10.1038/sj.ijo.0800923](#); pmid: [10454109](#)
20. A. Rissanen *et al.*, Acquired preference especially for dietary fat and obesity: A study of weight-discordant monozygotic twin pairs. *Int. J. Obes. Relat. Metab. Disord.* **26**, 973–977 (2002). pmid: [12080452](#)
21. A. E. Duncan *et al.*, Genetic and environmental contributions to BMI in adolescent and young adult women. *Obesity (Silver Spring)* **17**, 1040–1043 (2009). doi: [10.1038/oby.2008.643](#); pmid: [19165159](#)
22. M. Waldron, K. K. Bucholz, M. T. Lynskey, P. A. Madden, A. C. Heath, Alcoholism and timing of separation in parents: Findings in a midwestern birth cohort. *J. Stud. Alcohol Drugs* **74**, 337–348 (2013). pmid: [23384382](#)
23. Materials and methods are available as supplementary material on Science Online.
24. E. Kristiansson, P. Hugenholtz, D. Dalevi, ShotgunFunctionalizeR: An R-package for functional comparison of metagenomes. *Bioinformatics* **25**, 2737–2738 (2009). doi: [10.1093/bioinformatics/btp508](#); pmid: [19696045](#)
25. C. B. Newgard *et al.*, A branched-chain amino acid-related metabolic signature that differentiates obese and lean humans and contributes to insulin resistance. *Cell Metab.* **9**, 311–326 (2009). doi: [10.1016/j.cmet.2009.02.002](#); pmid: [19356713](#)
26. B. D. Muegge *et al.*, Diet drives convergence in gut microbiome functions across mammalian phylogeny and within humans. *Science* **332**, 970–974 (2011). doi: [10.1126/science.1198719](#); pmid: [21596990](#)
27. M. J. Keenan *et al.*, Effects of resistant starch, a non-digestible fermentable fiber, on reducing body fat. *Obesity (Silver Spring)* **14**, 1523–1534 (2006). doi: [10.1038/oby.2006.176](#); pmid: [17030963](#)
28. J. Zhou *et al.*, Dietary resistant starch upregulates total GLP-1 and PYY in a sustained day-long manner through fermentation in rodents. *Am. J. Physiol. Endocrinol. Metab.* **295**, E1160–E1166 (2008). doi: [10.1152/ajpendo.90637.2008](#); pmid: [18796545](#)
29. J. Zhou *et al.*, Failure to ferment dietary resistant starch in specific mouse models of obesity results in no body fat loss. *J. Agric. Food Chem.* **57**, 8844–8851 (2009). doi: [10.1021/jf901548e](#); pmid: [19739641](#)
30. D. Knights *et al.*, Bayesian community-wide culture-independent microbial source tracking. *Nat. Methods* **8**, 761–763 (2011). doi: [10.1038/nmeth.1650](#); pmid: [21765408](#)
31. J. P. Lessard, J. A. Fordyce, N. J. Gotelli, N. J. Sanders, Invasive ants alter the phylogenetic structure of ant communities. *Ecology* **90**, 2664–2669 (2009). doi: [10.1890/09-0503.1](#); pmid: [19886475](#)
32. M. T. Johnson, J. R. Stinchcombe, An emerging synthesis between community ecology and evolutionary biology. *Trends Ecol. Evol.* **22**, 250–257 (2007). doi: [10.1016/j.tree.2007.01.014](#); pmid: [17296244](#)
33. C. O. Webb, N. C. Pitman, Phylogenetic balance and ecological evenness. *Syst. Biol.* **51**, 898–907 (2002). doi: [10.1080/10635150290102609](#); pmid: [12554456](#)
34. P. J. Turnbaugh *et al.*, An obesity-associated gut microbiome with increased capacity for energy harvest. *Nature* **444**, 1027–1031 (2006). doi: [10.1038/nature05414](#); pmid: [17183312](#)
35. P. Gauffin Cano, A. Santacruz, A. Moya, Y. Sanz, Bacteroides uniformis CECT 7771 ameliorates metabolic and immunological dysfunction in mice with high-fat-diet induced obesity. *PLoS ONE* **7**, e41079 (2012). doi: [10.1371/journal.pone.0041079](#); pmid: [22844426](#)
36. S. H. Duncan *et al.*, Contribution of acetate to butyrate formation by human faecal bacteria. *Br. J. Nutr.* **91**, 915–923 (2004). doi: [10.1079/BJN20041150](#); pmid: [15182395](#)
37. M. A. Mahowald *et al.*, Characterizing a model human gut microbiota composed of members of its two dominant bacterial phyla. *Proc. Natl. Acad. Sci. U.S.A.* **106**, 5859–5864 (2009). doi: [10.1073/pnas.0901529106](#); pmid: [19321416](#)
38. Z. Gao *et al.*, Butyrate improves insulin sensitivity and increases energy expenditure in mice. *Diabetes* **58**, 1509–1517 (2009). doi: [10.2337/db08-1637](#); pmid: [19366864](#)
39. H. V. Lin *et al.*, Butyrate and propionate protect against diet-induced obesity and regulate gut hormones via free fatty acid receptor 3-independent mechanisms. *PLoS ONE* **7**, e35240 (2012). doi: [10.1371/journal.pone.0035240](#); pmid: [22506074](#)
40. H. Kuribayashi, M. Miyata, H. Yamakawa, K. Yoshinari, Y. Yamazoe, Enterobacteria-mediated deconjugation of taurocholic acid enhances ileal farnesoid X receptor signaling. *Eur. J. Pharmacol.* **697**, 132–138 (2012). doi: [10.1016/j.ejphar.2012.09.048](#); pmid: [23051670](#)
41. J. R. Swann *et al.*, Systemic gut microbial modulation of bile acid metabolism in host tissue compartments. *Proc. Natl. Acad. Sci. U.S.A.* **108** (suppl. 1), 4523–4530 (2011). doi: [10.1073/pnas.1006734107](#); pmid: [20837534](#)
42. Y. Zhang *et al.*, Loss of FXR protects against diet-induced obesity and accelerates liver carcinogenesis in ob/ob mice. *Mol. Endocrinol.* **26**, 272–280 (2012). doi: [10.1210/me.2011-1157](#); pmid: [22261820](#)
43. T. Inagaki *et al.*, Fibroblast growth factor 15 functions as an enterohepatic signal to regulate bile acid homeostasis. *Cell Metab.* **2**, 217–225 (2005). doi: [10.1016/j.cmet.2005.09.001](#); pmid: [16213224](#)
44. T. Li *et al.*, Transgenic expression of cholesterol 7 α -hydroxylase in the liver prevents high-fat diet-induced obesity and insulin resistance in mice. *Hepatology* **52**, 678–690 (2010). doi: [10.1002/hep.23721](#); pmid: [20623580](#)
45. Y. Handelsman, Role of bile acid sequestrants in the treatment of type 2 diabetes. *Diabetes Care* **34** (suppl. 2), S244–S250 (2011). doi: [10.2337/dc11-s237](#); pmid: [21525463](#)
46. T. R. Koves *et al.*, Peroxisome proliferator-activated receptor-gamma co-activator 1 α -mediated metabolic remodeling of skeletal myocytes mimics exercise training and reverses lipid-induced mitochondrial inefficiency. *J. Biol. Chem.* **280**, 33588–33598 (2005). doi: [10.1074/jbc.M507621200](#); pmid: [16079133](#)
47. T. R. Koves *et al.*, Mitochondrial overload and incomplete fatty acid oxidation contribute to skeletal muscle insulin resistance. *Cell Metab.* **7**, 45–56 (2008). doi: [10.1016/j.cmet.2007.10.013](#); pmid: [18177724](#)
48. D. M. Muoio *et al.*, Muscle-specific deletion of carnitine acetyltransferase compromises glucose tolerance and metabolic flexibility. *Cell Metab.* **15**, 764–777 (2012). doi: [10.1016/j.cmet.2012.04.005](#); pmid: [22560225](#)
49. J. S. Bakken *et al.*, Treating Clostridium difficile infection with fecal microbiota transplantation. *Clin. Gastroenterol. Hepatol.* **9**, 1044–1049 (2011). doi: [10.1016/j.cgh.2011.08.014](#); pmid: [21871249](#)

Acknowledgments: We thank D. O'Donnell, M. Karlsson, S. Wagoner, J. Guruge, R. Chamberland, M. Meier, and S. Deng for superb technical assistance; P. Ahern for help with FACS analysis; D. Hopper and S. Marion for their contributions to the recruitment of discordant twins from the MOAFTS cohort and for obtaining fecal samples for the present study; I. Halatchev for help in performing diet experiments; plus A. Reyes and N. McNulty for many helpful suggestions. S. Baumann and S. Fischer (Agilent Technologies, Santa Clara, CA) provided technical support for some of the metabolomics analyses including a gift of the Fiehn metabolite library. This work was supported in part by grants from the NIH (DK078669, DK70977, P30-AG028716, and DK58398), the Crohn's and Colitis Foundation of America, plus Kraft Foods and Mondelez International. Bacterial 16S rRNA pyrosequencing reads have been deposited in the European Bioinformatics Institute under accession numbers ERP003513 and ERP003512, as have shotgun pyrosequencing data sets from cecal microbial community DNA (ERP003514), microbial community RNA-Seq data sets (ERP003551), and draft genome data sets from cultured bacterial isolates (PRJEB3728–PRJEB3780). RNA-seq data sets have also been deposited in Gene Expression Omnibus (GEO) under accession number GSE48861. Author contributions: V.K.R. and J.I.G. designed the mouse experiments; A.C.H., A.E.D., and J.I.G. designed and implemented the clinical data collection; N.W.G., J.I.G., D.K.H., B.J.L., and M.C.M. designed the NHANES-based mouse diets; V.K.R., J.J.F., J.C., M.J.M., J.R.B., K.F., and O.I. generated the data; V.K.R., J.J.F., F.R., J.C., J.C.C., W.V.T., L.K.U., W.A.W., A.L.K., R.K., A.E.D., A.C.H., B.H., V.L., M.J.M., J.R.B., C.B.N., and J.I.G. analyzed the data; and V.K.R. and J.I.G. wrote the paper.

Supplementary Materials

www.sciencemag.org/cgi/content/341/6150/1241214/suppl/DC1

Materials and Methods
Supplementary Text
Figs. S1 to S17
Tables S1 to S17
References (50–76)

30 May 2013; accepted 12 July 2013
10.1126/science.1241214

Decades-Long Changes of the Interstellar Wind Through Our Solar System

P. C. Frisch,^{1*} M. Bzowski,² G. Livadiotis,³ D. J. McComas,^{3,4} E. Moebius,⁵ H.-R. Mueller,⁶ W. R. Pryor,⁷ N. A. Schwadron,⁵ J. M. Sokół,² J. V. Vallerga,⁸ J. M. Ajello⁹

The journey of the Sun through the dynamically active local interstellar medium creates an evolving heliosphere environment. This motion drives a wind of interstellar material through the heliosphere that has been measured with Earth-orbiting and interplanetary spacecraft for 40 years. Recent results obtained by NASA's Interstellar Boundary Explorer mission during 2009–2010 suggest that neutral interstellar atoms flow into the solar system from a different direction than found previously. These prior measurements represent data collected from Ulysses and other spacecraft during 1992–2002 and a variety of older measurements acquired during 1972–1978. Consideration of all data types and their published results and uncertainties, over the three epochs of observations, indicates that the trend for the interstellar flow ecliptic longitude to increase linearly with time is statistically significant.

Neutral interstellar gas, originating in the Local Interstellar Cloud (LIC) now surrounding the heliosphere (*1*), creates a wind through the heliosphere that traces the LIC velocity and temperature. During the 40 years over which spacecraft have measured the direction of the neutral interstellar wind, the relative Sun-LIC velocity of $23.2 \pm 0.3 \text{ km s}^{-1}$ (*2*) has carried the Sun over 1% of the distance to the LIC edge (*1*) and has carried a column of interstellar dust and neutral gas past Earth that is 200 astronomical units (AU) long (*2–4*). Turbulence in interstellar plasma is found over 12 orders of magnitude in spatial scale (*5, 6*), so that comparisons between the wind measurements obtained from NASA's Interstellar Boundary Explorer (IBEX) and older data can be used to look for temporal variations in the neutral interstellar wind.

Most recently, the IBEX mission (*7*) has measured neutral atoms in the interstellar wind. The interstellar neutral helium (He^0) wind velocity and temperature are obtained from in situ IBEX data collected during 2009–2011 (*2–4*) and from the in situ data collected during the 1990s with the Ulysses spacecraft (*8*). The He wind velocity vector obtained from IBEX versus Ulysses data differs by $3.6^\circ \pm 0.7^\circ$ in direction and $3.1 \pm$

0.5 km s^{-1} in speed; the main directional difference occurs in the ecliptic longitude of the He^0 flow direction (table S1). The difference between the IBEX and Ulysses measurements motivates a search for past temporal variations in the interstellar wind direction.

He is the most useful diagnostic of the interstellar wind because it is abundant and is only minimally affected by processes in the outer heliosheath, including effects of the interstellar magnetic field. Interstellar He^0 atoms follow ballistic trajectories from the heliopause to the inner heliosphere. Neutral He is depleted by ionization on the upwind side; on the downwind side it is concentrated by gravity into a focusing cone that follows the Sun as it moves through the LIC (supplementary text S1)

We used three types of historical data on the ecliptic longitude of the interstellar wind direction (Fig. 1 and table S1) to evaluate possible temporal variations: (i) direct in situ sampling of neutral interstellar He atoms (*2, 8*); (ii) resonant scattering of solar 584 Å emission off of the spatial interstellar He^0 distribution along the observation line of sight (*9–14*); and (iii) sampling the spatial He^0 , Ne^0 , and O^0 distributions inside of 1 AU through their production of pickup ions (*15–17*). Direct neutral atom imaging provides the full kinematic interstellar flow distribution in the inner heliosphere, taking advantage of the Sun's gravitational deflection of the flow to deduce the flow vector at infinity. Resonant scattering and pickup ion observations sense the spatial distribution of the interstellar gas in the inner heliosphere, as shaped by the combination of gravitational deflection and ionization loss, largely symmetric about the inflow axis. The 584 Å observations provide the line-of-sight integral for atoms with radial velocities sufficiently small to be influenced by variations in the solar 584 Å

emission line (supplementary text S2). Through pickup of newly ionized He atoms by the interplanetary magnetic field (IMF) and convection with the solar wind, the latter method maps the radial distribution inside the observer location into a pickup ion energy spectrum, affected by temporal variations of the solar wind and IMF (*18*). Less useful measurements that are not used here include the resonant fluorescence of solar H^0 Ly α (912 Å) emission off of interstellar H^0 , which is strongly sensitive to the phase of the solar cycle and the deflection of H^0 in the outer heliosheath; and the interstellar wind direction obtained from interstellar dust grains that couple to the time-variable solar wind magnetic field by the Lorentz force and, for smaller grains, respond to radiation pressure (supplementary text S3).

In order to compare the recent flow longitude found from the IBEX measurements with other values, we used the allowed longitude range that is independent of the fits to velocity and temperature, 76° to 82° [fig. 1 in (*2*)]. The extremes of this longitude range imply temperatures that are inconsistent with both IBEX and Ulysses cloud temperatures. We further narrowed the temperature range by using the LIC temperature obtained from measurements of interstellar gas toward the nearby star Sirius (supplementary text S4), in combination with the temperature-longitude relation as deduced from IBEX observations (*2*), to impose limits of $\lambda = 80.0^\circ (+2.0^\circ, -1.0^\circ)$ on the IBEX flow longitude.

Ulysses obtained in situ flow measurements over three time intervals during the years 1990–2002, and outside the ecliptic plane and thus farther from the Sun than IBEX and with reduced gravitational deflection of the He^0 trajectories. We used the He^0 flow directions for each time interval (table S1) rather than the best He^0 flow direction derived from 12 years of combined data, $75.4^\circ \pm 0.5^\circ$ (*8*).

The first measurements of the interstellar He^0 wind direction occurred in the 1970s and detected resonantly scattered solar 584 Å emission fluorescence from interstellar He^0 using data from Space Test Program 72-1 (STP 72-1) (*9*), Mariner 10 (*10, 11*), SOLRAD 11B (*12*), and Prognost 6 (*13*) (table S1 and supplementary text S2). Looking at the 1970s subset of data and summing uncertainties quadratically, we find that the average ecliptic longitude of the interstellar wind, $73.4^\circ \pm 1.3^\circ$, differs by $\sim 0.9\sigma$ from the interstellar wind longitude obtained from 584 Å measurements by the Extreme Ultraviolet Explorer (EUVE, table S1).

An obvious question is whether differences in modeling of the He^0 trajectories could explain the low values for the 1970s longitudes. The only early analysis that used a complete thermal ("hot") model for the interaction of the interstellar gas with the heliosphere was applied to the SOLRAD 11B data (*12*). This analysis yielded a flow longitude of $73.6^\circ \pm 3^\circ$, which differs from the IBEX

¹Department of Astronomy and Astrophysics, University of Chicago, Chicago, IL 60637, USA. ²Space Research Centre of the Polish Academy of Sciences, Warsaw, Poland. ³Southwest Research Institute, San Antonio, TX 78249, USA. ⁴University of Texas in San Antonio, San Antonio, TX 78249, USA. ⁵Space Science Center, University of New Hampshire, Durham, NH 03824, USA. ⁶Dartmouth College, Hanover, NH 03755, USA. ⁷Central Arizona College, Coolidge, AZ 85128, USA. ⁸Space Sciences Laboratory, University of California at Berkeley, Berkeley, CA 94720, USA. ⁹Jet Propulsion Laboratory, Pasadena, CA 91109, USA.

*To whom correspondence should be addressed. E-mail: frisch@oddjob.uchicago.edu

value by 2σ if the Sirius temperature constraints (supplementary text S4) are applied.

The symmetry axis of the gravitational focusing cone was derived from data collected by the Advanced Composition Explorer (ACE) during five crossings during 1998–2002 (15) and two crossings during 2006–2009 (17). During 2007–2009, MESSENGER made four passages through the gravitational focusing cone inside of 0.6 AU (17).

Pronounced temporal variations are found for the focusing cone geometry in He, Ne, and O pickup ion data acquired by the Solar Terrestrial Relations Observatory [STEREO (16)] during four orbits in 2007–2010. These ions trace abundant interstellar species that are partially neutral in the LIC (1). STEREO detected a broad upwind “crescent” in the He, Ne, and O pickup ions, where the observed rates maximize in the upwind direction and fall off symmetrically toward the sidewind directions because of ionization. STEREO also measured He and Ne in the focusing cone. Because of variations in the focusing cone count rates, STEREO data were analyzed using two methods. Analogous to the ACE anal-

ysis (15), the data were summed over all orbits in the first method and the sum was fit with a Gaussian to find the symmetry axis. The second method corrected for solar wind and IMF variations, mostly due to corotating interacting regions, by taking these effects into account when folding pickup spectra through the instrument response and before averaging over all four orbits. Compared with the simpler method 1, the focusing cone axis was found to be at a larger longitude by $+2.4^\circ$, with part of the shift due to the response function of the instrument (method 2 directions are listed in table S1). This difference suggests that systematic uncertainties in the average focusing cone axis obtained from the 1997–2002 ACE data (table S1) may have been underestimated.

These data (table S1) on the interstellar He flow direction, which represent three measurement techniques, 19 independent measurements, and data collected with 11 spacecraft over three epochs starting in 1972, show an increase of the flow longitude with time. Although the trend is weak for each data group alone, it appears independently in the He^o 584 Å fluorescence data,

in situ measurements, and pickup ion measurements of the focusing cone symmetry. Comparing results from the three different types of observations collected during the 1990s yields similar He flow directions (18). ACE measurements at different times (15, 17) yield a statistically significant increase of the flow longitude of $2.6^\circ \pm 1.6^\circ$ over a 10-year period. The significance of this trend depends on the measurement uncertainties of individual data sets, which are taken from the original publications (table S1 and supplementary text S2).

Consideration of all data types over the three epochs of observations indicates a statistically significant trend for the interstellar flow ecliptic longitude to increase with time, provided that the uncertainties are realistic. For normally distributed uncertainties, the best-fitting linear model of the flow longitude is $\lambda(\text{deg}) = 70.6 (\pm 1.6) + 0.17 (\pm 0.06) \times t_{1970}$, where t_{1970} is the elapsed time in years since 1970. This hypothesis is statistically highly likely, with a reduced χ^2 of 0.97 and a P value of 0.49 (where a P value of > 0.05 is likely; see the explanation in supplementary text S5). The alternate hypothesis that the flow direction has remained constant over the past 40 years is rejected with a P value of 0.031 and a reduced χ^2 of 1.71. It is possible that some of the uncertainties on the pre-2000 data were underestimated; thus we repeated the statistical analysis by scaling the uncertainties for all 20th-century data by a factor s . When the pre-2000 uncertainties were scaled according to $s > 1.77$, the hypothesis of a constant (invariant) flow longitude is more likely. When the pre-2000 uncertainties were scaled according to $0.47 < s < 1.77$, the hypothesis of a linearly increasing longitude is more likely. Thus, for the choice between the hypotheses that the longitude of the interstellar wind has either stayed constant over the past 40 years or increased linearly over the past 40 years, the latter choice is statistically more likely. The statistical model with normally distributed uncertainties suggests a variation of the He flow direction over the past 40 years of $6.8^\circ \pm 2.4^\circ$. The data and the statistical tests show that a single constant value of the flow longitude is statistically highly unlikely, with a linear increase being far more probable. However, these tests are not adequate to determine whether this temporal variation is actually either linear or some more nonlinear function (supplementary text S5).

The direction of the interstellar magnetic field shaping the heliosphere has been determined from the Ribbon of energetic neutral atoms detected by IBEX (7). The Ribbon forms where sightlines are perpendicular to the interstellar magnetic field draping over the heliosphere, and the field direction is given by the center of the Ribbon arc located at $\lambda, \beta = 221^\circ, 39^\circ$. If the LIC gas and magnetic field direction are decoupled over spatial scales of 200 AU and less, so that the field direction has remained unchanged over the past 40 years, a $\sim 6.8^\circ$ shift of the He^o flow direction between the 1970s and 2011 has increased the

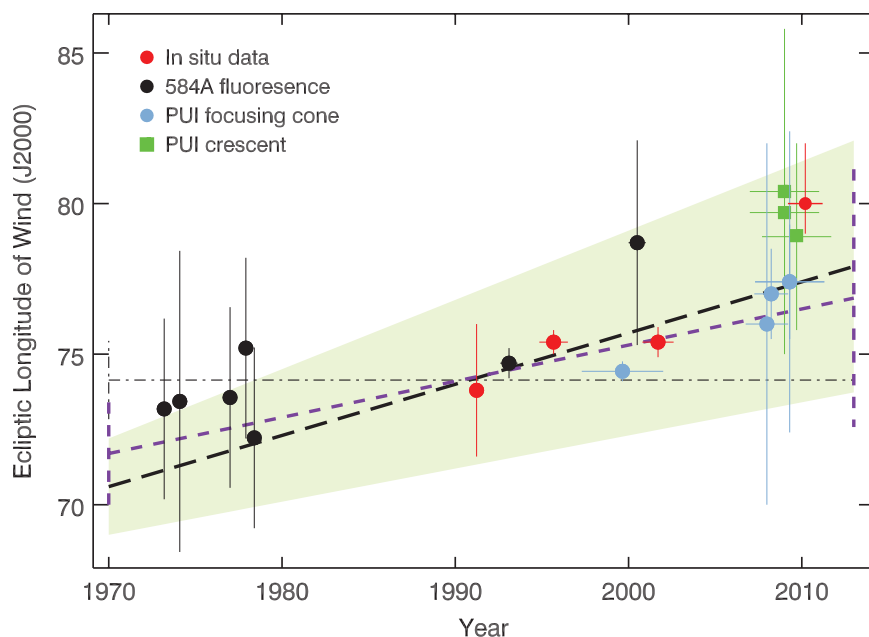


Fig. 1. Historical variations of the ecliptic longitude of the interstellar wind direction. PUI, pickup ions. Measurements of the interstellar wind longitude are plotted against the time span over which the data were acquired. The historical data (table S1) are based on observations of the He^o 584 Å backscattered emission (black), in situ He^o measurements (red), and pickup ion data showing the focusing cone (gray-blue) and upwind crescent (light green). All data are plotted with dots, except for the crescent data, which are plotted with squares. The black long-dashed line shows a statistically likely fit to a simple model in which the flow longitude increases linearly with time, calculated by considering the longitude uncertainties and window of time of the observations; the green shading shows the uncertainties on this fit (supplementary text S5). The purple short-dashed line shows a statistical fit to a model with linearly increasing flow longitudes, where only the longitude uncertainties are included; the two vertical purple short-dashed lines show the uncertainties at each end of the time interval under consideration (supplementary text S5). The black horizontal dash-dotted line shows the fit resulting from the statistically unlikely assumption that the flow longitude has been constant over time and uncertainties on that fit (vertical black dash-dotted line). For clarity, some of the STEREO and Prognos 6 data points are plotted using small shifts in the year of observation. The temporal interval over which some data were acquired is smaller than the plotted symbols.

angle between the gas velocity and magnetic field direction from 41.5° to the present 48.3° .

Temporal variations in the He flow direction have implications for the outer heliosphere and for the LIC. The 200-AU length of the column of interstellar gas passing over the Sun during 40 years is comparable to the collisional scale length in the LIC [≤ 300 AU (6)] and to the thickness of the heliosphere bow wave (19). The $\sim 6.8^\circ$ azimuthal shift corresponds to 24 AU at 200 AU. If this shift in the flow angle is due to nonthermal turbulent motions in an interstellar eddy, the angular scale of this eddy, $\delta\lambda$, for bulk flow velocity V_{bulk} (2) and turbulent velocity b_{turb} (supplementary text S4) would be $\delta\lambda \sim 2 b_{\text{turb}}/V_{\text{bulk}} \sim 8^\circ$, which is comparable to the observed shift.

There is no obvious bias in the data that would explain the longitude trend shown in Fig. 1, although possibly some uncertainties were underestimated. The variation in the interstellar wind longitude indicated by these historical data may

be evidence for variations in the galactic environment of the solar system.

References and Notes

1. P. C. Frisch, S. Redfield, J. Slavin, *Annu. Rev. Astron. Astrophys.* **49**, 237–279 (2011).
2. D. J. McComas *et al.*, *Science* **336**, 1291–1293 (2012).
3. E. Möbius *et al.*, *Astrophys. J. Suppl. Ser.* **198**, 11 (2012).
4. M. Bzowski *et al.*, *Astrophys. J. Suppl. Ser.* **198**, 12 (2012).
5. J. W. Armstrong, B. J. Rickett, S. R. Spangler, *Astrophys. J.* **443**, 209 (1995).
6. S. R. Spangler, A. H. Savage, S. Redfield, *Astrophys. J.* **742**, 30 (2011).
7. D. J. McComas *et al.*, *Science* **326**, 959–962 (2009).
8. M. Witte, *Astron. Astrophys.* **426**, 835–844 (2004).
9. C. S. Weller, R. R. Meier, *Astrophys. J.* **193**, 471 (1974).
10. J. M. Ajello, *Astrophys. J.* **222**, 1068 (1978).
11. J. M. Ajello, N. Witt, P. W. Blum, *Astron. Astrophys.* **73**, 260 (1979).
12. C. S. Weller, R. R. Meier, *Astrophys. J.* **246**, 386 (1981).
13. F. Dalaudier, J. L. Bertaux, V. G. Kurt, E. N. Mironova, *Astron. Astrophys.* **134**, 171 (1984).
14. J. Vallerga, R. Lallemand, M. Lemoine, F. Dalaudier, D. McMullin, *Astron. Astrophys.* **426**, 855–865 (2004).
15. G. Gloeckler *et al.*, *Astron. Astrophys.* **426**, 845–854 (2004).
16. C. Drews *et al.*, *Space Phys.* **117**, 9106 (2012).
17. D. J. Gershman *et al.*, *J. Geophys. Res. Space Phys.* **118**, 1389–1402 (2013).
18. E. Möbius *et al.*, *Astron. Astrophys.* **426**, 897–907 (2004).
19. G. P. Zank *et al.*, *Astrophys. J.* **763**, 20 (2013).

Acknowledgments: We thank everyone who made the IBEX mission a reality. IBEX is primarily funded by the NASA Explorers Program. Polish contributions were supported by a Polish Ministry of Science and Higher Education grant, N-N203-513-038. Additional support was provided by NASA grant NNX10AC44G. We thank R. R. Meier for many helpful comments and D. E. Welty for his reductions of the Sirius Ca⁺ data. IBEX data have been archived and are available from the IBEX project and the NASA National Space Science Data Center.

Supplementary Materials

www.sciencemag.org/cgi/content/full/341/6150/1080/DC1
Supplementary Text S1 to S5
Figs. S1 to S3
Tables S1 and S2
References (20–39)

1 May 2013; accepted 1 August 2013
10.1126/science.1239925

Radio Jets Clearing the Way Through a Galaxy: Watching Feedback in Action

Raffaella Morganti,^{1,2*} Judit Fogasy,³ Zsolt Paragi,⁴ Tom Oosterloo,^{1,2} Monica Orienti⁵

The energy released by an active galactic nucleus (AGN) has a strong impact on the surrounding interstellar medium (ISM). This feedback is considered to be the regulating factor for the growth of the central massive black hole and for the rate of star formation in a galaxy. We have located, using very-long-baseline interferometry, the fast outflow of neutral hydrogen in the young, restarted radio-loud AGN 4C12.50. The outflow is located 100 parsec from the nucleus where the radio jet interacts with the ISM, as well as around the associated radio lobe. These observations show that the radio plasma drives the outflow and removes gas from the central regions and that jet-driven outflows can play a relevant role in feedback mechanisms.

The important role for galaxy evolution of energetic feedback effects due to activity in the galaxy's nucleus has been put, in recent years, on more solid grounds thanks to the discovery of massive gas outflows in a growing number of galaxies with an active galactic nucleus (AGN). Many questions are still open, however—in particular, regarding the nature of the driving mechanism of these outflows [e.g., (1, 2)]. Answering these questions is important because it has implications for how ubiquitous the AGN-related feedback is, whether it is connected to

specific phases in the life of an AGN, and whether it is a recurrent phenomenon. One of the best ways to answer these questions is to identify the location of the outflowing gas and to image its distribution and kinematics. So far, this has not been achieved given the parsec-scale spatial resolution required to resolve the gas outflow.

The kinetic push of radio jets is often considered a possible mechanism for driving a gas outflow because of the high efficiency with which jets can transfer energy to the interstellar medium (ISM). However, their narrow opening angle is often used as an argument that their impact cannot be very high because a narrow jet would affect only a small part of the ISM. Yet, recent numerical simulations (3, 4) have shown that a radio jet, especially when the radio source is in an initial phase and surrounded by a porous, clumpy medium, may be able to efficiently clear up the gas in which it is enshrouded. This is because a large cocoon of disturbed and outflowing gas is created around the jet by the interaction of the radio

plasma, thus affecting a much larger region of the galaxy.

We have imaged, on parsec scales, the distribution and kinematics of the fast outflowing component of the neutral hydrogen in 4C12.50, one of the best-known ultraluminous infrared galaxies (ULIRGs) that hosts a young—recently restarted—radio-loud AGN. Galaxies like 4C12.50 are particularly relevant because they are considered to be the link between ULIRGs and AGNs (5); hence, they represent a particularly interesting phase in the evolution of a galaxy. The intriguing and fascinating characteristic of 4C12.50 is the presence of fast outflows not only of ionized gas (6, 7), but also of cold gas—in particular, atomic hydrogen (HI) and molecular gas (CO). An HI outflow of $\sim 1000 \text{ km s}^{-1}$ has been previously detected (8) that was later found (9) to have a markedly similar counterpart of molecular gas [CO(1-0) and (3-2)] (Fig. 1). These gaseous components have been interpreted as being part of the same fast outflow of cold gas.

In 4C12.50, all the possible mechanisms that could drive fast gas outflows are potentially present (10): starburst wind (connected to the relatively young stellar population), radiative AGN wind-driven outflows (connected to the bright optical AGN with high-ionization gas), and a powerful radio source. The presence of a particularly strong interaction between the radio jet and the ISM has been suggested by the presence of a hot spot with a very high fractional polarization (60%) at the end of the radio jet (11). Although the starburst wind has been ruled out as driving the outflow (10), the other possibilities remain. To locate the outflowing gas, we have performed observations with milliarcsecond (mas) angular resolution, using very-long-baseline interferometry (VLBI).

The observations were performed using a global VLBI network, including the Very Long Baseline Array (VLBA), one antenna of the Very Large

¹ASTRON, Netherlands Institute for Radio Astronomy, Postbus 2, 7990 AA, Dwingeloo, Netherlands. ²Kapteyn Astronomical Institute, University of Groningen, Post Office Box 800, 9700 AV Groningen, Netherlands. ³Eötvös Loránd University, Egyetem tér 1-3, 1053 Budapest, Hungary. ⁴Joint Institute for Very Long Baseline Interferometry (VLBI) in Europe, Postbus 2, 7990 AA Dwingeloo, Netherlands. ⁵Istituto Nazionale di Astrofisica (INAF)—Istituto di Radioastronomia, via Gobetti 101, I-40129, Bologna, Italy.

*Corresponding author. E-mail: morganti@astron.nl

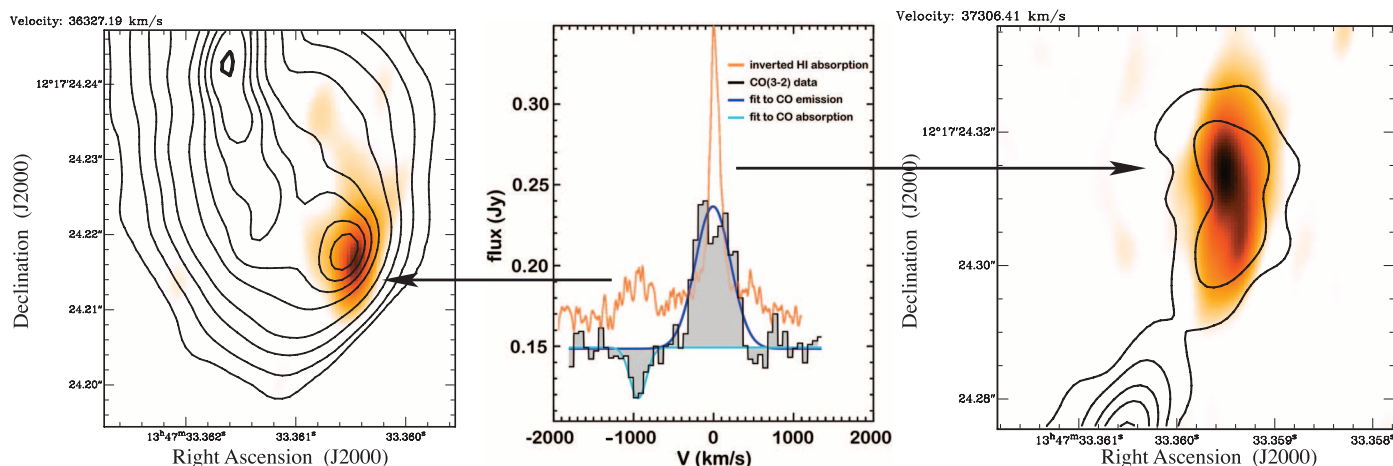


Fig. 1. The distribution of the HI in two velocity channels showing the location of the two clouds of HI detected in absorption (orange-white) superimposed on the continuum of 4C12.50 (contours). The integrated HI absorption profile is shown in the middle superimposed on the CO profile [taken from (9) with the HI from (8) and inverted for comparison]. The northern HI

cloud is at the systemic velocity (12) whereas the southern one is blueshifted ~ 1000 km/s relative to the systemic velocity. The location of the southern unresolved cloud producing the blueshifted HI absorption is cospatial (in projection) with the bright radio hot spot. A diffuse HI component is also observed. [Credit: Dasyra and Combes (9); reproduced with permission The European Southern Observatory]

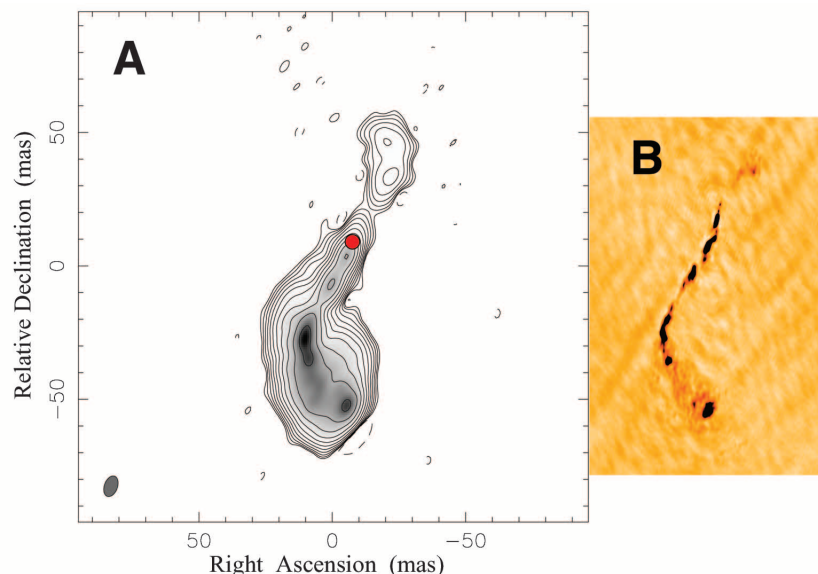


Fig. 2. Radio continuum images of 4C12.50 illustrating the morphology of the radio jet. (A) The continuum image derived from our VLBI data using the line-free channels. The red dot indicates the location of the radio core. The contour levels are $0.0003 \times (-1, 1, 2, 4, 8, 16, 32, 64, 128, 256, 512, 1024)$ Jy per beam with a peak brightness of 0.417 Jy per beam. (B) Continuum image taken from a previous, higher-spatial resolution study (11). The bent structure of the jet and the terminal hot spot in the southern lobe are clearly seen. This hot spot is characterized by an extremely high ($\sim 60\%$) fractional polarization (11). The two images are displayed on approximately the same scale. [Reproduced by permission of the American Astronomical Society]

Array (VLA), and three European VLBI Network (EVN) telescopes (Effelsberg, Westerbork, and Onsala). The central frequency, corresponding to the frequency of the redshifted HI, was set at 1266 MHz. These observations expand on the results obtained previously (12), which were limited by the width of the observing band. We have used a broader observing band (16 MHz, covering gas with kinematics deviating more than 1500 km/s from the systemic velocity) and a longer integration time (14 hours).

The angular resolution ranges from 12×4 mas [position angle (PA) of 12°] for the naturally weighted images and cubes, to 8×5 mas (PA 2°) for the full-resolution images. They correspond, at the redshift of 4C12.50 $z=0.1217$, to 32×11 pc and 21×13 pc, respectively. The noise level obtained is 0.65 and 0.90 mJy per beam per channel, respectively, for the different weightings, after Hanning smoothing. A continuum image was also obtained using the line-free channels (Fig. 2).

We detected the two HI absorption features previously seen in lower-resolution observations (8) and imaged them at parsec-scale resolution (Fig. 1). The outflowing component (~ 1000 km s $^{-1}$ blueshifted from the systemic velocity) is seen at the end of the distorted southern jet. This HI component appears to consist of a compact cloud (unresolved even by our high-resolution images) and a diffuse, tail-like structure. The compact cloud is seen—in projection—to be cospatial with the hot spot observed in radio continuum (11). The faint and diffuse component extends at least ~ 50 pc around and in front of the southern lobe (Fig. 1). This can be considered a lower limit to the actual extent due to the sensitivity limitations of the observations. Indeed, the profile from the naturally weighted image integrated over the southern lobe shows that we recover most of the HI absorption detected with the Westerbork Synthesis Radio Telescope (WSRT) (Fig. 3). The deeper HI absorption feature at the systemic velocity detected earlier (12) is confirmed by our observations to correspond to a cloud north of the nucleus (Fig. 1).

We have estimated the column density and the HI mass associated with the two clouds. In the southern part, the unresolved cloud has a column density of $N_{\text{HI}} = 4.6 \times 10^{21}$ cm $^{-2}$ [assuming the spin temperature ($T_{\text{spin}} = 100$ K)]. The derived mass of the cloud is $M_{\text{HI}} = 600$ solar masses (M_\odot); if we include the extended part, it reaches $M_{\text{HI}} = 1.6 \times 10^4 M_\odot$. The assumed value of T_{spin} likely represents a lower limit because the actual spin temperature, under the extreme conditions close to the AGN, may be at least a factor of 10 larger (6, 13). This implies that the mass of the cloud, as well, could be much higher. A recent study (9) suggests that the outflow carries an estimated cold H_2 mass of at least $4.2 \times 10^3 M_\odot$.

The larger HI cloud located in the northern part of the radio source is known to have an extremely high optical depth ($\tau = 0.6$) (12). This is

confirmed by our observations. The column density that we derived reaches $N_{\text{HI}} = 4.4 \times 10^{22} \text{ cm}^{-2}$ (again, assuming the conservative value of $T_{\text{spin}} = 100 \text{ K}$), and the corresponding mass of the cloud is $1.4 \times 10^5 M_{\odot}$, which is slightly higher than previously derived (12). Indeed, for this cloud, the broader band used in our observations has helped in recovering part of the HI that was missed before (in particular, a broad, blueshifted wing). The cloud appears clearly resolved, and we derived a size of $50 \times 80 \text{ pc}$. This represents a lower limit because the cloud could be more extended, outside the region covered by the radio continuum, where the HI cannot be traced in absorption.

For a number of radio sources, it has been proposed that the radio jet is responsible for the fast gas outflows. For 4C12.50, we could pinpoint the location of the outflow gas and recover the distribution of the cold gas associated with the most blueshifted HI absorption in relation to the radio jet. The extreme kinematics, together with the location (in projection) of the HI, suggests that we are indeed witnessing gas being expelled from the galaxy at a (projected) speed of 1000 km/s as a result of the interaction between the radio jet and a dense cloud in the ISM. The presence of such a strong interaction between the radio jet and the ISM had already been proposed for 4C12.50 following the study of the warm, ionized gas (6, 7). The emission lines show a complex structure with prominent blueshifted wings that have been interpreted as gas disturbed by the interaction with the radio plasma. However, the high spatial resolution of our data allowed us to study this in more detail.

The marked similarity of the blueshifted HI and CO absorption profiles points to a similarity in the distribution and kinematics of the gas in

these two phases. In the context of jet-ISM interactions, this would suggest that relatively dense clouds are present in the medium that do not get fully destroyed by such an interaction. The average densities derived for the compact clouds that we observed range between 150 and 300 cm^{-3} . These values are similar to those for the clouds in numerical simulations where a jet drives the lateral expansion of the medium around the jet, which, in turn, markedly affects the ISM of the host galaxy (3, 4). Thus, in 4C12.50, we may be witnessing this process in action.

The cold gas in the compact cloud may represent the core of an originally larger cloud that is encountered by the jet. The extended, diffuse trail observed against and around the radio lobe would instead represent the expanding medium dispersed after the interaction. Because of the similarity between the HI and CO blueshifted absorption profiles, we suggest that the two phases of the gas come from the same structure, with the HI likely an intermediate phase in the cooling process and the CO (H_2) the final stage. This gas must have undergone rapid cooling to be observed both in its HI and molecular phase. By following previous models (14), we found the cooling time for the southern cloud in 4C12.50, using the densities and velocities from our data, to be on the order of 10^4 years. Such a time scale is comparable to the age of the radio source, suggesting that the gas has indeed time to cool during the process of being expelled from the central regions of the galaxy.

An interaction between the radio jet and a clumpy medium surrounding the jet was also speculated to explain the region of extremely high polarization, ranging up to 60% (11). The colocation of this region with extremely high fractional po-

larization with the HI blueshifted cloud supports the suggestion that this feature is a termination shock or “working surface” where the jet encounters the ISM and rapidly decelerates. The high fractional polarization would result from the compression of a gas cloud and associated amplification of the magnetic field at that location.

The amount of energy in the outflow, as a fraction of the accretion energy of the AGN, is an important parameter for judging the relevance of the outflow. By combining the HI and optical results, it was found that the total observed outflow is between 16 and $29 M_{\odot}/\text{year}$, which would account for 0.2 to 0.3% of the available accretion energy (7). This contrasts with the requirements of most quasar feedback models (5 to 10% of the Eddington luminosity) but is similar to what is required in the “two phase” model proposed by (1). The morphology of the faint, diffuse gas seen in absorption in 4C12.50 is similar to that predicted by this model and suggests that we may indeed be witnessing the stretching and deformation of the ISM clouds required by (1) in order to increase the effective cross section of the interaction.

The detection of an extended (total size $\sim 150 \text{ kpc}$), low-surface brightness radio structure around 4C12.50 (15), likely the signature of a previous cycle of activity, suggests that the feedback of the radio jets on the ISM may be a repeating effect in the life of this galaxy. Indeed, most of the other radio sources known to have fast outflows are—like 4C12.50—young or restarted radio sources. This would underline the role of radio jets in feedback mechanisms because it implies that this type of feedback can act more than once in the life of a galaxy and therefore is even more relevant in its evolution. It could be that the stronger impact of the radio plasma occurs in the initial, young phase of the radio jet, where the young radio source clears up the central regions (see, e.g., the case of PKS1549-79) (16), and that at a later stage, the radio-loud activity corresponding with the 10 - to 100 -kpc-size radio jet provides a “maintenance” mode, with energy deposited at larger radii in the surrounding hot halo of the galaxy, providing a mechanism to prevent the gas in these halos from cooling (17).

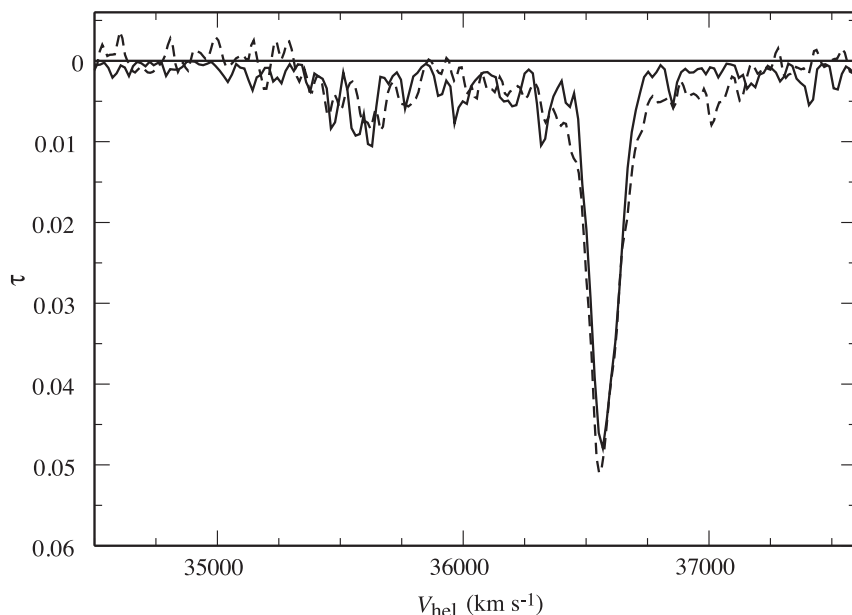


Fig. 3. Comparison of the HI absorption profiles from low- and high-resolution observations. The dashed profile represents the HI absorption from the WSRT observations (8) and is shown superimposed on the integrated profile from the VLBI observations presented here (in black).

References and Notes

1. P. F. Hopkins, M. Elvis, *Mon. Not. R. Astron. Soc.* **401**, 7–14 (2010).
2. A. C. Fabian, *Annu. Rev. Astron. Astrophys.* **50**, 455 (2012).
3. A. Y. Wagner, G. V. Bicknell, *Astrophys. J.* **728**, 29 (2011).
4. A. Y. Wagner, G. V. Bicknell, M. Umemura, *Astrophys. J.* **757**, 136 (2012).
5. N. Scoville et al., *Astron. J.* **119**, 991–1061 (2000).
6. J. Holt, C. N. Tadhunter, R. Morganti, *Mon. Not. R. Astron. Soc.* **342**, 227–238 (2003).
7. J. Holt, C. N. Tadhunter, R. Morganti, B. H. C. Emonts, *Mon. Not. R. Astron. Soc.* **410**, 1527 (2011).
8. R. Morganti, C. N. Tadhunter, T. A. Oosterloo, *Astron. Astrophys.* **444**, L9–L13 (2005).
9. K. M. Dasysa, F. Combes, *Astron. Astrophys.* **541**, L7 (2012).
10. D. Batcheldor et al., *Astrophys. J.* **661**, 70–77 (2007).

11. M. L. Lister *et al.*, *Astrophys. J.* **584**, 135–146 (2003).
12. R. Morganti *et al.*, *Astron. Astrophys.* **424**, 119 (2004).
13. J. N. Bahcall, R. D. Ekers, *Astrophys. J.* **157**, 1055 (1969).
14. G. Mellema, J. D. Kurk, H. J. A. Röttgering, *Astron. Astrophys.* **395**, L13–L16 (2002).
15. C. Stanghellini *et al.*, *Astron. Astrophys.* **443**, 891–902 (2005).
16. J. Holt *et al.*, *Mon. Not. R. Astron. Soc.* **370**, 1633–1650 (2006).
17. B. R. McNamara, P. E. J. Nulsen, *New J. Phys.* **14**, 055023 (2012).

Acknowledgments: The European VLBI Network is a joint facility of European, Chinese, South African, and other radio astronomy institutes funded by their national research councils. The National Radio Astronomy Observatory is a

facility of the National Science Foundation operated under cooperative agreement by Associated Universities, Inc. J.F. acknowledges the ASTRON/JIVE Summer Student Programme during which she carried out this project. Z.P. acknowledges partial support from the Hungarian Scientific Research Fund, grant OTKA K104539.

13 May 2013; accepted 24 July 2013
10.1126/science.1240436

Enhanced Seasonal Exchange of CO₂ by Northern Ecosystems Since 1960

H. D. Graven,^{1*} R. F. Keeling,¹ S. C. Piper,¹ P. K. Patra,² B. B. Stephens,³ S. C. Wofsy,⁴ L. R. Welp,¹ C. Sweeney,⁵ P. P. Tans,⁵ J. J. Kelley,⁶ B. C. Daube,⁴ E. A. Kort,^{7†} G. W. Santoni,⁴ J. D. Bent¹

Seasonal variations of atmospheric carbon dioxide (CO₂) in the Northern Hemisphere have increased since the 1950s, but sparse observations have prevented a clear assessment of the patterns of long-term change and the underlying mechanisms. We compare recent aircraft-based observations of CO₂ above the North Pacific and Arctic Oceans to earlier data from 1958 to 1961 and find that the seasonal amplitude at altitudes of 3 to 6 km increased by 50% for 45° to 90°N but by less than 25% for 10° to 45°N. An increase of 30 to 60% in the seasonal exchange of CO₂ by northern extratropical land ecosystems, focused on boreal forests, is implicated, substantially more than simulated by current land ecosystem models. The observations appear to signal large ecological changes in northern forests and a major shift in the global carbon cycle.

Observations of atmospheric CO₂ concentration from the longest-running Northern Hemisphere records at Mauna Loa, Hawaii (MLO, 20°N) and Barrow, Alaska (BRW, 71°N) show increasing trends in seasonal amplitude (Fig. 1) (1–4). Shorter records from other ground-based sites in the Northern Hemisphere also show increasing trends in amplitude, with the largest changes at high latitudes (5), but the long-term change and especially its spatial pattern have not been well characterized by existing data sets because only MLO and BRW have records extending back to the 1950s and 1960s (6–9). The two sites show similar trends in the timing of CO₂ drawdown, advancing by roughly 1 week, but differing trends in amplitude: The amplitude at MLO increased by $15 \pm 5\%$ over the past 50 years, while the amplitude at BRW increased by at least twice as much (Fig. 1). The best estimate for BRW is a 35% increase in amplitude, with a range of 30 to 49%, including uncertainty from changes in measure-

ment site location, sampling inlet height, and local vegetation effects (10, 11).

Here, we present seasonal CO₂ cycles observed by the recent High-Performance Instrumented Airborne Platform for Environmental Research (HIAPER) Pole-to-Pole Observations (HIPPO) large-scale aircraft campaign (12) and regular aircraft profiles over several fixed sites by the National Oceanic and Atmospheric Administration (NOAA) Carbon Cycle Group Aircraft Program from 2009 to 2011 and compare them to observations made 50 years earlier during the International Geophysical Year (IGY) (13). The IGY observations were obtained by 160 weather reconnaissance flights above the North Pacific and Arctic Oceans from 1958 to 1961 along 500 and 700 millibar (mb) pressure surfaces (~6 and 3 km altitude). To assess changes in seasonal CO₂ amplitude over time, we examine HIPPO and NOAA data over the same regions and pressure surfaces as the IGY data (14). The comparison reveals a strikingly large (~50%) amplitude increase north of 45°N, indicating that major ecological changes must have occurred in northern land ecosystems over the past 50 years.

We calculate an amplitude gain factor for the 1958 to 1961 and 2009 to 2011 observations in 10° latitude bands at 500 and 700 mb after detrending the data by subtracting the observed deseasonalized trend at MLO and after specifying the shape of the seasonal cycle in each pressure and latitude band using fits to the NOAA aircraft data, which have higher temporal resolution than the HIPPO and IGY data (14). This method does

not allow for the detection of changes in phase, which in any case are not clearly resolvable in the data (14), but shifts of up to 7 days as observed at MLO and BRW do not significantly affect the calculation of amplitude (1).

An increase in amplitude at least as large as that detected at Barrow is found over a wide range of pressures and at all latitudes north of 45°N (Fig. 2). The change in seasonal CO₂ amplitude north of 45°N is about +5 parts per million (ppm) at all pressures, representing a $57 \pm 7\%$ increase at 500 mb since 1958 to 1961 (Figs. 2 and 3) ($-0.9 \pm 0.1\%$ year⁻¹ over 50 years). The seasonal CO₂ amplitude increase is smaller between 35° and 45°N at 500 mb, $26 \pm 18\%$, whereas there is no distinguishable amplitude change south of 35°N (Fig. 2). The same pattern appears at 700 mb, although the IGY data are limited to 10° to 30°N and 65° to 90°N at 700 mb. Low-latitude amplitude changes in the aircraft data are consistent, within their uncertainties, with the surface measurements from Mauna Loa at ~670 mb.

Representativeness of the aircraft data is shown by the similarity between HIPPO and NOAA data for 2009 to 2011 (15), and between the IGY and independent data from 1963 to 1968 over the North Atlantic Ocean (16). The large changes in amplitude between 1958 to 1963 and 2009 to 2011 north of 45°N (35 to 66%) substantially exceed interannual variation at Barrow ($\pm 4\%$) (Fig. 1) and in high-latitude NOAA aircraft data for recent years ($\pm 15\%$) (15), indicating that the observations represent a long-term change rather than a short-term fluctuation.

Fossil fuel, wildfire, and ocean fluxes of CO₂ contribute only a few percent to the seasonal CO₂ cycle in the Northern Hemisphere (5, 17, 18), limiting their impact on trends in CO₂ amplitude to less than a few percent (19). Because midtropospheric amplitude changes north of 45°N are at least as large as those at Barrow, the observations cannot be explained solely by trends in the intensity of vertical mixing (19), although changes in transport may cause secondary effects. Model simulations also indicate that potential biases caused by uneven sampling within each latitude band are much smaller than the uncertainties in measured CO₂ amplitude change (19).

The large increase in CO₂ amplitude north of 45°N must therefore be attributed almost entirely to the terrestrial biosphere. We now focus on assessing the magnitude and driving factors for trends in the seasonal exchange of CO₂ from net ecosystem production (NEP) by calculating optimal estimates of NEP change that best match

¹Scripps Institution of Oceanography, University of California, San Diego, La Jolla, CA, USA. ²Research Institute for Global Change, Yokohama, Japan. ³National Center for Atmospheric Research, Boulder, CO, USA. ⁴School of Engineering and Applied Science, Harvard University, Cambridge, MA, USA. ⁵National Oceanic and Atmospheric Administration, Boulder, CO, USA. ⁶Institute of Marine Science, University of Alaska, Fairbanks, Fairbanks, AK, USA. ⁷Jet Propulsion Laboratory, California Institute of Technology, Pasadena, CA, USA.

*Corresponding author. E-mail: hgraven@ucsd.edu

†Present address: Department of Atmospheric, Oceanic and Space Sciences, University of Michigan, Ann Arbor, MI, USA.

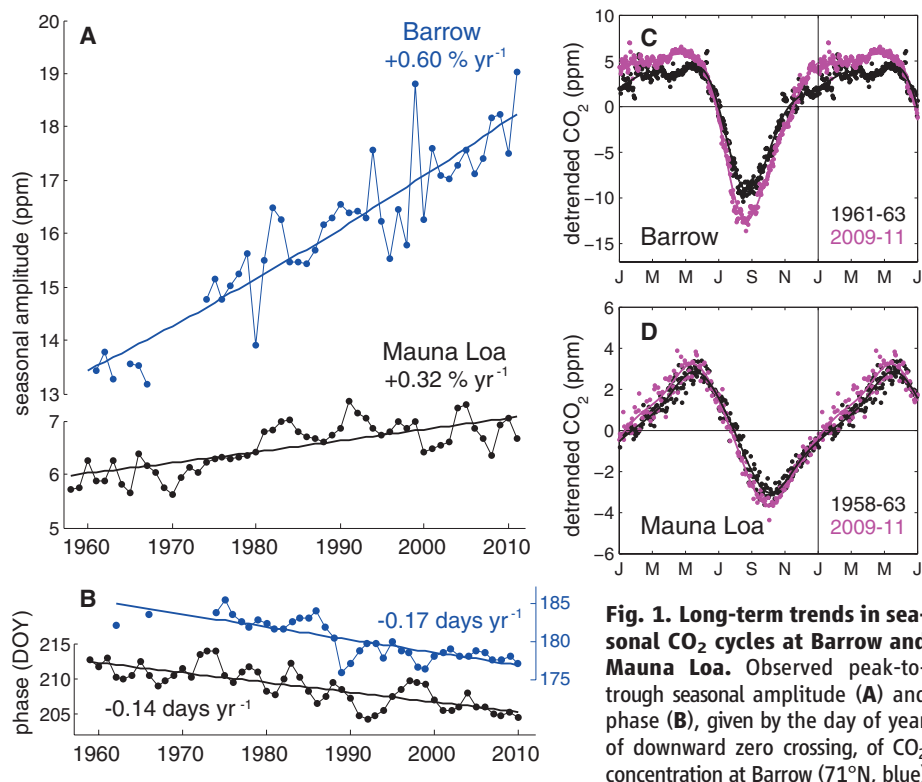


Fig. 1. Long-term trends in seasonal CO₂ cycles at Barrow and Mauna Loa. Observed peak-to-trough seasonal amplitude (A) and phase (B), given by the day of year of downward zero crossing, of CO₂ concentration at Barrow (71°N, blue) and Mauna Loa (20°N, black) measured by the Scripps CO₂ Program (7, 8) and the NOAA Global Monitoring Division (9). Growth rate of amplitude is given in percentage change per year, with 1 SD uncertainty of ± 0.05 to 0.07% year⁻¹. Seasonal CO₂ cycles observed at Barrow (C) and Mauna Loa (D) for the 1961 to 1963 or 1958 to 1963 and 2009 to 2011 time periods. The first 6 months of the year are repeated.

and Mauna Loa (20°N, black) measured by the Scripps CO₂ Program (7, 8) and the NOAA Global Monitoring Division (9). Growth rate of amplitude is given in percentage change per year, with 1 SD uncertainty of ± 0.05 to 0.07% year⁻¹. Seasonal CO₂ cycles observed at Barrow (C) and Mauna Loa (D) for the 1961 to 1963 or 1958 to 1963 and 2009 to 2011 time periods. The first 6 months of the year are repeated.

the atmospheric CO₂ amplitude change and then exploring potential mechanisms with historical simulations of terrestrial ecosystem models.

We begin with spatially resolved monthly estimates of NEP averaged over 2005 to 2010 that have been optimized using terrestrial ecosystem model simulations and current observations from the global CO₂ network in two atmospheric transport models, Atmospheric Chemistry Transport Model (ACTM) (20) and TM3 (21). We simulate separate tracers in ACTM and TM3 representing large regions (Fig. 3C) to assess their contribution to the seasonal CO₂ cycle at different tropospheric locations (Fig. 3, A and B), then we adjust monthly NEP for the large regions by a consistent fraction—that is, by changing the amplitude but not the phase in order to best match the observed CO₂ amplitude changes, roughly centered on 155°W (Fig. 3, D to F) (22).

Exploiting our observation that CO₂ amplitude changes are much larger north of 45°N, we optimize changes in NEP in boreal and Arctic regions (Case 1 in Fig. 3, D to F), the regions with stronger influence on CO₂ cycles at high latitudes compared with low latitudes (5) (Fig. 3, A and B). Due to isentropic transport, the seasonal cycle at 70°N and 500 mb is less sensitive to the Arctic than to regions farther south (Fig. 3B), showing that changes cannot only be occurring in the Arctic. The optimal uniform change in NEP amplitude in boreal and Arctic regions, fitting to CO₂ amplitude changes north of 45°N only, is an 85% [73 to 107% confidence interval (CI)] (23) increase. Extending NEP changes to include

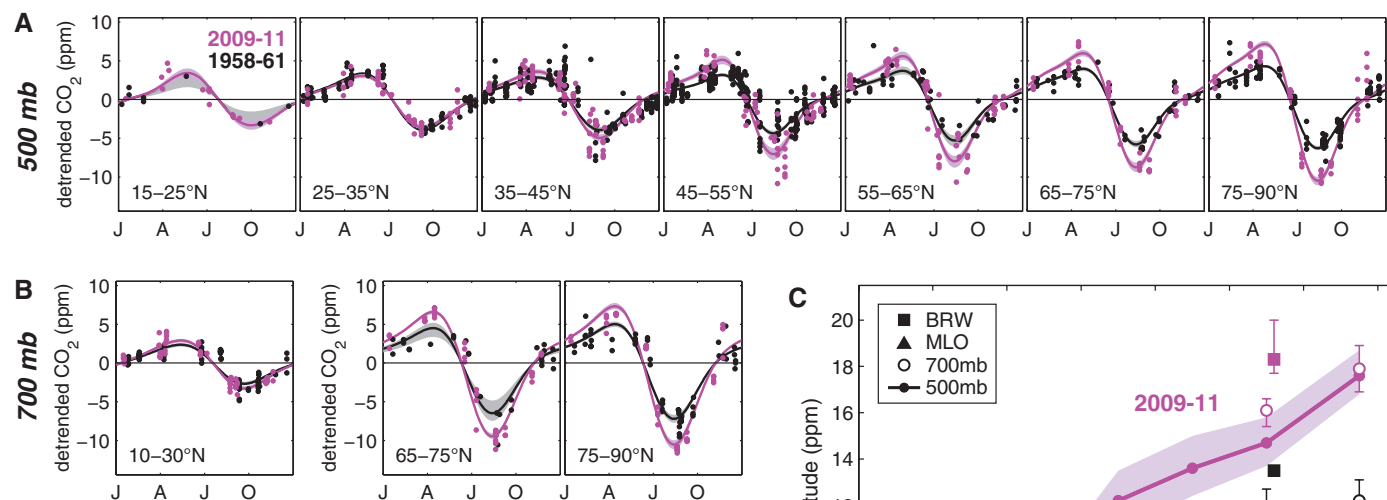
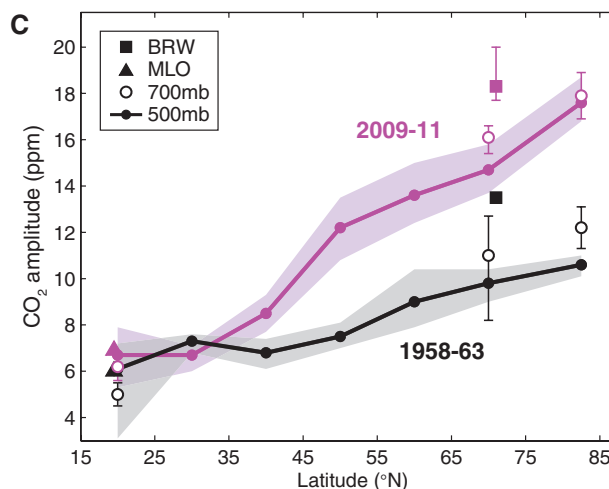


Fig. 2. Seasonal CO₂ cycles observed by aircraft in 1958 to 1961 and 2009 to 2011. Seasonal cycles of CO₂ at 500 mb in the upper row (A) and 700 mb in the lower row (B) for each latitude band with aircraft data in both periods. Curves show the seasonal cycles fit to the data, with uncertainties indicated by shaded areas. Amplitudes of the seasonal cycle of CO₂ for all locations with data available in both periods (C). The IGY aircraft data cover the period 1958 to 1961; the early BRW and MLO data cover 1961 to 1963 and 1958 to 1963. Uncertainties (55) are shown by the shaded areas for 500 mb data and by error bars for 700 mb and BRW in 2009 to 2011. Uncertainties for BRW in 1961 to 1963 and MLO in both periods are smaller than the symbol sizes.



temperate regions as well as Arctic and boreal regions results in an optimal increase of 53% (46 to 65% CI), assuming uniform change over these three regions (Case 2 in Fig. 3, D to F), or optimal zone-specific increases of 23% (12 to 42% CI) in the Arctic, 67% (57 to 87% CI) in the boreal, and 67% (54 to 89% CI) in the temperate region (Case 3 in Fig. 3, D to F).

Allowing for changes in the temperate region in Cases 2 and 3 improves the fit to high-latitude data compared to Case 1 while significantly decreasing the change attributed to Arctic and boreal regions. The simulations tend to produce fractional changes in amplitude that are more uniform with altitude than the observations, which show fractional changes in amplitude increase with height at high latitudes, and they tend to overestimate the CO₂ amplitude change at lower latitudes, which were not used in optimization. This may partly result from transport errors, caused by inaccuracies in modeled transport or unresolved transport changes since 1960, or from representation errors, caused by low resolution in the atmospheric transport models or in the terrestrial regions considered. Alternatively, the high-latitude effects on low-latitude CO₂ amplitudes may have been counteracted by decreasing NEP amplitudes

in subtropical and tropical land regions. Fitting to all data and allowing for changes in subtropical and tropical NEP results in a change of -15% (-31 to 9% CI) in the tropics and subtropics (Case 4 in Fig. 3, D to F) without significantly affecting the optimal zone-specific NEP increases in the Arctic and boreal regions, though the NEP increase in the temperate region is reduced from Case 3.

The observations therefore require a widespread increase in the seasonal exchange of carbon in northern regions. Our analysis suggests that an additional 1.3×10^{15} to 2.0×10^{15} g carbon (Pg C) is exchanged with the atmosphere seasonally by Arctic, boreal, and temperate ecosystems combined in 2009 to 2011 compared with 1958 to 1963, an increase of 32 to 59%. This seasonal exchange represents the accumulation of carbon on land during the growing season (typically May to August) and the release of carbon during the dormant season, after subtracting annual mean exchange (17). Our analysis does not distinguish between enhanced growing season uptake and enhanced dormant season release, but changes in these two opposing fluxes may not necessarily be in balance. We do find, counter to previous studies invoking dormant or early growing season trends alone (1, 24), that strong increases in CO₂ am-

plitude are unlikely to occur without enhanced uptake in the main growing season. This is because the intense fluxes in the main growing season (June and July) make a much larger contribution to the seasonal CO₂ amplitude than either the dormant season (September to April) or the shoulder seasons (May and August), as shown by calculations that examine contributions of the different seasons to the CO₂ cycle (25).

Enhancement in seasonal NEP is likely to be greatest in boreal regions, where all four cases require that the NEP amplitude changed by at least 53%. Less definitive is the requirement for decreased NEP amplitude in subtropical and tropical regions, although this may be consistent with the conversion of highly productive forests to crop or pasture lands and increased drought (26–30).

To explore potential mechanisms for changing NEP, we examine historical simulations of a subset of terrestrial ecosystem models currently participating in the fifth phase of the Coupled Model Intercomparison Project (CMIP5) (31). These models include simulations of CO₂ fertilization, climate change, and land use change, as well as nonlinear interactions between these processes; some additionally include dynamic vegetation

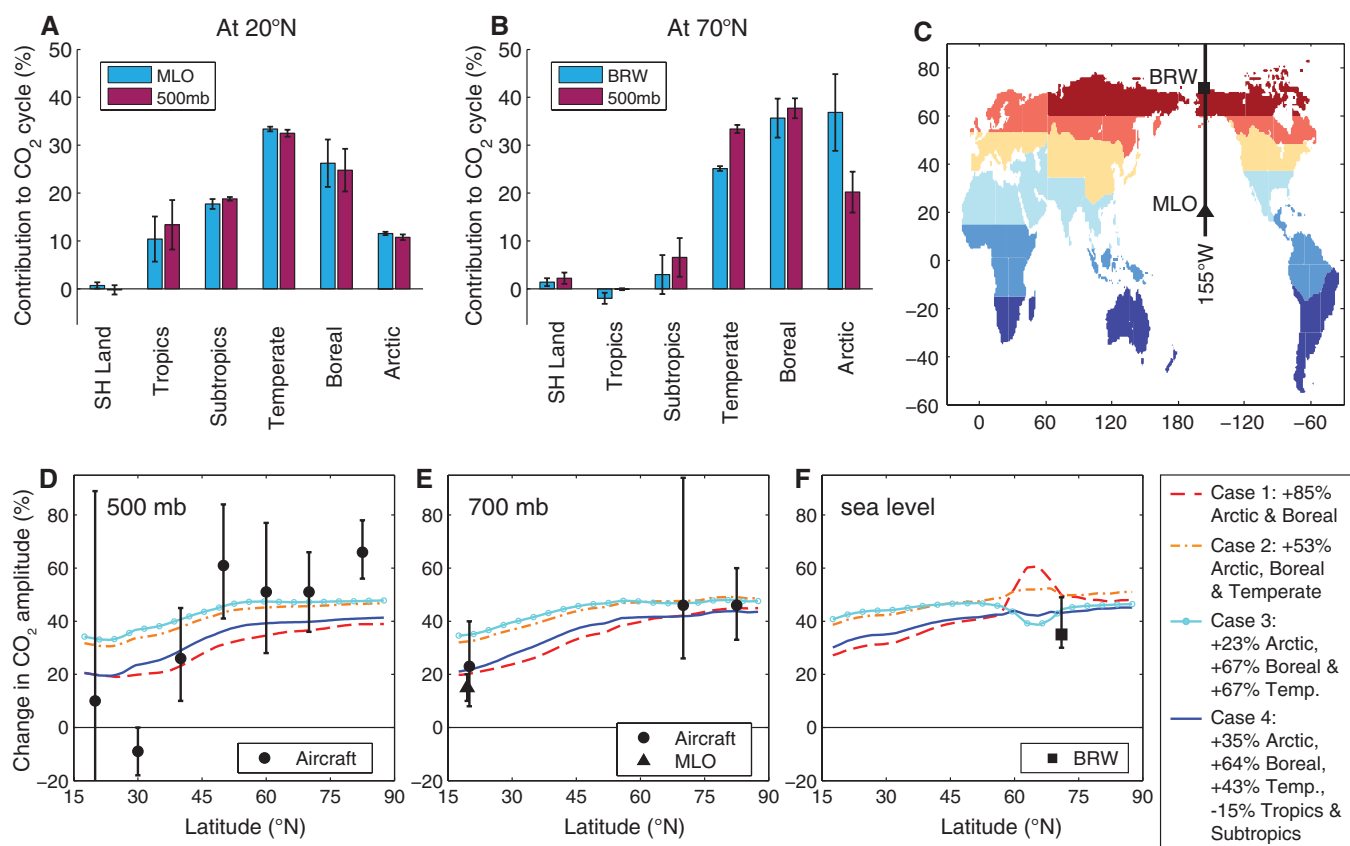


Fig. 3. Regional attribution of the seasonal CO₂ amplitude and its change over 50 years. Contributions of different terrestrial regions to the seasonal cycle of CO₂ at ground-based stations and at 500 mb for 20°N (A) and for 70°N (B) for 2009 to 2011, averaged over two atmospheric transport models, ACTM (20) and TM3 (21). Error bars reflect absolute differences between the two models. (C) Locations of the Mauna Loa and Barrow stations and the 155°W meridian, as

well as the terrestrial regions considered. Arctic (red); boreal (orange); temperate (yellow); subtropics, tropics, and Southern Hemisphere land (shades of blue). (D to F) Change in CO₂ amplitude, in percentages, in the observations and in simulations where the amplitude in NEP was optimally scaled in different regions, plotted by latitude along 155°W for different pressures: (D) 500 mb aircraft data, (E) 700 mb aircraft data and Mauna Loa (670 mb), and (F) Barrow at sea level.

change, coupled nitrogen cycling, or simple crop modeling (32). We use the ACTM and TM3 atmospheric transport models to estimate atmospheric CO₂ amplitudes resulting from the CMIP5 models' simulated monthly NEP (Fig. 4).

None of the CMIP5 models can account for the increase in CO₂ amplitude north of 45°N at 500 mb between 1958 to 1961 and 2009 to 2011 (Fig. 4). Moreover, the recent CO₂ amplitude varies strongly between models, with a range of 6 to 19 ppm compared with the observed value of 13.8 ± 0.7 ppm. Previous studies have similarly shown that most terrestrial ecosystem models underestimate the long-term trend in CO₂ amplitude at Mauna Loa (33) and include large errors in the seasonal amplitude of NEP at eddy flux sites (34).

Simulated CO₂ amplitude changes from the CMIP5 models are nearly proportional to their NEP amplitude changes in northern ecosystems (32), as found in our optimization (Fig. 3), implying that the models underestimate the 50-year changes in NEP. This underestimate is not surprising, considering that the models' parameterizations of the direct effects of rising CO₂ and temperature are informed by laboratory and field studies that show low response to manipulations of CO₂ and temperature. Observed enhancement factors (35–38) suggest that the increase in net primary productivity (NPP) from the observed 50-year increases in CO₂ (23%) (8) and northern temperature (1.0°C north of 30°N) (39) should be no larger than 20 to 30%. Correspondingly, simulated increases in seasonal NPP amplitude are in the range 6 to 22% in the CMIP5 models, accompanied by higher amplitudes in heterotrophic respiration in most cases (32). Independent of the models, an explanation for the NEP changes based solely on a direct physiological

response to warming is inconsistent with two features of the Barrow record (Fig. 1): (i) the weak interannual variability but strong long-term trend, and (ii) the increase in amplitude from the 1960s to the mid-1970s, a period when northern land temperatures did not rise but cooled slightly (39, 40).

We are led to conclude that ecological changes in boreal and temperate forests are driving additional increases in the summertime uptake of carbon. This inference from atmospheric data is qualitatively consistent with expanding evidence for substantial changes occurring in these ecosystems. Forest inventories show increased stand area and biomass (26, 28). Other ground-based studies show that evergreen shrubs and trees are migrating northward in response to warming (41–43), and that fire, logging, and other disturbances (44, 45) are shifting the age composition toward younger, early-successional forests that experience shorter, more intense periods of seasonal carbon uptake (46, 47). Satellite observations generally show trends toward increased greenness in northern ecosystems (4), although many areas of the boreal forest show browning trends in recent decades (48, 49). The atmospheric evidence helps to quantify the aggregate effect of these, and other, types of ecological changes over the past 50 years. The changes are evidently underrepresented in the CMIP5 models, including those that allow for dynamic vegetation (Fig. 4) and coupled nitrogen cycling (Community Climate System Model 4 and Norwegian Earth System Model 1-M) (50).

The increase in seasonal CO₂ amplitude may be closely related to the net sink of CO₂ in northern extratropical land ecosystems that is currently ~ 2 Pg C year⁻¹ (28, 51–53). The relationship depends on how the sink has changed over time, which is not well constrained observationally but

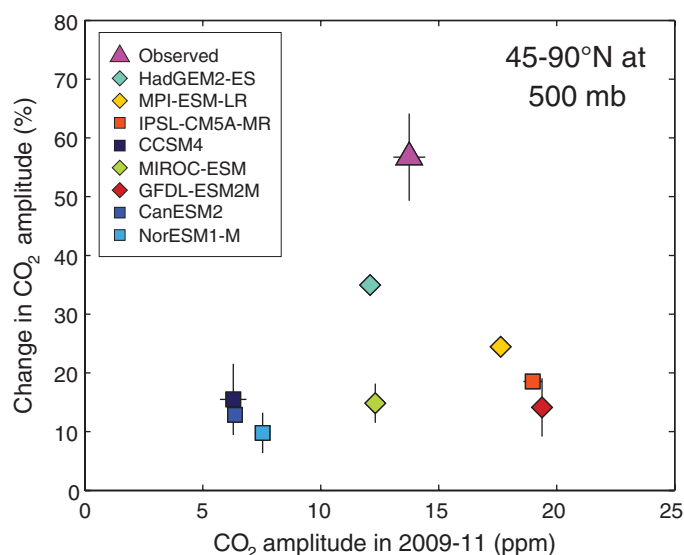
is likely to have increased since 1960 (54). Assuming that the sink was ~ 1 Pg C year⁻¹ in 1960, the observed 1.3 to 2.0 Pg C year⁻¹ increase in seasonal exchange over 50 years implies that growing season uptake increased by 40 to 60%, whereas dormant season release increased by only 20 to 50%, a result similar to the model scenarios described by Randerson *et al.* (5). A northern sink smaller than ~ 1 Pg C year⁻¹ in 1960 would imply an even larger imbalance between growing season and dormant season trends.

There is no evidence that northern ecosystem trends are slowing down, because the largest CO₂ amplitudes at Barrow have been observed in the past few years (Fig. 1). The inability of the CMIP5 models to account for the observed increase in the amplitude of atmospheric CO₂ indicates that they underestimate the widespread ecological changes that occurred over the past 50 years and are likely to underpredict future changes.

References and Notes

- C. D. Keeling, J. F. S. Chin, T. P. Whorf, *Nature* **382**, 146–149 (1996).
- G. I. Pearman, P. Hyson, *J. Geophys. Res.* **86**, 9839 (1981).
- R. B. Bacastow, C. D. Keeling, T. P. Whorf, *J. Geophys. Res.* **90**, 10529 (1985).
- R. B. Myneni, C. D. Keeling, C. J. Tucker, G. Asrar, R. R. Nemani, *Nature* **386**, 698–702 (1997).
- J. T. Randerson, M. V. Thompson, T. J. Conway, I. Y. Fung, C. B. Field, *Global Biogeochem. Cycles* **11**, 535–560 (1997).
- C. D. Keeling, *Tellus* **12**, 200–203 (1960).
- J. J. Kelley, "An Analysis of Carbon Dioxide in the Arctic Atmosphere near Barrow, Alaska 1961 to 1967," Scientific Report of the Office of Naval Research, Contract N00014-67-A-0103-0007 NR 307-252 (1969).
- R. F. Keeling, S. C. Piper, A. F. Bollenbacher, S. J. Walker, Atmospheric CO₂ records from sites in the SIO air sampling network. Trends: A Compendium of Data on Global Change (Carbon Dioxide Information Analysis Center, Oak Ridge National Laboratory, U.S. Department of Energy, Oak Ridge, TN, 2009).
- K. W. Thoning, D. R. Kitzis, A. Croftwell, Atmospheric Carbon Dioxide Dry Air Mole Fractions from quasi-continuous measurements at Barrow, Alaska; Mauna Loa, Hawaii; American Samoa; and South Pole, 1973–2011, Version: 2012-05-07, available at <http://ftp.cmdl.noaa.gov/ccg/co2/> in-situ (2012).
- Materials and methods are available as supplementary materials on Science Online.
- See section SM1 in the supplementary materials.
- S. C. Wofsy; HIPPO Science Team and Cooperating Modellers and Satellite Teams, *Philos. Trans. R Soc. A* **369**, 2073–2086 (2011).
- C. D. Keeling, T. B. Harris, E. M. Wilkins, *J. Geophys. Res.* **73**, 4511–4528 (1968).
- See section SM2 in the supplementary materials.
- See section SM3 in the supplementary materials.
- W. Bischof, B. Bolin, *Tellus* **18**, 155–159 (1966).
- M. Heimann, C. D. Keeling, C. J. Tucker, *Geophys. Monogr. Ser.* **55**, 277–303 (1989).
- See section SM5 in the supplementary materials.
- See section SM4 in the supplementary materials.
- P. K. Patra *et al.*, *Atmos. Chem. Phys.* **11**, 4163–4175 (2011).
- C. Roedenbeck, S. Houweling, M. Gloor, M. Heimann, *Tellus B Chem. Phys. Meteorol.* **55**, 488–497 (2003).
- See sections SM6 and SM8 in the supplementary materials.
- We specify the uncertainty in NEP amplitude change with 95% confidence intervals, assessed by varying parameters in the optimization and including jackknife estimates of the data.

Fig. 4. Comparison of observations with CMIP5 model simulations. Change in amplitude of the seasonal cycle of CO₂ between 1958 to 1961 and 2009 to 2011 versus amplitude of the seasonal cycle for 2009 to 2011 at 500 mb, averaged over 45° to 90°N, in observations and in simulations of the CMIP5 land models (56) using the two atmospheric transport models, ACTM and TM3. Diamonds indicate models with dynamic vegetation. Error bars in the simulated amplitude and change in amplitude show differences between ACTM and TM3. The simulations include changes in fossil fuel emissions and atmospheric transport between 1958 to 1961 and 2009 to 2011. Oceanic fluxes were given by the two models' atmospheric CO₂ inversions for the late 2000s and held constant for the 1958 to 1961 and 2009 to 2011 periods.



24. S. A. Zimov *et al.*, *Clim. Change* **33**, 111–120 (1996).
25. See section SM7 in the supplementary materials.
26. FRA, “Global Forest Resources Assessment 2010” (Food and Agriculture Organization of the United Nations, Rome, 2010).
27. G. C. Hurtt *et al.*, *Clim. Change* **109**, 117–161 (2011).
28. Y. Pan *et al.*, *Science* **333**, 988–993 (2011).
29. O. L. Phillips *et al.*, *Science* **323**, 1344–1347 (2009).
30. K. R. Gurney, W. J. Eckels, *Tellus B Chem. Phys. Meteorol.* **63**, 328–339 (2011).
31. K. E. Taylor, R. J. Stouffer, G. A. Meehl, *Bull. Am. Meteorol. Soc.* **93**, 485–498 (2012).
32. See section SM9 in the supplementary materials.
33. A. D. McGuire *et al.*, *Global Biogeochem. Cycles* **15**, 183–206 (2001).
34. K. Schaefer *et al.*, *J. Geophys. Res.* **117**, G03010 (2012).
35. L. Rustad *et al.*, *Oecologia* **126**, 543–562 (2001).
36. R. A. Houghton, *J. Geophys. Res.* **92**, 4223 (1987).
37. G. H. Kohlmaier *et al.*, *Tellus B Chem. Phys. Meteorol.* **41**, 487–510 (1989).
38. R. J. Norby *et al.*, *Proc. Natl. Acad. Sci. U.S.A.* **102**, 18052–18056 (2005).
39. P. D. Jones *et al.*, *J. Geophys. Res.* **117**, D05127 (2012).
40. J. Hansen, R. Ruedy, M. Sato, K. Lo, *Rev. Geophys.* **48**, RG4004 (2010).
41. G. R. Walther *et al.*, *Nature* **416**, 389–395 (2002).
42. S. C. Elmendorf *et al.*, *Nat. Clim. Change* **2**, 453–457 (2012).
43. K. E. N. Tape, M. Sturm, C. Racine, *Glob. Change Biol.* **12**, 686–702 (2006).
44. A. J. Soja *et al.*, *Global Planet. Change* **56**, 274–296 (2007).
45. E. S. Kasischke *et al.*, *Can. J. Res.* **40**, 1313–1324 (2010).
46. S. A. Zimov *et al.*, *Science* **284**, 1973–1976 (1999).
47. L. R. Welp, J. T. Randerson, H. P. Liu, *J. Geophys. Res.* **111**, G03007 (2006).
48. S. J. Goetz, A. G. Bunn, G. J. Fiske, R. A. Houghton, *Proc. Natl. Acad. Sci. U.S.A.* **102**, 13521–13525 (2005).
49. D. Verbyla, *Glob. Ecol. Biogeogr.* **17**, 547–555 (2008).
50. P. E. Thornton, J.-F. Lamarque, N. A. Rosenbloom, N. M. Mahowald, *Global Biogeochem. Cycles* **21**, GB4018 (2007).
51. P. P. Tans, I. Y. Fung, T. Takahashi, *Science* **247**, 1431–1438 (1990).
52. K. R. Gurney *et al.*, *Nature* **415**, 626–630 (2002).
53. B. B. Stephens *et al.*, *Science* **316**, 1732–1735 (2007).
54. C. D. Keeling, S. C. Piper, T. P. Whorf, R. F. Keeling, *Tellus B Chem. Phys. Meteorol.* **63**, 1–22 (2011).
55. We specify the uncertainty in CO₂ amplitude with 95% confidence intervals estimated using a jackknife procedure (fig. S3).
56. Only two models’ simulations extended to 2011 (HadGEM2-ES and NorESM-1). Other models’ output was available only through 2005, so NEP for 2009 to 2011 is given by the mean over 2001 to 2005. In these models, the change in NEP amplitude up to 2001 to 2005 may be 10% smaller than the change up to 2009 to 2011.

Acknowledgments: The Scripps CO₂ Program is supported by DOE grant DE-SC0005090. HIPPO was supported by NSF grants ATM-0628575, ATM-0628519, ATM-0628388, ATM-0628452, and ATM-1036399, and by the National Center for Atmospheric Research (NCAR). Recovery and updating of early aircraft, MLO, and BRW data was supported by NSF grant ATM-1036399.

L.R.W. was supported by NASA award NNX11AF36G. Early observations at BRW were funded by U.S. Navy/Office of Naval Research contract N00014-67-A-0103-0007. Online access to all observational data is summarized in section SM10 of the supplementary materials. NCAR is supported by the NSF. Any opinions, findings, and conclusions or recommendations expressed in this material are those of the authors and do not necessarily reflect the views of NOAA, NSF, DOE or NASA. We thank the HIPPO science team and the crew and support staff at the NCAR Research Aviation Facility. We acknowledge the World Climate Research Programme’s Working Group on Coupled Modelling, which is responsible for CMIP, and we thank the climate modeling groups for producing and making available their model output. Support of the CMIP data sets is provided by the Office of Science, U.S. Department of Energy. C. Roedenbeck provided assistance with the TM3 model. P.K.P. is partially supported by the Ministry of Education, Culture, Sports, Science and Technology Green Network of Excellence program. G.W.S. acknowledges support from the NSF Graduate Research Fellowship Program and the Environmental Protection Agency’s Science to Achieve Results program.

Supplementary Materials

www.sciencemag.org/cgi/content/full/science.1239207/DC1
Materials and Methods
Figs. S1 to S9
Tables S1 to S7
References (57–81)

16 April 2013; accepted 17 July 2013
Published online 8 August 2013;
10.1126/science.1239207

Expanding the Fluorine Chemistry of Living Systems Using Engineered Polyketide Synthase Pathways

Mark C. Walker,^{1*} Benjamin W. Thuronyi,^{2*} Louise K. Charkoudian,^{3†} Brian Lowry,⁴ Chaitan Khosla,^{3,4,5} Michelle C. Y. Chang^{1,2‡}

Organofluorines represent a rapidly expanding proportion of molecules that are used in pharmaceuticals, diagnostics, agrochemicals, and materials. Despite the prevalence of fluorine in synthetic compounds, the known biological scope is limited to a single pathway that produces fluoroacetate. Here, we demonstrate that this pathway can be exploited as a source of fluorinated building blocks for introduction of fluorine into natural-product scaffolds. Specifically, we have constructed pathways involving two polyketide synthase systems, and we show that fluoroacetate can be used to incorporate fluorine into the polyketide backbone *in vitro*. We further show that fluorine can be inserted site-selectively and introduced into polyketide products *in vivo*. These results highlight the prospects for the production of complex fluorinated natural products using synthetic biology.

The catalytic diversity of biological systems provides enormous potential for application of living cells to the scalable produc-

tion of pharmaceuticals, fuels, and materials (1–4). However, the scope of innovation of living organisms is typically limited to functions that confer a direct advantage for cell growth, thereby maximizing biomass as the end product rather than a distinct molecule or reaction of interest. In contrast, synthetic biology approaches allow us to disconnect some of these biochemical transformations from cell survival and reconnect them in different ways for the targeted synthesis of alternative classes of compounds. One particularly interesting area of opportunity is the development of methods to introduce fluorine into complex small-molecule scaffolds, which has become a

powerful strategy for the design of synthetic pharmaceuticals. Estimates indicate that 20 to 30% of drugs, including many of the top sellers, contain at least one fluorine atom (5–7). Recent innovations have expanded the scope of synthetic C–F bond-forming methodologies, but the unusual elemental properties of fluorine that serve as the basis for its success also continue to restrict the range of molecular structures that can be accessed (8–11). As such, the invention of alternative routes for the site-selective introduction of fluorine into structurally diverse molecules, particularly under mild conditions, remains an outstanding challenge.

In comparison to synthetic small molecules, fluorine has limited distribution in naturally occurring organic compounds; the only organofluorine natural products characterized to date consist of a small set of simple molecules associated with the fluoroacetate pathway of *Streptomyces cattleya*, a soil bacterium that has the ability to catalyze the formation of C–F bonds from aqueous fluoride (Fig. 1A) (12, 13). Although these compounds lack the intricacy typically expected of secondary metabolites, they represent a potentially rich source of modular organofluorine building blocks for the production of complex fluorinated natural products. In this regard, the backbones of several large classes of medicinally relevant natural products—including polyketides, isoprenoids, steroids, alkaloids, eicosanoids, leukotrienes, and others—are biosynthesized directly from the assembly and tailoring of simple acetate units (Fig. 1A). Introduction of the fluoroacetate monomer in place of acetate would allow us to incorporate fluorine into the backbone of these targets and create new molecular function by combining the medicinal

¹Department of Molecular and Cell Biology, University of California, Berkeley, Berkeley, CA 94720–1460, USA. ²Department of Chemistry, University of California, Berkeley, Berkeley, CA 94720–1460, USA. ³Department of Chemistry, Stanford University, Stanford, CA 94305, USA. ⁴Department of Chemical Engineering, Stanford University, Stanford, CA 94305, USA. ⁵Department of Biochemistry, Stanford University, Stanford, CA 94305, USA.

*These authors contributed equally to this work.

†Present address: Department of Chemistry, Haverford College, Haverford, PA 19041, USA.

‡Corresponding author. E-mail: mcchang@berkeley.edu

chemistry advantages of fluorine with the structural complexity and bioactivity of natural products. For example, the introduction of fluorine via synthetic or semisynthetic routes has enabled the improvement of the clinical properties of several natural products, but this remains challenging to achieve (14–17). Although previous studies have shown that distal fluorine substituents can be accommodated in natural-product biosynthetic pathways (18, 19), access to fluoromalonyl-coenzyme A (CoA), a fluorinated analog of one of nature's most powerful carbon nucleophiles, as an extender unit would enable a general method for direct incorporation of fluorine into any polyketide structure.

Many acetate-based natural products, polyketides in particular, are generated through the iterative condensation of activated thioesters, resulting in reactive β -keto units that condense further to produce a wide range of structures (20, 21) (Fig. 1B). The structural diversity of polyketides is especially notable given that the majority of polyketides draw on only two monomers, acetate and propionate, as the extender units that form their carbon skeletons (3, 20, 22). Although polyketide synthases (PKSs) have been observed

to be accommodating with regard to their starter units (23), the encoding of extender units has been found to be quite selective, and many cellular acyl-CoAs are excluded from the backbone (22). However, progress in engineering extender-unit incorporation has been made by domain engineering (23–25) or incorporation via a domain that encodes a rare extender unit (17, 26). Although fluoroacetate serves as a starter unit in nature to produce highly toxic ω -fluoro fatty acids (Fig. 1A) (13), fluorine has never been observed to date within the backbone, implying that chain-extension reactions with the fluorinated acyl-CoA do not occur in these systems. The apparent inability of living systems to use fluoroacetate for the biosynthesis of complex small molecules probably results in part from the extreme properties of fluorine that affect biological and chemical synthesis. For example, the pK_a (where K_a is the acid dissociation constant) of the α proton, electrophilicity of the carbonyl group, and the stability of the acyl-CoA and its corresponding carbanion are all highly affected by fluorine substitution. Furthermore, the fluoroacetyl group bears a clear similarity to the fluoromethylketone motif used for the design of covalent inhibitors, suggesting

that the irreversible alkylation of active-site nucleophiles could also create problems (27). Thus, the development of a system to incorporate fluorinated extender units could dramatically increase the range of complex structures that can be accessed but must also address the challenges in activating the fluoroacetate monomer for the downstream C–C bond-forming chemistry involved in chain-extension reactions.

Chain elongation in polyketides and related fatty acid-based natural products relies on a separate pool of extender units formed by carboxylation of acyl-CoAs at the α position. These malonyl-CoA derivatives are then used as masked enolates for C–C bond formation after decarboxylation. The fluorinated extender, fluoromalonyl-CoA, can be made through two routes: either (i) a two-step activation of the biogenic fluoroacetate or (ii) a direct ligation of CoA to fluoromalonate (Fig. 2). We reasoned that the acetate kinase (AckA)–phosphotransacetylase (Pta) pair would be effective at fluoroacetate activation, as mutations in this gene locus have been shown to lead to fluoroacetate resistance in *Escherichia coli* (28). The enzymes from *E. coli* were overexpressed and characterized biochemically, confirming that AckA

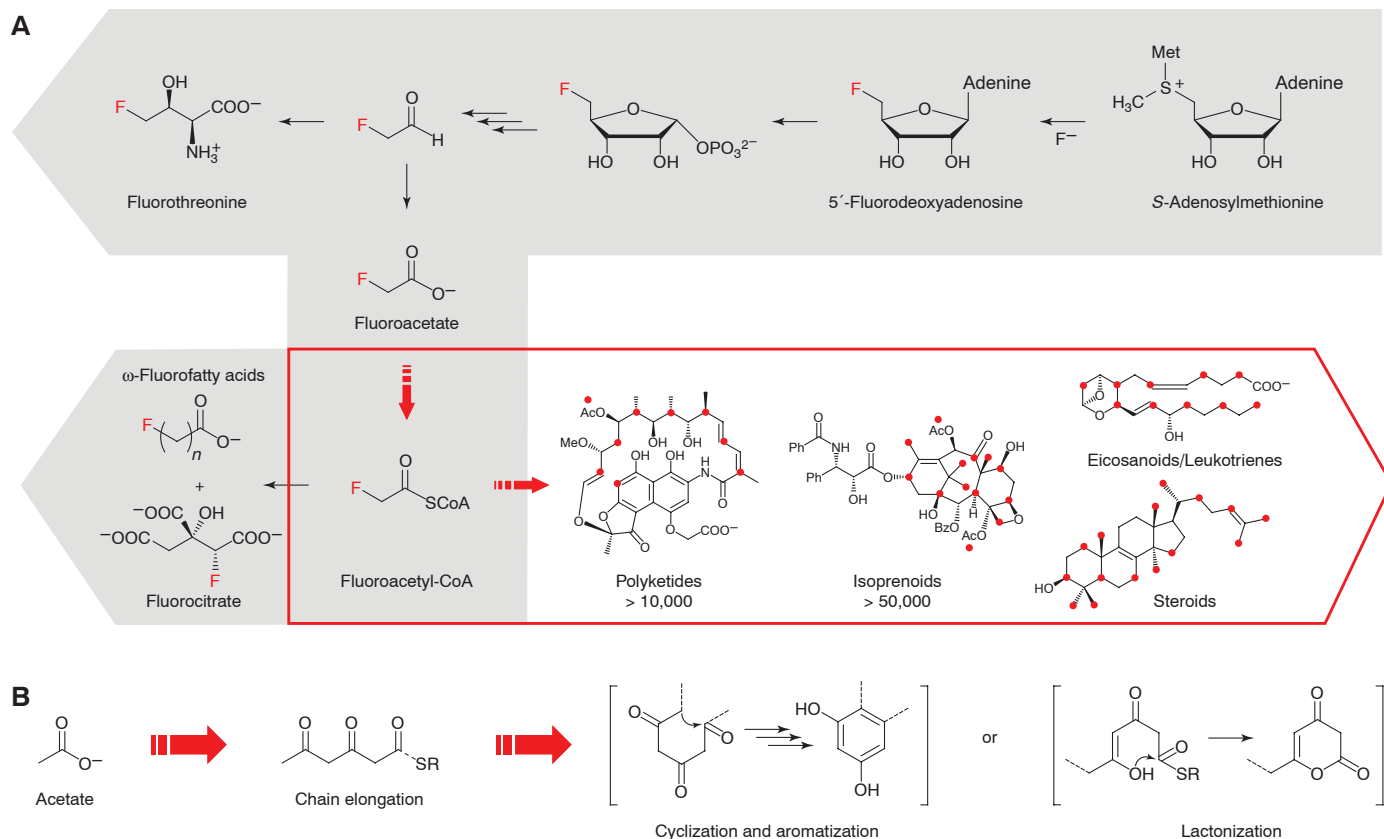


Fig. 1. Synthetic biology of fluorine. (A) The fluoroacetate pathway and its metabolites represent the known scope of biological fluorine chemistry, starting with fluoride and S-adenosylmethionine, to produce fluoroacetate and fluorothreonine as the end products (right to left, gray box). This scope could be greatly expanded by engineering downstream pathways to use fluoroacetate as a building block for site-selective introduction of fluorine into large families of natural products constructed

from acetate backbones (left to right, red box). Red dots represent positions that could, in principle, be fluorinated by incorporation of a fluoroacetate monomer without altering the carbon skeleton, including locations where fluorine would replace a methyl group derived from propionate or where downstream tailoring steps have occurred on the final structure. (B) Assembly of acetate units in the biosynthesis of polyketide natural products. R, CoA or PKS.

and Pta serve as an effective activation system to rapidly produce both acetyl- and fluoroacetyl-CoA in nearly quantitative yield (figs. S1 and S2). Analysis of the kinetic parameters for these enzymes with respect to fluorinated substrates indicated that neither appears to be affected by the fluorine substituent beyond inductive effects that alter the nucleophilicity of the carboxylic acid (AckA) or electrophilicity of the carbonyl (Pta) (29). Next, we purified the individual AccABCD subunits that make up the acetyl-CoA carboxylase (ACCase) from *E. coli* and added these enzymes to the AckA-Pta system to carry out the carboxylation of fluoroacetate in a one-pot reaction to generate the fluoromalonyl-CoA extender unit (Fig. 2A and fig. S1). Under these conditions, the ligation of CoA by AckA-Pta to produce the acyl-CoA is rapid, and production of the carboxylated product is limited by the ACCase. Although the rate of conversion is 4.5 times slower for fluoroacetate as compared with acetate, the overall extent of reaction is similar for both congeners, which suggests that covalent inactivation of the ACCase by fluoroacetyl-CoA is not important if it occurs. In addition to the route from fluoroacetate, we also tested a malonyl-CoA synthetase (MatB) (30) for coupling CoA directly to fluoromalonate. Although MatB exhibits a 10^3 -fold selectivity for malonate over fluoromalonate,

fluoromalonyl-CoA is still produced at reasonable efficiency (Fig. 2B and figs. S3 and S4). Both of these systems also provide in situ regeneration capacity that can amplify product yields from polyketide synthases, and we found that either system increased polyketide production by tetrahydronaphthalene synthase (31) compared with simple addition of malonyl-CoA (fig. S5).

We next turned our attention to the use of the fluoromalonyl-CoA monomer for downstream chain-elongation reactions. To start, we examined the behavior of a simple polyketide synthase system with regard to one cycle of chain extension and ketoreduction, which is a key functionality of larger multimodular systems for controlling downstream cyclization and rearrangements within the polyketide backbone (Fig. 3A) (3, 20). We constructed a synthetic gene encoding NphT7 (32), which appears to be a free-standing ketosynthase that is related at the structural level to the ketosynthase domain of more complex polyketide synthases (fig. S6), and we isolated the heterologously expressed enzyme for biochemical characterization (fig. S1). With the use of a coupled assay with an *R*-hydroxyl forming acetoacetyl-CoA reductase (PhaB), we found that NphT7 is competent to catalyze the formation of acetoacetyl-CoA, using an acetyl-CoA starter

and fluoromalonyl-CoA extender with only a five-fold defect in catalytic efficiency (k_{cat}/K_M , where k_{cat} is the turnover rate and K_M is the Michaelis constant) derived from a drop in k_{cat} with the fluorinated substrate (Fig. 3). This lower turnover rate observed with the fluorinated substrate is possibly related to the reduced reactivity of the enolate species, which would be stabilized by the fluorine substituent. However, the overall yield was comparable for both fluorinated and nonfluorinated substrates, which shows that a decarboxylative Claisen condensation with fluoromalonyl-CoA can take place at a similar extent of conversion compared to malonyl-CoA. Furthermore, these experiments also show that the 2-fluoro-3-keto motif produced with the fluoromalonyl-CoA extender can be accepted by ketoreductases, as PhaB is capable of efficiently reducing the acetoacetyl-CoA substrate (fig. S7). The ^1H and ^{19}F nuclear magnetic resonance (NMR) spectra of the reduced product indicate that both diastereomers are produced in this reaction (fig. S7), which may result from lack of stereochemical preference of NphT7 with respect to the fluorine substituent or from racemization of the product before reduction by PhaB. Although PhaB does not appear to show diastereoselectivity with respect to the fluorine group, the polyketide synthase ketoreductases are known to be selective with regard to their native α substituent and could potentially carry out the stereochemical resolution of the fluorine modification upon reduction (33).

With this information in hand, we sought to extend our biosynthetic method for fluorine introduction to more complex polyketide synthase systems, which use the chain-elongation reaction for the biosynthesis of many bioactive and clinically important natural products, such as erythromycin and rapamycin (3, 20). Of the multimodular polyketide systems, 6-deoxyerythronolide B synthase (DEBS) is probably the best understood and is responsible for production of the erythromycin precursor (34). We therefore focused our studies on the sixth module of DEBS, including the terminal thioesterase (DEBS_{Mod6}+TE) (35). Using a diketide substrate [natural diketide *N*-acetyl cysteine thioester (NDK-SNAC)], DEBS_{Mod6}+TE can catalyze a single round of chain elongation with its native methylmalonyl-CoA extender unit and then cyclize the tethered product to form a methyltriketide lactone (TKL) (Fig. 4A, R = CH₃; Fig. 4B, 1; and fig. S8) (36). We found that DEBS_{Mod6}+TE is also able to accept the fluorinated monomer in chain-extension catalysis to form the 2-fluoro-2-desmethyltriketide lactone (F-TKL) and incorporate fluorine into the polyketide backbone (Fig. 4B, 2 to 4; and fig. S9). The identity of the F-TKL was established by comparison to an authentic synthetic standard using reverse-phase liquid chromatography–mass spectrometry (LC-MS) monitored by electrospray ionization (ESI) and further confirmed by characterization of the isolated compound by high-resolution MS, gas chromatography–mass spectrometry, and ^{19}F NMR spectroscopy (figs. S10 to S13). Although the

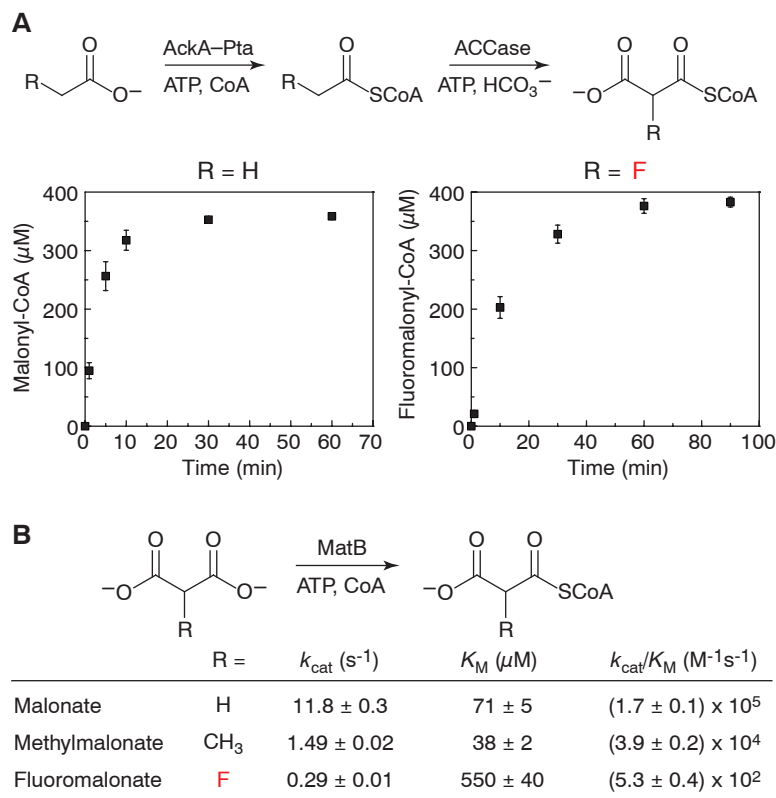


Fig. 2. Enzymatic production of activated extender units for C–C bond-formation reactions. (A) Formation of malonyl-CoA (left) and fluoromalonyl-CoA (right) from 500 μM CoA and either acetate or fluoroacetate, respectively. Values are reported as the mean ± SD ($n = 3$ replicates). **(B)** Kinetic parameters for malonate activation. Kinetic parameters are reported as mean ± SE ($n = 3$), as determined from nonlinear curve-fitting. Error in the k_{cat}/K_M parameter was obtained from propagation of error from the individual kinetic terms.

2S keto tautomer is generated in $\geq 94\%$ diastereomeric excess (figs. S12 and S13), this ratio appears to be set by the compound's stereoelectronic factors rather than the stereochemical preference of DEBS_{Mod6}+TE, as the F-TKL is fully enolized in aqueous solution. The F-TKL can also be produced directly from fluoroacetate using the AckA-Pta/ACCase activation system in either a multistage (Fig. 4B, 5 and 6) or single-pot reaction (Fig. 4B, 7 and 8) with DEBS_{Mod6}+TE in a similar yield to the MatB reaction, which allows us to connect fluorinated polyketide production directly to the biosynthetically available fluorinated building block (Fig. 1A and scheme S1).

In contrast to the chain-extension reaction catalyzed by NphT7, DEBS_{Mod6}+TE does not incorporate fluorinated extender units into the triketide lactone product as efficiently as its native methylmalonyl-CoA extender. Preliminary studies indicate that the reduced efficiency of DEBS_{Mod6}+TE with the fluorinated extender is not due to covalent inactivation of the enzyme (fig. S14), but rather to the more complex biochemistry of polyketide synthases with regard to monomer selection (37). Extender unit hydrolysis, which occurs even for the native substrate (table S2), appears to limit fluoromalonyl-CoA incorporation based on the observations that MatB and adenosine triphosphate (ATP) are needed for fluoromalonyl-CoA regeneration and that fluoromalonnate remains the major organofluorine species, even in their presence (fig. S15). The fluoromalonyl-CoA extender is, however, incorporated at higher efficiency by DEBS_{Mod6}+TE than malonyl-CoA (R = H), which is reported to be naturally excluded by DEBS (38). In fact, DEBS_{Mod6}+TE produces at least 10 times more F-TKL than H-TKL in a direct competition experiment with equimolar amounts (1 mM) of fluoromalonyl-CoA and malonyl-CoA (table S3).

To address the issue of site- or regioselective fluorine incorporation, we turned our attention to exploiting the greater reactivity of the fluorinated extender unit toward acylation reactions. In this regard, we hypothesized that it would be possible for a fluorinated substrate to selectively acylate either the acyltransferase (AT) or acyl carrier protein domains of individual DEBS modules in the presence of a catalytically compromised or inactive AT domain, an approach that has been shown to facilitate malonyl incorporation by DEBS (39). Experiments with DEBS_{Mod6}+TE showed that not only does F-TKL yield increase as expected, but fluorine selectivity also improves upon introduction of a key S2107A (Ser²¹⁰⁷→Ala²¹⁰⁷) mutation, reversing the selectivity of the wild-type module (Fig. 4C). When the NDK-SNAC substrate is used with its native module, DEBS_{Mod2}, in conjunction with the analogous S2652A mutation, extension with fluoromalonyl-CoA to form F-TKL reaches 30% efficiency compared with methylmalonyl-CoA (fig. S16). Furthermore, we found that the stand-alone trans-AT from the disorazole polyketide synthase (40, 41) accepts fluoromalonyl-CoA and can further en-

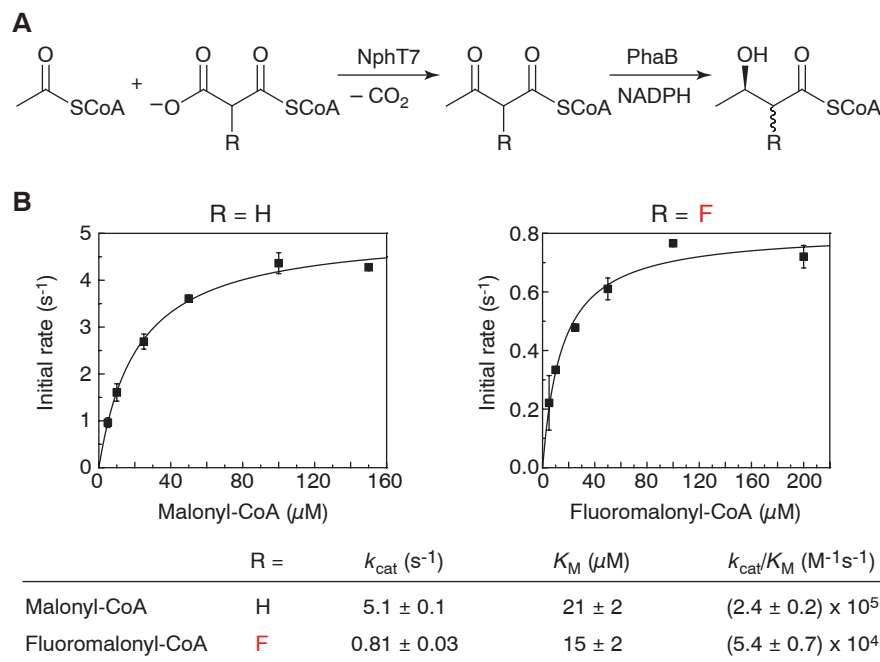


Fig. 3. A chain-extension and ketoreduction cycle with a fluorinated extender using a simple polyketide synthase, NphT7. (A) Reactions catalyzed by NphT7 and PhaB. NADPH, reduced form of nicotinamide adenine dinucleotide phosphate. **(B)** Steady-state kinetic parameters for NphT7-catalyzed C–C bond formation measured using a coupled assay with PhaB. Data points are reported as the mean \pm SD ($n = 3$). Kinetic parameters are reported as mean \pm SE ($n = 3$), as determined from nonlinear curve-fitting. Error in the k_{cat}/K_M parameter was obtained from propagation of error from the individual kinetic terms.

hance F-TKL formation by the AT-null mutant (Fig. 4C). Using this approach, we began to explore the possibility of site-selective fluorine incorporation with a mini-PKS model system, consisting of DEBS_{Mod2} and DEBS_{Mod3}+TE, that was designed to carry out two chain-extension reactions from the NDK-SNAC substrate (42). Using the appropriate AT-null constructs, we were able to observe exclusive production of either regioisomer of the fluoro-methyl tetraketide lactone (tetraKL). The identity of the 2-fluoro-4-methyl tetraKL and 2-methyl-4-fluoro tetraKL was established by both high-resolution ESI-MS and LC-MS on the basis of their different retention times, as well as their mass fragmentation patterns, which are consistent with the incorporation of fluorine at the expected sites (Fig. 4D and fig. S17). These studies also indicate that further chain extension after fluorine insertion can be achieved and that fluorinated intermediates could potentially be tolerated in downstream reactions. This observation is consistent with previous work that has shown that intermediates with non-native substituents, including fluorine, can be extended and tailored to the final structure (3, 17–20, 23) and gives promise that larger fluorinated polyketide targets may be accessible through this approach.

The observed selectivity for fluoromalonyl- over malonyl-CoA extender units suggests that polyketide chain-extension reactions with fluoromalonyl-CoA could possibly be catalyzed *in vivo* in *E. coli*, which contains a sizable malonyl-CoA pool (~ 35 μM

(43) but almost no methylmalonyl-CoA (44, 45). We carried out preliminary ¹⁹F-NMR studies of cells expressing MatB, NphT7, and PhaB and fed with nontoxic levels of fluoromalonnate. Analysis of the media and cell extracts indicated that flux through fluoromalonyl-CoA could reach 100 μM to 1 mM, which is sufficient for use by PKSs in live cells (table S4). Next, we tested the ability of DEBS_{Mod6}+TE to catalyze chain elongation in cell lysates prepared from *E. coli* BAP1 coexpressing DEBS_{Mod6}+TE and MatB. Under these conditions, F-TKL is produced with no observable H-TKL upon addition of only NDK-SNAC, fluoromalonnate, CoA, ATP, and the ATP regeneration system (fig. S18A). Negative controls with either no DEBS_{Mod6}+TE/MatB expressed or no NDK-SNAC substrate show no production of F-TKL (fig. S18A). These results demonstrate that the intracellular level of expression of the DEBS_{Mod6}+TE and MatB enzymes is sufficient for the incorporation of the fluorinated extender unit. They also further imply that fluorine could be introduced into the polyketide backbone inside living cells, which are capable of generating ATP through normal metabolic processes. Therefore, we cultured *E. coli* BAP1 coexpressing DEBS_{Mod6}+TE and MatB and harvested the cells after induction. These cells were then fed with the fluoromalonnate precursor, which resulted in the production of F-TKL upon addition of NDK-SNAC (Fig. 4B, 9; and fig. S18B). The identity of the F-TKL under these conditions was established by LC-MS, co-injection with an

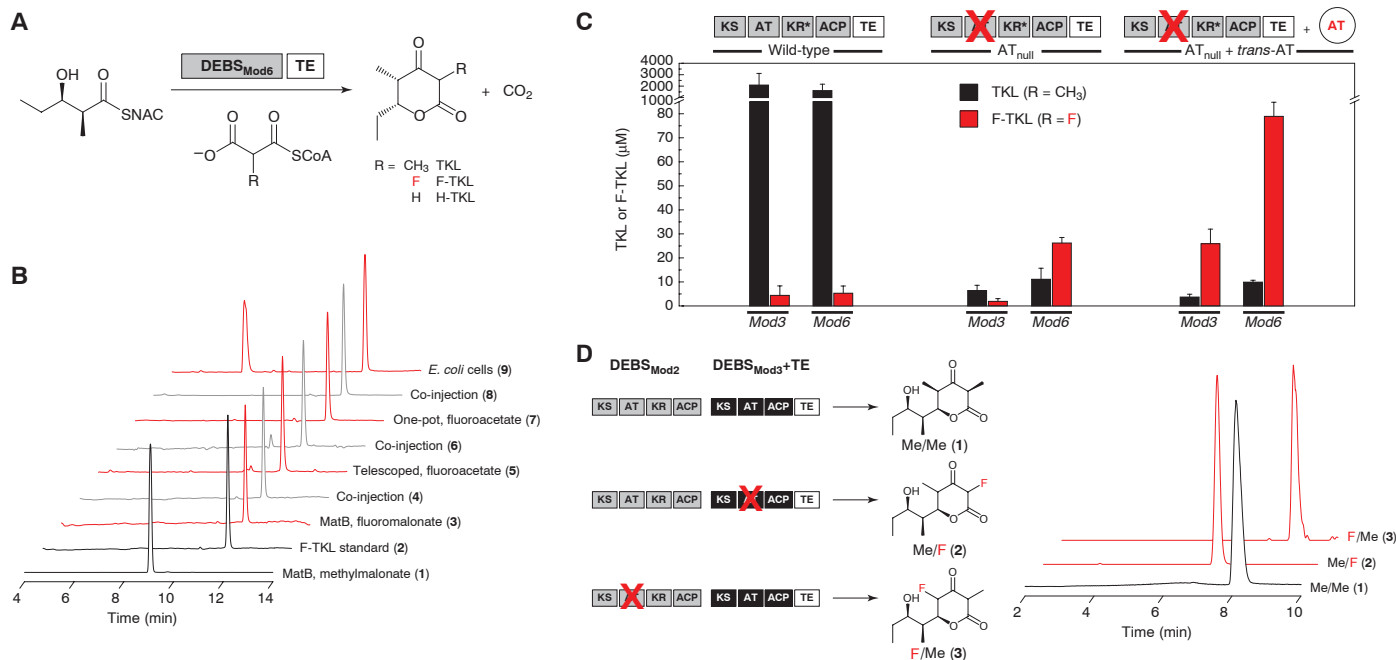


Fig. 4. Production of fluorinated polyketides in vitro and in vivo.

(A) Reaction catalyzed by DEBS_{Mod6}+TE using the NDK-SNAC substrate with various extender units (NDK-SNAC, (2S,3R)-2-methyl-3-hydroxypentanoyl-*N*-acetylcysteamine thioester). **(B)** Chain extension by DEBS_{Mod6}+TE to form triketide lactones monitored by LC-MS [TKL, mass/charge ratio (*m/z*) = 169; F-TKL, *m/z* = 173]. CoA, ATP, and ATP regeneration system are included in all in vitro reactions. Data are normalized with respect to the TKL peak. **(C)** Selectivity of DEBS_{Mod6}+TE and DEBS_{Mod3}+TE for the methylmalonyl-CoA versus fluoromalonyl-CoA extender unit, as monitored by TKL (*m/z* = 169) and F-TKL (*m/z* = 173) formation. Conditions include wild-type modules, AT⁰ modules, and AT⁰ modules in conjunction with the trans-AT from the disorazole PKS (DszaAT).

Values are reported as the mean ± SD (*n* = 3). KR* denotes that the KR domain of Mod3 is inactive. **(D)** LC-MS traces showing regioselective tetraketide lactone formation using the DEBS mini-PKS consisting of DEBS_{Mod2} and DEBS_{Mod3}+TE (Me/Me, 2-methyl-4-methyl-tetraketide lactone, *m/z* = 227; Me/F, 2-fluoro-4-methyl-tetraketide lactone, *m/z* = 231; F/Me, 2-methyl-4-fluoro-tetraketide lactone, *m/z* = 231). Me/Me was produced using DEBS_{Mod2}/DEBS_{Mod3}+TE and methylmalonate (1). Me/F was produced using DEBS_{Mod2}/DEBS_{Mod3}AT⁰+TE, DszaAT, methylmalonyl-CoA, and fluoromalonnate (2). F/Me was produced using DEBS_{Mod2}AT⁰/DEBS_{Mod3}+TE, methylmalonyl-CoA, and fluoromalonnate (3). Data are normalized with respect to the Me/Me peak. All reactions contained MatB and the ATP regeneration system.

authentic standard, as well as high-resolution MS. Moreover, F-TKL can also be produced directly in cell culture with the simple addition of a mixture of both substrates to the media after induction of DEBS_{Mod6}+TE and MatB (fig. S18C). Taken together, these studies show that the natural selectivity of the polyketide synthase allows for the site-selective introduction of fluorine over hydrogen into the polyketide backbone inside living cells.

Using engineered pathways to link simple biogenic organofluorine building blocks into more complex fluorinated small-molecule targets, we have demonstrated that we can expand the fluorine chemistry of living systems. Because of the modular nature of the biosynthetic pathways used to produce polyketides and related acetate-derived natural products, these findings open the door to general strategies for exploring the fluorine synthetic biology of complex natural products.

References and Notes

1. D. K. Ro *et al.*, *Nature* **440**, 940–943 (2006).
2. S. Atsumi, T. Hanai, J. C. Liao, *Nature* **451**, 86–89 (2008).
3. D. E. Cane, C. T. Walsh, C. Khosla, *Science* **282**, 63–68 (1998).
4. A. M. Weeks, M. C. Y. Chang, *Biochemistry* **50**, 5404–5418 (2011).
5. K. Müller, C. Faeh, F. Diederich, *Science* **317**, 1881–1886 (2007).

6. D. O'Hagan, *Chem. Soc. Rev.* **37**, 308–319 (2008).
7. T. Furuya, A. S. Kamlet, T. Ritter, *Nature* **473**, 470–477 (2011).
8. N. D. Ball, M. S. Sanford, *J. Am. Chem. Soc.* **131**, 3796–3797 (2009).
9. D. A. Watson *et al.*, *Science* **325**, 1661–1664 (2009).
10. V. Raunyar, A. D. Lackner, G. L. Hamilton, F. D. Toste, *Science* **334**, 1681–1684 (2011).
11. E. Lee *et al.*, *Science* **334**, 639–642 (2011).
12. C. Dong *et al.*, *Nature* **427**, 561–565 (2004).
13. D. O'Hagan, *J. Fluor. Chem.* **127**, 1479–1483 (2006).
14. A. Rivkin, K. Biswas, T.-C. Chou, S. J. Danishefsky, *Org. Lett.* **4**, 4081–4084 (2002).
15. J.-P. Bégue, D. Bonnet-Delpon, *J. Fluor. Chem.* **127**, 992–1012 (2006).
16. B. Llano-Sotelo *et al.*, *Antimicrob. Agents Chemother.* **54**, 4961–4970 (2010).
17. S. Mo *et al.*, *J. Am. Chem. Soc.* **133**, 976–985 (2011).
18. W. Rungphaphan, J. J. Mares, S. E. O'Connor, *Proc. Natl. Acad. Sci. U.S.A.* **106**, 13673–13678 (2009).
19. R. J. M. Goss *et al.*, *ChemBioChem* **11**, 698–702 (2010).
20. J. Staunton, K. J. Weissman, *Nat. Prod. Rep.* **18**, 380–416 (2001).
21. R. Croteau, T. M. Kutchan, N. G. Lewis, in *Biochemistry and Molecular Biology of Plants*, R. B. Buchanan, W. Gruissem, R. Jones, Eds. (American Society of Plant Biologists, Rockville, MD, 2000), pp. 1250–1318.
22. Y. A. Chan, A. M. Podelvels, B. M. Kevany, M. G. Thomas, *Nat. Prod. Rep.* **26**, 90–114 (2009).
23. R. McDaniel *et al.*, *Proc. Natl. Acad. Sci. U.S.A.* **96**, 1846–1851 (1999).
24. U. Sundermann *et al.*, *ACS Chem. Biol.* **8**, 443–450 (2013).
25. I. Koryakina, J. B. McArthur, M. M. Draelos, G. J. Williams, *Org. Biomol. Chem.* **11**, 4449–4458 (2013).
26. A. S. Eustáquio, D. O'Hagan, B. S. Moore, *J. Nat. Prod.* **73**, 378–382 (2010).
27. J. C. Powers, J. L. Asgarian, Ö. D. Ekici, K. E. James, *Chem. Rev.* **102**, 4639–4750 (2002).
28. T. D. K. Brown, M. C. Jones-Mortimer, H. L. Kornberg, *J. Gen. Microbiol.* **102**, 327–336 (1977).
29. M. C. Walker, M. Wen, A. M. Weeks, M. C. Y. Chang, *ACS Chem. Biol.* **7**, 1576–1585 (2012).
30. A. J. Hughes, A. Keatinge-Clay, *Chem. Biol.* **18**, 165–176 (2011).
31. M. Izumikawa *et al.*, *J. Ind. Microbiol. Biotechnol.* **30**, 510–515 (2003).
32. E. Okamura, T. Tomita, R. Sawa, M. Nishiyama, T. Kuzuyama, *Proc. Natl. Acad. Sci. U.S.A.* **107**, 11265–11270 (2010).
33. A. P. Siskos *et al.*, *Chem. Biol.* **12**, 1145–1153 (2005).
34. C. Khosla, Y. Tang, A. Y. Chen, N. A. Schnarr, D. E. Cane, *Annu. Rev. Biochem.* **76**, 195–221 (2007).
35. R. S. Gokhale, S. Y. Tsuji, D. E. Cane, C. Khosla, *Science* **284**, 482–485 (1999).
36. N. Wu, F. Kudo, D. E. Cane, C. Khosla, *J. Am. Chem. Soc.* **122**, 4847–4852 (2000).
37. S. A. Bonnett *et al.*, *Chem. Biol.* **18**, 1075–1081 (2011).
38. G. F. Liou, J. Lau, D. E. Cane, C. Khosla, *Biochemistry* **42**, 200–207 (2003).
39. P. Kumar, A. T. Koppisch, D. E. Cane, C. Khosla, *J. Am. Chem. Soc.* **125**, 14307–14312 (2003).
40. F. T. Wong, A. Y. Chen, D. E. Cane, C. Khosla, *Biochemistry* **49**, 95–102 (2010).
41. F. T. Wong, X. Jin, I. I. Mathews, D. E. Cane, C. Khosla, *Biochemistry* **50**, 6539–6548 (2011).
42. S. Y. Tsuji, D. E. Cane, C. Khosla, *Biochemistry* **40**, 2326–2331 (2001).

43. B. D. Bennett *et al.*, *Nat. Chem. Biol.* **5**, 593–599 (2009).
 44. T. Haller, T. Buckel, J. Rétey, J. A. Gerlt, *Biochemistry* **39**, 4622–4629 (2000).
 45. B. A. Pfeifer, S. J. Admiraal, H. Gramajo, D. E. Cane, C. Khosla, *Science* **291**, 1790–1792 (2001).

Acknowledgments: We thank B. Bond-Watts and I. Aanei for assembly and cloning of the synthetic *nph77* gene, X. Yu for providing plasmids for the *E. coli* ACCase, C. Harvey for synthetic chemistry assistance, F. T. Wong for helpful discussions, and A. Lingel (Novartis) for QCI-F CryoProbe use.

The College of Chemistry NMR Facility at the University of California, Berkeley (UC Berkeley) is supported in part by the NIH (grants 1510R023679-01 and S10 RR16634-01). M.C.W. and B.W.T. acknowledge the support of a NIH National Research Service Award Training Grant (1 T32 GM066698) and the Gerald K. Branch Predoctoral Fellowship and UC Cancer Research Council Committee Predoctoral Fellowship (to B.W.T.). L.K.C. acknowledges support from the National Cancer Institute (grant F32 CA137994). This work was funded by generous support from UC Berkeley and the NIH (grant 1 DP2 OD008696 to M.C.Y.C. and grant R01 GM087934 to C.K.).

Supplementary Materials

www.sciencemag.org/cgi/content/full/341/6150/1089/DC1
 Materials and Methods
 Figs. S1 to S18
 Tables S1 to S4
 Scheme S1
 References (46–60)

24 June 2013; accepted 5 August 2013
 10.1126/science.1242345

Observation of Partial Wave Resonances in Low-Energy O₂–H₂ Inelastic Collisions

Simon Chefdeville,^{1,2} Yulia Kalugina,^{3,4} Sebastiaan Y. T. van de Meerakker,⁵ Christian Naulin,^{1,2} François Lique,^{3*} Michel Costes^{1,2*}

Partial wave resonances predicted to occur in bimolecular collision processes have proven challenging to observe experimentally. Here, we report crossed-beam experiments and quantum-scattering calculations on inelastic collisions between ground-state O₂ and H₂ molecules that provide state-to-state cross sections for rotational excitation of O₂ (rotational state $N = 1, j = 0$) to O₂ ($N = 1, j = 1$) in the vicinity of the thermodynamic threshold at 3.96 centimeter⁻¹. The close agreement between experimental and theoretical results confirms the classically forbidden character of this collision-induced transition, which occurs exclusively in a purely quantum mechanical regime via shape and Feshbach resonances arising from partial waves with total angular momentum (J) = 2 to 4.

The accurate description of collisions between individual molecules remains a long-standing goal in physical chemistry. In a classical picture, the outcome of a collision is determined by the interaction potential and initial conditions such as relative velocity and impact parameter, that is, the distance of closest approach between the molecules in the absence of any interaction. Surely, molecules are quantum objects in nature, and the collisions must be described in terms of interfering quantum-scattering states, or partial waves, instead. Each partial wave is the quantum mechanical analog of a classical trajectory with a given impact parameter and is characterized by a definite value of total angular momentum, J , which is conserved throughout the collision (*1*).

The contribution of individual partial waves to the scattering cross sections constitutes the ultimate information that can be obtained about a collision event. Whereas molecular scattering processes are nowadays described successfully by quantum mechanical methods throughout, the direct observation of individual partial waves in

molecular collision experiments remains highly challenging. In fact, partial waves can only be distinguished when giving rise to scattering resonances that manifest as resolved peaks in differential or integral cross sections (DCSs and ICSs) as measured in crossed-beam experiments. Such very rare findings then provide a unique insight in the most critical part of the potential energy surface (PES), the transition state region (*2*). However, in most cases, the collision energy spread and the participation of many overlapping partial waves corresponding to the energetically allowed values of J tend to average the individual resonance signatures and still render them elusive to experimental observation.

Partial wave resonances were first observed for a few elastic collisions that involve simple atoms (3–5) and then for the F + HD → HF + D system. In this textbook three-atom reaction, the resonances could be identified by comparison of experimentally determined cross sections with the outcome of high-level electronic structure and quantum-scattering calculations. A clear oscillatory structure assigned to $J = 12$ to 14 partial waves appears in the collision energy dependence of the state and angle-resolved DCS (*6*), whereas a steplike feature characterizes the resonance behavior of the total ICS (*7*). More recently, resonance structures have been revealed in total ICSs for Penning ionization reactions of metastable He with H₂ or Ar in the cold regime (*8*) and in state-to-state ICSs for low-energy inelastic scattering of CO with H₂ (*9*). Yet, the identification of the contributing partial waves suffered from

imperfect agreement with theory in the latter studies. Here, we report a joint experimental and theoretical study on O₂–H₂ inelastic collisions for O₂ ($N = 1, j = 0 \rightarrow N = 1, j = 1$) rotational excitation, a transition which violates the semi-classical propensity rules for rotational energy transfer involving a molecule in a ³Σ state (*10*). The results demonstrate the purely quantum mechanical nature of the process and offer a complete characterization of fully resolved partial wave resonances with close agreement between theory and experiment.

We performed our experiments with a crossed-beam apparatus, which allowed us to tune the collision energy (the relative translational energy of colliding partners with reduced mass μ and relative velocity v_r) by varying the beam intersection angle, χ , between 12.5° and 90°: $E_T = \frac{1}{2}\mu v_r^2 = \frac{1}{2}\mu(v_{O_2}^2 + v_{H_2}^2 - 2v_{O_2}v_{H_2}\cos\chi)$ (*9, 11*). H₂ and O₂ beams with low and matched velocities and high velocity resolution and quantum state purity were obtained by using cryogenically cooled Even-Lavie fast-pulsed valves (*12*) [see table S1 (*13*)]. Neat beams of *para*-H₂ and *normal*-H₂ were used and were characterized in the crossing region by 3 + 1 resonance-enhanced multiphoton ionization (REMPI) time-of-flight mass spectrometry using three-photon (C¹Π_u, $v = 0 \leftarrow X^1\Sigma_g^+$, $v = 0$) *R* branch transitions near 99,150 cm⁻¹ (*14*). Populations >95% for $j = 0$ and <5% for $j = 1$ were deduced when using freshly prepared samples of *para*-H₂ and 25% $j = 0$, 75% $j = 1$ when using *normal*-H₂. The O₂ beam (0.3% O₂ in He) was probed by using 2 + 1 (³Σ₀⁻, $v = 2 \leftarrow X^3\Sigma_g^-$, $v = 0$) and (³Σ₁⁻, $v = 2 \leftarrow X^3\Sigma_g^-$, $v = 0$) REMPI transitions around 88,900 cm⁻¹ (*15*). The relative populations of the three fine-structure components of ground rotational state $N = 1$ were estimated to be >85% in $j = 0$, <15% in $j = 2$ at $E_{1,2} = 2.08$ cm⁻¹, and <0.5% in $j = 1$ at $E_{1,1} = 3.96$ cm⁻¹, whereas those of first excited rotational state $N = 3$ were negligible (*13*). Cross-section measurements attributed to $N = 1, j = 0 \rightarrow N = 1, j = 1$ rotational energy transfer were performed by probing the collision-induced population in the $N = 1, j = 1$ level as a function of the crossing angle. The initial residual population in $N = 1, j = 1$ level was offset by shot-to-shot background subtraction when triggering the probe laser and the O₂ beam at 10 Hz with the H₂ beam at 5 Hz. The integral cross sections for O₂–*para*-H₂ collisions between $E_T = 3.7$ cm⁻¹ and 20 cm⁻¹ are displayed in Figs. 1A and 2. Those for O₂–*normal*-H₂ collisions are shown in Fig. 2. The excitation function displays well-

¹Université de Bordeaux, Institut des Sciences Moléculaires, 33400 Talence, France. ²CNRS, UMR 5255, 33400 Talence, France. ³Laboratoire Ondes et Milieux Complexes, UMR 6294 CNRS–Université du Havre, 25 rue Philippe Lebon, BP 540, 76058 Le Havre, France. ⁴Department of Optics and Spectroscopy, Tomsk State University, 36 Lenin av., Tomsk 634050, Russia. ⁵Radboud University Nijmegen, Institute for Molecules and Materials, Heijendaalseweg 135, 6525 AJ Nijmegen, Netherlands.

*Corresponding author. E-mail: michel.costes@u-bordeaux1.fr (M.C.); francois.lique@univ-lehavre.fr (F.L.)

resolved peaks (a, b, and c), with no observable difference for the collision partners *para*-H₂ or *normal*-H₂. The excitation function also appears unusual for a molecular collision process. The O₂ ($N = 1, j = 0 \rightarrow N = 1, j = 1$) transition violates the propensity rules in rotationally inelastic collisions of diatomic molecules in $^3\Sigma$ electronic states (10). Thus, normal scattering cannot occur. Scattering can only arise from resonances, and the three observed peaks are proof of this resonance behavior.

To gain insight into the resonance structure, we performed full quantum close-coupling scattering calculations by using a four-dimensional ab initio PES treating O₂ and H₂ as rigid rotors, which had been recently obtained by the coupled cluster method while using single and double excitation with perturbative contributions from connected triple excitations and large sets of atomic basis orbitals (16). Because the well depth of the PES strongly affects the energy, width, and intensity of the scattering resonances, we performed additional electronic structure calculations at a higher level of theory to obtain a better

description of this critical parameter (fig. S1) (13). We estimated that 5% of the interaction energy was missing in the potential well. Therefore, we scaled the global PES by a factor of 1.05. A previous theoretical study on O₂-H₂ inelastic scattering neglecting the fine structure showed that rotation of H₂ has almost no influence on the magnitude of the cross sections, including the resonances (16). We thus restricted the calculations to the $j = 0$ level of H₂ (i.e., the PES was averaged over H₂ rotations), considering that our results should also be valid for H₂ ($j = 1$). For the scattering calculations, we solved the quantal coupled equations in the intermediate coupling scheme by using the MOLSCAT code (17) modified to take into account the fine structure of the O₂ energy levels (18, 19). Cross sections were obtained up to $E_T = 50 \text{ cm}^{-1}$ on a 0.05-cm^{-1} grid. The results are presented in Fig. 1B for partial waves $J = 1$ to 7, which contribute at the collision energies sampled in the experiment. The theoretical ICSs convoluted with the experimental collision energy spread are also reported in Fig. 1A.

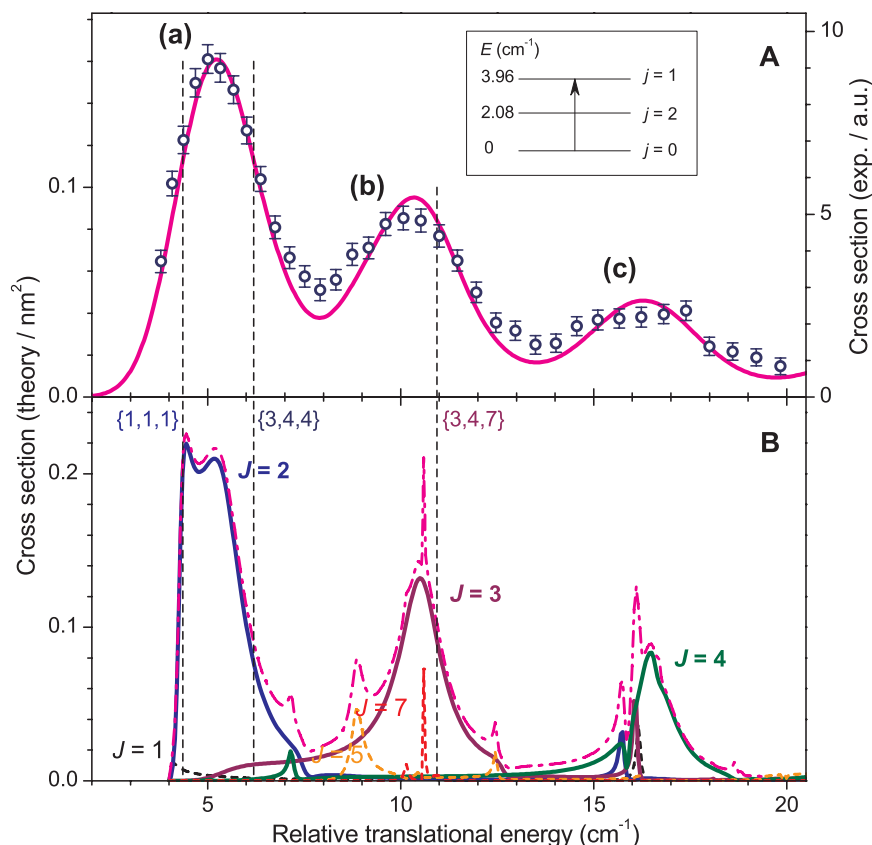


Fig. 1. Collisional energy dependence of the integral cross sections for O₂ excitation ($N = 1, j = 0 \rightarrow N = 1, j = 1$). (A) Experimental data with *para*-H₂ (open circles, with error bars representing the statistical uncertainties at 95% of the confidence interval). Each point corresponds to 40 consecutive scans of the beam intersection angle acquired between 30° and 12.5° with -0.5° decrement and 100 laser shots per angle; theoretical ICSs were convoluted with the experimental collision energy spread (solid line). (Inset) Energy-level diagram and excitation scheme of O₂ in the $N = 1$ state. (B) Theoretical results: partial waves $J = 2, 3$, and 4 (solid lines); partial waves $J = 1$ and $J = 5$ to 7 (dashed lines); integral cross section (dashed-dotted line). Positions of the bound and quasi-bound states (see Fig. 3) labeled with their quantum numbers $\{N, j, l\}$ (see text) are shown by vertical dashed lines. a.u., arbitrary units.

The agreement between experiment and theory in Fig. 1 is very good. The convoluted theoretical curve reproduces well the position and width of the three experimental peaks. The experimental excitation function falls almost to zero at $E_T = 20 \text{ cm}^{-1}$, which indicates a negligible contribution of collision energy transfer in the final observed state $N = 1, j = 1$ from $N = 1, j = 2$ residual population in the O₂ beam (see also fig. S2) (13). Furthermore, Fig. 2 demonstrates that inelastic scattering with H₂ ($j = 1$) behaves the same as with H₂ ($j = 0$), which justifies the theoretical assumption made (vide supra).

A comparison of experimental and theoretical data shows that each peak in the experimental excitation function corresponds to an almost pure partial wave: peak a to $J = 2$, peak b to $J = 3$, and peak c to $J = 4$. The contributions from partial waves $J = 1$ and $J > 4$ and the overlaps between $J = 2, 3$, and 4 remain marginal. To gain insight into the nature of the peaks, we calculated adiabatic-bender potentials (20) and searched for all van der Waals stretch levels supported by these curves (21). The levels are labeled as N, j , and l , where l is the orbital angular momentum. Figure 3 shows the $J = 2$ potential curve, which correlates with O₂ ($N = 1, j = 1$) + H₂ ($j = 0$). This curve supports one quasi-bound state at $E_{1,1,2} = 4.36 \text{ cm}^{-1}$, slightly above the asymptotic value at $E_{1,1} = 3.96 \text{ cm}^{-1}$ but trapped below the centrifugal barrier. Tunneling through the barrier thus gives rise to a shape (or orbiting) resonance (5, 22). Another $J = 2$ curve, which correlates with the asymptotically closed channel O₂ ($N = 3, j = 4$) + H₂ ($j = 0$) at $E_{3,4} = 16.39 \text{ cm}^{-1}$, furnishes a different scenario. The O₂-H₂ complexes are temporally trapped in the bound state at $E_{3,4,4} = 6.19 \text{ cm}^{-1}$ before dissociating to O₂ ($N = 1, j = 1$) + H₂ ($j = 0$), yielding a Feshbach resonance (23). Therefore peak a can be regarded as the juxtaposition of a shape

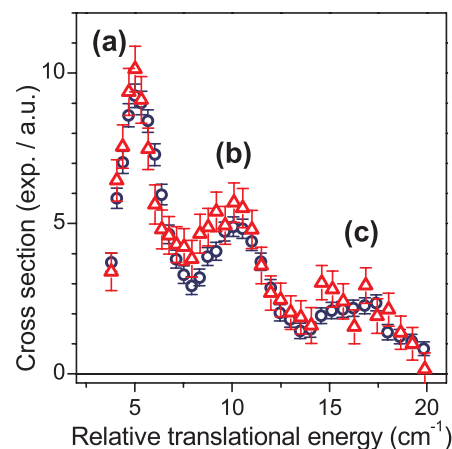


Fig. 2. Collisional energy dependence of the integral cross sections for O₂ excitation ($N = 1, j = 0 \rightarrow N = 1, j = 1$). Experimental data with *para*-H₂ (open circles, data of Fig. 1A) and *normal*-H₂ (open triangles). Error bars and scan parameters for *normal*-H₂ as defined in Fig. 1A but with 29 consecutive scans of the beam intersection angle.

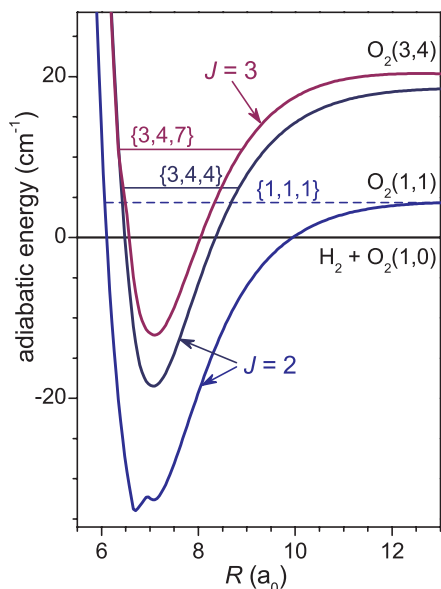


Fig. 3. Adiabatic bend curves with total angular momentum $J = 2$ and 3 that correlate with O_2 states $(N, j) = (1, 1)$ and $(3, 4)$. Quasi-bound states below (solid lines) or above (dashed lines) the dissociation limit are labeled with their quantum numbers $\{N, j, l\}$ (see text).

resonance in its rising edge and a Feshbach resonance in its falling edge. The $J = 3$ curve, which correlates with the O_2 ($N = 3, j = 4$) + H_2 ($j = 0$) closed channel, supports a bound state at $E_{3,4,7} = 10.94 \text{ cm}^{-1}$ in good agreement with the center of peak b. Peak b is thus a pure Feshbach resonance. Analysis of $J = 4$ is less straightforward, because adiabatic-bender potentials correlating with O_2 ($N = 3, j = 2, 3, 4$) + H_2 ($j = 0$) closed channels at $E_{3,2} = 16.25 \text{ cm}^{-1}$, $E_{3,3} = 18.34 \text{ cm}^{-1}$,

and $E_{3,4} = 16.39 \text{ cm}^{-1}$ are found to support six bound and quasi-bound states situated between 15.3 and 17.1 cm^{-1} (fig. S3). Peak c is a composite of Feshbach resonances.

Our results highlight the purely quantum mechanical nature of this inelastic collision process. None of the partial waves exhibits a long tail, which would indicate nonresonant rotational energy transfer. Successful O_2 ($N = 1, j = 0 \rightarrow N = 1, j = 1$) excitation exclusively occurs via shape and Feshbach resonances. Our results also validate the PES, which can now be used with confidence to calculate precise fine-structure resolved low-temperature rate coefficients for rotational (de-)excitation of O_2 ($X^3\Sigma_g^-$) by H_2 . This regime is of particular importance for astrophysics because, in the interstellar medium, O_2 rotational level populations result both from radiative transitions and from inelastic collisions with overwhelmingly abundant H_2 . Evaluation of O_2 abundance from spectral line data (24) requires the accurate knowledge of these rate coefficients.

References and Notes

1. R. D. Levine, R. B. Bernstein, *Molecular Reaction Dynamics and Chemical Reactivity* (Oxford Univ. Press, Oxford, 1987).
2. G. C. Schatz, *Science* **288**, 1599–1600 (2000).
3. A. Schutte, D. Bassi, F. Tommasini, G. Scoles, *Phys. Rev. Lett.* **29**, 979–982 (1972).
4. R. S. Grace, D. L. Johnson, J. G. Skofronick, *J. Chem. Phys.* **67**, 2443 (1977).
5. J. P. Toennies, W. Welz, G. Wolf, *J. Chem. Phys.* **71**, 614 (1979).
6. W. Dong *et al.*, *Science* **327**, 1501–1502 (2010).
7. R. T. Skodje *et al.*, *Phys. Rev. Lett.* **85**, 1206–1209 (2000).
8. A. B. Henson, S. Gersten, Y. Shagam, J. Narevicius, E. Narevicius, *Science* **338**, 234–238 (2012).
9. S. Chefdeville *et al.*, *Phys. Rev. Lett.* **109**, 023201 (2012).
10. M. H. Alexander, P. J. Dagdigan, *J. Chem. Phys.* **79**, 302 (1983).
11. M. Lara *et al.*, *Phys. Rev. Lett.* **109**, 133201 (2012).
12. D. Pentleher *et al.*, *Rev. Sci. Instrum.* **80**, 043302 (2009).
13. Materials and methods are detailed in the supplementary materials on Science Online.
14. S. T. Pratt, P. M. Dehmer, J. L. Dehmer, *Chem. Phys. Lett.* **105**, 28–33 (1984).
15. R. J. Yokelson, R. J. Lipert, W. A. Chupka, *J. Chem. Phys.* **97**, 6153 (1992).
16. Y. Kalugina, O. D. Alpizar, T. Stoecklin, F. Lique, *Phys. Chem. Chem. Phys.* **14**, 16458–16466 (2012).
17. J. M. Hutson, S. Green, MOLSCAT computer code, version 14, 1994, distributed by Collaborative Computational Project No. 6 of the Engineering and Physical Sciences Research Council (UK).
18. F. Lique, M.-L. Senent, A. Spielfiedel, N. Feautrier, *J. Chem. Phys.* **126**, 164312 (2007).
19. F. Lique, *J. Chem. Phys.* **132**, 044311 (2010).
20. M. H. Alexander, S. Gregurick, P. J. Dagdigan, *J. Chem. Phys.* **101**, 2887 (1994).
21. D. T. Colbert, W. H. Miller, *J. Chem. Phys.* **96**, 1982 (1992).
22. D. W. Chandler, *J. Chem. Phys.* **132**, 110901 (2010).
23. H. Feshbach, *Ann. Phys.* **5**, 357–390 (1958).
24. B. Larsson *et al.*, *Astron. Astrophys.* **466**, 999–1003 (2007).

Acknowledgments: This work extends the objectives of ANR-12-BS05-0011-02 contract with the Agence Nationale de la Recherche and contract 2007.1221 with the Conseil Régional d'Aquitaine, for which financial support is gratefully acknowledged. S.C., S.Y.T.v.d.M., C.N., and M.C. acknowledge support of Partenariat Hubert Curien Van Gogh 2013–28484TH contract. S.Y.T.v.d.M. acknowledges support from the Netherlands Organisation for Scientific Research (NWO) via a VIDI grant and from the Université de Bordeaux for a visiting professorship. Y.K. acknowledges the support of High Performance Computing SKIF-Cyberia (Tomsk State University). Y.K. and F.L. acknowledge the financial support of the CNRS national program Physique et Chimie du Milieu Interstellaire and of the Contrat de Projets Etat-Région Haute-Normandie/Centre National de Recherche Technologique/Energie, Electronique, Matériaux.

Supplementary Materials

www.sciencemag.org/cgi/content/full/341/6150/1094/DC1
Materials and Methods
Figs. S1 to S3
Table S1
References (25–33)

3 June 2013; accepted 18 July 2013
10.1126/science.1241395

Direct Determination of Absolute Molecular Stereochemistry in Gas Phase by Coulomb Explosion Imaging

Martin Pitzer,¹ Maksim Kunitski,¹ Allan S. Johnson,^{1,2} Till Jahnke,¹ Hendrik Sann,¹ Felix Sturm,¹ Lothar Ph. H. Schmidt,¹ Horst Schmidt-Böcking,¹ Reinhard Dörner,¹ Jürgen Stohner,³ Julia Kiedrowski,⁴ Michael Reggelin,⁴ Sebastian Marquardt,⁴ Alexander Schießer,⁴ Robert Berger,^{4,*} Markus S. Schöffler^{1*}

Bijvoet's method, which makes use of anomalous x-ray diffraction or dispersion, is the standard means of directly determining the absolute (stereochemical) configuration of molecules, but it requires crystalline samples and often proves challenging in structures exclusively comprising light atoms. Herein, we demonstrate a mass spectrometry approach that directly images the absolute configuration of individual molecules in the gas phase by cold target recoil ion momentum spectroscopy after laser ionization-induced Coulomb explosion. This technique is applied to the prototypical chiral molecule bromochlorofluoromethane and the isotopically chiral methane derivative bromodichloromethane.

A molecule that cannot be superposed with its mirror image by pure translation and rotation is termed chiral, with the non-

identical mirror images called enantiomers. If it were not for the predicted tiny contributions due to parity-violating weak interactions (I), which

are currently searched for in high-precision molecular physics experiments on chiral molecules (2, 3), the energy levels of both enantiomers would be equal. The enantiomers can be distinguished by their interaction with other chiral objects; for instance, left- or right-handed molecules and left- or right-handed circularly polarized photons. The interaction with polarized light led Louis Pasteur, more than one and a half centuries ago, to the discovery of molecular chirality by observing optical rotation in aqueous solutions of manually separated enantiomorphic crystals from double salts of tartaric acid (4). van't Hoff (5) and Le Bel (6) independently ascribed Pasteur's

¹Institute for Nuclear Physics, Johann Wolfgang Goethe-Universität Frankfurt, Max-von-Laue-Straße 1, 60438 Frankfurt, Germany. ²University of Ottawa, Ottawa, ON K1N 6N5, Canada.

³Institute of Chemistry and Biological Chemistry, Zurich University of Applied Sciences, Campus Reidbach, Einsiedlerstrasse 31, 8820 Wädenswil, Switzerland. ⁴Clemens-Schöpf Institute, Technische Universität Darmstadt, Petersenstraße 22, 64287 Darmstadt, Germany.

*Corresponding author. E-mail: schoeffler@atom.uni-frankfurt.de (M.S.S.); robert.berger@tu-darmstadt.de (R.B.)

observation to an underlying three-dimensional (3D) structure of molecules, which can result in two nonidentical mirror image structures.

Enantiomers can be distinguished comparatively easily by their chiroptical signals, such as optical rotation, that are of (nearly, due to parity violation) equal magnitude but opposite sign. This is manifested by the frequently used phenomenological (+/−) terminology. The microscopic structure, on the other hand, is classified with the systematic *R/S* or *P/M* stereodescriptors (7). However, assigning the absolute (stereo-

chemical) configuration—that is, establishing which of the two possible mirror image spatial structural models gives rise to optical rotation with positive or negative sign—still poses a challenge.

The standard approach to directly determining absolute configuration is Bijvoet's method (8) of 1951, but in 2001 the technique of Coulomb explosion imaging (CEI) (9) was shown to be a potential means to determine the handedness of chiral molecules (10). Before 1951, chemical or biochemical conversions were used that relate compounds of unknown configuration to others

with known configuration, a method that is still applied today. For this purpose, Fischer (11) had arbitrarily assigned a given 3D structural model (denoted as the *D* form) of saccharic acid to the compound that is weakly (+) rotating in aqueous solution and its mirror image (*L* form) to the (−) rotating counterpart. Subsequently [see also (12) for the historical development], catalogs of the *D* and *L* series were established, the components of which were chemically related, either directly to *D*- or *L*-saccharic acid or to other chiral molecules already filed in the catalog. Bijvoet finally confirmed (8) Fischer's arbitrary choice by studying the sodium rubidium double salt of tartaric acid with anomalous x-ray diffraction. Heavy elemental scatterers induce a pronounced phase and intensity shift when irradiated with x-rays near their absorption edge, which allows the determination of absolute configuration. Although typically quite conclusive, Bijvoet's method is limited by requiring crystalline samples. A promising new approach using x-ray diffraction has recently been presented by Inokuma *et al.* (13). They diffused a dissolved chiral compound into a crystalline host framework containing heavy atoms. As a result of the interaction, the framework's symmetry changed to a chiral space group, thus allowing the application of anomalous x-ray diffraction. Nonetheless, conventional crystallographic challenges and flaws—such as misassigned atoms, symmetry problems, and guest disorder—persist and, hence, require support from mass spectrometry or nuclear magnetic resonance (NMR) (13).

The lack of versatile direct approaches has led to the active exploration of indirect physicochemical approaches based on optical rotation and circular dichroism. Indirect methods rely on quantum chemical calculations or empirical rules to interpret the experimental data. Alternatively, liquid chromatography with an enantioselective stationary phase is a widespread method for chiral discrimination. Its drawback for assignment lies in the need for a suitable analog with known stereochemical configuration. Recent activities focus on NMR spectroscopy, either by seeking to turn NMR directly into a chiroptical method (14) or by exploring possibilities to use residual dipolar couplings in chiral nonracemic alignment media (15). Also, photoelectron circular dichroism has received renewed interest (16), and promising three-wave mixing strategies to obtain chiroptical signals in microwave spectroscopy have been reported recently (17).

Herein, we focus on direct determination of absolute configuration in the gas phase by a molecular imaging technique that displays the 3D structure of individual chiral molecules on a detector and thereby permits assignment of absolute configuration on a single-molecule basis. As an alternative to displaying the full structure, one can also 3D-align the molecule and image decisive fragments (18). Kitamura *et al.* used a similar approach to ours, but with highly charged argon atoms from an ion source as ionizing agents, to detect dynamical chirality in perdeuterated

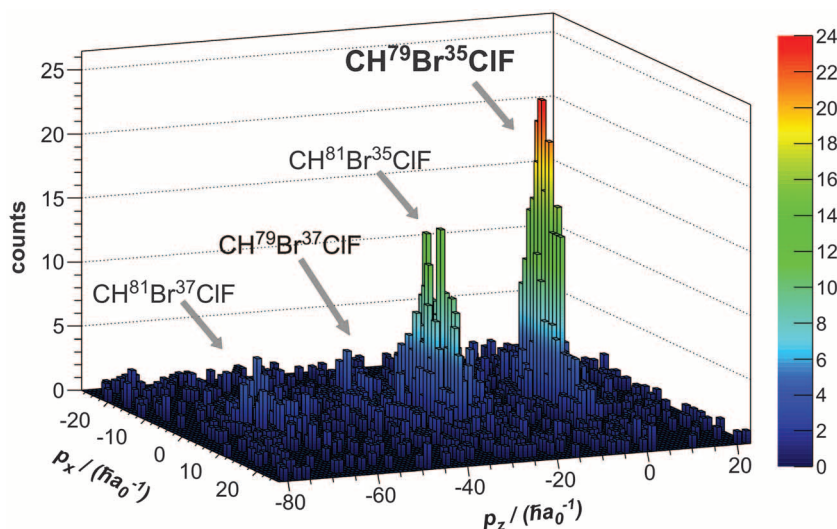


Fig. 1. Sum of linear momentum (*p*) components in fivefold ionization of CHBrClF, demonstrating the excellent resolution achieved in this experiment. Those events detected with p_x and p_z close to zero correspond to a fragment assignment to $^{79}\text{Br}^+$, $^{35}\text{Cl}^+$, $^{19}\text{F}^+$, $^{12}\text{C}^+$, and $^1\text{H}^+$ (denoted in bold). Fragments of other isotopologues can also be identified but are not used in the present analysis. The atomic unit for momentum is defined as $\hbar a_0^{-1} \approx 1.992 \cdot 10^{-24} \text{ kg m s}^{-1}$ (\hbar , Planck's constant h divided by 2π ; a_0 , Bohr radius).

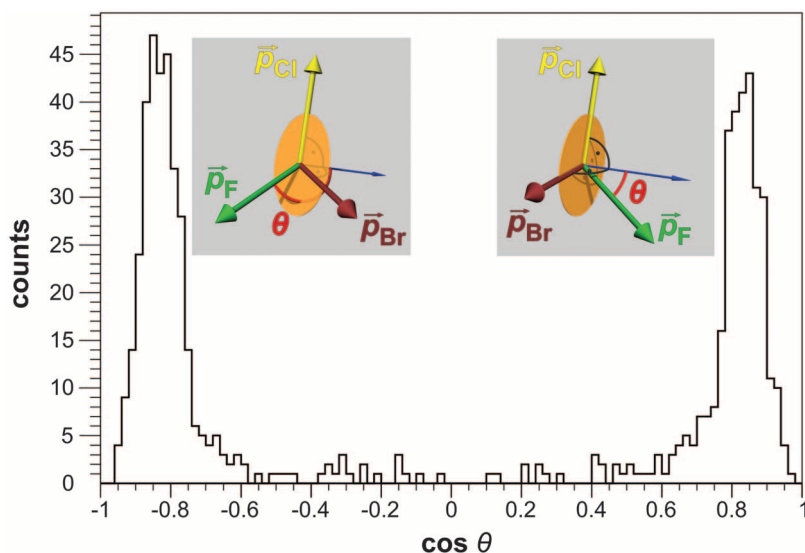


Fig. 2. Chiral discrimination for CHBrClF. The histogram for the cosine of the chirality angle θ shows the clear separation between enantiomers in our racemic sample of CHBrClF. As is illustrated in the insets, the angle is defined via $\cos(\theta) = \vec{p}_F \cdot (\vec{p}_{\text{Cl}} \times \vec{p}_{\text{Br}}) / (|\vec{p}_F| |\vec{p}_{\text{Cl}} \times \vec{p}_{\text{Br}}|)^{1/2}$. The peak at negative values of $\cos(\theta)$ corresponds to the *S* enantiomer, whereas the one at positive values corresponds to the *R* enantiomer.

methane (10) and pointed out the possibility of detecting molecular handedness. In 2008, Gagnon *et al.* employed a related variant to study the structure of achiral dichloromethane (CH_2Cl_2) (19) by CEI. For the direct assignment of the absolute configuration, high count rates for four-fold or higher fragmentation coincidence events are required. The laser systems commercially available in 2008 were unable to produce such

rates. To overcome these technical limitations for stereochemical assignments, we combine the latest high-power femtosecond lasers [with repetition rates that are 10 to 100 times higher (100 kHz)] with improved fast hexanode delay-line detectors to surmount otherwise prohibitively long data acquisition time. In addition, we employ high-performance data recording techniques, together with an offline analysis protocol,

to cope with the increasing complexity emerging for polyatomic molecules (20). These improvements enable the use of CEI to determine the absolute configuration of the prototypical chiral compound bromochlorofluoromethane (CHBrClF) and isotopically chiral methane derivatives in natural abundance such as $\text{CHBr}^{37}\text{Cl}^{35}\text{Cl}$.

CHBrCl_2 is commercially available and was used without further purification, as impurities

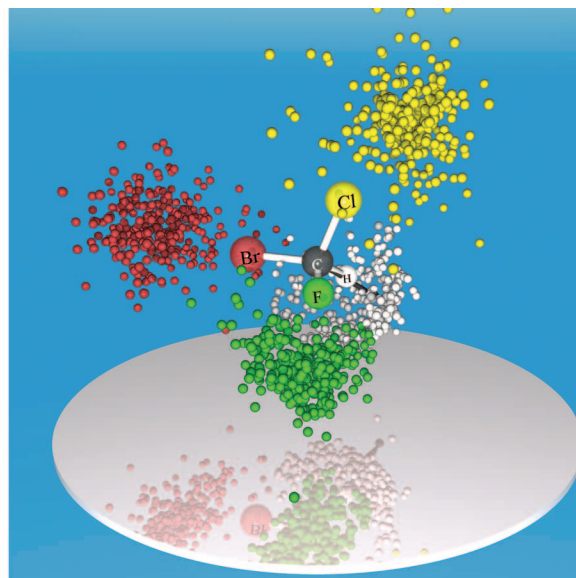
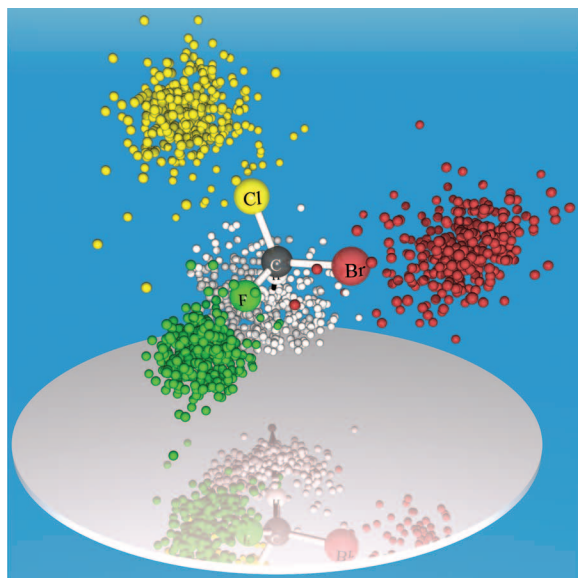


Fig. 3. Linear momenta in fivefold fragmentation of CHBrClF enantiomers. Measured linear momenta in the fivefold fragmentation of (left) $(S)\text{-CHBrClF}$ [$\cos(\theta) < -0.6$] and (right) $(R)\text{-CHBrClF}$ [$\cos(\theta) > 0.6$] are indicated by the following color codes: C, gray arrow; H, white; F, green; Cl, yellow; Br, red. Momenta are rotated to the molecular frame of reference, defined by the momentum of the carbon ion and the momentum sum of the bromine and chlorine ions. All momenta are

normalized with respect to the carbon momentum. For better visibility, hydrogen momenta are expanded by a factor of 2. Whereas the substituents are expelled during the Coulomb explosion into the directions expected from the classical structural model, the central atom C is also accelerated away from the center of mass and ejected in a similar direction as hydrogen. An animated version of the figure can be found in the supplementary materials (movies S1 and S2).

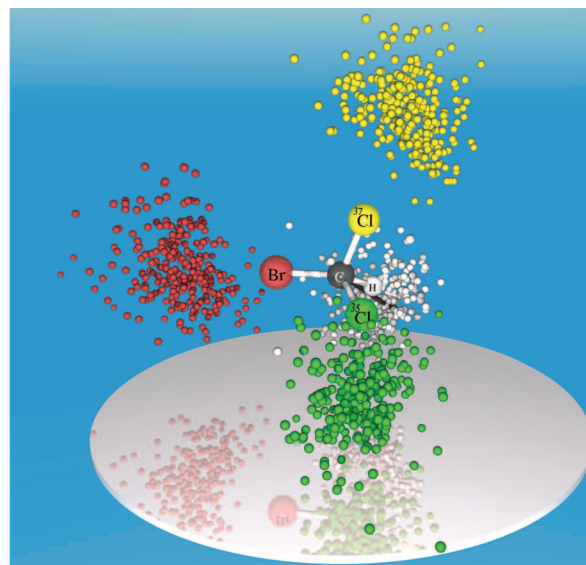
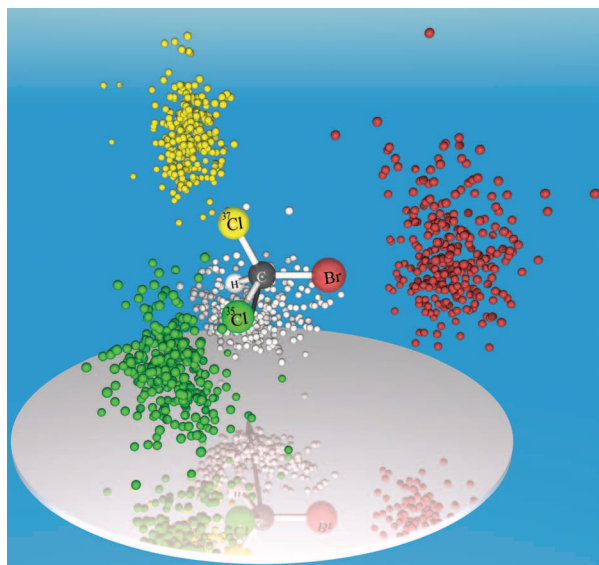


Fig. 4. Measured linear momenta in the fivefold fragmentation of $(S)\text{-CH}^{79}\text{Br}^{37}\text{Cl}^{35}\text{Cl}$ (left) and $(R)\text{-CH}^{79}\text{Br}^{37}\text{Cl}^{35}\text{Cl}$ (right). The color codes used correspond to: C, gray arrow; H, white; ^{35}Cl , green; ^{37}Cl , yellow; Br, red. Momenta are rotated to the molecular frame of reference, defined by the momentum of the carbon ion and the momentum sum of ^{79}Br and ^{35}Cl , and

normalized with respect to the momentum of the carbon ion. Again, the hydrogen momentum is scaled by a factor of 2. A histogram and an animated version of the figure can be found in the supplementary materials (fig. S5 and movies S3 and S4). For a wider angle of vision, see fig. S7, where a few outlier signals also become clearly visible.

are easily discarded in the analysis step of coincidence experiments. Racemic CHBrClF was synthesized as described in (27) by reacting CHBr_2Cl with HgF_2 . The spectrometer system employed was described in detail in (22). For the present study, the setup was augmented by an assembly of cold traps to recycle the volatile sample compounds.

The approach for direct determination of absolute configuration employs the well-established cold target recoil ion momentum spectroscopy (COLTRIMS), as depicted in fig. S1 in the supplementary materials. A supersonic gas jet of chiral molecules (y axis in the laboratory system) crosses a high-power femtosecond laser (laboratory x axis) to induce multiple ionization and the resulting Coulomb explosion. Charged fragments are projected by a static electric field along the laboratory z axis onto a position- and time-sensitive multichannel plate detector (MCP) with hexagonal delay-line readout (23), where all fragments are detected in coincidence (fig. S2). From the impact position on the detector (x , y) and the known distance between the ionization zone and MCP, as well as the measured time-of-flight, the velocities of all cations (formed in coincidence) can be derived. By assigning masses and charges to the various fragments, corresponding linear momenta of all detected particles can be obtained. In molecular multiple ionization and fragmentation, the momenta of photons and electrons are usually negligible compared with the momenta of the Coulomb exploding ionic fragments. Hence, in a cold molecular beam, the sum of the ion momentum vectors must be close to zero because of momentum conservation. The mass assignment can, therefore, be confirmed by checking this computed total momentum of all ions. Assignment of absolute configuration is, in principle, already possible, once four charged fragments (e.g., Br^+ , Cl^+ , F^+ , and CH^+ for CHBrClF) are detected in coincidence. Signatures of those breakups could be found in the data and used for assignment (results not reported here). Herein, however, we focus on the complete fragmentation into five singly charged ions, because analysis and interpretation are more straightforward. Additionally, the background can be suppressed quite efficiently. Mass resolution in COLTRIMS is sufficient to distinguish various isotopes of bromine and chlorine in natural abundance, thereby even allowing stereochemical characterization of isotopically chiral molecules. Further details of the measurement method can be found in the supplementary materials (24).

Figure 1 shows the sum of all ion momenta in the case where five fragments of CHBrClF are measured in coincidence. The peak at zero total momentum shows events with the correct mass assignment: $^{79}\text{Br}^+$, $^{35}\text{Cl}^+$, $^{19}\text{F}^+$, $^{12}\text{C}^+$, and $^1\text{H}^+$. These events were used for the determination of the absolute configuration. The peaks at lower momentum in the z direction are contributions from other isotopologues.

Figure 2 demonstrates the capability to distinguish enantiomers in our racemic sample. For

this purpose, an angle θ is defined, indicating if the momenta of bromine, chlorine, and fluorine form a right- or left-handed coordinate system. As distinct peaks are obtained in the histogram, almost all events can be assigned clearly to one enantiomer or the other. This shows the robustness of our method against the laser pulse length: Being ~40-fs long, our pulses are not short enough to consider the hydrogen frozen during multiple ionization. The clear separation of enantiomers in the histogram indicates, however, that the motion of hydrogen during the laser pulse does not alter bond angles to an extent that would prevent identification of enantiomers. These results also show that reconstruction of the exact geometric structure is not necessary for the determination of absolute configuration. Classical molecular dynamics simulations confirm that the enantiomers are mapped unambiguously onto their momentum space analogs that are presented here.

Figure 3 overlays measured linear momenta on a rigid structural model of neutral CHBrClF, with the linear momentum of carbon fixed along the x axis, the momentum sum of chlorine and bromine defining the xy plane, and all other linear momenta being oriented relative to these. For better visibility, momenta are normalized with respect to the carbon momentum. The momentum of hydrogen, being very small due to the low mass, is expanded by a factor of 2 in this figure. It is evident that the configuration of the two enantiomers is directly imaged on the detector. As a racemic mixture of CHBrClF was employed, an equal ratio for the S and R configurations was obtained within the statistical uncertainty [329 and 302 events for S and R , respectively, with $|\cos(\theta)| > 0.6$ in each case]. At first sight, one might be surprised that the carbon ion is detected in the same direction as the proton. This is due to the fact that the position of the center of mass is conserved; thus, H^+ and C^+ , as the lightest two ions of the system, are repelled from the slowly moving heavier ions, as has been confirmed with the help of molecular dynamics simulations.

For CHBrClF, the direct assignment of absolute configuration works unequivocally in the majority of fivefold coincidence events because of the comparatively large mass difference between the ions. The situation is considerably more challenging for the case of isotopically chiral systems. In the case of CHBrCl_2 (Fig. 4), not all fivefold fragmentation events allow an unambiguous assignment of the isotope masses to each fragment; hence, no determination of absolute configuration is possible for such events. However, a subset of events that permit a conclusive assignment can be selected by a procedure detailed in the supplementary materials (figs. S3 and S4 and supplementary text). Again, as a racemic sample was used, an almost 50:50 ratio of S : R is detected [282:273 events (not corrected for outliers) with $|\cos(\theta)| > 0.6$] (see fig. S5).

The technique still has several limitations: Volatile molecules and a large amount of sub-

stance are required due to the molecular beam source. Comparatively simple, rigid structures were studied. In the case of more complicated molecules, the kinematic properties of the fragments may not directly illustrate the geometric structure, making the identification of the absolute configuration less straightforward. In this case, geometrical reconstruction or comparison with simple molecular dynamics simulations might become necessary, especially when several stereogenic elements are present. On a technical level, the probability of multifragment detection decreases dramatically with the increasing amount of fragments, as both the fragmentation yield and the detection efficiency diminish exponentially with the increasing number of fragments.

Stepwise fragmentation is a limitation as well. Additionally, when multiple ionization is slow compared with vibrational time scales, assignment can be hampered or even completely prohibited. For this purpose, faster ionization schemes with shorter laser pulses and higher laser intensity are required.

The present imaging approach allows for determination of absolute configuration of gas phase molecules on a per-molecule basis. Apart from a rigid structural model, it does not require theoretical input. Besides structure determination, as demonstrated herein, the coincidence technique creates opportunities to study chirality in single molecules.

References and Notes

- R. Berger, in *Relativistic Electronic Structure Theory, Part 2: Applications*, P. Schwerdtfeger, Ed. (Elsevier, Netherlands, 2004), pp. 188–288.
- C. Daussy *et al.*, *Phys. Rev. Lett.* **83**, 1554–1557 (1999).
- M. Quack, J. Stohner, M. Willeke, *Annu. Rev. Phys. Chem.* **59**, 741–769 (2008).
- L. Pasteur, in *Leçons de Chimie Professées en 1860 par MM. Pasteur, Cahours, Wurtz, Berthelot, Sainte-Claire Deville, Barral et Dumas* (Hachette, Paris, 1861), pp. 1–48.
- J. H. van't Hoff, *Arch. Néerl. Sci. Exactes Nat.* (French transl.) **9**, 445–454 (1874).
- J.-A. Le Bel, *Bull. Soc. Chir. Paris* **T22**, 337–347 (1874).
- R. S. Cahn, C. Ingold, V. Prelog, *Angew. Chem. Int. Ed. Engl.* **5**, 385–415 (1966).
- J. M. Bijvoet, A. F. Peerdeman, A. J. van Bommel, *Nature* **168**, 271–272 (1951).
- Z. Vager, R. Naaman, E. P. Kanter, *Science* **244**, 426–431 (1989).
- T. Kitamura, T. Nishide, H. Shiromaru, Y. Achiba, N. Kobayashi, *J. Chem. Phys.* **115**, 5 (2001).
- E. Fischer, *Ber. Dtsch. Chem. Ges.* **24**, 2683–2687 (1891).
- F. W. Lichtenhaler, *Angew. Chem. Int. Ed. Engl.* **31**, 1541–1556 (1992).
- Y. Inokuma *et al.*, *Nature* **495**, 461–466 (2013).
- A. D. Buckingham, *Chem. Phys. Lett.* **398**, 1–5 (2004).
- R. Berger *et al.*, *Angew. Chem. Int. Ed.* **51**, 8388–8391 (2012).
- C. Lux *et al.*, *Angew. Chem. Int. Ed.* **51**, 5001–5005 (2012).
- D. Patterson, J. M. Doyle, *Phys. Rev. Lett.* **111**, 023008 (2013).
- J. L. Hansen *et al.*, *J. Chem. Phys.* **136**, 204310 (2012).
- J. Gagnon, K. F. Lee, D. M. Rayner, P. B. Corkum, V. R. Bhardwaj, *J. Phys. B* **41**, 215104 (2008).

20. B. Wales *et al.*, *Nucl. Instrum. Methods Phys. Res. A* **667**, 11–15 (2012).
21. J. Hine, A. M. Dowell, J. E. Singley, *J. Am. Chem. Soc.* **78**, 479–482 (1956).
22. J. Ullrich *et al.*, *Rep. Prog. Phys.* **66**, 1463–1545 (2003).
23. O. Jagutzki *et al.*, *IEEE Trans. Nucl. Sci.* **49**, 2477–2483 (2002).
24. Further details on the measurement principle, with six additional figures and four movies, are available in the supplementary materials on Science Online.

Acknowledgments: This paper is dedicated to Helmut Schwarz on the occasion of his 70th birthday. We thank D. Avnir, T. Isaev, and F. Lichtenthaler for discussion; M. Meckel for help with some figures; and A. Czasch for support concerning data analysis. This work was supported by the State Initiative for the Development of Scientific and Economic Excellence (LOEWE) in the LOEWE-Focus ELCH. The momentum data used to draw the figures are provided in the supplementary materials. Raw data are archived at the University of Frankfurt and are available upon request.

Supplementary Materials

www.sciencemag.org/cgi/content/full/341/6150/1096/DC1
Supplementary Text
Figs. S1 to S7
Reference (25)
Movies S1 to S5
Databases S1 and S2

10 May 2013; accepted 2 August 2013
10.1126/science.1240362

Achieving the Convention on Biological Diversity's Goals for Plant Conservation

L. N. Joppa,^{1*} P. Visconti,¹ C. N. Jenkins,² S. L. Pimm^{3*}

Identifying which areas capture how many species is the first question in conservation planning. The Convention on Biological Diversity (CBD) aspires to formal protection of at least 17% of the terrestrial world and, through the Global Strategy for Plant Conservation, 60% of plant species. Are these targets of protecting area and species compatible? We show that 67% of plant species live entirely within regions that comprise 17% of the land surface. Moreover, these regions include most terrestrial vertebrates with small geographical ranges. However, the connections between the CBD targets of protecting area and species are complex. Achieving both targets will be difficult because regions with the most plant species have only slightly more land protected than do those with fewer.

Protected areas are broadly effective (1–6) and thus usually necessary, if not always sufficient, to protect species. Their effective allocation is vital to slow present extinction rates that are 100 to 1000 times faster than the natural background rate (7). The Convention on Biological Diversity's (CBD's) 20 Aichi Targets—agreed in October 2010 in Nagoya, Japan—extend to 2020 an international commitment to halt biodiversity loss (www.cbd.int/sp/targets/). Target 11 seeks formal protection of >17% of the terrestrial world. One can use the most taxonomically complete and spatially best-resolved data on species distributions (8)—birds (9), mammals (10), and amphibians (10)—to assess this target (11). Unfortunately, these are a taxonomically limited subset of ~23,000 terrestrial species from more than a million described animal species with many more as-yet unknown (12). This raises concerns about their representativeness for setting global conservation priorities. By contrast, plants form a large taxonomic sample with >350,000 described species and ~15% awaiting description (13). Important in themselves, plants influence the diversity of insects (14) and other animals. In 2010, the CBD updated the Global Strategy for Plant Conservation (GSPC) (11), seeking protection for 60% of plant species as a critical indicator

toward CBD goals. Are these targets of protecting area and species compatible?

Satisfying the joint aspirations of the CBD's Aichi Target 11 and the GSPC will be difficult. First, by 2009, the world had protected ~13% of global land area (15), but half of the world's major habitat divisions—ecoregions (16)—did not meet a target of 10% coverage. Some ~75% of them had <10% of their area strictly protected (15). Present conservation efforts bias toward lands that are high, cold, dry, or otherwise far from people—often a mismatch with where conservation needs are pressing (17). These statistics show that protected areas are not representative of terrestrial environments, but they do not address species targets directly.

Second, for plants, as for most taxa, unresolved issues of taxonomy generate uncertainties in how many species there are amid existing catalogs of described species and how many are still missing from them (13, 18). Target 1 of the GSPC is to complete “a widely accessible working list of all known plant species, as a step toward a complete world flora” (19). Major international botanic gardens responded in 2010 with “The Plant List” (www.theplantlist.org)—a working list of all known plant species. Here, we analyze a subset of ~109,000 species taken from the World Checklist of Selected Plant Families (WCSP) (20). For this subset, literature compilers and taxonomists have attempted a consensus overview of the current state of knowledge of select families, including correct names for currently accepted species and their synonyms. For this quarter of the world's plant species, we pre-

viously predicted where as-yet undescribed species likely live (18).

Third, species' distributional data are imperfect (21). Elsewhere, we map birds, mammals, and amphibians on a scale of 10 km by 10 km (8). We compare them to plant distributions below. The details of these animal distributions are exceptional; plant distributional data are coarser. Flowering plant species in the WCSP are tagged to one or more of the 369 countries or geographic regions delineated by the International Taxonomic Database Working Group (22). Further details on the species and regions are in the supplementary materials (23). Nonetheless, this spatial scale captures the essential first step of comparing targets of area protected to species protected.

More problematic is that plant distributional data are species lists from regions where the largest region is 2 million times the area of the smallest. For the biodiversity hotspots of Myers *et al.* (24), the ratio is ~130. The relationships of numbers of species (S) to area (A) are well described by $S = cA^z$; c and z are parameters. Because z is <1, species densities, S/A , generally decline with increasing area. This makes objective comparisons of areas—and the designation of conservation priorities—challenging. On the basis of species' totals alone, apparent priorities tend to be the largest regions; those based on species' densities, the smallest ones. Further complicating matters, z depends on circumstance: Islands, continuous areas within continents, and biogeographically unrelated regions have different characteristic values (25). This fact dashes hopes of a single, global correction of species' numbers by a simple function of area to permit regional comparisons.

We can address this issue directly, because our results fall from quantitative databases and not the expert opinions used by Myers *et al.*, which are impossible to replicate or update. Our solution uses a greedy algorithm to accumulate species found only within a progressively larger set of regions (“endemic densities”; Fig. 1 and table S1b). We scale our results to 100,000 plant species and to 1000 km².

Regions with the highest densities enter first, followed by those adding progressively fewer new species to the aggregated total. Thus, the first 43 regions to enter are all islands, followed by Costa Rica. In the data that we consider, Costa Rica has 791 endemics and adds all of these, reducing the accumulated endemic density to 29. Panama enters next. It has 775 endemics, but adds

¹Microsoft Research, 21 Station Road, Cambridge CB1 2FB, UK. ²Department of Biological Sciences, North Carolina State University, Box 7617, Raleigh, NC 27606, USA. ³Nicholas School of the Environment, Duke University, Box 90328, Durham, NC 27708, USA.

*Corresponding author. E-mail: stuartpimm@me.com

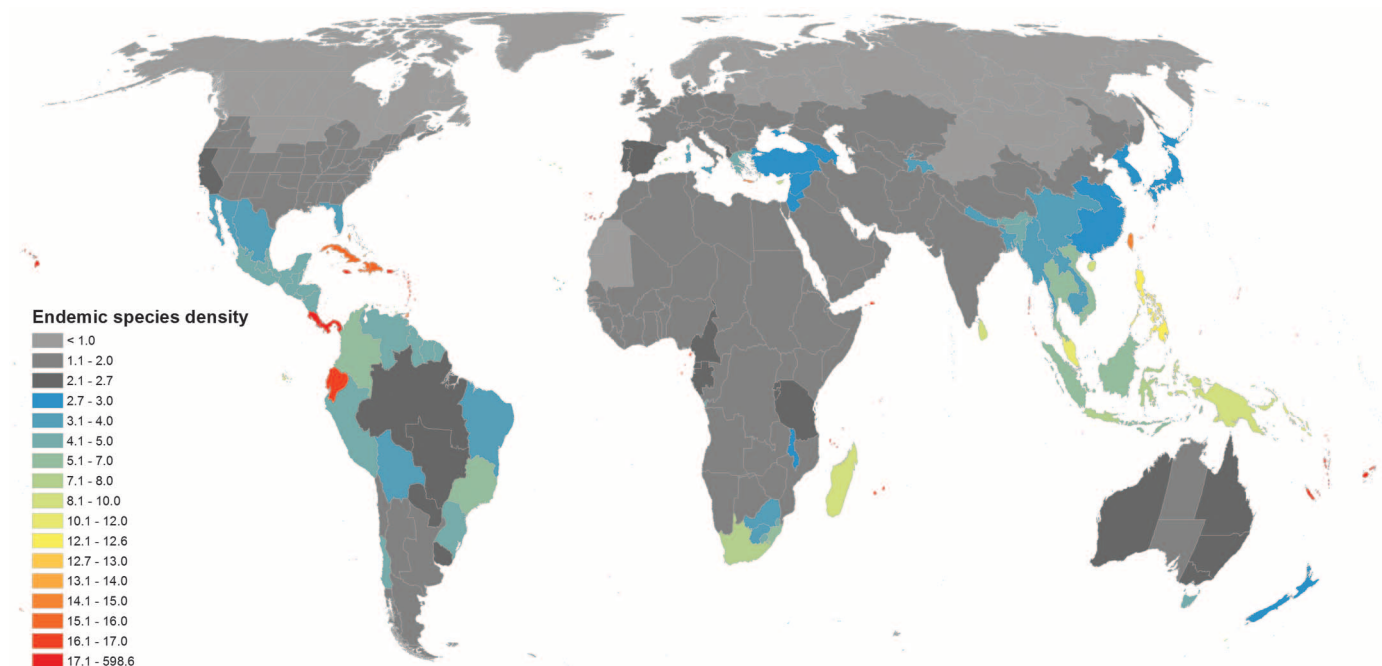


Fig. 1. Endemic accumulation map. Colors show the numbers of endemic species as they add to the total, given the inclusion of higher priority regions within the accumulated set scaled to 100,000 plant species and by 1000 km² of accumulated area.

1309 species to the accumulated total because additional species are endemic to Panama and Costa Rica combined. The accumulated endemic density of these 45 regions is now 25.

We obtain a broadly similar map when optimizing for species richness instead of number of endemic species (“richness densities”; fig. S1 and table S2).

As much as the discrete and variable areas of the plant regions permit, the advantage of greedy algorithms is that they create a continuous curve of increasing areas and species. Figure 2 shows the accumulation curve optimized to capture species only found within an accumulated set of regions (endemics) and those incidentally captured (all species) by this set.

Unlike the biodiversity hotspot approach in which areas and species are either included or not, our accumulations provide a continuous ranking on which the Aichi targets are entirely arbitrary benchmarks. Nonetheless, considering the 17% target—an area of ~24.3 million km²—allows useful comparisons.

First, the regions that we select encompass part of the ranges of 81% of the plant species and all of the ranges of 67%. We are not suggesting that we could protect all of these regions and nothing else, but this hypothetical 17% sets the bar for achieving the GSPC goal via CBD Target 11, as shown by the red crossed lines in Fig. 2. (By optimizing just for species richness, a similar set of regions captures 86% of species in the same total area; see fig. S2 and table S1a).

Second, for any benchmark, we must ask whether our greedy accumulation algorithm is optimal. Moreover, to what extent do other almost-

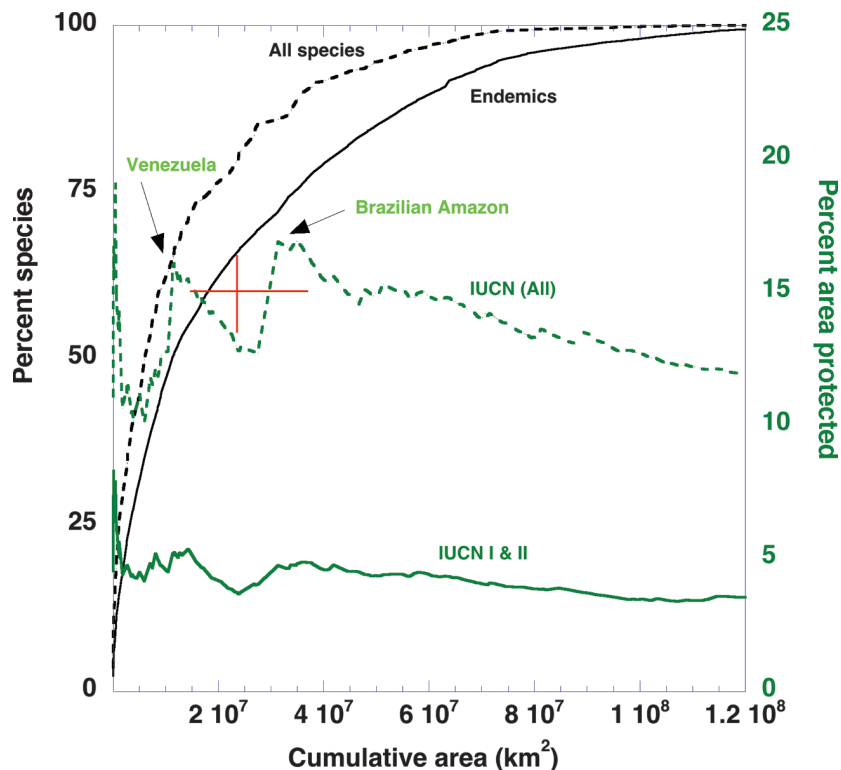


Fig. 2. Species and protected area accumulations. Black lines: species found within (dashed line) or only within (solid line) accumulating areas. The red cross shows targets of 60% species and 17% of land area protected. Green lines: the cumulative percentages of areas receiving some protection (dashed line, IUCN classes I to VI plus indigenous and other areas) and the greatest protection (solid line, IUCN classes I and II).

as-good solutions surround this optimum? The supplementary materials detail our use of a genetic algorithm to answer these questions.

Third, our selected regions are important for terrestrial vertebrates. We find that 89% of bird species, 80% of amphibians, and 74% of

mammals live within them. Percentages for species with ranges smaller than the median geographical size—those with a much higher risk of being threatened—are 88, 82, and 73%, respectively (Fig. 3).

Fourth, biodiversity hotspots cover only ~17.4 million km² and capture 44% of endemic species (24). Not surprisingly, our formal optimization performs better, capturing 59% in the

same amount of area. It also captures 74% of all plant species, a number Myers *et al.* could not estimate. What is notable is not the better performance of our approach, but the similarities and differences in the regions chosen between the two approaches (Fig. 4).

The areas that we omit have much to do with spatial resolution. Hotspots include montane forest of East Africa and the Western Ghats of

India, plus southwestern Australia, and the coastal moist forests of West and East Africa. These areas are not included in our selections because they are embedded in much larger regions. The finer-scale vertebrate data also show the importance of these regions, plus others including the forests along Australia's eastern seaboard (Fig. 3). Conversely, Myers *et al.* considered levels of habitat loss and so excluded

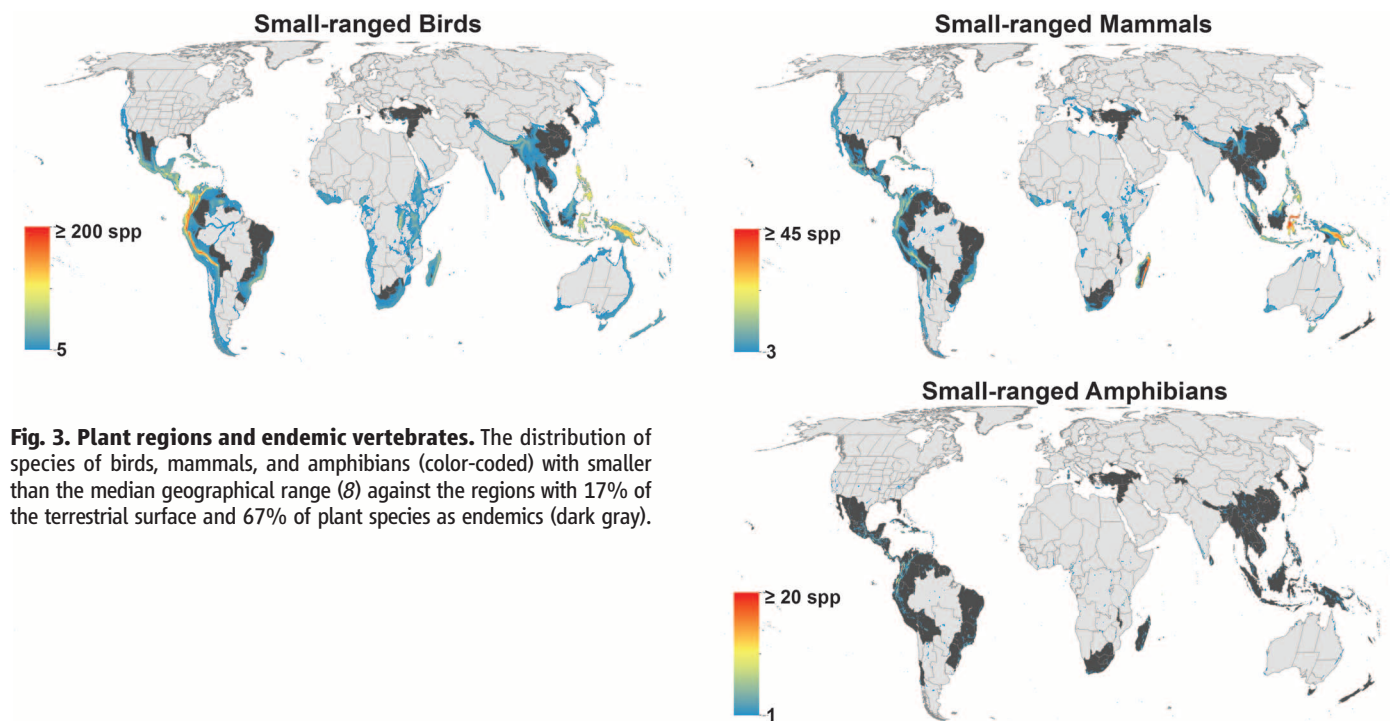


Fig. 3. Plant regions and endemic vertebrates. The distribution of species of birds, mammals, and amphibians (color-coded) with smaller than the median geographical range (8) against the regions with 17% of the terrestrial surface and 67% of plant species as endemics (dark gray).

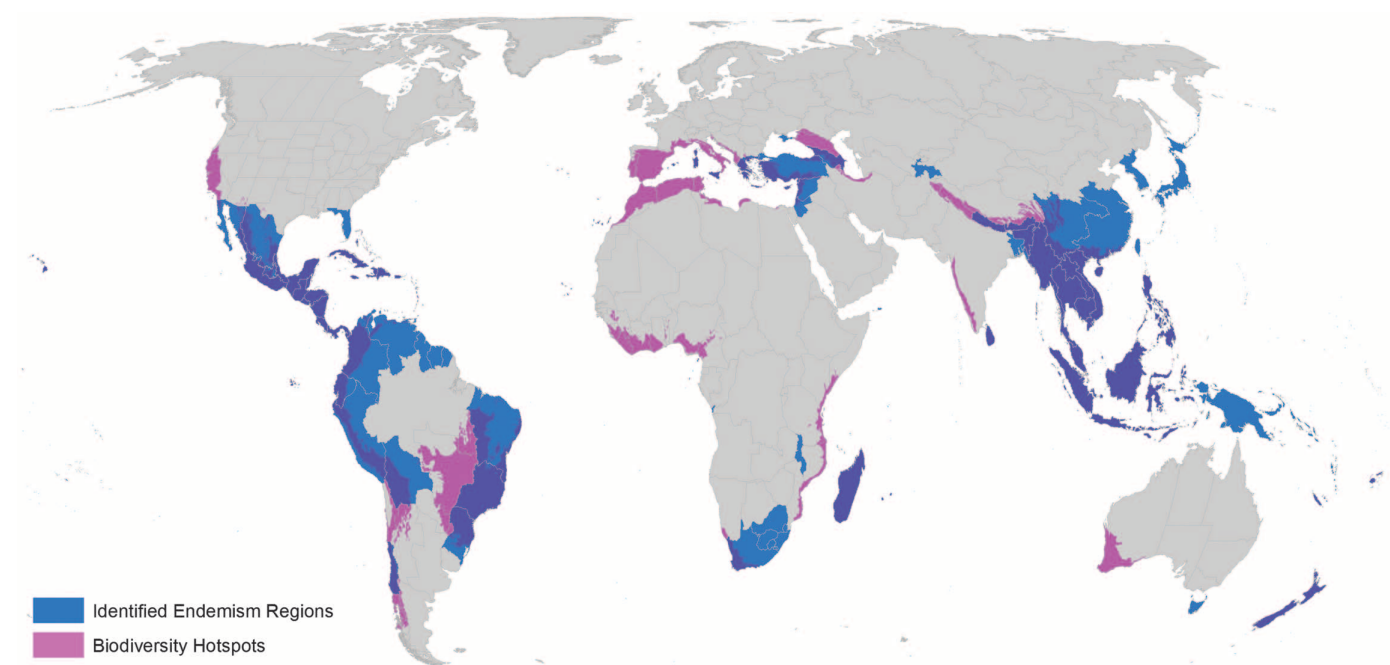


Fig. 4. A comparison of this paper's identified regions (blue) and biodiversity hotspots (24).

New Guinea, which we do not. Our inclusion of Turkey and the Middle East, Japan, Korea, and more of China, northern South America, and Southern Africa reflects our estimates of their numbers of endemic species.

Our results have five consequences.

1) Broadly, tropical and subtropical islands, moist tropical and subtropical forests (especially those in mountains), and Mediterranean ecosystems hold concentrations of plant endemics. The majority of as-yet undescribed plant species also live in these regions (18). Further discoveries would likely enhance their importance.

2) Our figures suggest the achievement of Aichi goals by concentrating protected areas in regions of highest endemism. Had nations already implemented this strategy, we would see proportionally greater protection rates where species densities are high. Figure 2 shows that, within the regions we select, strict protected areas [International Union for Conservation of Nature (IUCN) classes I and II (26)] occur at only slightly higher rates than in nonselected regions. The most important areas include Costa Rica and Panama, which have >10% of their land in IUCN classes I and II. This is a weak trend, however. When considering all the categories of protection (IUCN I to VI plus indigenous territories), the total protected is much higher, but the trend similar.

3) The ability of protected areas to protect depends upon the nature and location of threats (2, 5). For example, within our 17% set, 9.4% of plant species are endemic to a total of ~1.9 million km² of islands. Island plants suffer greatly from introduced species (27), something the establishment of protected areas does not completely address.

4) Figure 2 (and see table S1b) show a hitherto poorly appreciated effect of indigenous areas. In tropical South America, these protect large areas of tropical moist forest with high plant richness.

5) Overall, the global land area currently protected, ~13%, is close to Aichi's 17%. This seems encouraging. However, of the 17% that contains the entire range of 67% of the world's plant species, only 14% is protected in some way, barely more than the global average.

The total area protected imperfectly measures species' protection, however. Even with perfect data on species' distributions, the "Noah's Ark effect" (28) renders simple optimal allocation of priority areas meaningless. A small total area—a metaphorical "ark"—can capture many species but ignore long-term viability. Numerous protected areas of large aggregate size may house many species, but be individually too small to maintain viable populations. How small is "too small" depends on the species—tigers demand more area than tiger lilies—as well as the distribution of habitat fragments (29) and levels of threat (2, 5). How much area countries should protect—and where—are ecological questions. Political practicalities dominate actions, as the Aichi target of 17% testifies.

The spatial resolution of presently available data is inadequate to address this key concern at the spatial scales at which conservation actions are taken and protected areas established. Nonetheless, we show that how protected areas are allocated within and across regions constrains how efficiently plant diversity can be sustained. Understanding this is necessary to achieve the Convention on Biological Diversity's conservation goals.

References and Notes

1. J. M. Adeney, N. L. Christensen, S. L. Pimm, *PLoS ONE* **4**, e5014 (2009).
2. K. S. Andam, P. J. Ferraro, A. Pfaff, G. A. Sanchez-Azofeifa, J. A. Robalino, *Proc. Natl. Acad. Sci. U.S.A.* **105**, 16089–16094 (2008).
3. J. Geldmann *et al.*, *Biol. Conserv.* **161**, 230–238 (2013).
4. L. N. Joppa, S. R. Loarie, S. L. Pimm, *Proc. Natl. Acad. Sci. U.S.A.* **105**, 6673–6678 (2008).
5. A. Nelson, K. M. Chomitz, *PLoS ONE* **6**, e22722 (2011).
6. L. N. Joppa, A. Pfaff, *Proc. Biol. Sci.* **278**, 1633–1638 (2011).
7. S. L. Pimm, G. J. Russell, J. L. Gittleman, T. M. Brooks, *Science* **269**, 347–350 (1995).
8. C. N. Jenkins, S. L. Pimm, L. N. Joppa, *Proc. Natl. Acad. Sci. U.S.A.* **110**, E2602–E2610 (2013).
9. BirdLife International, Bird species distribution maps of the world (BirdLife International, Cambridge, UK, 2011), vol. 2013; www.birdlife.org/datazone/info/spcdownload.
10. International Union for the Conservation of Nature, IUCN Red List of Threatened Species. Version 2010.4 (2013); www.iucnredlist.org/technical-documents/spatial-data.
11. L. Cantú-Salazar, C. D. L. Orme, P. C. Rasmussen, T. M. Blackburn, K. J. Gaston, *Biodivers. Conserv.* **22**, 1033–1047 (2013).
12. B. R. Scheffers, L. N. Joppa, S. L. Pimm, W. F. Laurance, *Trends Ecol. Evol.* **27**, 501–510 (2012).
13. L. N. Joppa, D. L. Roberts, S. L. Pimm, *Proc. R. Soc. B* **278**, 554–559 (2011).
14. D. R. Strong, J. H. Lawton, S. R. Southwood, *Insects on Plants. Community Patterns and Mechanisms* (Blackwell Scientific Publications, Oxford, 1984).

15. C. N. Jenkins, L. Joppa, *Biol. Conserv.* **142**, 2166–2174 (2009).
16. D. M. Olson *et al.*, *Bioscience* **51**, 933 (2001).
17. L. N. Joppa, A. Pfaff, *PLoS ONE* **4**, e8273 (2009).
18. L. N. Joppa, D. L. Roberts, N. Myers, S. L. Pimm, *Proc. Natl. Acad. Sci. U.S.A.* **108**, 13171–13176 (2011).
19. A. Paton, E. Nic Lughadha, *Bot. J. Linn. Soc.* **166**, 250–260 (2011).
20. WCPSP 2008 World checklist of selected plant families. The Board of Trustees of the Royal Botanic Gardens, Kew. See www.kew.org/wcpssp.
21. C. N. Jenkins *et al.*, *Divers. Distrib.* **17**, 652–662 (2011).
22. N. Brummitt, S. Bachman, J. Moat, *Endanger. Species Res.* **6**, 127–135 (2008).
23. Materials and methods are available as supplementary materials on Science Online.
24. N. Myers, R. A. Mittermeier, C. G. Mittermeier, G. A. da Fonseca, J. Kent, *Nature* **403**, 853–858 (2000).
25. M. L. Rosenzweig, *Species Diversity in Space and Time* (Cambridge Univ. Press, Cambridge, 1995).
26. International Union for the Conservation of Nature and United Nations Environment Programme, World Conservation Monitoring Centre, The World Database on Protected Areas (WDPA) July Release (Cambridge, UK, 2012); www.protectedplanet.net.
27. D. F. Sax, S. D. Gaines, *Proc. Natl. Acad. Sci. U.S.A.* **105** (suppl. 1), 11490–11497 (2008).
28. S. L. Pimm, J. H. Lawton, *Science* **279**, 2068–2069 (1998).
29. J. K. Schnell, G. M. Harris, S. L. Pimm, G. J. Russell, *Conserv. Biol.* **27**, 520–530 (2013).

Acknowledgments: The original data for this paper are in public archives from BirdLife International (9), IUCN (10), WCPSP (20), and WCMC (26). We thank those responsible for access to them and especially the many professionals and amateurs who collected them.

Supplementary Materials

www.sciencemag.org/cgi/content/full/341/6150/1100/DC1
Materials and Methods
Figs. S1 to S3
Table S1

10 June 2013; accepted 7 August 2013
10.1126/science.1241706

Caffeoyl Shikimate Esterase (CSE) Is an Enzyme in the Lignin Biosynthetic Pathway in *Arabidopsis*

Ruben Vanholme,^{1,2†} Igor Cesarino,^{1,2‡} Katarzyna Rataj,^{3§} Yuguo Xiao,^{3§} Lisa Sundin,^{1,2} Geert Goeminne,^{1,2} Hoon Kim,⁴ Joanna Cross,^{1,2} Kris Morreel,^{1,2} Pedro Araujo,^{1,2} Lydia Welsh,³ Jurgen Hastraete,⁵ Christopher McClellan,³ Bartel Vanholme,^{1,2} John Ralph,⁴ Gordon G. Simpson,^{3,6} Claire Halpin,^{3,*†} Wout Boerjan^{1,2,*†}

Lignin is a major component of plant secondary cell walls. Here we describe caffeoyl shikimate esterase (CSE) as an enzyme central to the lignin biosynthetic pathway. *Arabidopsis thaliana cse* mutants deposit less lignin than do wild-type plants, and the remaining lignin is enriched in *p*-hydroxyphenyl units. Phenolic metabolite profiling identified accumulation of the lignin pathway intermediate caffeoyl shikimate in *cse* mutants as compared to caffeoyl shikimate levels in the wild type, suggesting caffeoyl shikimate as a substrate for CSE. Accordingly, recombinant CSE hydrolyzed caffeoyl shikimate into caffeate. Associated with the changes in lignin, the conversion of cellulose to glucose in *cse* mutants increased up to fourfold as compared to that in the wild type upon saccharification without pretreatment. Collectively, these data necessitate the revision of currently accepted models of the lignin biosynthetic pathway.

The evolutionary emergence of lignin, a phenolic polymer deposited in the secondary cell wall, allowed the development of vas-

cular land plants. The hydrophobic and strengthening nature of lignin enables conducting xylem vessels to transport water and nutrients from the

roots to photosynthetic organs while withstanding the negative pressure caused by transpiration (1, 2). The strengthening of fiber cells by lignification allows vascular plants to grow tall and stand upright (1, 3, 4). However, these very same physicochemical properties of lignin are a barrier to the isolation of cellulose fibers by chemical pulping and the enzymatic hydrolysis of cell wall polysaccharides in biorefining. Biomass feedstocks with less lignin or with more-degradable lignin would reduce the high processing costs and carbon footprint of paper, biofuels, and chemicals (5).

The lignin biosynthetic pathway has been extensively studied (6–10). In dicotyledonous plants, lignin is mainly synthesized from two monomers or monolignols, coniferyl alcohol and sinapyl alcohol (6, 11, 12), that upon incorporation into lignin give rise to guaiacyl (G) and syringyl (S) units, respectively. *p*-Coumaryl alcohol gives rise to the less abundant *p*-hydroxyphenyl (H) lignin units. 3-Hydroxylation of the aromatic ring, catalyzed by *p*-coumarate 3-hydroxylase (C3H, Fig. 1), diverts flux away from H lignin and toward G and S lignin. The discovery that C3H accepts *p*-coumaroyl shikimate and quinate esters as substrates (13–15) led to the identification of hydroxycinnamoyl-CoA:shikimate/quinat hydroxycinnamoyltransferase (HCT) as the enzyme catalyzing the preceding step, the production of *p*-coumarate esters from *p*-coumaroyl-coenzyme A (CoA) (16) (Fig. 1). The suggestion that HCT also catalyzes a second reaction in the lignin pathway, converting the resulting caffeate esters into caffeoyl-CoA (16), was attractive because it brought the interpreted pathway back to the next expected intermediate, caffeoyl-CoA. Here we describe caffeoyl shikimate esterase (CSE, encoded by At1g52760) as an enzyme in the lignin biosynthetic pathway that, together with 4-coumarate:CoA ligase (4CL), bypasses the second HCT reaction.

CSE was first identified through a potential function in phospholipid repair upon oxidative stress (17). However, we identified CSE as a candidate for involvement in lignification, based on analyses designed to identify genes coexpressed with known components of the lignin biosynthetic pathway. Of 13 genes identified by each of

three different coexpression software tools and publicly available data sets, 9 were established lignin pathway genes, but three, including *CSE*, had no known role in lignin biosynthesis (fig. S1 and table S1). Of these three, only *CSE* was also identified as being coexpressed with lignin pathway genes in a set of lignin mutants (7). Consistent with the coexpression analysis, CSE-reporter fusion proteins expressed from transgenes (composed of the native *CSE* promoter, exons, and introns, fused to a reporter gene) were detected in lignifying vascular tissue of primary transformants (fig. S2).

To investigate a role for CSE in lignification, we studied two transfer DNA insertion mutants: *cse-1*, a knockdown mutant with an insertion in the promoter, and *cse-2*, a knockout mutant with an insertion in the second exon (fig. S3). Although *cse-1* did not show developmental abnormalities, the inflorescence stems of *cse-2* mutants were 37% smaller and 42% lighter at senescence than were those of the wild type (Fig. 2 and fig. S4). *CSE* transcript levels analyzed by quantitative reverse transcription polymerase chain reaction were 6.3% of that in the wild type in *cse-1* and undetectable in *cse-2*, the weak and strong mutant alleles, respectively (fig. S3).

Analysis of transverse sections of *cse-1* and *cse-2* mutant stems revealed reduced autofluorescence and less intense Wiesner and Mäule staining in vessels and fibers of *cse-2*, indicative of reduced lignin content and fewer lignin S units (Fig. 2 and fig. S5). In addition, *cse-2* mutants had collapsed vessel elements (Fig. 2), a phenotype typical of plants with weakened secondary cell walls (18). The mutant phenotype of *cse-2* was complemented in stable transgenic lines in which expression of *CSE* was driven by the cauliflower mosaic virus 35S promoter (Fig. 2 and figs. S4 and S5), verifying that the mutation of *CSE* is the cause of the observed phenotypes.

In order to examine the connection between CSE and lignification in more detail, senesced inflorescence stems of *cse-1* and *cse-2* were subjected to compositional analyses. The fraction of the dry weight made up by cell wall polymers after soluble molecules had been extracted (i.e., the cell wall residue) was significantly reduced from 79.8% in the wild type to 72.9% in the *cse-2* mutant ($0.05 > P > 0.01$) (table S2). The fraction of acetyl bromide-soluble lignin released from this cell wall residue was reduced by 17 and 36% in the *cse-1* and *cse-2* mutants as compared to their corresponding wild-type controls (Fig. 2 and table S2). The lignin composition of *cse-2*, determined by thioacidolysis and nuclear magnetic resonance (NMR), revealed that the relative proportion of H units increased over 30-fold (Fig. 2, fig. S6 and table S2). Milder compositional shifts were apparent in the lignin of *cse-1* (table S2). The increase in the proportion of H units in both mutants suggests that CSE is active in the general phenylpropanoid pathway after the branch leading to H units but before the pathways for G and S units diverge. At this part of the pathway, HCT, C3H, and caffeoyl-CoA *O*-methyltransferase (CCoAOMT) are also active (Fig. 1) and, accordingly, plants with reduced HCT and C3H activity also have lignin enriched in H units (14, 19, 20).

Because lignin composition was altered in both *cse* mutant alleles, we expected to find a shift in phenolic metabolism. We analyzed methanol-soluble phenolics of stem extracts of both *cse* mutant alleles by liquid chromatography mass spectrometry (LC-MS) (5). The abundance of two compounds, both oligolignols containing G and S units, was reduced in each mutant allele (compounds 28 and 29; figs. S7 and S8 and table S3). These findings are consistent with the reduced biosynthesis of lignin in the *cse* mutants, because the abundance of oligolignols during *Arabidopsis*

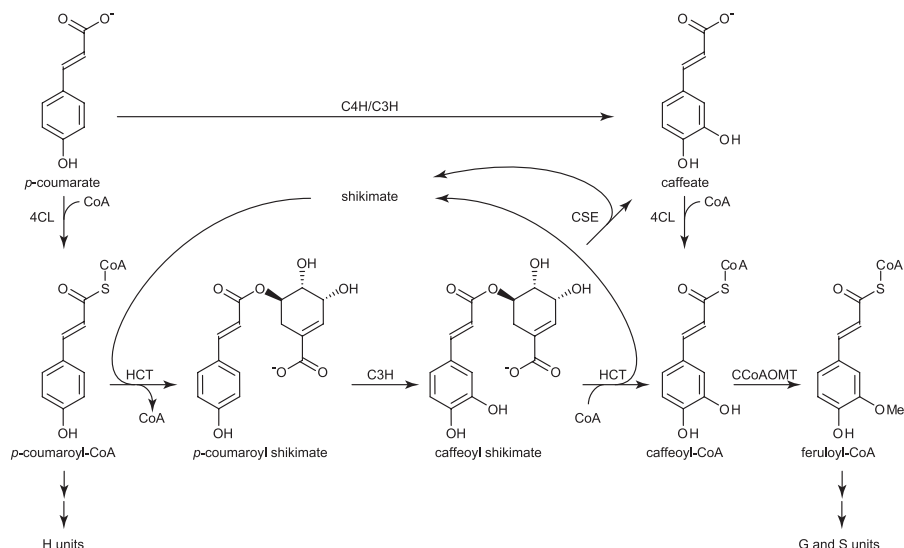


Fig. 1. The lignin biosynthetic pathway incorporating the CSE-dependent reaction established in this study.

¹Department of Plant Systems Biology, VIB (Flanders Institute for Biotechnology), Technologiepark 927, B-9052 Ghent, Belgium.

²Department of Plant Biotechnology and Bioinformatics, Ghent University, Technologiepark 927, B-9052 Ghent, Belgium.

³Division of Plant Sciences, College of Life Sciences, University of Dundee at the James Hutton Institute, Dundee DD2 5DA, UK.

⁴Departments of Biochemistry and Biological Systems Engineering, and the Department of Energy Great Lakes Bioenergy Research Center, the Wisconsin Energy Institute, University of Wisconsin, Madison, 1552 University Avenue, Madison, WI 53726, USA.

⁵Protein Service Facility, Department for Molecular Biomedical Research, VIB, Ghent University, Technologiepark 927, B-9052 Ghent, Belgium. ⁶Cell and Molecular Science, James Hutton Institute, Invergowrie, Dundee DD2 5DA, UK.

*Corresponding author. E-mail: wout.boerjan@psb.vib-ugent.be (W.B.); c.halpin@dundee.ac.uk (C.H.)

†These authors contributed equally to this work.

‡These authors contributed equally to this work.

§These authors contributed equally to this work.

stem development is correlated with the amount of lignin (7). Of the 27 compounds with increased abundance in the *cse* mutants as compared to the wild type, 21 could be identified. Nineteen were caffeate- and ferulate-derived products (figs. S7 and S8), of which caffeoyl shikimate was most abundant (Fig. 3). In addition, (hexosylated) H unit-containing oligolignols accumulated in the *cse* mutants, as well as a neolignan containing an H unit and ferulate (figs. S7 and S8). These data also support the hypothesis that CSE functions after the branch in the lignin pathway where G and S unit biosynthesis diverges from that of H units.

Some of the compounds that accumulate in *cse* mutants relative to the wild type might be substrates for CSE. In order to test this possibility, we incubated purified recombinant CSE enzyme with extracts of *cse-1* mutants, after the complexity of the extract had been reduced by chromatographic separation into 96 fractions. Three compounds decreased in abundance upon treatment with CSE, and new compounds appeared in the same fractions (fig. S9 and tables S4 and S5). Caffeoyl shikimate, which was the compound that showed greatest abnormal accumulation in *cse* mutants, was almost completely hydrolyzed

(97%) by recombinant CSE into caffeic acid (fig. S9). Modeling the structure of CSE revealed that caffeoyl shikimate could fit into the active site (fig. S10). Correspondingly, crude extracts from *cse-2* lignifying tissues were less able to hydrolyze caffeoyl shikimate into caffeate than those of the wild type (fig. S11). We therefore suggest that caffeoyl shikimate is a substrate for CSE in vivo. Because caffeoyl shikimate is an accepted intermediate in lignin biosynthesis (Fig. 1) (13, 15, 21), this places CSE in the lignin biosynthetic pathway. The Michaelis-Menten constant (K_m) and maximum reaction velocity (V_{max}) values of CSE for caffeoyl shikimate were 96.5 μ M and 9.3 picokatal (pkat) per μ g of protein, respectively (Fig. 3). We also tested *p*-coumaroyl shikimate, which is structurally similar to caffeoyl shikimate and an intermediate in the phenylpropanoid pathway, as a potential substrate of CSE (13, 15). The K_m and V_{max} values of CSE for *p*-coumaroyl shikimate were 211 μ M and 0.66 pkat per μ g of protein, respectively. Thus, CSE showed a higher affinity for caffeoyl shikimate, with a V_{max}/K_m value that is 31 times greater than that for *p*-coumaroyl shikimate, suggesting that caffeoyl shikimate is the preferred CSE substrate.

Current lignin pathway models indicate that caffeoyl shikimate is converted to caffeoyl-CoA (Fig. 1) (1, 6, 16). When we tested whether this reaction could also be catalyzed by CSE with caffeoyl shikimate and CoA as substrates, only caffeate, but not caffeoyl-CoA, was produced (fig. S12). Our data suggest that current lignin biosynthetic pathway models should be revised to include the CSE-catalyzed conversion of caffeoyl shikimate into caffeate, although we cannot exclude the possibility that CSE can convert caffeoyl shikimate into other phenolic compounds in vivo.

Because the *Arabidopsis* 4CLs involved in lignification (4CL1 and 4CL2) have K_m and V_{max} values of the same order of magnitude for both *p*-coumarate and caffeate (7, 22, 23), caffeate might be used by 4CL to form caffeoyl-CoA in vivo (Fig. 1). Current pathway models indicate direct conversion by HCT of caffeoyl shikimate and CoA into caffeoyl-CoA (1, 6, 16). We confirmed that purified recombinant *Arabidopsis* HCT enzyme could indeed catalyze this reaction (fig. S13). These data show that caffeoyl shikimate may be a substrate for both CSE and HCT in vivo. A HCT-dependent route from caffeoyl shikimate to caffeoyl-CoA (Fig. 1) may explain how residual lignin in the *cse-2* null mutant is synthesized. In addition, the C3H/C4H (cinnamate 4-hydroxylase) heteromeric complex may contribute to carbon flux toward lignin (Fig. 1), because homologs of these enzymes from poplar have been shown to

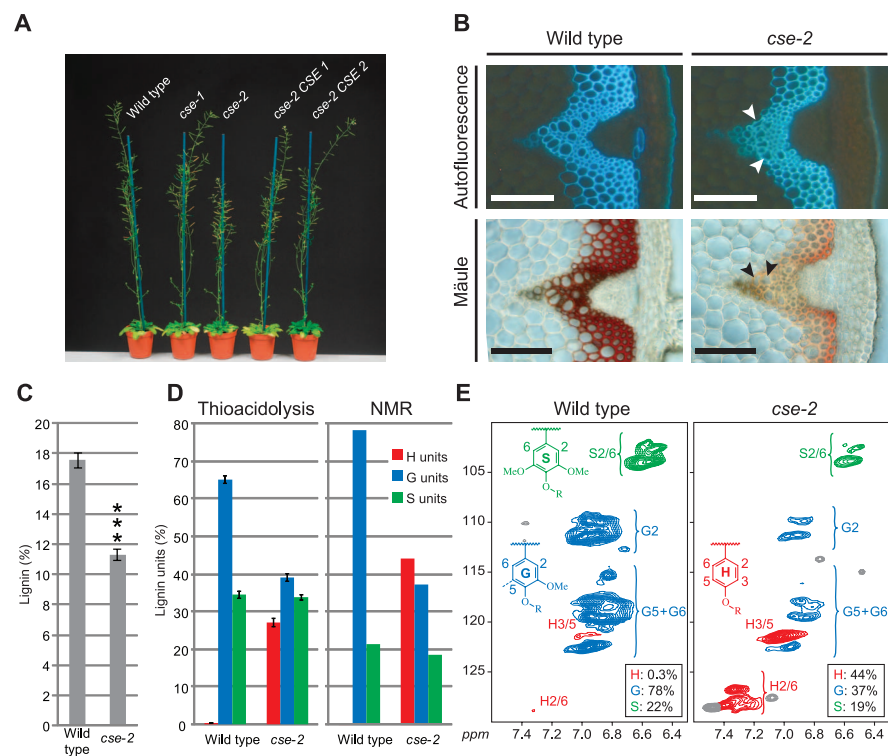


Fig. 2. Phenotype and lignin characteristics of *cse* mutants. (A) Fully grown plants after cultivation for 8 weeks in short day photoperiods and for 5 weeks in long day photoperiods. Height and weight measurements are in fig. S5. (B) Transverse stem sections of *cse-2* mutants and wild-type plants. Wiesner staining and additional images of *cse-1*, *cse-2* CSE 1, and *cse-2* CSE 2 sections are in fig. S5. Collapsed vessel elements are indicated by arrowheads. Scale bar, 100 μ m. (C) Lignin levels determined by the acetyl bromide method. See table S2 for lignin data of *cse-1*. ***0.001 > *P*; unpaired two-sided *t* test (D) Relative H:G:S lignin composition as determined by thioacidolysis (left) and from whole-cell wall NMR integrals (right). See table S2 for full thioacidolysis details. (E) Partial short-range ^{13}C - ^1H [heteronuclear single-quantum coherence (HSQC)] spectra (aromatic region) of the cell walls of *cse-2* mutants and wild-type plants. For the side-chain region of the HSQC spectra, see fig. S6. Error bars indicate \pm SEM.

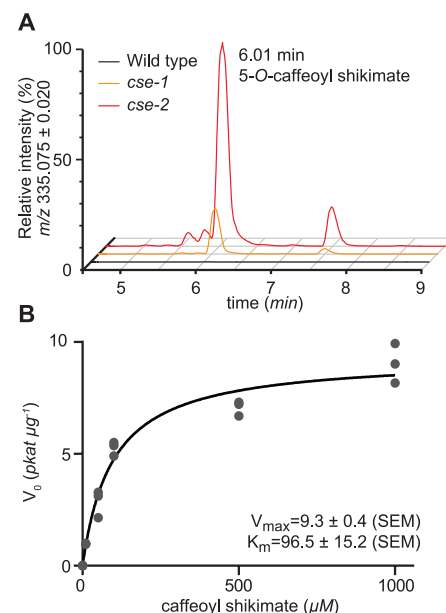


Fig. 3. Caffeoyl shikimate accumulates in *cse* mutants and is hydrolyzed by CSE. (A) Representative LC-MS chromatograms of wild type, *cse-1*, and *cse-2* plants, showing the increased peak of caffeoyl shikimate in the *cse* mutants. See fig. S7 and table S3 for full details. *m/z*, mass-to-charge ratio. (B) Enzyme kinetics curve measured with the recombinant CSE, showing that CSE accepts caffeoyl shikimate as a substrate.

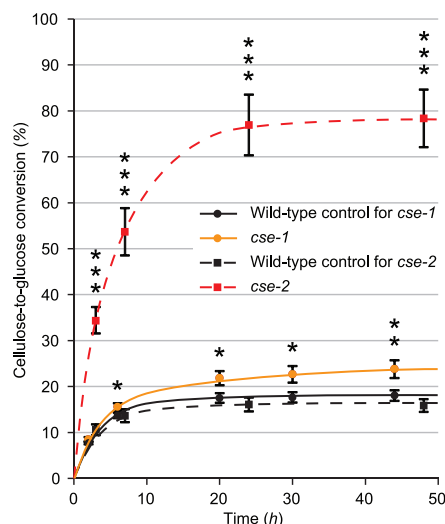


Fig. 4. Cellulose-to-glucose conversion during saccharification of the senesced inflorescence stems of *cse* mutants. h, hours. Error bars indicate \pm SEM. * $0.05 > P > 0.01$, ** $0.01 > P > 0.001$, *** $0.001 > P$; unpaired two-sided *t* test.

convert *p*-coumarate to caffeate (24). However, these alternative routes to lignin biosynthesis do not fully compensate for a loss of CSE activity, because *cse* mutants are compromised in lignification and development. Likewise, the accumulation of caffeoyl shikimate that occurs in *cse* mutants suggests that HCT is relatively ineffective at metabolizing this substrate in vivo.

Lignin limits the processing of plant biomass to fermentable sugars (25, 26). Processing of *cse* mutant plants, which have reduced lignin content, might yield more sugars on saccharification. We compared cellulose-to-glucose conversion of senesced stems from both *cse* mutants and wild-type plants. Cell wall residues of senesced inflorescence stems of *cse-1* have normal amounts of cellulose, whereas those of *cse-2* have 73% of the normal amount of cellulose (table S2). The cellulose-to-glucose conversion of the untreated cell wall residue was monitored over a period of 48 hours (Fig. 4); when the plateau was reached, the conversion had increased from ~18% in the wild type to ~24% in *cse-1* (i.e., a relative increase of 32%) and to ~78% (fourfold higher than in the wild type) in *cse-2*. Therefore, saccharification efficiency increases as lignin content decreases. On a plant basis, *cse-2* mutants released 75% more glucose than the wild type. Saccharification efficiency from material derived from *cse-2* plants is similar to that of *ccr1-3*, a mutant in the lignin pathway gene for cinnamoyl-CoA reductase that has the highest saccharification efficiency described so far (26).

We found orthologs of CSE in a wide range of plant species (fig. S14), including biofuel feedstocks such as poplar, eucalyptus, and switchgrass. Consistent with a potential conserved role in lignification, CSE copurifies with lignin biosynthetic enzymes in extracts from poplar xylem

(27). The characterization of CSE in other species will reveal how widely the revision of the lignin biosynthetic pathway we propose here applies and whether CSE could be a generally useful target for reducing cell wall recalcitrance to digestion or industrial processing in biomass crops.

References and Notes

1. J. K. Weng, C. Chapple, *New Phytol.* **187**, 273–285 (2010).
2. F. Yang *et al.*, *Plant Biotechnol. J.* **11**, 325–335 (2013).
3. N. Mitsuda *et al.*, *Plant Cell* **19**, 270–280 (2007).
4. R. Zhong, E. A. Richardson, Z. H. Ye, *Planta* **225**, 1603–1611 (2007).
5. R. Vanholme *et al.*, *New Phytol.* **196**, 978–1000 (2012).
6. W. Boerjan, J. Ralph, M. Baucher, *Annu. Rev. Plant Biol.* **54**, 519–546 (2003).
7. R. Vanholme *et al.*, *Plant Cell* **24**, 3506–3529 (2012).
8. F. Chen *et al.*, *Plant J.* **48**, 113–124 (2006).
9. J. M. Humphreys, C. Chapple, *Curr. Opin. Plant Biol.* **5**, 224–229 (2002).
10. N. D. Bonawitz, C. Chapple, *Annu. Rev. Genet.* **44**, 337–363 (2010).
11. K. Freudenberg, A. C. Neish, in *Constitution and Biosynthesis of Lignin*, vol. 2 of *Molecular Biology, Biochemistry and Biophysics*, A. Kleinzeller, G. F. Springer, H. G. Wittman, Eds. (Springer-Verlag, New York, 1968), pp. 1–129.
12. J. Ralph *et al.*, *Phytochem. Rev.* **3**, 29–60 (2004).
13. G. Schoch *et al.*, *J. Biol. Chem.* **276**, 36566–36574 (2001).
14. R. Franke *et al.*, *Plant J.* **30**, 47–59 (2002).
15. R. Franke *et al.*, *Plant J.* **30**, 33–45 (2002).
16. L. Hoffmann, S. Maury, F. Martz, P. Geoffroy, M. Legrand, *J. Biol. Chem.* **278**, 95–103 (2003).
17. W. Gao, H. Y. Li, S. Xiao, M. L. Chye, *Plant J.* **62**, 989–1003 (2010).
18. S. R. Turner, C. R. Somerville, *Plant Cell* **9**, 689–701 (1997).
19. X. Li, N. D. Bonawitz, J.-K. Weng, C. Chapple, *Plant Cell* **22**, 1620–1632 (2010).
20. S. Besseau *et al.*, *Plant Cell* **19**, 148–162 (2007).
21. H. D. Coleman, J.-Y. Park, R. Nair, C. Chapple, S. D. Mansfield, *Proc. Natl. Acad. Sci. U.S.A.* **105**, 4501–4506 (2008).
22. J. Ehling *et al.*, *Plant J.* **19**, 9–20 (1999).
23. J. Raes, A. Rohde, J. H. Christensen, Y. Van de Peer, W. Boerjan, *Plant Physiol.* **133**, 1051–1071 (2003).
24. H.-C. Chen *et al.*, *Proc. Natl. Acad. Sci. U.S.A.* **108**, 21253–21258 (2011).
25. F. Chen, R. A. Dixon, *Nat. Biotechnol.* **25**, 759–761 (2007).

26. R. Van Acker *et al.*, *Biotechnology for Biofuels*, www.biotechnologyforbiofuels.com/content/6/1/46 (2013).
27. R. Nilsson *et al.*, *Mol. Cell. Proteomics* **9**, 368–387 (2010).

Acknowledgments: The authors thank A. Bleys for help in preparing the manuscript and K. Graham for technical support. We gratefully acknowledge funding through the European Commission's Directorate-General for Research within the 7th Framework Program (FP7/2007–2013) under grant agreements 211982 (RENEWALL) and 270089 (MULTIBIOPRO); Stanford University's Global Climate and Energy Project (Towards New Degradable Lignin Types, Novel Mutants Optimized for Lignin, Growth and Biofuel Production via Re-Mutagenesis, and Efficient Biomass Conversion: Delineating the Best Lignin Monomer-Substitutes); the Hercules program of Ghent University for the Synapt Q-ToF (grant AUG014); the Bijzonder Onderzoeksfonds-Zware Apparatuur of Ghent University for the Fourier transform ion cyclotron resonance mass spectrometer (174PZA05); and the Multidisciplinary Research Partnership Biotechnology for a Sustainable Economy (01MRB510W) of Ghent University. R.V. is indebted to the Research Foundation-Flanders for a postdoctoral fellowship and L.S., I.C., and P.A. to the Agency for Innovation by Science and Technology (IWT), CAPES-Brazil (grant 201660/2010-5), and the CNPq-Brazil sandwich Ph.D. (grant 201998/2011-4), respectively, for predoctoral fellowships. J.R. and H.K. were funded in part by the U.S. Department of Energy's Great Lakes Bioenergy Research Center (DOE Office of Science BER DE-FC02-07ER64494). G.G.S. was partially funded by the Scottish Government. W.B. is on the Science Advisory Board of the NSF-funded project Regulation and Modeling of Lignin Biosynthesis, DBI-0922391. A patent application, "Modified plants" PCT/GB2013/051206, on the modification of CSE expression to improve processes that require carbohydrate extraction, has been filed jointly by the University of Dundee and the Flanders Institute for Biotechnology (VIB).

Supplementary Materials

www.sciencemag.org/cgi/content/full/science.1241602/DC1
Materials and Methods
Figs. S1 to S14
Table S1 to S5
References (28–55)

7 June 2013; accepted 5 August 2013
Published online 15 August 2013;
10.1126/science.1241602

Epigenetic Regulation of Mouse Sex Determination by the Histone Demethylase Jmjd1a

Shunsuke Kuroki,¹ Shogo Matoba,² Mika Akiyoshi,¹ Yasuko Matsumura,¹ Hitoshi Miyachi,¹ Nathan Mise,^{2*} Kuniya Abe,² Atsuo Ogura,² Dagmar Wilhelm,^{3†} Peter Koopman,³ Masami Nozaki,⁴ Yoshiakira Kanai,⁵ Yoichi Shinkai,^{6‡} Makoto Tachibana^{1,7‡}

Developmental gene expression is defined through cross-talk between the function of transcription factors and epigenetic status, including histone modification. Although several transcription factors play crucial roles in mammalian sex determination, how epigenetic regulation contributes to this process remains unknown. We observed male-to-female sex reversal in mice lacking the H3K9 demethylase Jmjd1a and found that Jmjd1a regulates expression of the mammalian Y chromosome sex-determining gene *Sry*. Jmjd1a directly and positively controls *Sry* expression by regulating H3K9me2 marks. These studies reveal a pivotal role of histone demethylation in mammalian sex determination.

The development of two sexes is essential for the survival and evolution of most animal species. Although several transcrip-

tion factors, including the factor encoded by the Y chromosome gene *Sry* (1, 2), have been shown to play crucial roles in mammalian sex differen-

tiation, the contribution of epigenetic regulation to this process is largely unknown. *Sry* is required for male development (3), with sufficient and temporally accurate expression being critical for triggering the testis-determining pathway (4, 5).

Posttranslational modifications of histones are correlated with various chromatin functions, including control of gene expression. Among them, methylation of lysine 9 and lysine 4 of histone H3 (H3K9 and H3K4) are hallmarks of transcriptionally suppressed and activated chromatin, respectively (6). *Jmjd1a* (also called Tsga/Jhdm2a/Kdm3a), an enzyme that demethylates H3K9, is crucial for gene activation in spermiogenesis and metabolism (7–12).

¹Experimental Research Center for Infectious Diseases, Institute for Virus Research, Kyoto University, 53 Shogoin, Kawara-cho, Sakyo-ku, Kyoto, Japan. ²Bioresource Center, RIKEN Tsukuba Institute, 3-1-1 Koyadai, Tsukuba, Japan. ³Institute for Molecular Bioscience, The University of Queensland, Brisbane, Queensland 4072, Australia. ⁴Research Institute for Microbial Diseases, Osaka University, Suita, Osaka 565-0871, Japan. ⁵Department of Veterinary Anatomy, The University of Tokyo, Yayoi 1-1-1, Bunkyo-ku, Tokyo 113-8657, Japan. ⁶Cellular Memory Laboratory, RIKEN Advanced Science Institute, 2-1 Hirosawa, Wako-shi, Saitama 351-0198, Japan. ⁷Graduate School of Biostudies, Kyoto University, 53 Shogoin, Kawara-cho, Sakyo-ku, Kyoto, Japan.

*Present address: Department of Environmental Preventive Medicine, Jichi Medical University, 3311-1, Yakushiji, Shimotsuke, Tochigi, Japan.

†Present address: Department of Anatomy and Developmental Biology, Monash University, Clayton, VIC 3800, Australia.

‡Corresponding author. E-mail: yshinkai@riken.jp (Y.S.); mtachiba@virus.kyoto-u.ac.jp (M.T.)

When analyzing *Jmjd1a*-deficient (*Jmjd1a*Δ/Δ) mice, which had been established from C57BL/6 (B6) × CBA F1 embryonic stem cells (11), we found that XY animals were frequently sex-reversed (table S1), either partially (12 of 58 animals) with a testis and an ovary (Fig. 1A) or completely (34 of 58 animals) with two ovaries (fig. S1). In contrast, all XY *Jmjd1a*^{+/+} and XY *Jmjd1a*Δ/+ mice had two testes (Fig. 1B and table S1). Notably, some of the completely sex-reversed animals were fertile (tables S1 and S2). The generation and comparison of XY *Jmjd1a*-deficient mice, carrying the Y chromosome from either CBA (Y^{CBA}) or B6 (Y^{B6}) on a B6 autosomal background (fig. S2), revealed that the sex-reversal phenotype was dependent on not only the loss of *Jmjd1a* but also the genetic origin of the Y chromosome combined with the B6 background. In total, 88% of XY^{CBA} but only 14% of XY^{B6} *Jmjd1a*-deficient mice displayed abnormal sex differentiation (Fig. 1B). Spermiogenesis defects were observed in XY^{CBA} as well as XY^{B6} *Jmjd1a*-deficient testes (fig. S1), as demonstrated previously (9, 12). XX *Jmjd1a*-deficient mice underwent normal sex differentiation and were fertile (table S1 and fig. S1).

To investigate the etiology of sex reversal, we examined expression of the testicular Sertoli cell marker Sox9 (13) and the ovarian somatic cell marker Foxl2 (14) in fetal gonads after sex determination at embryonic day 13.5 (E13.5) (Fig. 1C). XY *Jmjd1a*-deficient gonads contained both

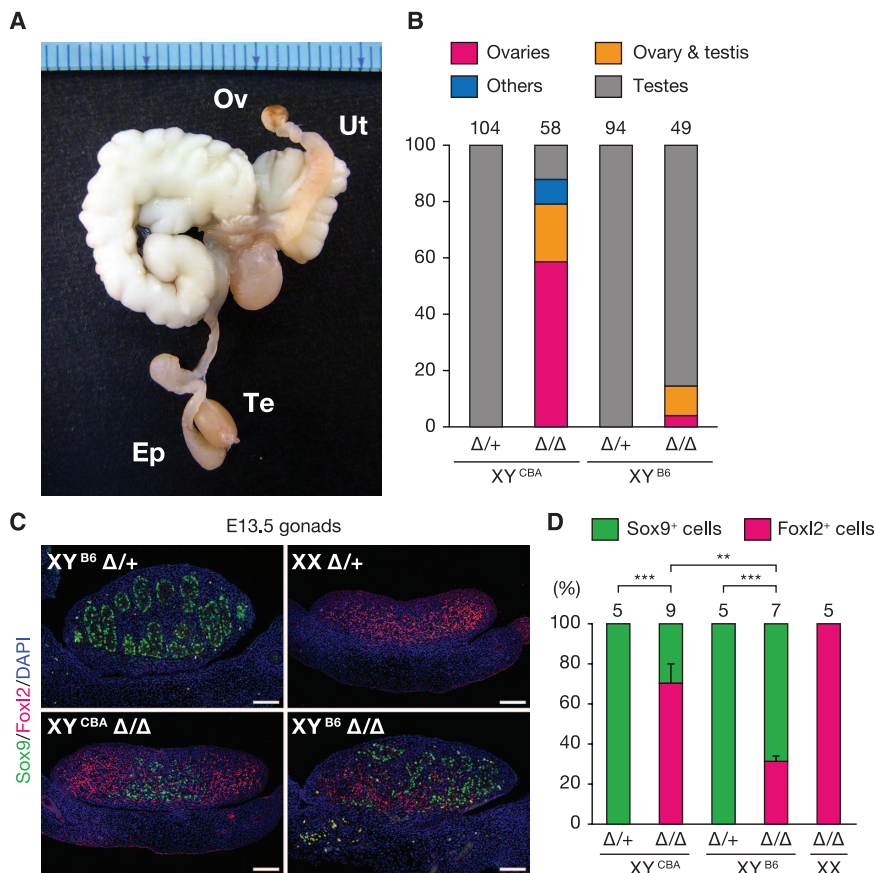
Sox9- and Foxl2-positive cells (Fig. 1D), indicative of ovotestes and therefore partial primary sex reversal, resulting from early failure of the testis-determining pathway. The number of Sox9-positive cells in XY^{B6} *Jmjd1a*-deficient gonads was higher than that in XY^{CBA}. This phenotypic difference was sustained even after the ninth generation of backcrossing to B6 (fig. S3).

To address the molecular basis of this phenotype, we determined the expression levels of *Sry* and its downstream target gene, *Sox9*. A quantitative real-time fluorescence polymerase chain reaction (RT-qPCR) analysis revealed that the *Sry* expression levels were reduced to approximately 30% in XY *Jmjd1a*-deficient gonads at E11.5 [corresponding to 17 to 19 tail somite (ts) stages (Fig. 2A)]. Expression of *Sry* was significantly lower in XY^{CBA}, as compared to XY^{B6}, in control and mutant gonads. It is conceivable that the *Sry* expression levels in *Jmjd1a*-deficient gonads at E11.5 might be near the threshold level for inducing the male pathway, and therefore the genetic background-dependent difference of *Sry* expression may critically affect the subsequent sexual development. *Sox9* expression was also reduced in XY *Jmjd1a*-deficient gonads (Fig. 2B).

A coimmunofluorescence analysis demonstrated that the number of Sry- and Sox9-positive cells was reduced to ~25% in XY *Jmjd1a*-deficient gonads at E11.5 (Fig. 2, C to F). The number of Sry-positive cells in XY^{CBA} gonads was slightly, but significantly, lower than that of XY^{B6} gonads

Fig. 1. *Jmjd1a*-deficient mice show XY sex reversal.

(A) Internal genitalia of partially sex-reversed XY *Jmjd1a*-deficient mice. Ov, ovary; Ut, uterus; Te, testis; Ep, epididymis. (B) Frequency analysis of abnormal sex differentiation between XY^{CBA} and XY^{B6} mice, determined by examining internal genitalia of adult mice. Genital classification is described in table S1 and fig. S1. Numbers of examined animals are shown above the bars. (C) Immunofluorescence analysis of E13.5 gonads. Sox9 and Foxl2 mark testicular Sertoli and ovarian somatic cells, respectively. Scale bar, 100 μm. (D) Quantification of Sox9- and Foxl2-positive cells in E13.5 gonads. Numbers of examined embryos are shown above the bars. Data are presented as mean ± SE. ***P* < 0.01; ****P* < 0.001 (Student's *t* test).



at E11.5 (fig. S4), presumably due to the different *Sry* mRNA amounts between them. On the other hand, the number of cells expressing Nr5a1, an orphan nuclear receptor expressed in gonadal somatic cells (15), was unchanged by *Jmjd1a* deficiency (fig. S5). A terminal deoxynucleotidyl transferase-mediated deoxyuridine triphosphate nick end labeling (TUNEL) assay and antibody to Ki67 immunostaining analysis demonstrated that *Jmjd1a* deficiency led to neither an increase in apoptosis nor a decrease in proliferation (fig. S6). In addition, we established a transgenic mouse line (LN#9) in which the gonadal somatic cells were specifically tagged with the cell surface marker protein CD271. The gonadal somatic cells were immunomagnetically isolated from these mice with high efficiency (fig. S7). Using these mice, we determined the numbers of gonadal somatic cells and found that control and mutant embryos contained similar numbers at E11.5 ($\sim 4 \times 10^4$ cells per gonad pair) (fig. S8), indicating that *Jmjd1a* deficiency did not affect gonadal somatic cell numbers. Thus, the critical role of *Jmjd1a* during mammalian sex determination is to ensure *Sry* expression above the threshold level.

To identify the critical step in the male sex-determining pathway that is controlled by *Jmjd1a*, we used two different approaches. First, we performed a microarray analysis to address whether *Jmjd1a* deficiency results in perturbed expression

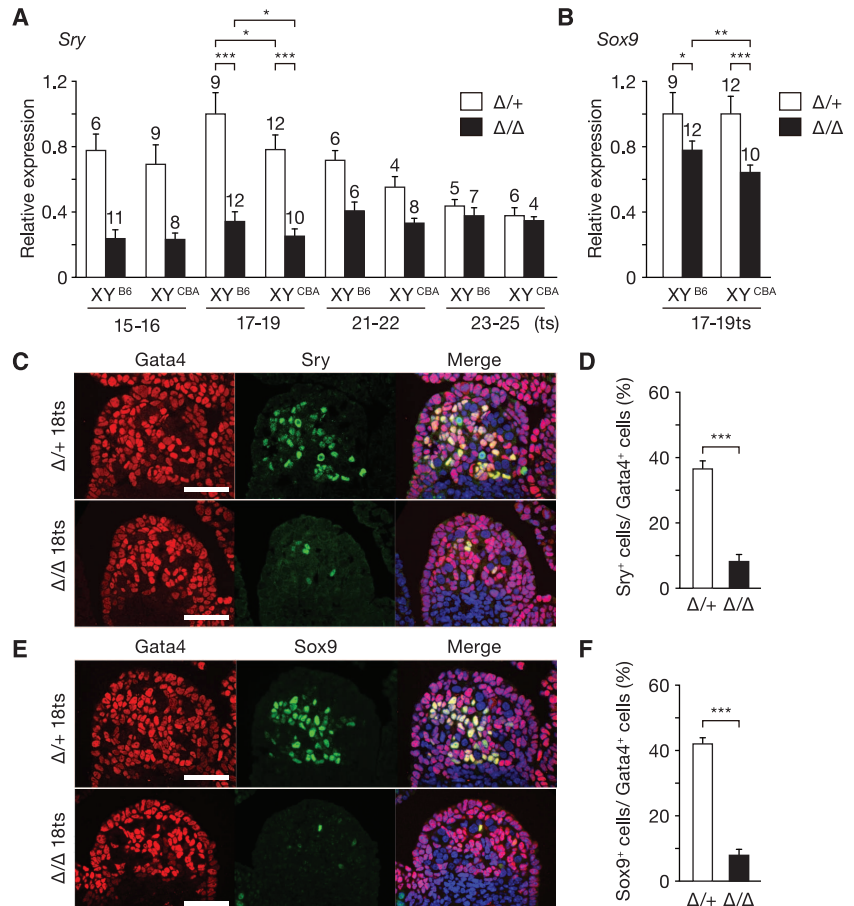
of known genes required for *Sry* expression. The analysis of a total of 41,181 probes revealed 131 genes, including *Sry*, with reduced (<0.5 -fold) expression in XY *Jmjd1a* Δ/Δ , as compared to XY *Jmjd1a* Δ^+ (table S3). However, *Jmjd1a* deficiency did not compromise expression of known *Sry* regulators (fig. S9), indicating that *Jmjd1a* contributes to a different mode of *Sry* regulation. Second, we attempted to rescue the mutant phenotype by experimentally restoring *Sry* function, by crossing the *Hsp-Sry* transgenic mouse line (16) into the *Jmjd1a*-deficient background. Forced expression of *Hsp-Sry* transgene rescued the defect of testis cord development in XY *Jmjd1a*-deficient gonads to the similar levels of those of XY control gonads (fig. S10). Furthermore, virtually no Foxl2-positive cells were observed in XY *Jmjd1a*-deficient gonads expressing the *Hsp-Sry* transgene (fig. S10), indicating that *Sry* acts epistatically to *Jmjd1a* in regulating male sex determination in mice.

We next investigated the expression profile of *Jmjd1a* protein during gonadal development. *Jmjd1a* was detected in gonadal somatic and germ cells but not in mesonephric cells at E11.5 (18 ts) (Fig. 3A). A comparative RT-qPCR analysis revealed that *Jmjd1a* was the most highly transcribed gene in E11.5 gonadal somatic cells, among those encoding enzymes involved in the maintenance of H3K9 methylation (fig. S11). An

RNA expression analysis indicated that the amount of *Jmjd1a* mRNA increased from E10.5 (8 to 10 ts) and reached a plateau around E11.5 in gonadal somatic cells (Fig. 3B). This temporal expression profile is consistent with direct regulation of *Sry* expression by *Jmjd1a*. An immunofluorescence analysis demonstrated that *Jmjd1a* deficiency resulted in an approximately two-fold increase in the signal intensities of H3K9me2 in gonadal cells at E11.5 (Fig. 3, C and D), indicating its substantial contribution to H3K9 demethylation. *Sry* expression is triggered in the center of XY gonads at around 12 ts (17, 18). We observed low levels of H3K9me2 throughout XY gonads at 12 ts (fig. S12), suggesting that *Jmjd1a* demethylates H3K9me2 before *Sry* expression. Abundant *Jmjd1a* expression and low levels of H3K9me2 were also observed in XX gonads at E11.5 (fig. S13).

To prove the direct link between *Jmjd1a* function and *Sry* expression, a chromatin immunoprecipitation (ChIP) analysis was performed, using purified gonadal somatic cells at E11.5. *Jmjd1a* was bound to regulatory regions within the *Sry* locus in wild-type cells (Fig. 4, A and B). *Jmjd1a* deficiency led to a significant increase in H3K9me2 levels within the *Sry* locus (Fig. 4C), without changing histone H3 occupancy (Fig. 4D). The H3K9me2 levels of the *Sry* locus were indistinguishable between XY^{B6} and XY^{CBA}

Fig. 2. *Jmjd1a* deficiency perturbs the expression of *Sry*. (A and B) RT-qPCR analyses of *Sry* (A) and *Sox9* (B) in XY gonads. Each of the samples included one pair of gonads/mesonephros. Results were normalized to *Gapdh*, and the expression levels in XY^{B6} *Jmjd1a* Δ^+ were defined as 1. Numbers of examined embryos are shown above the bars. (C and E) Coimmunostaining profiles of *Sry* (C) and *Sox9* (E) with the gonadal somatic cell marker, *Gata4*, in XY^{CBA} gonads. (D and F) The ratios of the cells positive for *Sry* (D) and *Sox9* (F) to the cells positive for *Gata4*. Scale bar, 50 μ m. All data are presented as mean \pm SE. * $P < 0.05$; ** $P < 0.01$; *** $P < 0.001$ (Student's *t* test).



gonads at E11.5 (fig. S14), demonstrating the conserved role of *Jmjd1a* between these genetic backgrounds. The unchanged levels of H3K9me3 at the *Sry* locus, with or without *Jmjd1a*, indicated H3K9me2-specific demethylation by *Jmjd1a* (Fig. 4E). *Jmjd1a* deficiency resulted in perturbed H3K4 methylation of the *Sry* locus (Fig. 4F). In contrast to *Sry*, the H3K9me2 levels of *Sox9* were unchanged by *Jmjd1a* deficiency (fig. S15), indicat-

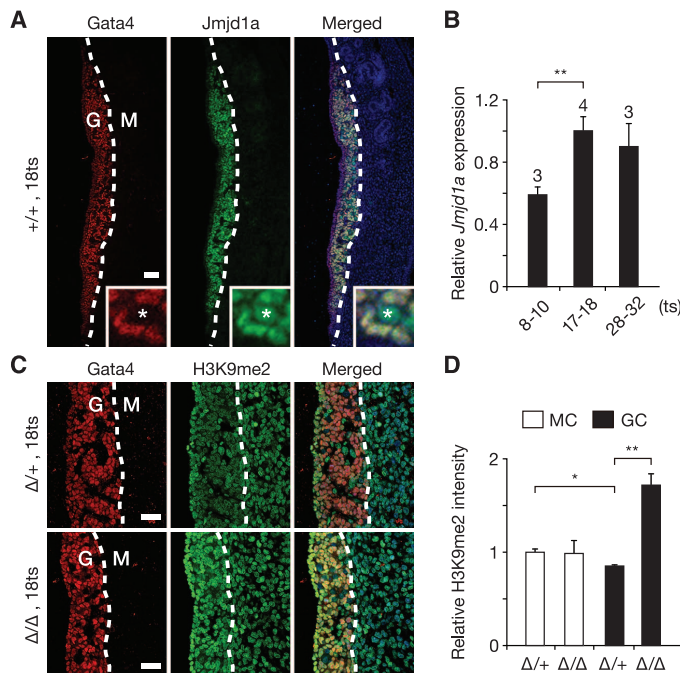
ing that *Jmjd1a* does not control *Sox9* expression directly. Coordinated H3K9 demethylation/H3K4 methylation was commonly observed in other *Jmjd1a* target genes (fig. S15), suggesting that *Jmjd1a*-mediated H3K9 demethylation is required for subsequent H3K4 methylation for transcriptional activation. Since *Sry* is located on the heterochromatic Y chromosome, *Jmjd1a*-mediated H3K9 demethylation may induce deheterochro-

matinization of *Sry*, to allow the access of the H3K4 methyltransferase and transcription factors (fig. S16).

This work shows a crucial role of a histone demethylase in *Sry* expression. Another chromatin regulator, Cbx2, reportedly plays a role in *Sry* expression in mice (19). However, in contrast to *Jmjd1a*, Cbx2 up-regulates the expression of several positive regulators of *Sry*, such as *Dax1*, *Gata4*, *Wt1*, and *Nr5a1* (19), suggesting that they might be involved in different phases of *Sry* expression. The discovery of the critical role of chromatin modification on *Sry* regulation not only provides new insights into the earliest steps of mammalian sex determination but also demonstrates the importance of epigenetic regulation in spatiotemporal gene regulation during embryonic development.

Fig. 3. *Jmjd1a* is expressed in developing gonads and catalyzes H3K9 demethylation.

(A) Coimmunostaining profiles of Gata4 and *Jmjd1a* on sections of XY^{CBA} gonads. Enlarged box indicates that *Jmjd1a* signals were observed in gonadal somatic cells as well as germ cells (asterisks). G, gonad; M, mesonephros. Scale bar, 50 μ m. (B) Quantitative analysis of *Jmjd1a* transcripts in purified gonadal somatic cells. Expression is normalized to *Gapdh*. Numbers of examined embryos are shown above the bars. (C) Coimmunostaining profiles of Gata4 and H3K9me2 in XY^{CBA} gonads. G, gonad; M, mesonephros. Scale bar, 50 μ m. (D) Quantitative comparison of the immunofluorescence intensities of H3K9me2 signals between gonadal and mesonephric cells. The intensities of H3K9me2 signals in *Jmjd1a* Δ^+ mesonephric cells were defined as 1. MC, mesonephric cells; GC, gonadal cells. All data are presented as mean \pm SE. * P < 0.05; ** P < 0.01 (Student's *t* test).



References and Notes

- R. Sekido, R. Lovell-Badge, *Trends Genet.* **25**, 19–29 (2009).
- K. Kashimada, P. Koopman, *Development* **137**, 3921–3930 (2010).
- P. Koopman, J. Gubbay, N. Vivian, P. Goodfellow, R. Lovell-Badge, *Nature* **351**, 117–121 (1991).
- R. Hiramatsu et al., *Development* **136**, 129–138 (2009).
- D. Wilhelm et al., *Mech. Dev.* **126**, 324–336 (2009).
- S. M. Koistra, K. Helin, *Nat. Rev. Mol. Cell Biol.* **13**, 297–311 (2012).
- K. Yamane et al., *Cell* **125**, 483–495 (2006).
- M. Tachibana, M. Nozaki, N. Takeda, Y. Shinkai, *EMBO J.* **26**, 3346–3359 (2007).
- Y. Okada, G. Scott, M. K. Ray, Y. Mishina, Y. Zhang, *Nature* **450**, 119–123 (2007).
- K. Tateishi, Y. Okada, E. M. Kallin, Y. Zhang, *Nature* **458**, 757–761 (2009).
- T. Inagaki et al., *Genes Cells* **14**, 991–1001 (2009).
- Z. Liu et al., *J. Biol. Chem.* **285**, 2758–2770 (2010).
- J. Kent, S. C. Wheatley, J. E. Andrews, A. H. Sinclair, P. Koopman, *Development* **122**, 2813–2822 (1996).
- K. A. Loffler, D. Zarkower, P. Koopman, *Endocrinology* **144**, 3237–3243 (2003).
- K. Morohashi, S. Honda, Y. Inomata, H. Handa, T. Omura, *J. Biol. Chem.* **267**, 17913–17919 (1992).
- T. Kidokoro et al., *Dev. Biol.* **278**, 511–525 (2005).
- M. Bullejos, P. Koopman, *Dev. Dyn.* **221**, 201–205 (2001).
- K. H. Albrecht, E. M. Eicher, *Dev. Biol.* **240**, 92–107 (2001).
- Y. Katoh-Fukui et al., *Endocrinology* **153**, 913–924 (2012).

Acknowledgments: We are especially grateful to T. Nakano for critical advice during the manuscript preparation. We thank K. Morohashi for antibodies to Nr5a1; H. Kimura for antibodies to histone; and T. Hara for fluorescence-activated cell sorting analysis support. We are also grateful to T. Matsui, G. Nagamatsu, and the members of the Tachibana laboratory for technical support. This work was supported by grants from the Funding Program for Next Generation World-Leading Researchers (M.T.). The microarray data have been deposited in the Gene Expression Omnibus and given the accession number GSE49513.

Supplementary Materials

www.sciencemag.org/cgi/content/full/341/6150/1106/DC1
Figs. S1 to S16
Tables S1 to S4
References (20–23)

30 April 2013; accepted 6 August 2013
10.1126/science.1239864

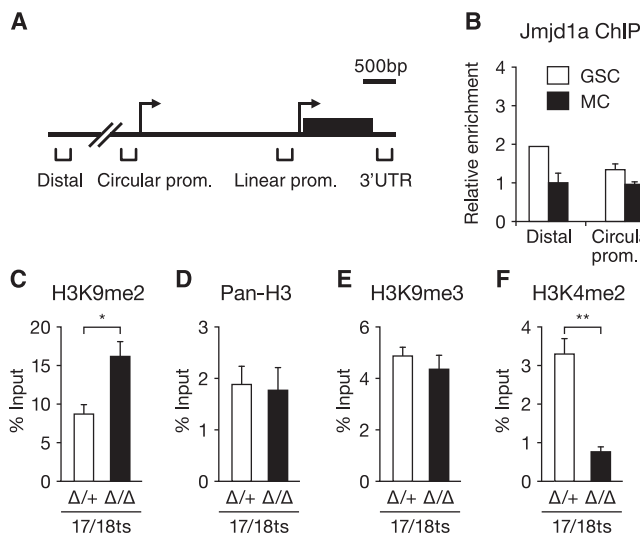


Fig. 4. *Jmjd1a* directly regulates H3K9 demethylation in the *Sry* locus.

(A) Diagram of the *Sry* locus and the location of primer sets for ChIP-qPCR. (B) ChIP analysis with antibody to *Jmjd1a*, using purified XY^{CBA} gonadal somatic cells. GSC, gonadal somatic cells; MC, mesonephric cells. (C to F) ChIP analysis for H3K9me2 (C), pan-H3 (D), H3K9me3 (E), and H3K4me2 (F) at the *Sry* linear promoter region of purified XY^{CBA} gonadal somatic cells. All data are presented as mean \pm SE. * P < 0.05; ** P < 0.01 (Student's *t* test).

F) ChIP analysis for H3K9me2 (C), pan-H3 (D), H3K9me3 (E), and H3K4me2 (F) at the *Sry* linear promoter region of purified XY^{CBA} gonadal somatic cells. All data are presented as mean \pm SE. * P < 0.05; ** P < 0.01 (Student's *t* test).

Single-Cell DNA-Methylation Analysis Reveals Epigenetic Chimerism in Preimplantation Embryos

Chanchao Lorthongpanich,^{1*†} Lih Feng Cheow,^{2†} Sathish Balu,¹ Stephen R. Quake,^{2,3} Barbara B. Knowles,^{1,4} William F. Burkholder,^{2,5,6‡} Davor Solter,^{1,7} Daniel M. Messerschmidt^{1,8‡}

Epigenetic alterations are increasingly recognized as causes of human cancers and disease. These aberrations are likely to arise during genomic reprogramming in mammalian preimplantation embryos, when their epigenomes are most vulnerable. However, this process is only partially understood because of the experimental inaccessibility of early-stage embryos. Here, we introduce a methodologic advance, probing single cells for various DNA-methylation errors at multiple loci, to reveal failed maintenance of epigenetic mark results in chimeric mice, which display unpredictable phenotypes leading to developmental arrest. Yet we show that mouse pronuclear transfer can be used to ameliorate such reprogramming defects. This study not only details the epigenetic reprogramming dynamics in early mammalian embryos but also suggests diagnostic and potential future therapeutic applications.

Genomic imprinting ensures adequate monoallelic, parent-of-origin-specific gene expression patterns in mammals (1). The importance of this process is reflected in increasing recognition of human syndromes related to imprinting defects (2, 3). Because genomic imprinting relies on locus-specific differentially methylated regions (DMRs), these defects can arise from both genetic and epigenetic mutations. These epimutations often simultaneously affect multiple loci, causing complex and little-understood phenotypes (2, 3).

Recent studies suggest that imprints are established in a two-step process of DNA methylation in the germline and subsequent, site-specific DNA-methylation maintenance during reprogramming in the preimplantation embryo (4, 5). DNA methyltransferase 1 (DNMT1), primordial germ cell protein 7 (PGC7)/STELLA, zinc finger protein 57 (ZFP57), and tripartite motif-containing 28 (TRIM28) are each required for DMR protection in the face of global DNA demethylation (6–13). It has been proposed that detrimental epimutations most likely occur when these maintenance mechanisms fail (2, 4). ZFP57, which only binds methylated imprinted alleles, mediates

specific DNA-methylation maintenance, recruiting DNMT1 through the scaffolding protein TRIM28 (10, 14, 15). Active targeting of DNMT1 is thought to be required because nuclear DNMT1 levels are very low in the preimplantation embryo facilitating genome-wide DNA demethylation (16). Disrupting this targeting complex very early in development, by eliminating maternal *Trim28*, causes stochastic DMR demethylation, which results in the phenotypic variability proposed to be caused by epigenetic chimerism (11, 12). Similarly, loss of the oocyte-specific DNMT1

variant results in mosaic defects in postimplantation embryos, whereas full deletion of DNMT1 causes complete loss of imprinting (6, 7, 13). Although it has been inferred that epigenetic mosaicism could emerge during the early preimplantation phase of development (6, 12), how such chimerism is established in time and space has not been conclusively demonstrated. To address these dynamics, we combined methylation-sensitive restriction digestion (17) and multiplexed quantitative real-time polymerase chain reaction (PCR) in a microfluidics device (Fig. 1A, detailed description in supplementary information) to analyze, simultaneously, six imprinted loci in single cells. The assay was validated by addressing DMR methylation in control oocytes (*Trim28*^f). Attesting to its robustness, we found that paternally imprinted regions were indeed unmethylated (Fig. 1B, *Trim28*^f), whereas maternally imprinted loci were reliably shown to be methylated (Fig. 1C, *Trim28*^f). We next used a *Zp3-cre* knock-out strategy (11) to genetically remove *Trim28* from oocytes (*Trim28*^{matΔ}) and addressed the effect of its absence on DMR methylation. DMR-methylation patterns remained unchanged compared with those of controls (Fig. 1, B and C, *Trim28*^{matΔ}), demonstrating that TRIM28 is not required for imprinting maintenance in growing and mature oocytes.

In contrast to the stable environment in the mature oocyte, epigenetic reprogramming initiates shortly after fertilization (18). Because the oocyte and embryo are transcriptionally silent until zygotic gene activation (ZGA) at the late two-cell stage, early embryonic processes, such as protection of

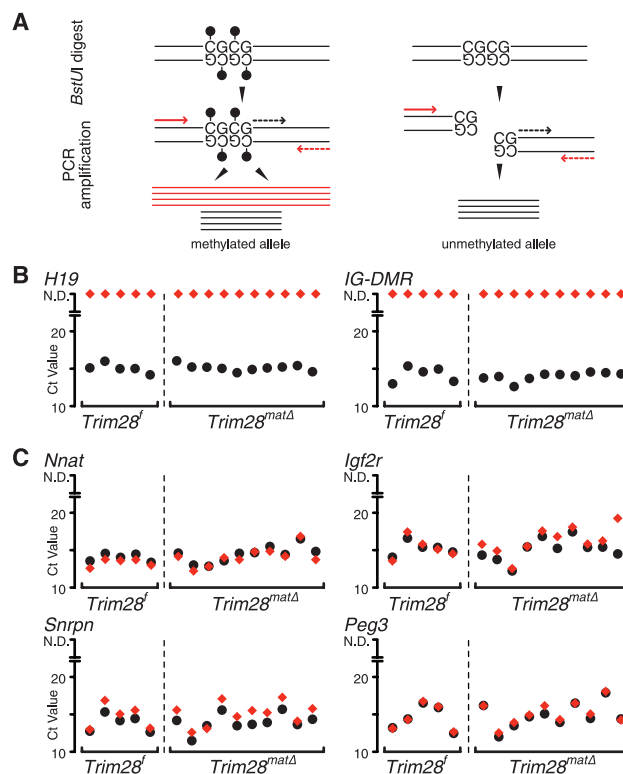


Fig. 1. Single-cell DNA-methylation analysis. (A) Illustration of the single-cell DMR-methylation assay. DNA methylation (lollipops) prevents *Bst*UI digest; both primer combinations will generate PCR products (red/black). If unmethylated, *Bst*UI cuts and the large amplicon (red) cannot be generated. Analysis of (B) paternally methylated and (C) maternally methylated DMRs in *Trim28*-null oocytes. Black dots represent cycle threshold (Ct) values of the short amplicon (positive control); red diamonds represent Ct values for the amplicon spanning the *Bst*UI restriction site. N.D., not detectable.

¹Mammalian Development Group, Institute of Medical Biology (IMB), A*STAR, Singapore. ²Microfluidics Systems Biology Lab, Institute of Molecular and Cell Biology (IMCB), A*STAR, Singapore. ³Department of Bioengineering and Department of Applied Physics, Stanford University and Howard Hughes Medical Institute, Stanford, CA, USA. ⁴The Jackson Laboratory, Bar Harbor, ME, USA. ⁵Genome Institute of Singapore, A*STAR, Singapore. ⁶Nanyang Technological University, Singapore. ⁷Duke-National University of Singapore, Graduate Medical School, Singapore. ⁸Developmental Epigenetics and Disease, IMCB, A*STAR, Singapore.

*Present address: Siriraj Center of Excellence for Stem Cell Research (SISR), Faculty of Medicine Siriraj Hospital, Mahidol University, Thailand.

†These authors contributed equally to this work.

‡Corresponding author. E-mail: danielm@imcb.a-star.edu.sg (D.M.M.); wfburkholder@gmail.com (W.F.B.)

inherited imprints, rely on maternal gene products. Mutation, reduction, or lack of maternal factors; developmental noise; or even environmental cues can result in epimutations at imprinted gene loci. Maternal deletion of *Trim28* causes such a defect, which cannot be rescued by *Trim28* reexpression from the paternal allele at ZGA (11). We and others have previously proposed that a combination of DNA-methylation-dependent targeting of TRIM28/DNMT1 through ZFP57, maternal absence, and paternal reexpression of TRIM28 could cause stochastic and mosaic imprinting defects in these embryos (12).

To conclusively demonstrate the occurrence and frequency of such defects, we used the single-cell assay to examine imprinted DMR states in maternal *Trim28*-null (*Trim28^{matΔ/+}*) and control (*Trim28^{f/+}*) eight-cell embryos. Single-cell resolution was achieved by mechanically separating embryos into eight blastomeres (14), which were

individually analyzed (Fig. 2A). Nearly all control blastomeres (99.3%, $n = 288$ DMRs) carried methylated alleles for each examined locus (Fig. 2B and fig. S1A), demonstrating very robust imprint maintenance during ongoing epigenetic reprogramming. However, blastomeres derived from maternal *Trim28*-null embryos displayed highly variable degrees of hypomethylation at all tested loci (Fig. 2B and fig. S1B). Loss of DNA methylation was not uniform across analyzed DMRs, embryos, or even among blastomeres of a given embryo. A histogram of the number of demethylated loci per cell, observed in 121 blastomeres from 16 maternal mutant embryos (Fig. 2B and fig. S1B), followed a Poisson distribution, showing that the loss of DNA methylation occurred randomly and independently at similar average rates across all cells (Fig. 2D). In agreement with observations in postimplantation maternal-null *Trim28* embryos (11), we

noted that the *H19* locus had a significantly higher incidence of demethylation (44/116 blastomeres) compared with the demethylation rate averaged across all loci (Fisher's exact test, $P = 6.2 \times 10^{-5}$). However, the degree of demethylation is notably lower than predicted assuming full penetrance of the maintenance defect and semiconservative DNA replication. This scenario should result in six demethylated and two hemimethylated blastomeres at the eight-cell stage, which is only occasionally observed (fig. S1B), considering that *BstUI* is inhibited by DNA hemimethylation (19). This incomplete penetrance can be explained by methylation protection, mediated by factors such as PGC7/STELLA and possibly by rare ZFP57/TRIM28-independent binding of DNMT1. It is important to note that ZFP57 can interact with a hemimethylated target sequence (20), which can attract paternal TRIM28 translated after ZGA (11) to restore full methylation. However, ZFP57 cannot interact with demethylated loci, which are not restored.

Despite incomplete penetrance, examining only 6 of 21 known germline DMRs reveals the prodigious potential for imprinting defect combinations, the phenotypic outcome of which will further depend on blastomere viability, and their contribution to the embryo proper. This mosaicism may account for phenotypic traits, such as occasional hemi-anophthalmia in maternal-null *Trim28* fetuses (Fig. 2E), which are hard to explain by simple genetics. Additionally, this chimerism translates into incomplete demethylation patterns when analyzing DMR methylation of DNA from whole-embryo lysates (Fig. 2F).

Although highly expressed in oocytes (11), the role of TRIM28 in imprint maintenance is restricted to postfertilization stages. To further define the temporal requirement for TRIM28, we created two different embryonic scenarios by pronuclei transfer (21). Transferring control (*Trim28^{f/+}*) pronuclei into enucleated mutant (*Trim28^{matΔ/+}*) zygotes should create a temporal reduction of maternal TRIM28, phenocopying the maternal *Trim28*-null defects. On the other hand, placing maternal *Trim28*-null pronuclei into enucleated control zygotes should provide TRIM28 to the mutant genome much earlier than achieved by ZGA, thus rescuing the defects. Control transfers (control pronuclei placed into control recipients) generated 64% viable weanlings (Fig. 3A). Yet, when control pronuclei were transferred into *Trim28*-null recipients, this survival was strongly reduced (25%, Fig. 3B), supporting our premise that maternal TRIM28 is required immediately postfertilization, before, and possibly beyond ZGA. However, 25% survival contrasts with no survival of unmanipulated maternal *Trim28*-null embryos (Fig. 3D). Carry-over of DNA-bound TRIM28 in control pronuclei may increase the yield of viable offspring.

Transferring the genetic material from a defective into a healthy, enucleated recipient egg or zygote can overcome mitochondrial disease (22–24). We asked whether early epigenetic defects

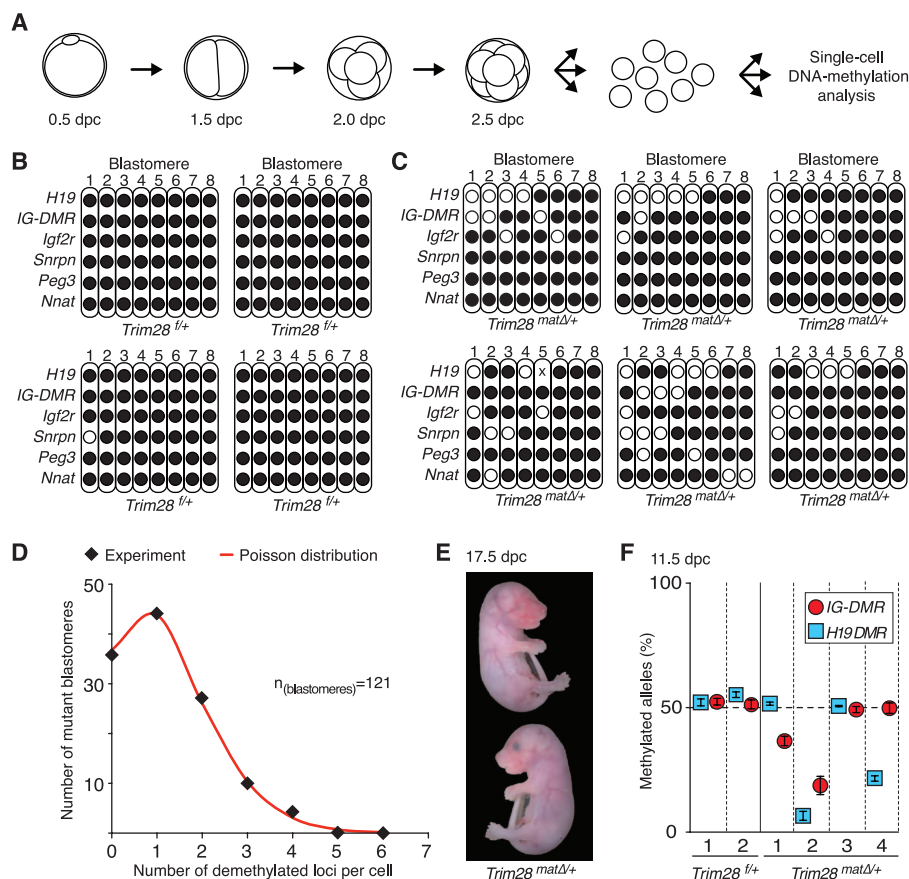


Fig. 2. Mosaic DMR-demethylation defects in maternal *Trim28* mutants. (A) Eight-cell embryos were dissected, and blastomeres were subjected to analysis. The methylation state for six DMRs in single blastomeres of (B) four *Trim28^{f/+}* and (C) six *Trim28^{matΔ/+}* eight-cell embryos is shown. Black dot indicates DNA methylation, both amplicons were detected after *BstUI* digest; white dot, no DNA methylation, only the small amplicon was detected; X, neither amplicon was detected. (D) The number of demethylated loci per cell follows a Poisson distribution (Poisson parameter λ equals the experimental mean, 1.2; data were pooled across six loci for maternal *Trim28*-null 121 blastomeres). (E) Both missing and developing eye of an 18.5-days postcoitus (dpc) maternal *Trim28*-null fetus is shown. (F) Control and maternal-mutant 11.5-dpc embryos were tested for *H19*/IG-DMR methylation by bisulfite conversion/pyrosequencing. Methylation levels in mutants range between normal (50%) and fully unmethylated, indicating chimeric imprinting defects. Error bars, standard deviation of three technical replicates.

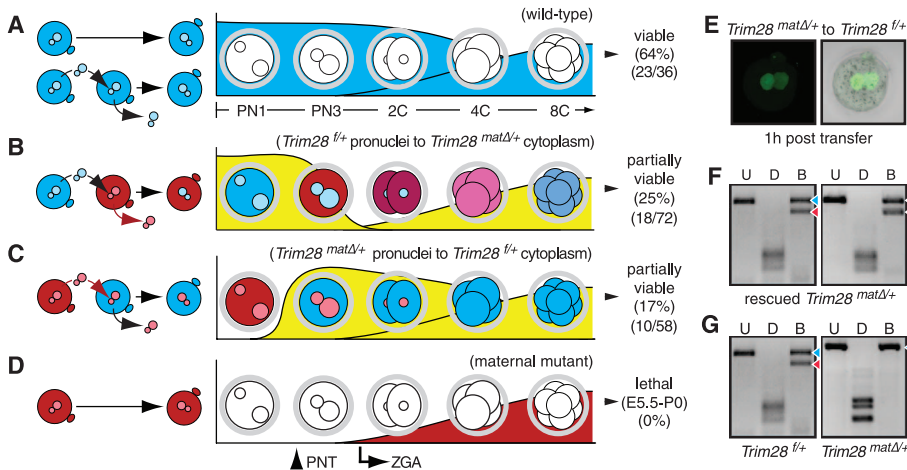


Fig. 3. Phenocopy and rescue of the maternal *Trim28*-null phenotype. (A) Control pronuclear transfer (64% viability) and schematic representation of early preimplantation development depicting maternal/zygotic *Trim28* expression. Mutant and control-derived embryos, pronuclei, and nuclei are shaded red and blue, respectively. PN, pronuclear stage; C, cell embryo; PNT, pronuclear transfer. (B) Phenocopy by transfer of control pronuclei into maternal *Trim28*-null zygotes (25% viability). (C) Partial rescue by transfer of mutant pronuclei into enucleated control zygotes (17% viability). (D) Zygotic expression of *TRIM28* alone is not sufficient to support development (0% viability). E5.5, embryonic day 5.5; P0, postnatal day 0. (E) Immunostaining of *TRIM28* in maternal *Trim28*-mutant pronuclei 1 hour posttransfer. (F) *H19* DMR methylation in tail biopsies from rescued mice displaying methylated (red arrowhead) and unmethylated (blue arrowhead) alleles comparable to a [(G), left] control transfer animal and in contrast to a [(G), right] maternal-null 12.5-dpc embryo with hypomethylated *H19* DMR. *Dral* digestion shows efficiency of bisulphite conversion; the *Bst*UI restriction site is protected from bisulphite mutagenesis if methylated. U, undigested; D, *Dral*; B, *Bst*UI.

caused by maternal deficiencies could also be rescued by this approach (Fig. 3C). Maternal *Trim28*-null pronuclei, when placed into enucleated control zygotes, displayed nuclear *TRIM28* within 1 hour of transfer (Fig. 3E). Indeed, early *TRIM28* presence allowed 17% of these embryos to develop into pups, in contrast to the total lack of viable pups obtained from unmanipulated maternal *Trim28*-null zygotes (Fig. 3D). These “rescue pups” became fertile adults and showed normal *H19* DMR methylation (the most frequently affected imprinted locus in maternal-null *Trim28* mutants) in tail biopsies (10/10), comparable to controls and in contrast to maternal-null embryos (Fig. 3, F and G). The rescue again shows that *Trim28* is not necessary during oocyte maturation because *Trim28* null-derived pronuclei do support normal development. The incompleteness of the rescue is most likely explained by a very early, postfertilization requirement for *TRIM28*. Simultaneous transfer of both pronuclei requires their close proximity, which is reached only at the late pronuclear stage 3, when reprogramming and replication is well under way (25). Prolonged exposure to a maternal *Trim28*-null environment could cause sufficient, irreversible damage to some pronuclei and thus reduce rescue efficiency.

During early embryonic development, DNA methylation at imprinted gene loci is robustly maintained by several maternal factors, including *TRIM28*. By analyzing preimplantation embryos on a single-cell level, we show that absence of

maternal *Trim28* causes highly asynchronous, aberrant demethylation. This creates complex chimeras, providing an explanation for the innumerable permutations of defects and composite phenotypes previously described (11). Similar scenarios are likely to apply to other maternal factors but also to human imprinting syndromes. The variable degree of DMR hypomethylation observed in patients (2) likely reflects pools of normally and aberrantly imprinted cells, similar to the case of the maternal-null *Trim28* embryos (Fig. 2F). This type of mosaicism has been proposed for several imprinting syndromes, including transient neonatal diabetes (TND) (26). Moreover, other rare human syndromes or embryonic defects resulting in molar pregnancies and abortion could also have their yet-unrecognized basis in the random multiplicity of epimutations (2). The single-cell DNA-methylation assay is a powerful tool to address such defects and is well suited for accurate diagnosis in these patients or to address the occurrence of rare, random imprinting defects suspected to result from assisted reproductive technology (27). Last, we provide initial evidence for a potential therapeutic approach. In mice, pronuclear transfer into healthy enucleated zygotes can ameliorate epimutations caused by the absence of maternal *Trim28*, a scenario that might apply to other maternal epigenetic regulators or to any maternal cytoplasmic defect. Homozygous mutations in *ZFP57* have been described in some TND pedigrees (28), yet it remains to be seen whether homozygous female

patients are fertile and their (maternal-null) progeny display imprinting defects. A pronuclear transfer approach, as it is already explored in humans to prevent mitochondrial disease (22–24), may be developed to prevent the development of epimutation-based imprinting syndromes.

References and Notes

1. A. C. Ferguson-Smith, *Nat. Rev. Genet.* **12**, 565–575 (2011).
2. S.-I. Tomizawa, H. Sasaki, *J. Hum. Genet.* **57**, 84–91 (2012).
3. J. T. Lee, M. S. Bartolomei, *Cell* **152**, 1308–1323 (2013).
4. G. Kelsey, R. Feil, *Philos. Trans. R. Soc. London Ser. B* **368**, 20110336 (2013).
5. R. Strogantsev, A. C. Ferguson-Smith, *Brief Funct. Genomics* **11**, 227–239 (2012).
6. C. Y. Howell *et al.*, *Cell* **104**, 829–838 (2001).
7. R. Hirasawa *et al.*, *Genes Dev.* **22**, 1607–1616 (2008).
8. T. Nakamura *et al.*, *Nat. Cell Biol.* **9**, 64–71 (2007).
9. X. Li *et al.*, *Dev. Cell* **15**, 547–557 (2008).
10. S. Quenneville *et al.*, *Mol. Cell* **44**, 361–372 (2011).
11. D. M. Messerschmidt *et al.*, *Science* **335**, 1499–1502 (2012).
12. D. M. Messerschmidt, *Epigenetics* **7**, 969–975 (2012).
13. M. Toppings *et al.*, *Hum. Reprod.* **23**, 807–818 (2008).
14. C. Lorthongpanich, T. P. Y. Doris, V. Limviphuvadh, B. B. Knowles, D. Solter, *Development* **139**, 3722–3731 (2012).
15. X. Zuo *et al.*, *J. Biol. Chem.* **287**, 2107–2118 (2012).
16. R. Hirasawa, R. Feil, *Dev. Cell* **15**, 487–488 (2008).
17. M. Kantelechner *et al.*, *Nucleic Acids Res.* **39**, e44 (2011).
18. P. Hajkova, *Curr. Opin. Cell Biol.* **22**, 342–350 (2010).
19. R. J. Roberts, T. Vincze, J. Posfai, D. Macelis, *Nucleic Acids Res.* **38**, D234–D236 (2010).
20. Y. Liu, H. Toh, H. Sasaki, X. Zhang, X. Cheng, *Genes Dev.* **26**, 2374–2379 (2012).
21. J. McGrath, D. Solter, *Science* **220**, 1300–1302 (1983).
22. L. Craven *et al.*, *Nature* **465**, 82–85 (2010).
23. D. Paull *et al.*, *Nature* **493**, 632–637 (2013).
24. M. Tachibana *et al.*, *Nature* **493**, 627–631 (2013).
25. M. Wossidlo *et al.*, *Nat. Commun.* **2**, 241 (2011).
26. D. J. G. Mackay *et al.*, *Hum. Genet.* **120**, 262–269 (2006).
27. T. Kohda, F. Ishino, *Philos. Trans. R. Soc. London Ser. B* **368**, 20120353 (2013).
28. D. J. G. Mackay *et al.*, *Nat. Genet.* **40**, 949–951 (2008).

Acknowledgments: We thank H. Wollmann for scientific input and proofreading the manuscript. This work was supported by IMB, IMCB, and a Visiting Investigator Program grant from the Joint Council Office, A*STAR to S.R.Q. (project 0921100080). S.R.Q. is a founder, consultant, member of the advisory board, and equity holder of Fluidigm.

Supplementary Materials

www.sciencemag.org/cgi/content/full/341/6150/1110/DC1
Materials and Methods

Fig. S1
Table S1
References

16 May 2013; accepted 5 August 2013
10.1126/science.1240617

Neuroendocrine Control of *Drosophila* Larval Light Preference

Naoki Yamanaka,^{1*} Nuria M. Romero,^{2*} Francisco A. Martin,^{2*} Kim F. Rewitz,³ Mu Sun,⁴ Michael B. O'Connor,^{1†} Pierre Léopold^{2†}

Animal development is coupled with innate behaviors that maximize chances of survival. Here, we show that the prothoracicotrophic hormone (PTTH), a neuropeptide that controls the developmental transition from juvenile stage to sexual maturation, also regulates light avoidance in *Drosophila melanogaster* larvae. PTTH, through its receptor Torso, acts on two light sensors—the Bolwig's organ and the peripheral class IV dendritic arborization neurons—to regulate light avoidance. We found that PTTH concomitantly promotes steroidogenesis and light avoidance at the end of larval stage, driving animals toward a darker environment to initiate the immobile maturation phase. Thus, PTTH controls the decisions of when and where animals undergo metamorphosis, optimizing conditions for adult development.

Animal development is associated with multiple primitive, innate behaviors, allowing inexperienced juveniles to choose an environment that maximizes their survival fitness before the transition to adulthood. In insects, this transition is timed by a peak of ecdysone production induced by the prothoracicotrophic hormone (PTTH) (1). In the larval brain of *Drosophila*, PTTH is produced by two pairs of neurosecretory cells projecting their axons onto the prothoracic gland (PG), where ecdysone is produced (2, 3). Transition to adulthood is associated with drastic changes in larval behavior: Feeding larvae remain buried in the food, where-

as wandering larvae (at the end of larval development) crawl out and find a spot where they immobilize and pupariate (4, 5). Mechanisms allowing proper coordination of these behavioral changes with the developmental program remain elusive.

Two pairs of neurons in the central brain were recently reported to control larval light avoidance (6). Using specific antibodies to PTTH, we established that these neurons labeled by the *NP0394-Gal4* and *NP0423-Gal4* lines correspond to the PTTH-expressing neurons (Fig. 1A and fig. S1). Moreover, silencing the *ptth* gene by using *NP0423-Gal4* or a ubiquitous driver (*tub-Gal4*) impaired light avoidance (Fig. 1B and fig. S2), indicating that PTTH itself controls this behavior. PTTH activates Torso, a receptor tyrosine kinase whose knockdown in the PG prevents ecdysone production and induces a developmental delay (fig. S3, A to C) (7). In contrast, knocking down *torso* in the PG [as shown in (7)] did not cause any change in light avoidance (Fig. 1B), indicating that the role of PTTH in ecdysteroidogenesis is functionally distinct from its role in light avoidance behavior.

Because in *Drosophila* the PTTH-producing neurons only innervate the PG (2, 3) (Fig. 1A and fig. S2), we reasoned that PTTH is secreted into the hemolymph and reaches the cells or organs involved in light avoidance. Consistent with this, inactivation of PTTH-expressing neurons affects light avoidance with 8 to 10 hours delay (Fig. 2A and fig. S4), arguing against PTTH neurons projecting directly on their target cells to control light avoidance. PTTH peptide is present in the PTTH-expressing neurons throughout larval development (Fig. 2B and fig. S5) and shows a marked increase before wandering (Fig. 2B), correlating with the rapid increase of ecdysteroidogenesis at this stage (3, 8). Using an enzyme-linked immunosorbent assay (ELISA), we found that PTTH is readily detected in the hemolymph with a fluctuation pattern similar to that of its accumulation in the PTTH-expressing neurons (Fig. 2C). Furthermore, hemolymph PTTH levels were significantly decreased upon RNA interference (RNAi)-mediated knockdown of *ptth* in the PTTH-expressing neurons (Fig. 2C), suggesting that in addition to the paracrine control of ecdysteroidogenesis in the PG, PTTH also carries endocrine function.

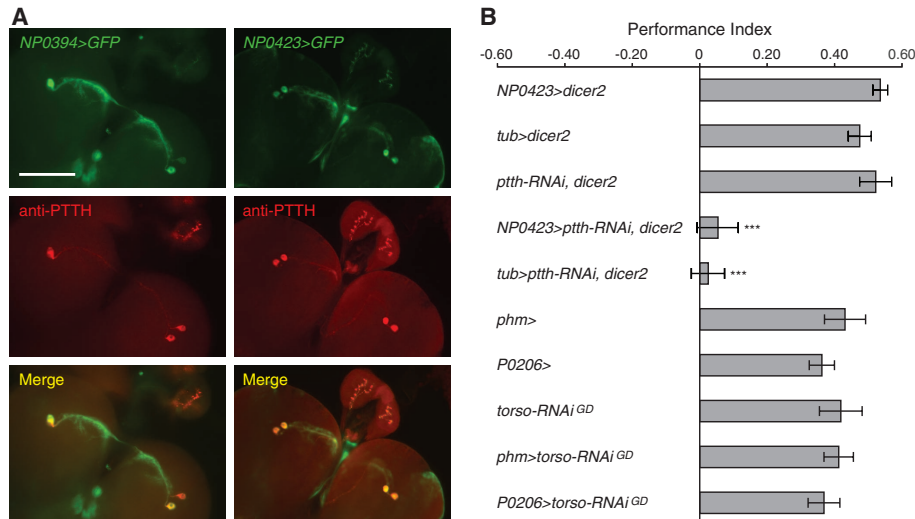
Pan-neuronal knockdown of *torso* (*elav>torso-RNAi^{GD}*) recapitulated the loss of light avoidance observed upon *torso* ubiquitous knockdown (*tub>torso-RNAi^{GD}*) (Fig. 3A), suggesting that PTTH acts on neuronal cells to control light avoidance. We specifically tested the potential role of *torso* in two neuronal populations previously identified as light sensors in *Drosophila* larvae (5): (i) the Bolwig's organ (BO) (9, 10) and (ii) the class IV dendritic arborization (da) neurons tiling the larval body wall (11). An enhancer trap analysis of *torso*, as well as *in situ* hybridization using a *torso* antisense probe, confirmed *torso* expression in class IV da neurons (fig. S6A). In parallel, *torso* transcripts were detected by means of quantitative reverse transcription polymerase chain reaction in larval anterior tips containing the BO, and their levels were efficiently knocked

¹Department of Genetics, Cell Biology and Development, University of Minnesota, Minneapolis, MN 55455, USA. ²University of Nice–Sophia Antipolis, CNRS, INSERM, Institute of Biology Valrose, Parc Valrose, 06108 Nice, France. ³Department of Biology, Cell and Neurobiology, University of Copenhagen, DK-2200 Copenhagen, Denmark. ⁴Neurodegeneration Discovery Performance Unit, GlaxoSmithKline Research and Development, Shanghai 201203, China.

*These authors contributed equally to this work.

†Corresponding author. E-mail: moconnor@umn.edu (M.B.O.); leopold@unice.fr (P.L.)

Fig. 1. PTTH controls *Drosophila* light preference. (A) Wandering third instar larval brain expressing *CD8-GFP* under the control of *NP0394-Gal4* or *NP0423-Gal4* drivers (green) were stained with antibody to PTTH (red). Scale bar, 100 μ m. (B) Foraging larvae were tested in a light/dark assay; $n \geq 15$ tests. Statistical analyses for all figures are available in the supplementary materials.



down by using the BO-specific drivers *Kr5.1-Gal4* (12) and *Rh5-Gal4* (10), demonstrating *torso* expression in the BO (fig. S6, B and C). The knockdown of *torso* in the BO (*Kr5.1>torso-RNAi^{GD}* and *GMR>torso RNAi^{GD}*) or in the class IV da neurons (*ppk>torso-RNAi^{GD}*) (11, 13) abolished larval light avoidance (motoneurons serve as a negative control: *OK6>torso-RNAi^{GD}*) (Fig. 3A) (14). Knocking down *torso* in both neuronal populations (*ppk>*, *GMR>torso-RNAi^{GD}*) mimicked the effect observed with the BO driver or class IV da neurons or in the BO had no effect on the pupariation timing (fig. S3A). Taken together,

these results indicate that PTTH/Torso signaling is required for light avoidance behavior in two distinct populations of light-sensing neurons and that this function is separate from its role in controlling developmental progression.

Drosophila light-sensing cells use photosensitive opsins that upon exposure to light, activate transient receptor potential (TRP) cation channels, thus depolarizing the membrane and triggering neural activation (15). Although the BO and class IV da neurons use different photosensitive molecules and TRP channels (5), one can

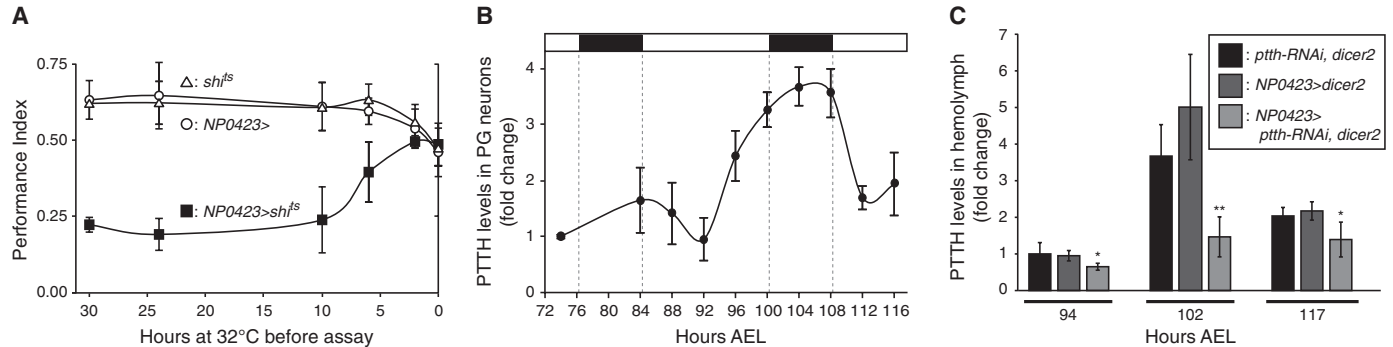
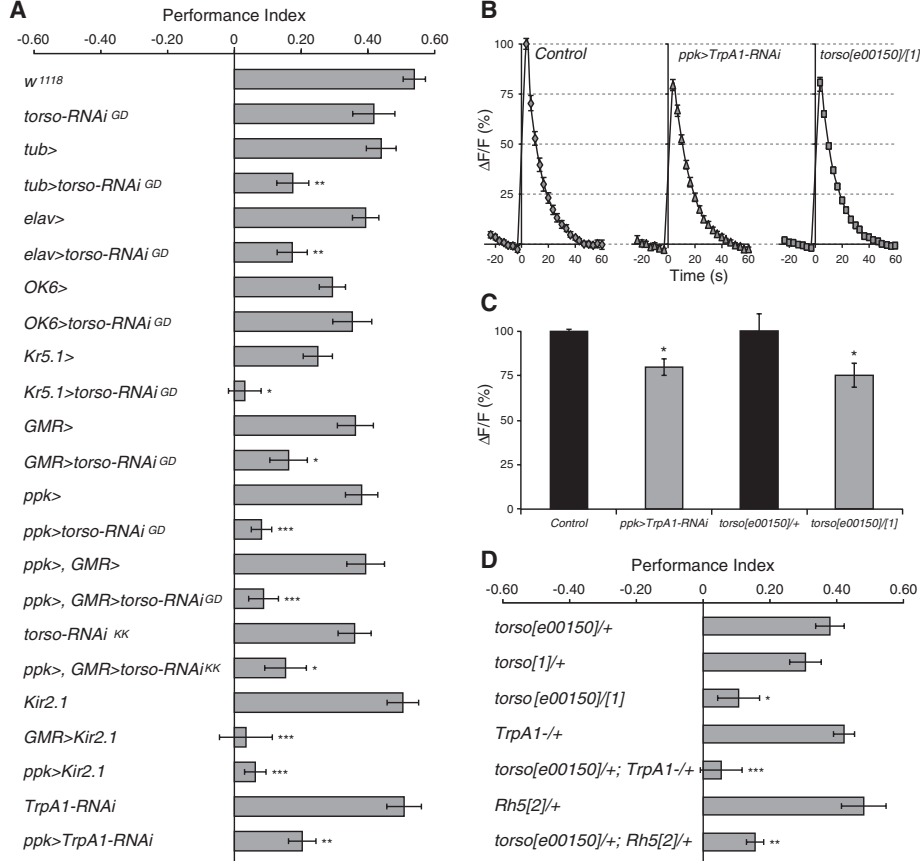


Fig. 2. Endocrine function of PTTH. (A) *NP0423>*, *UAS-shi^{ts}*, and *NP0423>shi^{ts}* third instar larvae were tested in a light/dark assay after being exposed to *Gal80^{ts}* restrictive temperature (32°C) for the indicated times; $n \geq 9$ tests for each time point. (B) PTTH protein levels in the cell bodies of PTTH-expressing neurons, measured from confocal images of

wild-type larval brains stained with antibody to PTTH. Larvae were raised on 16/8-hour light/dark cycles, with dark periods highlighted in black. Quantification is in arbitrary units relative to the 74 hours after egg laying (AEL) time point. (C) Hemolymph level of PTTH at given time points AEL was determined by means of ELISA using antibody to PTTH.

Fig. 3. PTTH/Torso signaling promotes light sensing in the BO and the class IV da neurons. (A) Light/dark preference of third instar larvae assayed in tissue-targeted RNAi or *Kir2.1* overexpression larvae; $n \geq 15$ tests. (B) Activation of GCaMP3-expressing class IV da neurons after 2-s blue light (470 nm) illuminations ($t = 0$). (C) Quantification of the maximum somatic fluorescence ($\Delta F/F$) of GCaMP3-expressing class IV da neurons; $n > 20$ neurons. (D) Light/dark preference of third instar larvae carrying *torso*, *TrpA1*, and/or *Rh5* mutations; $n \geq 15$ tests.



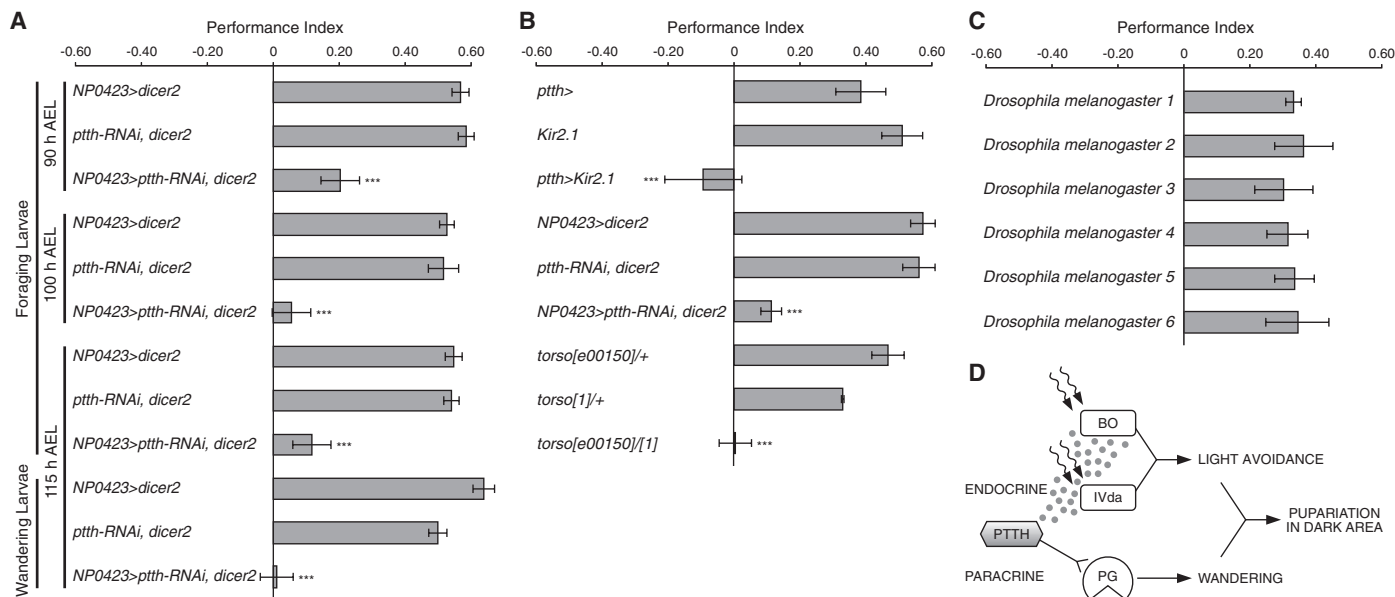


Fig. 4. PTTH/Torso signaling promotes light avoidance during the entire larval period, allowing animals to move to a dark place for pupal development. (A) Foraging and wandering larvae with indicated genotypes were tested in a light/dark assay; $n \geq 9$ tests. **(B)** Light/dark preference for

pupariation assayed on animals with indicated genotypes; $n \geq 9$ tests. **(C)** Light/dark preference for pupariation in six different isogenic wild *Drosophila melanogaster* lines; $n \geq 7$ tests. **(D)** Schematic representation of the two separate PTTH/Torso signaling functions at pupariation.

assume that PTTH/Torso signaling regulates the phototransduction pathway through a similar mechanism in both types of neurons. Immunohistochemical detection of Rh5, the opsin involved in light avoidance behavior in the BO (5), showed no difference in protein level in *torso* mutant background (fig. S8, A to C). PTTH/Torso signaling knockdown did not change the expression level of *Gr28b*, a gustatory receptor family gene that plays an opsin-like role in class IV da neurons (fig. S8D) (11). These results strongly suggest that PTTH affects signaling components downstream of the photoreceptors.

We next investigated the neural activity of the light sensors using the calcium indicator GCaMP3 for live calcium imaging. *torso* mutant class IV da neurons showed a 25% reduction of their response to light as compared with that of control (Fig. 3, B and C). This was accompanied by a loss of light avoidance (Fig. 3D), indicating that such partial reduction of the GCaMP3 signal corresponds to a reduction of neural activity strong enough to exert a behavioral effect. Indeed, blocking the firing of class IV da neurons by using *TrpA1-RNAi* (11) caused a similar 25% reduction of the GCaMP3 signal (Fig. 3, B and C) and behavioral effect (Fig. 3A). This suggests that in da neurons, PTTH/Torso signaling exerts its action upstream of TrpA1 channel activation. Accordingly, we observed a strong genetic interaction between *torso* and *TrpA1* mutants for light preference (Fig. 3D). We also detected a genetic interaction between *torso* and *Rh5* mutants (Fig. 3D), further supporting that PTTH/Torso signaling affects a step in phototransduction between the photoreceptor molecule and the TRP channel. Collectively, these data are consistent with the notion that PTTH/Torso sig-

naling acts to facilitate TRP activation downstream of photoreceptor-dependent light sensing.

A previous study suggested that larval photophobic behavior diminishes at the end of larval development, perhaps facilitating larval food exit and entry into the wandering phase (16). Our present finding and the increase of PTTH at the beginning of the wandering stage (Fig. 2, B and C) appear to contradict such a hypothesis. Indeed, we detected a sustained larval light avoidance mediated by PTTH that persisted through the wandering stage (Fig. 4A). These results imply that wandering behavior is triggered by a signal distinct from light preference. Consistent with this notion, the timing of wandering initiation in *ppk>torso-RNAi^{GD}* or *Kr5.1>torso-RNAi^{GD}* larvae was found comparable with that of control animals (fig. S3D), despite the fact that these animals are not photophobic (Fig. 3A).

As found in other insects, wandering is either directly or indirectly triggered by PTTH-induced ecdysone production (17). Therefore, concomitant PTTH-mediated photophobia could ensure that wandering larvae maintain a dark preference for pupariation site, providing better protection from predators and dehydration during the immobile pupal stage. To test this hypothesis, we developed a light/dark preference assay for pupariation (fig. S9). When exposed to a light/dark choice, larvae indeed showed a strong preference to pupariate in the dark (Fig. 4B). This behavior was abolished either by inactivating PTTH-expressing neurons (*ptth>Kir2.1*), by silencing *ptth* in the PTTH-expressing neurons (*NP0423>ptth-RNAi, dicer2*), or by introducing a *torso* mutant background (*torso[e00150]/[1]*) (Fig. 4B). Dark site preference for pupariation was observed in *Drosophila* populations collected in the wild (Fig. 4C), con-

firmed that this innate behavior was selected in a natural environment.

Our work illustrates the use of a single biochemical messenger, PTTH, for the concomitant control of two major functions during larval development (Fig. 4D). PTTH establishes a neuroendocrine link between distinct neuronal components previously shown to be involved in light avoidance. In contrast to previous interpretations (16) but consistent with another study (18), we show that wandering is independent of light preference and that PTTH maintains a strong light avoidance response through to the time of pupariation. High levels of circulating PTTH during the wandering stage could reinforce the robustness of light avoidance, which might otherwise be compromised by active roaming. This eventually promotes larvae to pupariate in the dark, a trait potentially beneficial for ecological selection. PTTH is thus at the core of a neuroendocrine network, promoting developmental progression and appropriate innate behavioral decisions to optimize fitness and survival.

References and Notes

1. N. Yamanaka, K. F. Rewitz, M. B. O'Connor, *Annu. Rev. Entomol.* **58**, 497–516 (2013).
2. T. Siegmund, G. Korge, *J. Comp. Neurol.* **431**, 481–491 (2001).
3. Z. McBrayer et al., *Dev. Cell* **13**, 857–871 (2007).
4. D. Bodenstein, in *Biology of Drosophila*, M. Demerec, Ed. (John Wiley & Sons, New York, 1950), pp. 275–367.
5. A. C. Keene, S. G. Sprecher, *Trends Neurosci.* **35**, 104–110 (2012).
6. Z. Gong et al., *Science* **330**, 499–502 (2010).
7. K. F. Rewitz, N. Yamanaka, L. I. Gilbert, M. B. O'Connor, *Science* **326**, 1403–1405 (2009).
8. J. T. Warren et al., *Dev. Dyn.* **235**, 315–326 (2006).
9. J. Hassan, B. Iyengar, N. Scantlebury, V. Rodriguez Moncalvo, A. R. Campos, *J. Comp. Neurol.* **481**, 266–275 (2005).
10. E. O. Mazzoni, C. Desplan, J. Blau, *Neuron* **45**, 293–300 (2005).

11. Y. Xiang *et al.*, *Nature* **468**, 921–926 (2010).
12. D. Schmucker, H. Taubert, H. Jäckle, *Neuron* **9**, 1025–1039 (1992).
13. W. B. Grueber, L. Y. Jan, Y. N. Jan, *Development* **129**, 2867–2878 (2002).
14. S. Sanyal, *Gene Expr. Patterns* **9**, 371–380 (2009).
15. C. Montell, *Trends Neurosci.* **35**, 356–363 (2012).
16. E. P. Sawin-McCormack, M. B. Sokolowski, A. R. Campos, *J. Neurogenet.* **10**, 119–135 (1995).
17. O. S. Dominick, J. W. Truman, *J. Exp. Biol.* **117**, 45–68 (1985).
18. T. A. Markow, *Behav. Neural Biol.* **31**, 348–353 (1981).

Acknowledgments: We thank G. Jarretou and B. Polo for technical assistance; F. Casares, J. Bessa, M. Bate, W. Johnson, C. Desplan, F. Pichaud, Y. N. Jan, and stock centers in Kyoto, Bloomington, and Vienna for fly stocks; B. Prud'homme and N. Gompel for wild *D. melanogaster* isolates; L. Vollborn for antibody to PTTH; P. Baroni for light-emitting diode spectrum analysis; and F. Rouyer, J. Simon, S. Sprecher, and laboratory members from O'Connor and Léopold groups for comments on the manuscript. This work was supported by the CNRS, INSERM, Agence Nationale de la Recherche, Fondation pour la Recherche Médicale, European Research Council (grant 268813) to N.M.R., F.A.M., and P.L.; NIH grant K99

HD073239 to N.Y.; Danish Council for Independent Research, Natural Sciences grant 11-105446 to K.F.R.; and NIH grant R01 GM093301 to M.B.O. Materials are available from CNRS under a material transfer agreement.

Supplementary Materials

www.sciencemag.org/cgi/content/full/341/6150/1113/DC1
Materials and Methods
Figs. S1 to S10
References (19–29)

29 May 2013; accepted 9 August 2013
10.1126/science.1241210

Conserved Regulation of Cardiac Calcium Uptake by Peptides Encoded in Small Open Reading Frames

Emile G. Magny,¹ Jose Ignacio Pueyo,¹ Frances M.G. Pearl,^{1,2} Miguel Angel Cespedes,¹ Jeremy E. Niven,¹ Sarah A. Bishop,¹ Juan Pablo Couso^{1*}

Small open reading frames (smORFs) are short DNA sequences that are able to encode small peptides of less than 100 amino acids. Study of these elements has been neglected despite thousands existing in our genomes. We and others previously showed that peptides as short as 11 amino acids are translated and provide essential functions during insect development. Here, we describe two peptides of less than 30 amino acids regulating calcium transport, and hence influencing regular muscle contraction, in the *Drosophila* heart. These peptides seem conserved for more than 550 million years in a range of species from flies to humans, in which they have been implicated in cardiac pathologies. Such conservation suggests that the mechanisms for heart regulation are ancient and that smORFs may be a fundamental genome component that should be studied systematically.

Thousands of small open reading frames (smORFs) exist in animal and plant genomes, yet their relevance and functionality has rarely been addressed because of their challenging properties (1). Detection of small peptides requires specific biochemical and bioinformatics techniques that are rarely used in the characterization of whole genomes. Thus, the number of translated smORFs and their biological functions are still unknown. We and others previously characterized a *Drosophila* gene, *tarsal-less (talpri)*, encoding four smORFs as short as 11 amino acids that are translated and provide essential functions during development (2–4). These results demonstrate that extremely short smORFs can be functional and suggest, when extrapolated by bioinformatics and combined with the latest data from deep RNA sequencing, that hundreds of smORF-encoding transcripts exist in the fly genome (5). However, the *tal* gene is a single example and seems present only in arthropods (2, 3, 6), leaving the questions about the conservation and wider relevance of smORFs unanswered. The characterization of several smORFs displaying conservation of amino-acid sequence, translation, and biological function of the encoded

peptides throughout evolution would be a powerful indicator that smORFs represent an important but neglected part of our genomes.

Using a bioinformatics method (5), we scrutinized the pool of polyadenylated, polysome-associated putative noncoding RNAs in which *tal* was initially included (7) and identified two potentially functional smORFs of 28 and 29 amino acids in the transcript encoded by the gene *putative noncoding RNA 003 in 2L (pncr003:2L)* (Fig. 1A) (6). As with *tal*, these smORFs have similar amino acid sequences to one another and follow strong Kozak sequences (fig. S1A). These peptides are highly hydrophobic, with a predicted alpha-helical secondary structure (fig. S1B).

We corroborated the structure and sequence of the *pncr003:2L* transcript by means of reverse transcription polymerase chain reaction (RT-PCR). Next, we studied *pncr003:2L* expression by means of in situ hybridization, which showed strong expression in somatic muscles and in the post-embryonic heart (Fig. 1, B to D, and fig. S2, A to F). We tested the in vivo translation and subcellular localization of these peptides by generating C-terminal green fluorescent protein (GFP)-tagged fusions within the *pncr003:2L* cDNA of each ORF and expressing these *UAS-smORF-GFP* fusions (fig. S8) in muscles with *Dmef2-Gal4*. We observed the GFP signal at the dyads (Fig. 1E and fig. S1, C and D) (8)—the structures in which

the sarco-endoplasmic reticulum (SER) membrane lies closest to both the plasma membrane and the sarcomeres—in order to facilitate the conversion of the voltage signal into calcium release and muscle contraction (fig. S2G). Similar results were obtained with N-terminal Flag-hemagglutinin-tagged smORFs (*UAS-FH-smORF*) (Fig. 1F and figs. S1, E and F, and S8).

To obtain a null mutant for *pncr003:2L*, we generated two small overlapping deficiencies around the {WH}f02056 insertion (Fig. 1A). Together, these two deletions generate a synthetic homozygous deficiency [“*Df(2L)scl*”] eliminating the *pncr003:2L* transcript and the *CG13283* and *CG13282* genes and represents our null condition for the *pncr003:2L* locus, as corroborated with RT-PCR and in situ hybridization (fig. S2, A to F).

Df(2L)scl mutants showed no behavioral or morphological muscle phenotype, even at the ultrastructural level (fig. S2, H to Q). We analyzed muscle function using time-lapse recordings of adult fly hearts (9), which provide an excellent read-out of muscle contraction (Fig. 2A). *Df(2L)scl* mutants showed significantly more arrhythmic cardiac contractions than those of wild-type flies (Fig. 2, A and B; tables S5 and S6; and movies S1 and S2). These effects are due to a requirement for *pncr003:2L* peptides and not the other genes removed in *Df(2L)scl* because the phenotype (i) is mimicked by RNA interference on *pncr003:2L* and (ii) is rescued by restoring expression of *UAS-pncr003:2L* or either of its encoded peptides in *Df(2L)scl* mutants, but is not rescued by smORFs carrying frameshifts in the peptide sequence (Fig. 2B, figs. S3A and S8, and tables S5 and S6). Correspondingly, intracellular electrophysiology recordings in cardiac cells show irregular action potentials (APs), involving “double” and occasionally failed APs in the nonrescued mutants (Fig. 2C, fig. S3C, and table S7).

Because the smORF peptides localize in the dyads, we checked a possible physiological function related to Ca^{2+} trafficking during muscle contraction by visualizing intracellular Ca^{2+} (9). During heart contraction, the Ca^{2+} transients of *pncr003:2L* mutants showed significantly higher amplitudes and steeper decay than those of wild-type controls (Fig. 2D; fig. S3, D and E; and table S8). Overexpression of either peptide in a wild-type fly—but not of frameshifted smORFs—produced reciprocal effects on Ca^{2+} transients but similar arrhythmias to *Df(2L)scl*. Altogether, these results suggest (i) a primary role for the *pncr003:2L* gene during Ca^{2+} trafficking at the SER, which

¹School of Life Sciences, University of Sussex, Falmer, Brighton, East Sussex BN1 9QG, UK. ²Division of Cancer Therapeutics, Institute of Cancer Research, Sutton, Surrey SM2 5NG, UK.

*Corresponding author. E-mail: j.p.couso@sussex.ac.uk

Fig. 1. *pncr003:2L* peptide expression in muscles and heart. (A) Annotated genomic region from the Flybase Genome Browser displaying *pncr003:02L*, nearby genes and deficiencies generated in this work, *Df(2L)scl¹²* (green bar), and *Df(2L)scl⁹⁶* (dark blue bar). As transheterozygous, these two deficiencies generate a homozygous deletion (*Df(2L)scl*, red bar), eliminating the *pncr003:2L* transcript and the *CG13283* and *CG13282* genes. (B to D) Expression of *pncr003:2L* mRNA in *Drosophila* muscles (arrowhead), in (B) stage 17 embryos; (C) larval somatic muscles (arrowhead) and heart (arrow), and (D) in the adult heart (arrow). (E to E'') ORFA-GFP expression (green; arrowheads) surrounding the phalloidin-stained sarcomeres (magenta) in adult transversal heart fibers. (F to F'') FH-ORFA peptides display a reticular pattern (green; arrowheads) in adult longitudinal heart fibers labeled with phalloidin (magenta). Blue, 4',6-diamidino-2-phenylindole (DAPI)-stained nuclei.

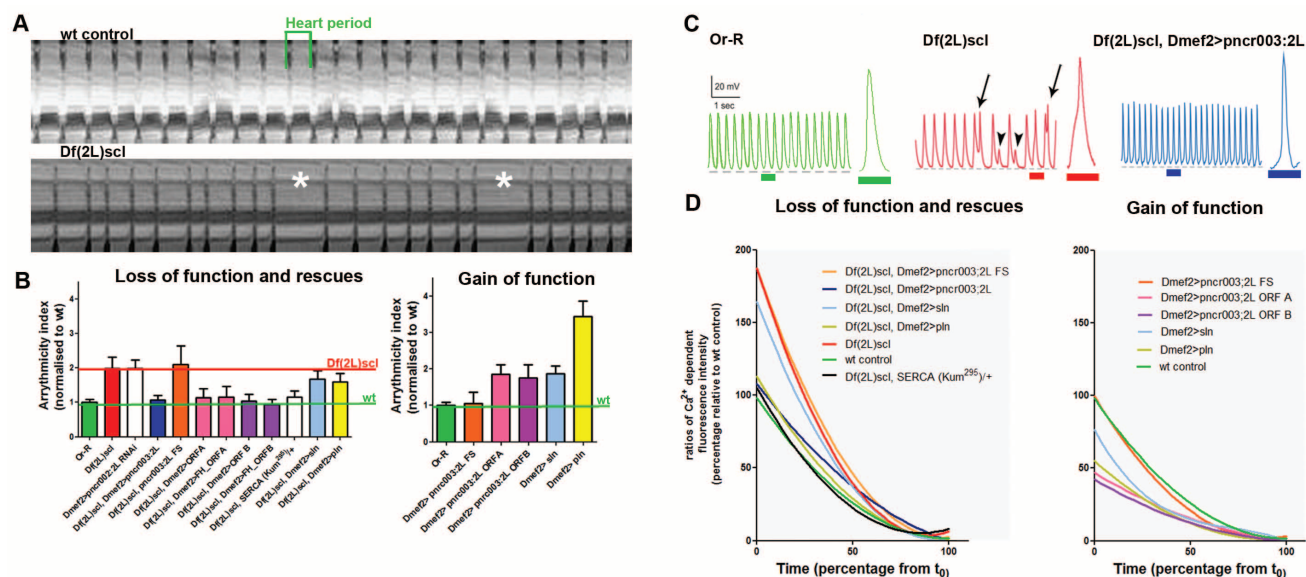
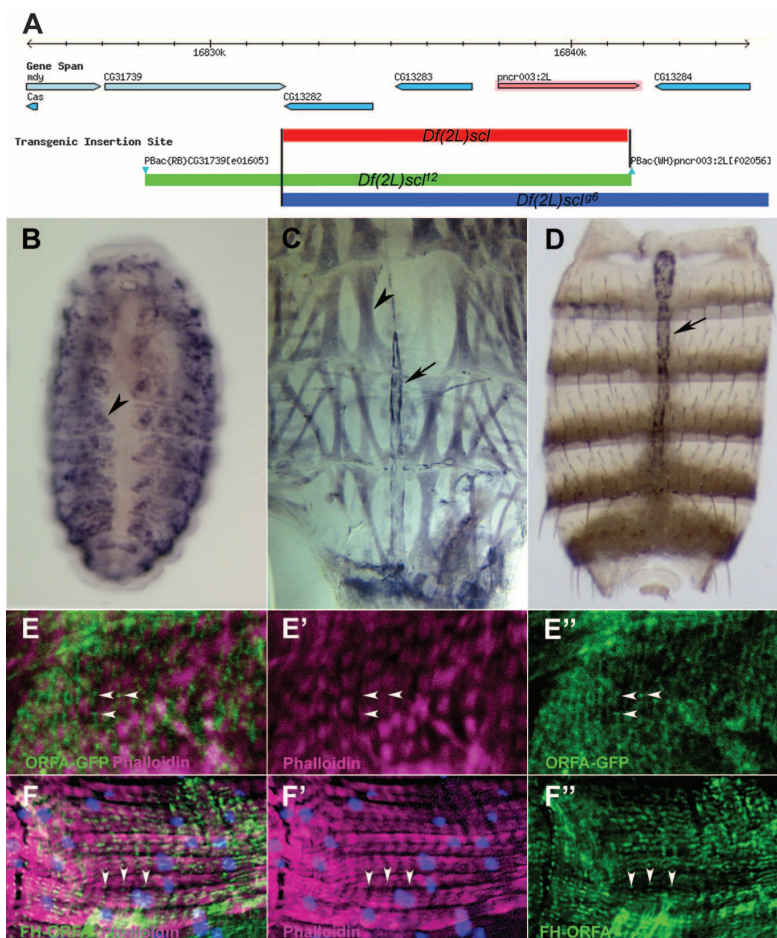
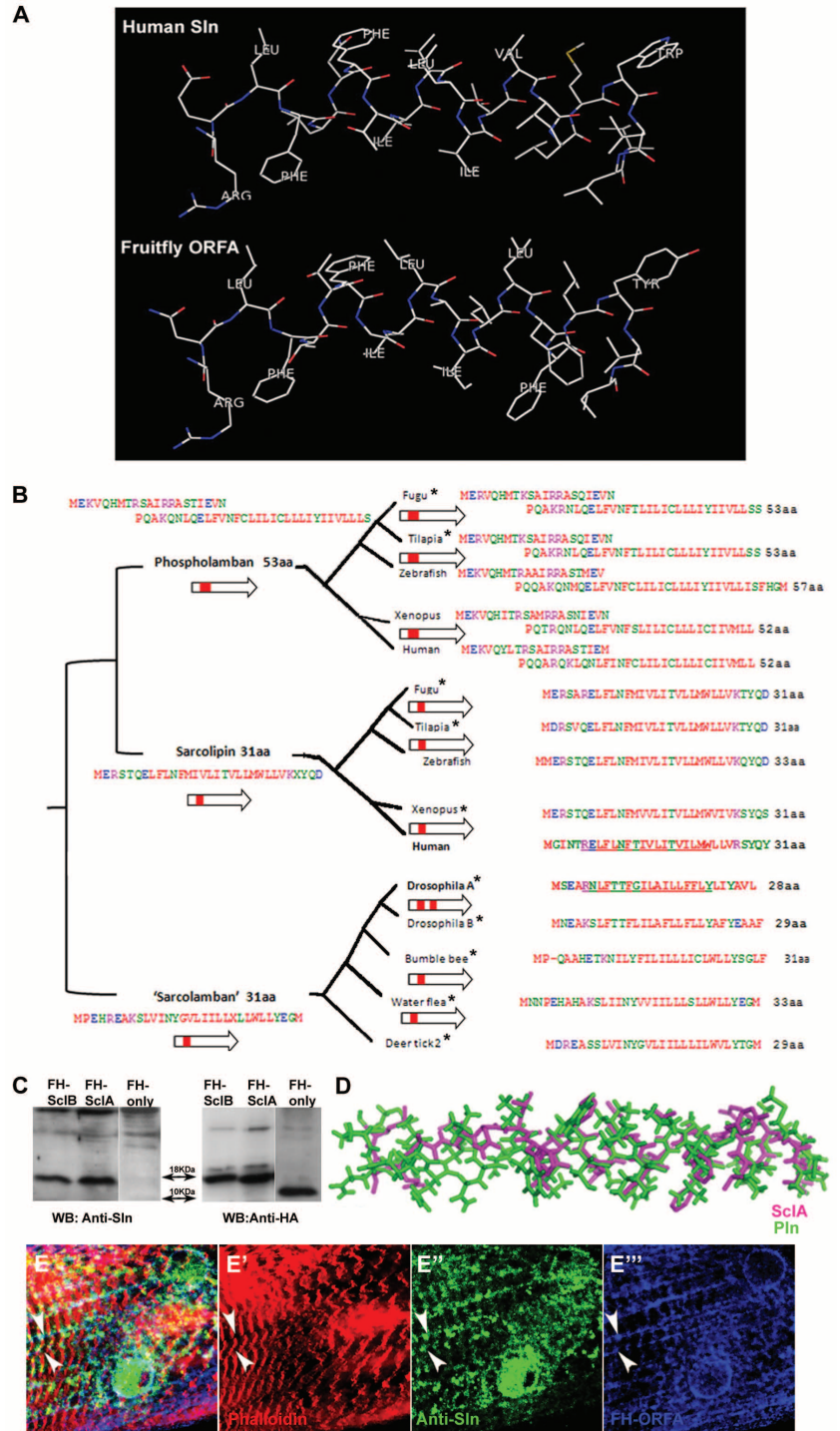


Fig. 2. Role of *pncr003:2L* in cardiac muscle contraction. (A) Kymographs comparing the pattern of heart contractions for wild-type and *Df(2L)scl* hearts. The mutant shows irregular periods, some being abnormally long (asterisk). A normal heart period is indicated (green). (B) Arrhythmicity index of *pncr003:2L* loss-of-function and rescue genotypes (left) and excess of function genotypes (right), normalized to age matched wild-type controls (9). Columns represent mean, and error bars represent SE. (C) Sample traces of intracellular recordings from adult cardiomyocytes of wild-type (green); *Df(2L)scl* (red); and *Df(2L)scl* rescued by *UAS-pncr003:2L* (blue). Arrows indicate “double” action

potentials. Arrowheads indicate failed action potentials. Gray dashed line indicates resting potentials. Sample peaks from each trace (underlined) appear magnified. (D) Ca^{2+} transients during heart contraction of *Df(2L)scl* and rescue genotypes (left) and gain-of-function genotypes (right) color-coded as in (B). The fluorescent Ca^{2+} sensor G-CaMP3 was used to visualize calcium levels. Y axis values are ratios of calcium dependent fluorescence on its decay phase normalized to basal intensities and presented as percentages relative to wild-type controls; x axis values are percentage of time from the point of maximum transient amplitude.

Fig. 3. Putative homology of sequence and structure between human and *Drosophila* peptides. (A) Secondary structure of the conserved domain [underlined in (B)] of Sarcolipin (top) and *Drosophila pncr003:2L* ORFA peptide (bottom). Blue, nitrogen atoms; red, oxygen atoms. (B) Phylogenetic tree of vertebrate and arthropod (*pncr003:2L*, labeled “Sarcolamban”) peptides. Asterisks indicate sequences identified in this study (supplementary data file S1). Putative ancestral consensus sequences (left) and further analysis (fig. S4) (9) suggest that the two vertebrate peptides arose from a duplication of a single ancestor that also diverged independently into the different arthropod Sarcolamban peptides. Analysis of RNA (cDNA) sequences (arrows) indicates that all peptides arise from single smORFs (red boxes) uninterrupted by exons, suggesting that ancestral peptides were also encoded by smORFs. (C) Western blots from *Drosophila* S2 cells showing that the antibody to human Sarcolipin (left lanes) recognizes the *Drosophila* FH-tagged Sarcolamban18-kD peptides SclA and SclB, but not the 10-kD FH-tag alone. Right lanes show positive controls, with antibody to HA recognizing all peptides. (D) A compatible structure for Sarcolamban-A (magenta) is obtained by threading it onto the C-terminal domain of vertebrate Phospholamban (green). (E to E’’) *Drosophila* FH-SclA peptides (arrowheads) surrounding the sarcomeres (red) are recognized by antibodies to Sarcolipin (green) and Flag (blue) in larval somatic muscles.



would be secondarily required for regular muscle contraction; and (ii) that such a role is mediated by the peptides encoded by the 28- and 29-amino acid smORFs.

We searched for conservation of these smORFs in other species by using Basic Local Alignment Search Tool (BLAST) and only identified them in other Drosophilids [with K_a/K_s scores of <0.2 supporting translation (10)]. Because the *pncr003:2L* peptides have a predicted helical structure, we searched for possible structural homologs (9) and retrieved the 30-amino acid human *sarcolipin*

(Sln) peptide (Fig. 3A and tables S1 and S2) (11). However, the Sln and *pncr003:2L* peptides display noticeable differences in their amino acid sequences (Fig. 3B). If they were true homologs, peptides with intermediate sequences should exist in the stem lineages to both flies and humans. We devised a bioinformatics protocol (9) to identify possible *pncr003:2L* homologs in arthropods (Fig. 3B and fig. S4) plus nonannotated homologs of *sln* and its longer paralogue *phospholamban* (*pln*) (Fig. 3B and fig. S4) (12), until basal arthropod smORFs identified basal vertebrate homologs with

the expected intermediate amino acid changes (fig. S4, A to C). Supporting their putative homology, we found that (i) antibodies to sarcolipin recognize the *pncr003:2L* peptides (Fig. 3, C and E, and fig. S5, A and B), and (ii) threading the *pncr003:2L* amino acid sequences on the Pln three-dimensional (3D) structure (13) also produces a compatible structure (Fig. 3D and tables S1 and S2).

A phylogenetic tree of all these peptides suggests that Sln and Pln emerged from a gene duplication in vertebrates, whereas an independent and more recent duplication in flies gave rise to

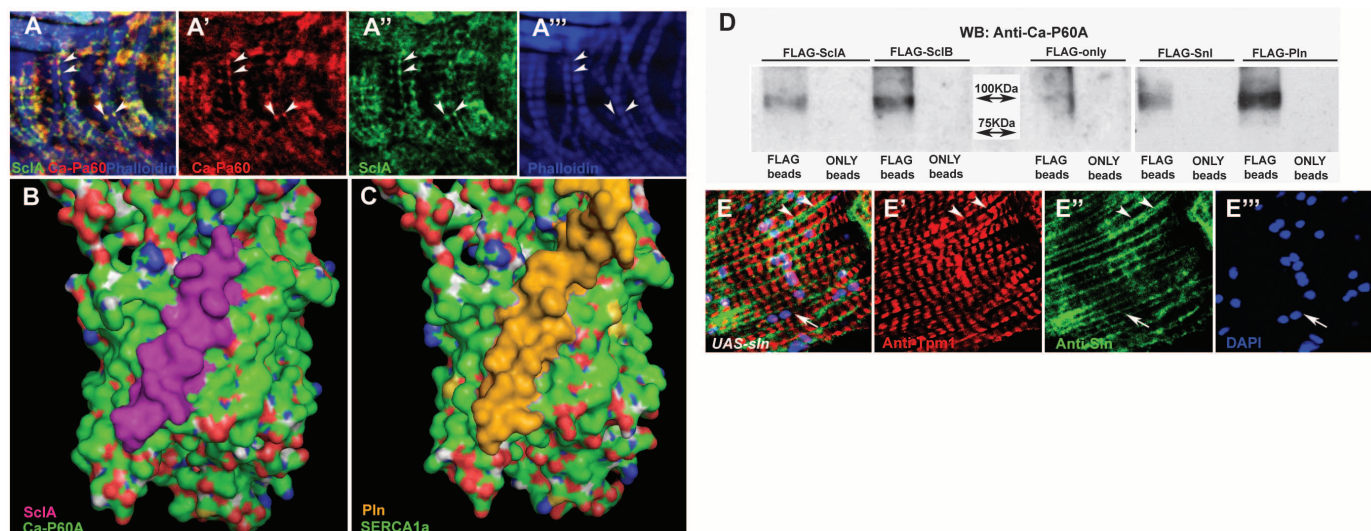


Fig. 4. Sarcolamban interacts with Ca-P60A SERCA. (A to A'') Co-localization of sarcolamban FH-SclA peptides (green) and Ca-P60A SERCA (red) in the SER and dyads (arrowheads) surrounding the adult heart sarcomeres (blue, phalloidin). (B and C) Interaction between the *Drosophila* SclA (magenta) and Ca-P60A, modeled from vertebrate SERCA1a in the EI conformation (9). SclA docks onto Ca-P60A similarly as Phospholamban (yellow) and Sarcolipin (fig. S5, D and E) onto human SERCA1a (C). Peptide C-termini

are down. (D) FH-tagged *Drosophila* SclA and SclB and the human Sln and Pln peptides pull-down the 100-kD *Drosophila* Ca-P60A (revealed with antibody to Ca-P60) from transfected S2 cells. Negative control lanes with Flag-only peptides or beads without antibodies ("ONLY beads") do not show similar Ca-P60A signal. (E to E'') Human Sln peptides (green; arrowheads) expressed in the *Drosophila* adult heart surround the sarcomeres (red; labeled with antibody to Tropomyosin1). Blue, DAPI-stained nuclei (arrow).

pncr003:2L ORFA and ORFB peptides. The tree, sequence alignments, and further bioinformatics analysis (fig. S4, supplementary data file S1, and tables S1 and S2) (9) are altogether compatible with a single origin for the Sln, Pln, and *pncr003:2L* peptides from an ancestral peptide-encoding smORF of ~30 amino acids (Fig. 3B and fig. S4B). We suggest that *pncr003:2L* and its arthropod homologs should be renamed *sarcolamban* (*scl*) in order to reflect their similarity and probable homology to vertebrate *sln* and *pln*.

Conservation of smORFs across such an evolutionary distance (>550 million years of divergence) has not been described; therefore, we scrutinized their functional homology. Sln and Pln regulate Ca^{2+} traffic in mammal muscles by dampening the activity of the Sarco-endoplasmic Reticulum Ca^{2+} adenosine triphosphatase (SERCA), whose function is to retrieve Ca^{2+} from the cytoplasm back into the SER, leading to muscle relaxation (fig. S2G) (14). The effects of removing *sln* upon the vertebrate muscle Ca^{2+} transients are remarkably similar to the effects we observed in *Df(2L)scl* mutants (Fig. 2D) (15). Furthermore, abnormal levels of Sln expression have been related to human heart arrhythmias (16), and Sln and Pln have been shown to bind SERCA (17). In flies, the Scl peptides colocalize with *Drosophila* SERCA (Ca-P60A) (Fig. 4A and fig. S5C) and coimmunoprecipitate with it (Fig. 4D). Furthermore, the arrhythmia and abnormal transients of *Df(2L)scl* mutants are corrected by reducing the function of *Ca-P60A* (Fig. 2, B to D), a genetic interaction that is consistent with a down-regulating role of Scl upon SERCA activity (18). Last, threading the sequence of Ca-P60A onto the

3D structure of vertebrate SERCA produces a compatible structure that seems able to dock Scl similarly to Sln and Pln binding to SERCA (Fig. 4, B and C; fig. S5, D and E; and tables S3 and S4) (17).

Our studies suggest that Sln and Pln can bind fly Ca-P60A and can resemble Scl function. Modeling suggests that fly and vertebrate peptides could bind each other's SERCA (tables S3 and S4), and indeed human peptides can pull down fly Ca-P60A (Fig. 4D). Sln and Pln expressed in fly muscles and cultured cells localize similarly to Scl and Ca-P60A (Fig. 4E and figs. S5F and S6) and produce arrhythmias and Ca^{2+} transients similar to those produced by overexpressing fly Scl peptides (Fig. 2, B and D). Furthermore, expression of human Pln in *Df(2L)scl* flies can rescue the mutant Ca^{2+} transients toward wild type, and the strong arrhythmia phenotype of ectopic Pln is itself reduced (Fig. 2, B and D). The human peptide overexpression and rescue effects do not completely reproduce those observed with fly peptides, and this suggests that although this family of peptides may share a regulatory function on Ca^{2+} pumps, each seems finely tuned to its own species-specific SERCA regulation.

Altogether, our results suggest that this family of peptides may represent an ancient system for the regulation of Ca^{2+} traffic, whose alteration can result in irregular muscle contractions. We propose that the *Drosophila sarcolamban* (*scl*) gene, previously annotated as the long noncoding RNA *pncr003:2L*, actually encodes two functional smORFs of 28 and 29 amino acids that are translated into bioactive peptides. The analysis of related amino acid sequences across multiple species is compatible with a conservation of these

peptides and their putative molecular structure from flies to vertebrates, correlated with the conservation of their biological role in regulating Ca^{2+} uptake at the SER. We speculate that this remarkable conservation, together with previous reports on the *tal* gene (2–4), might indicate that smORFs can reveal both sequence conservation and important biological functions. Bioinformatics predictions (1, 5) and recent ribosomal profiling data from vertebrates (19) suggest that translated smORFs may be abundant. We believe that smORFs cannot be dismissed as irrelevant, but that their functionality should be considered whenever encountered.

References and Notes

1. M. A. Basrai, P. Hieter, J. D. Boeke, *Genome Res.* **7**, 768–771 (1997).
2. M. I. Galindo, J. I. Pueyo, S. Fouix, S. A. Bishop, J. P. Couso, *PLoS Biol.* **5**, e106 (2007).
3. J. I. Pueyo, J. P. Couso, *Dev. Biol.* **355**, 183–193 (2011).
4. T. Kondo et al., *Science* **329**, 336–339 (2010).
5. E. Ladoukakis, V. Pereira, E. G. Magny, A. Eyre-Walker, J. P. Couso, *Genome Biol.* **12**, R118 (2011).
6. J. Savard, H. Marques-Souza, M. Aranda, D. Tautz, *Cell* **126**, 559–569 (2006).
7. J. L. Tupy et al., *Proc. Natl. Acad. Sci. U.S.A.* **102**, 5495–5500 (2005).
8. R. I. Razzaq A et al., *Genes Dev.* **15**, 22 (2001).
9. Material and methods are available as supplementary materials on Science Online.
10. A. Nekrutenko, K. D. Makova, W. H. Li, *Genome Res.* **12**, 198–202 (2002).
11. A. Wawrzynow et al., *Arch. Biochem. Biophys.* **298**, 620–623 (1992).
12. P. Bhupathy, G. J. Babu, M. Periasamy, *J. Mol. Cell. Cardiol.* **42**, 903–911 (2007).
13. K. Okenoid, J. J. Chou, *Proc. Natl. Acad. Sci. U.S.A.* **102**, 10870–10875 (2005).

14. M. Periasamy, A. Kalyanasundaram, *Muscle Nerve* **35**, 430–442 (2007).
15. G. J. Babu et al., *Proc. Natl. Acad. Sci. U.S.A.* **104**, 17867–17872 (2007).
16. M. Shanmugam et al., *Biochem. Biophys. Res. Commun.* **410**, 97–101 (2011).
17. M. Asahi et al., *Proc. Natl. Acad. Sci. U.S.A.* **100**, 5040–5045 (2003).
18. G. J. Babu et al., *J. Biol. Chem.* **281**, 3972–3979 (2006).
19. N. T. Ingolia, L. F. Lareau, J. S. Weissman, *Cell* **147**, 789–802 (2011).

Acknowledgments: We thank Rose Phillips, Roger Phillips, and J. Thorpe for technical support; M. Ramaswami for the antibody to Ca-P60A; and F. Casares, M. Baylies, I. Galindo, C. Alonso, and laboratory members for manuscript comments. E.M. was supported by Conacyt, F.P. was supported by a Daphne Jackson Fellowship and the UK Medical Research Council, and J.N. was supported by a Royal Society University Fellowship. Otherwise, this work was funded by a Wellcome Trust Fellowship (ref 087516) awarded to J.P.C. The GenBank accession number for *Drosophila* Scl sequences is NR_001662.

Supplementary Materials

www.sciencemag.org/cgi/content/full/341/6150/1116/DC1
Materials and Methods
Figs. S1 to S8
Tables S1 to S9
References (20–34)
Movies S1 and S2
Supplementary data file S1

5 April 2013; accepted 7 August 2013
10.1126/science.1238802

A Causative Link Between Inner Ear Defects and Long-Term Striatal Dysfunction

Michelle W. Antoine,¹ Christian A. Hübner,² Joseph C. Arezzo,¹ Jean M. Hébert^{1,3*}

There is a high prevalence of behavioral disorders that feature hyperactivity in individuals with severe inner ear dysfunction. What remains unknown is whether inner ear dysfunction can alter the brain to promote pathological behavior. Using molecular and behavioral assessments of mice that carry null or tissue-specific mutations of *Slc12a2*, we found that inner ear dysfunction causes motor hyperactivity by increasing in the nucleus accumbens the levels of phosphorylated adenosine 3',5'-monophosphate response element-binding protein (pCREB) and phosphorylated extracellular signal-regulated kinase (pERK), key mediators of neurotransmitter signaling and plasticity. Hyperactivity was remedied by local administration of the pERK inhibitor SL327. These findings reveal that a sensory impairment, such as inner ear dysfunction, can induce specific molecular changes in the brain that cause maladaptive behaviors, such as hyperactivity, that have been traditionally considered exclusively of cerebral origin.

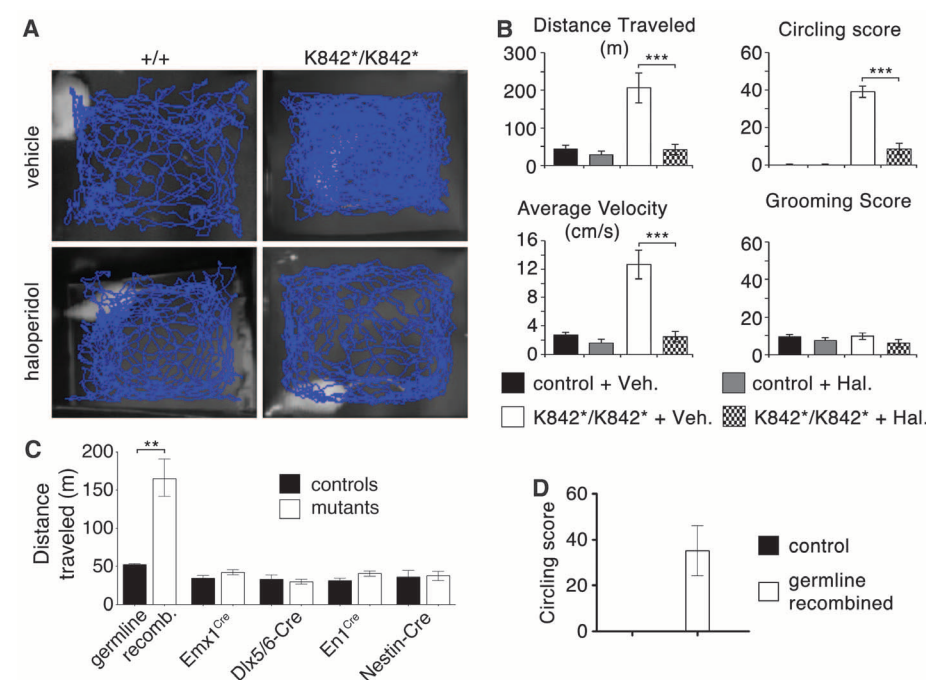
The inner ear contains the cochlea, devoted to hearing, and the vestibular end organs, dedicated to balance. In 20 to 95% of children with severe hearing loss, auditory and vestibular dysfunction occur concurrently (1, 2). In such cases, there is a high incidence of behavioral

disorders that feature hyperactivity as a core diagnostic symptom (3–5). Although socioenvironmental variables have been proposed as risk factors (6), it is unclear whether sensory impairments, such as inner ear defects, can directly induce specific changes in the brain that lead to

maladaptive behavior. In nonhuman vertebrates, including rodents and frogs, surgical or pharmacological lesions to the vestibulo-auditory system are also linked to long-term changes in locomotor activity, although, to date, the associations between ear dysfunction and behavior remain unexplained (7–9). Genetic mouse models of inner ear dysfunction can exhibit increased levels of locomotor hyperactivity (10), but because the gene is mutated in the brain, as well as the inner ear, the causal neural underpinnings of this behavior remain unknown.

Slc12a2 (also known as *Nkcc1*) is a gene that encodes a sodium-potassium-chloride cotransporter broadly expressed in tissues, including the inner ear and central nervous system (CNS) (11, 12). The *Slc12a2* mutant mice used in this study arose spontaneously in our mouse colony and exhibit increased levels of motor hyperactivity, including locomotion, circling, and head tossing (Fig. 1, A and B; movie S1; and fig. S1A),

Fig. 1. *Slc12a2*^{K842*/K842*} mutants display a dopamine receptor-mediated increase in locomotor activity that cannot be explained by disruption of *Slc12a2* in the brain. (A) Traces and (B) quantification of mouse locomotion in an open field showing that haloperidol alleviates locomotor activity and circling in *Slc12a2*^{K842*/K842*} mice without affecting grooming [****P* < 0.0001; repeated measures analysis of variance (ANOVA) with Bonferroni post hoc comparison]. (C) Germline recombination of *Slc12a2*^{flx/flx} mice recapitulates the increased locomotion of the *Slc12a2*^{K842*/K842*} mutant (*P* = 0.0032, unpaired two-tailed test). Mice lacking *Slc12a2* in the neocortex and hippocampus (*Emx1*^{Cre/+}; *Slc12a2*^{flx/rec}), striatum (*Dlx5/6-Cre*; *Slc12a2*^{flx/flx}), cerebellum (*En1*^{Cre/+}; *Slc12a2*^{flx/flx}), and CNS (*Nestin-Cre*; *Slc12a2*^{flx/flx}) display normal levels of motor activity (unpaired two-tailed test). (D) Germline recombination of the *Slc12a2*^{K842*/K842*} mutants. *n* = 4 to 11 mice per genotype. All data are means ± SEM.



¹Department of Neuroscience, Albert Einstein College of Medicine, Bronx, NY 10461, USA. ²Jena University Hospital, Institute of Human Genetics, Jena 07743, Germany. ³Department of Genetics, Albert Einstein College of Medicine, Bronx, NY 10461, USA.

*Corresponding author. E-mail: jean.hebert@einstein.yu.edu

as with previously characterized *Slc12a2* mutants (13–16). The spontaneous mutation was identified as an A to T mutation in exon 17 that changes codon 842 of *Slc12a2* from encoding a lysine (K) to a stop codon (*) (hereafter referred to as *Slc12a2*^{K842*}), which results in no detectable SLC12A2 protein, as shown by antibodies raised to either the N or C terminus (fig. S1, B to E). The inner ear of *Slc12a2*^{K842*/K842*} mice revealed a collapse of Reissner's membrane and the membranes of the vestibular compartments (fig. S1F). These morphological defects were associated with profound deafness and balance deficits (figs. S1G and S2) (15).

An increase in locomotor activity is not readily explained by dysfunction of the inner ear but rather points to a disruption of brain functions that regulate movement. Consistent with this notion, the dopaminergic antagonist haloperidol, which acts in the brain to alleviate increased motor behavior in humans (17), normalized the open-field locomotor behavior of *Slc12a2*^{K842*/K842*} mice (Fig. 1, A and B). The same dose of haloperidol did not decrease the locomotor activity in littermate controls, which indicated that the dose used was not sedating. Haloperidol did not affect grooming in either mutants or controls, nor did it ameliorate performance of mutants on a rotating

rod (rotarod) test, which requires an intact inner ear, and which therefore indicates a specificity in the behaviors modified by haloperidol (Fig. 1B and fig. S2).

To test whether loss of *Slc12a2* expression in the brain leads to increased locomotor activity, we deleted a floxed *Slc12a2* allele (*Slc12a2*^{flx}) specifically from individual brain areas that control movement using *Emx1*^{Cre} for the cortex, *Dlx5/6*-*Cre* for the striatum, *En1*^{Cre} for the cerebellum, and *Nestin*-*Cre* for the entire CNS. With these lines, recombination occurs before neurogenesis and expression of *Slc12a2* (18–21). Western blot analyses confirmed the loss of *Slc12a2* specifically in the expected tissues (fig. S3, A and C). Although mice having a germline deletion of the *Slc12a2*^{flx} allele, which lack expression in all tissues, are behaviorally indistinguishable from *Slc12a2*^{K842*/K842*} mice, mice with deletions in the cortex, striatum, cerebellum, or entire CNS are behaviorally normal (Fig. 1, C and D, and fig. S3B), which indicates that loss of *Slc12a2* from any single or combination of brain areas does not cause the behavior. Note that inner ear morphology and *Slc12a2* expression were normal in *Nestin*-*Cre*;*Slc12a2*^{flx/flx} mutants (fig. S3C).

To determine whether loss of *Slc12a2* expression in the inner ear causes the behavioral

phenotype, the *Foxg1*^{Cre} line was used to delete *Slc12a2* from the embryonic precursors of the inner ear (Fig. 2A). However, because *Foxg1*^{Cre} also targets the telencephalon (neocortex, hippocampus, and striatum) (Fig. 2B), we deleted *Slc12a2* from the inner ear using a combination of *Pax2*-*Cre* and *Tbx1*^{Cre}, which together sufficiently deleted *Slc12a2* to result in the anatomical ear defects indicative of dysfunction (fig. S4). In *Pax2*-*Cre*;*Tbx1*^{Cre}-driven mutants, *Slc12a2* deletion also occurred in the mid-hindbrain area, but not the telencephalon. Both the *Pax2*-*Cre*;*Tbx1*^{Cre} and *Foxg1*^{Cre}-driven mutants recapitulated all the hyperactive features of *Slc12a2*^{K842*/K842*} mice (Fig. 2C, movie S2, and fig. S4). Together with the absence of the behavioral phenotype, when *Slc12a2* is deleted from the entire CNS, these results demonstrate that inner ear dysfunction caused the abnormal behavior of these mice.

Because increased locomotor activity and a responsiveness to haloperidol are indicative of brain, rather than ear, dysfunction, we reasoned that inner ear defects may cause abnormal functioning of the striatum, a central brain area that regulates motor output levels. Striatal levels of 26 candidate proteins involved in neurotransmitter signaling were examined by Western blot (Fig. 3, A and B, and fig. S5). Initially, *Slc12a2*^{K842*/K842*}

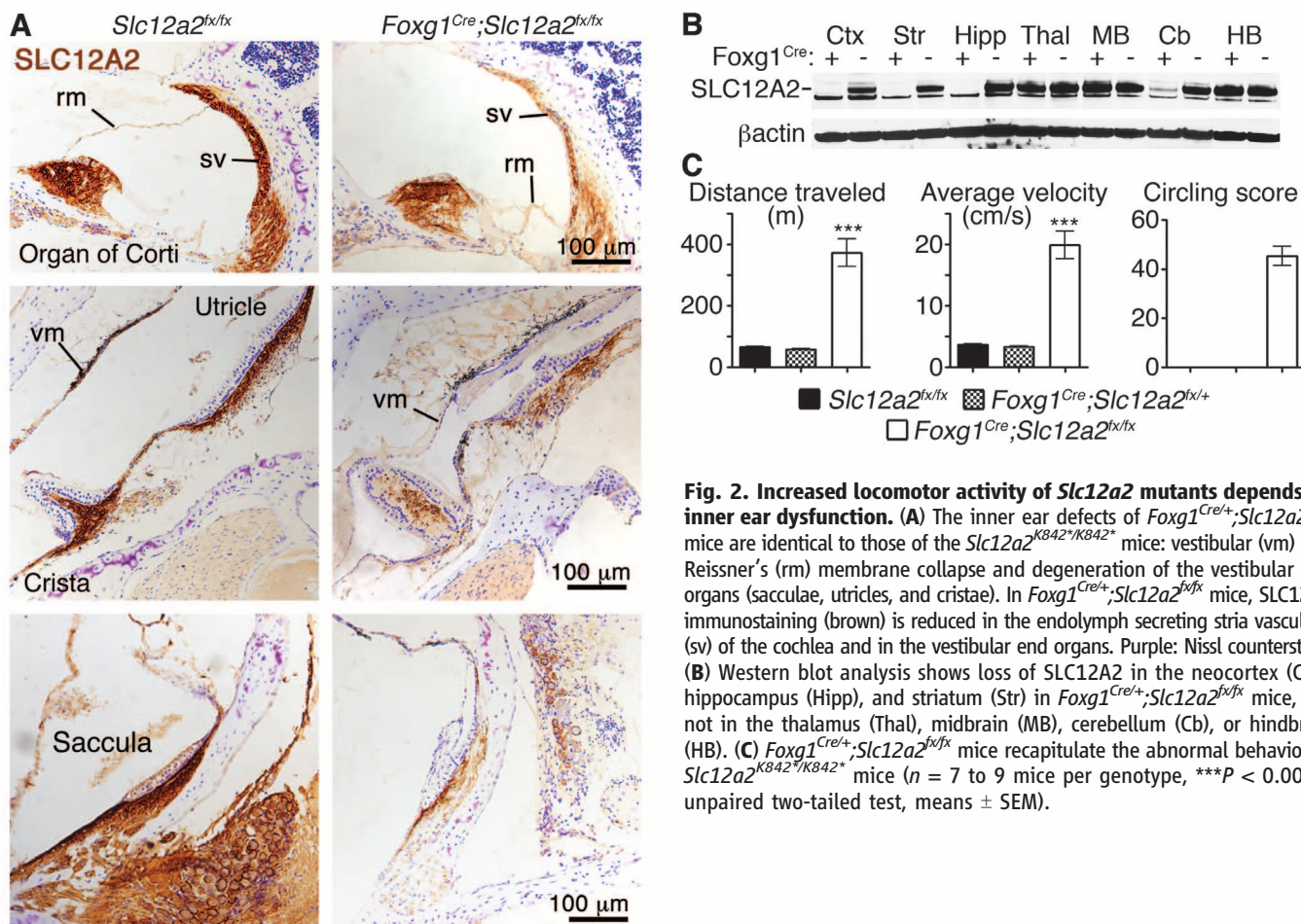


Fig. 2. Increased locomotor activity of *Slc12a2* mutants depends on inner ear dysfunction. (A) The inner ear defects of *Foxg1*^{Cre};*Slc12a2*^{flx/flx} mice are identical to those of the *Slc12a2*^{K842*/K842*} mice: vestibular (vm) and Reissner's (rm) membrane collapse and degeneration of the vestibular end organs (sacculae, utricles, and cristae). In *Foxg1*^{Cre};*Slc12a2*^{flx/flx} mice, SLC12A2 immunostaining (brown) is reduced in the endolymph secreting stria vascularis (sv) of the cochlea and in the vestibular end organs. Purple: Nissl counterstain. (B) Western blot analysis shows loss of SLC12A2 in the neocortex (Ctx), hippocampus (Hipp), and striatum (Str) in *Foxg1*^{Cre};*Slc12a2*^{flx/flx} mice, but not in the thalamus (Thal), midbrain (MB), cerebellum (Cb), or hindbrain (HB). (C) *Foxg1*^{Cre};*Slc12a2*^{flx/flx} mice recapitulate the abnormal behavior of *Slc12a2*^{K842*/K842*} mice ($n = 7$ to 9 mice per genotype, *** $P < 0.0001$, unpaired two-tailed test, means \pm SEM).

Fig. 3. Inner ear dysfunction contributes to the up-regulation of pERK1 in striatal neurons. (A) Western blot analyses reveal increased (arrowheads) pERK1 (upper band of doublet) and its common target pCREB in mice with inner ear defects and increased motor activity (*Slc12a2*^{K842*/K842*} and *Foxg1*^{Cre/+}; *Slc12a2*^{fx/fx} mice) but not in phenotypically normal mice. (B) Quantification of Western analyses (pERK: $P = 0.009$ for *Slc12a2*^{K842*/K842*}; $P = 0.006$ for *Foxg1*^{Cre/+}; *Slc12a2*^{fx/fx}; pCREB: $P = 0.028$ for *Slc12a2*^{K842*/K842*}; $P = 0.033$ for *Foxg1*^{Cre/+}; *Slc12a2*^{fx/fx}; $n = 3$ to 6 mice per genotype; unpaired two-tailed t test). (C) Immunohistochemical analysis showed an increase in the number of pERK+ cells in the ventral striatum of mutants ($n = 4$ mice per genotype, $**P = 0.0066$, $***P = 0.00046$, unpaired two-tailed t test). (D) In both controls and mutants, pERK+ cells in the ventral striatum are primarily DARPP32+, whereas in the dorsal striatum they are somatostatin+ (SST+) interneurons ($n = 3$ mice per genotype) (means \pm SEM).

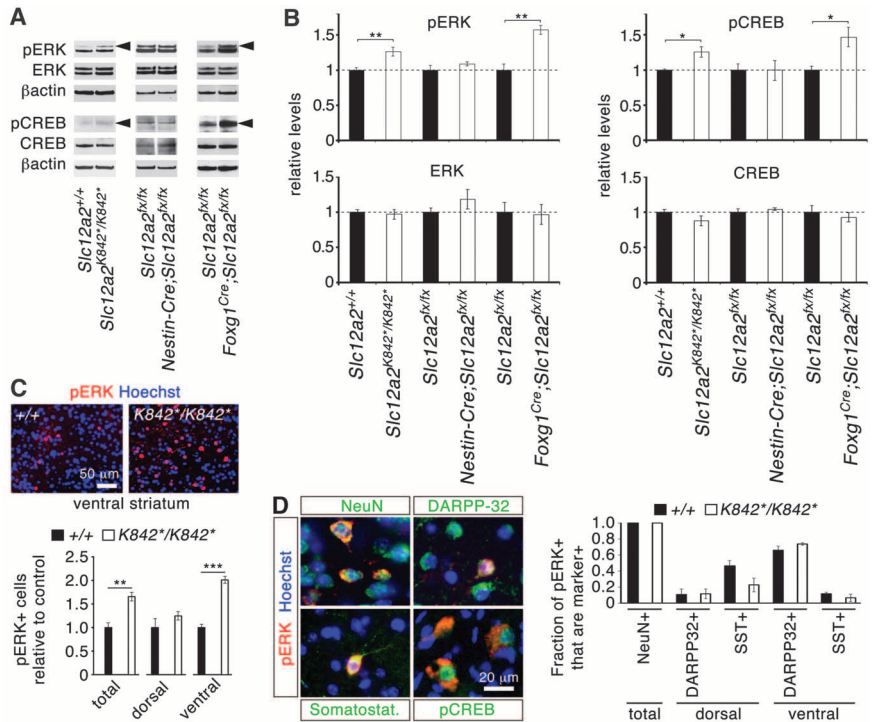
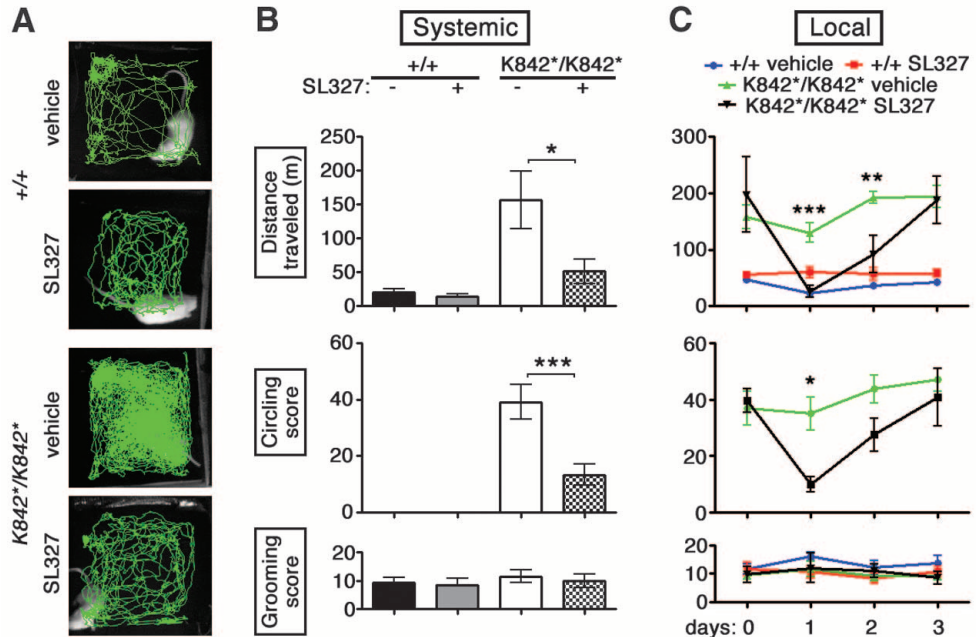


Fig. 4. The increased striatal pERK levels induced by inner ear defects promote increased locomotor activity. (A) Traces and (B) quantification of motor activity in an open-field 1 hour after systemic SL327 administration, which ameliorates both locomotion and circling in the *Slc12a2*^{K842*/K842*} mutants while having little effect on grooming ($n = 6$ mice per genotype, $*P = 0.015$, $***P = 0.0002$). (C) Local SL327 administration to the nucleus accumbens of *Slc12a2*^{K842*/K842*} mice restored open-field activity and circling to control levels, which were unaffected by treatment, for 2 days postinjection, without affecting grooming ($n = 5$ to 7 mice per genotype and per treatment condition, $***P = 0.0025$, $**P = 0.0082$, $*P = 0.018$; means \pm SEM; two-way repeated measures ANOVA with Bonferroni post hoc comparison).



mutants were examined, and proteins showing significant differences in expression levels compared with controls were then also examined in striata from *Nestin-Cre*; *Slc12a2*^{fx/fx} and *Foxg1*^{Cre/+}; *Slc12a2*^{fx/fx} mice to identify the relevant changes that correlate with the presence of the ear defects and behavioral phenotype. Among the proteins examined, we observed significant increases only in the levels of phosphorylated extracellular signal-regulated kinase (pERK), a key component of dopamine and glutamate neu-

rotransmission in the striatum, and its common downstream target, phosphorylated adenosine 3',5'-monophosphate response element-binding protein (pCREB-Ser133) (22–24) (Fig. 3, A and B). Although phosphorylated forms were elevated, total ERK and CREB were unaffected. Increased pERK and pCREB were specific to the striatum and not observed in other forebrain regions (fig. S5D). Immunohistochemical analysis of *Slc12a2*^{K842*/K842*} mutants revealed that the number of pERK-positive (pERK+) cells was up-regulated specif-

ically in the nucleus accumbens, the ventral part of the striatum (Fig. 3C). All pERK+ cells were NeuN+, which indicated that they were neurons. Of these, most were DARPP32+ medium-sized spiny neurons (MSNs) and a few were somatostatin+ interneurons (Fig. 3D) but not calretinin+, parvalbumin+, or choline acetyltransferase (ChAT)+ interneurons. The proportions of pERK+ cell types in the mutants were nevertheless similar to those of controls. In addition, pCREB+ cells were pERK+ (Fig. 3D).

Robust increases in pERK occur in MSNs of the nucleus accumbens in response to psychostimulants and other drugs of abuse and are considered critical for enabling their long-lasting behavioral changes (22, 25, 26). The induction of such behaviors is inhibited by the local or systemic application of MAPK kinase (MEK) or ERK kinase inhibitors, such as SL327 (22, 27–29). To determine whether striatal ERK phosphorylation was necessary for the abnormal increase in locomotor activity, *Slc12a2*^{K842*/K842*} mice were given an intraperitoneal injection or a local injection of SL327 to the nucleus accumbens. In both sets of experiments, SL327 administration restored locomotor activity to normal levels without affecting the levels of activity in controls (Fig. 4). Mutant mice treated with local SL327 returned to their baseline, presurgery locomotor levels of activity by day 3, which suggested that the injection did not cause permanent damage. SL327 administration did not affect grooming, which suggested that increased striatal pERK selectively elevates locomotor activity levels and not general activity.

This study demonstrates that inner ear dysfunction can induce molecular changes in the striatum that promote increased motor hyperactivity. The neural circuits linking inner ear defects to abnormal striatal function are likely transmitted by the normal auditory and vestibular input pathways, primarily via the thalamus and neocortex (30), but this remains to be demonstrated. Our results also suggest that a neurobiological cause, rather than simply socioenvironmental factors, contributes to the high incidence of behavioral disorders associated with inner ear dysfunction in

children and adolescents. Moreover, disruption of the ERK pathway in the striatum provides a potential target for intervention. Finally, it is intriguing to ponder whether sensory impairments other than those associated with inner ear defects could also cause or contribute to psychiatric or motor disorders that have traditionally been considered exclusively of cerebral origin.

References and Notes

- P. A. Selz, M. Girardi, H. R. Konrad, L. F. Hughes, *Otolaryngol. Head Neck Surg.* **115**, 70–77 (1996).
- S. L. Cushing, B. C. Papsin, J. A. Rutka, A. L. James, K. A. Gordon, *Laryngoscope* **118**, 1814–1823 (2008).
- P. Vostanis, M. Hayes, M. Du Feu, J. Warren, *Child Care Health Dev.* **23**, 233–246 (1997).
- P. Hindley, L. Kroll, *J. Deaf Stud. Deaf Educ.* **3**, 64–72 (1998).
- T. van Eldik, P. D. Treffers, J. W. Veerman, F. C. Verhulst, *Am. Ann. Deaf* **148**, 390–395 (2004).
- T. van Gent, A. W. Goedhart, P. A. Hindley, P. D. Treffers, *J. Child Psychol. Psychiatry* **48**, 950–958 (2007).
- L. Stiles, Y. Zheng, C. L. Darlington, P. F. Smith, *Behav. Brain Res.* **227**, 150–158 (2012).
- M. Schirmer *et al.*, *Brain Res.* **1155**, 179–195 (2007).
- F. M. Lambert, D. Combes, J. Simmers, H. Straka, *Curr. Biol.* **22**, 1649–1658 (2012).
- M. S. Deol, *J. Mol. Genet.* **5**, 137–158 (1968).
- J. J. Crouch, N. Sakaguchi, C. Lytle, B. A. Schulte, *J. Histochem. Cytochem.* **45**, 773–778 (1997).
- M. D. Plotkin, M. R. Kaplan, *et al.*, *Am. J. Physiol. Cell Physiol.* **272**, C173–C183 (1997).
- E. Delpire, J. Lu, R. England, C. Dull, T. Thorne, *Nat. Genet.* **22**, 192–195 (1999).
- M. J. Dixon *et al.*, *Hum. Mol. Genet.* **8**, 1579–1584 (1999).
- M. Flagella *et al.*, *J. Biol. Chem.* **274**, 26946–26955 (1999).
- A. J. Pace *et al.*, *J. Clin. Invest.* **105**, 441–450 (2000).
- R. J. Baldessarini, in *Goodman and Gilman's The Pharmacological Basis of Therapeutics*, L. L. Brunton, J. S. Lazo, K. Parker, I. Buxton, D. Blumenthal, Eds. (McGraw Hill, New York, ed. 11, 2006), pp. 317–399.

- N. C. Dubois, D. Hofmann, K. Kaloulis, J. M. Bishop, A. Trumpp, *Genesis* **44**, 355–360 (2006).
- J. A. Gorski *et al.*, *J. Neurosci.* **22**, 6309–6314 (2002).
- R. A. Kimmel *et al.*, *Genes Dev.* **14**, 1377–1389 (2000).
- J. Stenman, H. Toresson, K. Campbell, *J. Neurosci.* **23**, 167–174 (2003).
- E. Valjent *et al.*, *Proc. Natl. Acad. Sci. U.S.A.* **102**, 491–496 (2005).
- E. S. Choe, J. Q. Wang, *Neuroreport* **13**, 1013–1016 (2002).
- A. J. Silva, J. H. Kogan, P. W. Frankland, S. Kida, *Annu. Rev. Neurosci.* **21**, 127–148 (1998).
- T. V. Gerdjikov, G. M. Ross, R. J. Beninger, *Behav. Neurosci.* **118**, 740–750 (2004).
- J. Salzmann, C. Marie-Claire, S. Le Guen, B. P. Roques, F. Noble, *Br. J. Pharmacol.* **140**, 831–838 (2003).
- C. M. Atkins, J. C. Selcher, J. J. Petraitis, J. M. Trzaskos, J. D. Sweatt, *Nat. Neurosci.* **1**, 602–609 (1998).
- M. F. Favata *et al.*, *J. Biol. Chem.* **273**, 18623–18632 (1998).
- J. C. Selcher, C. M. Atkins, J. M. Trzaskos, R. Taylor, J. D. Sweatt, *Learn. Mem.* **6**, 478–490 (1999).
- T. Shiroyama, T. Kayahara, Y. Yasui, J. Nomura, K. Nakano, *J. Comp. Neurol.* **407**, 318–332 (1999).

Acknowledgments: We thank K. Khodakhah and P. Calderon for support with surgical approaches, rotarod, and early inputs to the project; G. Fishell for the Nestin-CreER mice in which *Slc12a2*^{K842*} arose; S. Zukin for Western blotting; C. Heinze for *Slc12a2*^{K842*} genotyping; University of California at Davis and NIH NeuroMab for antibodies; and the Developmental Studies Hybridoma Bank for the T4 antibody developed by Lytle and Forbush. This work was supported by the Tourette Syndrome Association (J.M.H. and K. Khodakhah), NIH R21NS073761 and R01MH083804 (J.H.), and Deutsche Forschungsgemeinschaft HU 800/5-1 (C.A.H.).

Supplementary Materials

www.sciencemag.org/cgi/content/full/341/6150/1120/DC1
Materials and Methods

Figs. S1 to S5

Movies S1 and S2

References (31–40)

13 May 2013; accepted 8 August 2013

10.1126/science.1240405

Topographic Representation of Numerosity in the Human Parietal Cortex

B. M. Harvey,^{1*} B. P. Klein,¹ N. Petridou,² S. O. Dumoulin¹

Numerosity, the set size of a group of items, is processed by the association cortex, but certain aspects mirror the properties of primary senses. Sensory cortices contain topographic maps reflecting the structure of sensory organs. Are the cortical representation and processing of numerosity organized topographically, even though no sensory organ has a numerical structure? Using high-field functional magnetic resonance imaging (at a field strength of 7 teslas), we described neural populations tuned to small numerosities in the human parietal cortex. They are organized topographically, forming a numerosity map that is robust to changes in low-level stimulus features. The cortical surface area devoted to specific numerosities decreases with increasing numerosity, and the tuning width increases with preferred numerosity. These organizational properties extend topographic principles to the representation of higher-order abstract features in the association cortex.

Humans and many other animals use numerosity to guide behavior and decisions (1–4). Numerosity perception becomes less precise as the size of numbers increases (4–8) and is particularly effective for small numbers

(9). Animals, infants, and tribes with no numerical language perceive numerosity (1, 10–12), although they cannot count or use symbolic representations of number. Thus, numerosity processing is an evolutionarily preserved cognitive

function, distinct from counting and humans' unique symbolic and mathematical abilities (12). Because aspects of numerosity processing mirror primary sensory perception, it has been referred to as a “number sense” (2, 3).

The primary sensory and motor cortices in the brain are organized topographically. Is the neural organization for numerosity similarly topographic? The neural representation of numerosity resides in higher-order association cortices, including the posterior parietal cortex. Human functional magnetic resonance imaging (fMRI) consistently identifies this region as particularly responsive to numerosity manipulations (6, 12–14), and in similar regions, macaque neurophysiology describes neurons tuned to visual numerosity (4, 5, 7, 15). Both human fMRI and macaque neurophysiological response properties are closely linked to behavioral numerosity performance (4, 6).

We elicited responses to visual patterns with varying numerosity in study participants, while

¹Department of Experimental Psychology, Helmholtz Institute, Utrecht University, Utrecht, 3584 CS, Netherlands. ²Department of Radiology, Rudolf Magnus Institute of Neuroscience, University Medical Center Utrecht, Utrecht, 3584 CX, Netherlands.

*Corresponding author. E-mail: b.m.harvey@uu.nl

Fig. 1. Stimuli, responses, and neural population tuning.

(A) Illustration of stimulus conditions, with examples representing different numerosities. (B) Two example fMRI time courses from sites in the posterior parietal cortex, separated by about 2 cm, elicited by the numerosity stimulus sequence (top inset). BOLD, blood oxygen level-dependent. Points represent mean response amplitudes; error bars represent the standard error over repeated runs. In the upper panel, the largest response amplitude occurs after the presentation of low numerosities, whereas in the lower panel the largest response occurs with higher numerosities, considering the hemodynamic response delay. To quantify these differences, we developed a novel data-analysis method that extracts numerosity tuning from the time courses, following methods we developed in the visual cortex (17) (fig. S4). The numerosity model captures about 90% of the variance (R^2) in the time courses, as indicated by the colored lines. (C) Representation of the neural model that best fits each time course. The model describes a Gaussian tuning function in logarithmic numerosity space with two parameters: preferred numerosity and tuning width defined by the full width at half maximum (FWHM). Different model parameters explain the differences seen in (B), capturing a similar amount of the variance.

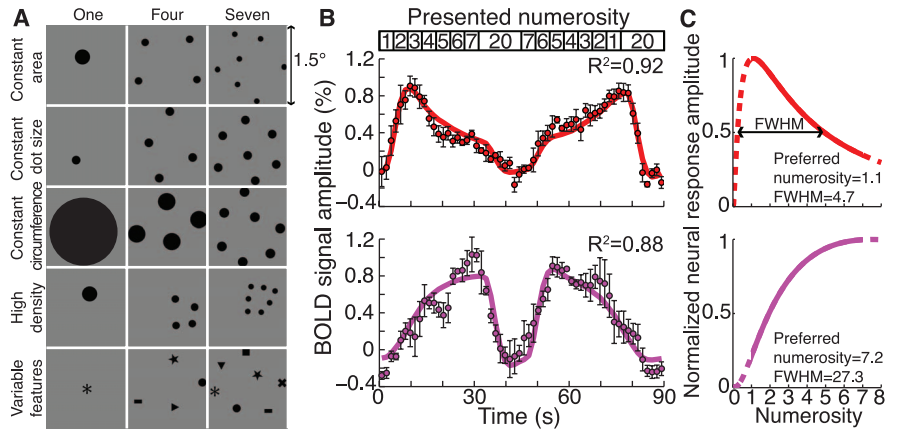
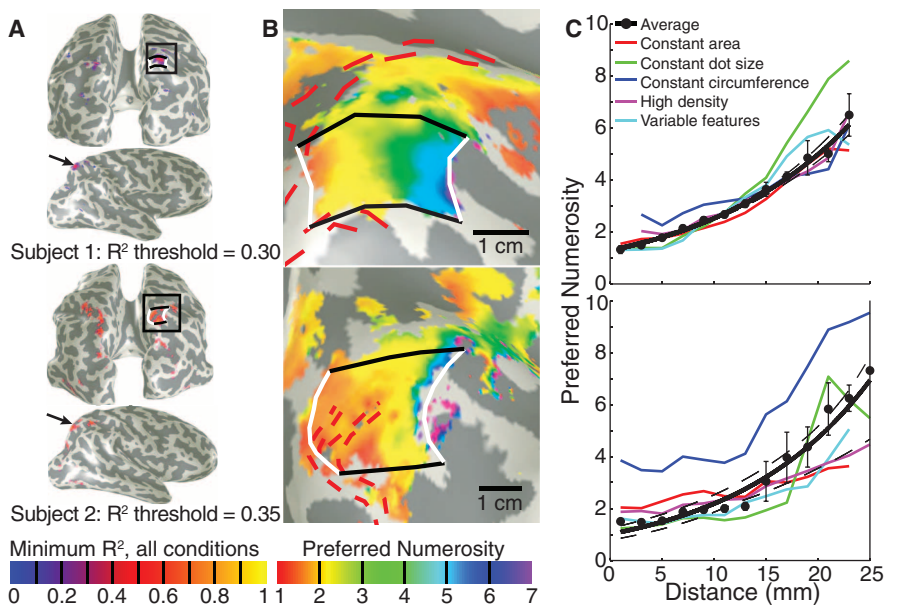


Fig. 2. Topographic representation of numerosity.

(A) The variance explained by the model (R^2) highlighted a region in the right parietal cortex where neural populations demonstrated numerosity tuning in all stimulus conditions (Fig. 1A). The black square is enlarged in (B). (B) Numerosity preferences for data averaged from all stimulus conditions, showing preferred numerosity increasing from the medial to lateral ends (white lines) of the region of interest (ROI) (black and white lines). Areas of low signal intensity, corresponding to pial surface veins (red dashed lines, fig. S3), were excluded from further analysis (30). (C) Numerosity preference progression from medial to lateral along the ROI for all conditions. All recording sites were organized by their distances from the two white lines. Dots represent the mean preferred numerosity in each distance bin, with error bars showing the standard error. We fitted the binned points with a logarithmic function (solid black line), with 95% confidence intervals to the fit (dashed black lines) determined by bootstrapping. More cortical area is devoted to lower number; i.e., cortical magnification decreases at higher numerosity. Different stimulus conditions are represented as colored lines joining the condition-specific bin means.



acquiring high-field (7 teslas) fMRI data. Changing numerosity in a visual display affects visual features such as luminance, contrast, density, and total edge length. Therefore, establishing numerosity selectivity requires several control conditions (Fig. 1A and figs. S1 and S2) (15). Consequently, we included conditions in which total dot area (“constant area” condition), individual dot size (“constant dot size”), or total dot circumference (“constant circumference”) were constant. A further condition contained much higher dot pattern density (“high density”). Finally, to check generalization to other objects, we replaced dots with different shapes (“variable features”). During stimulus presentation, participants reported when dots were shown in white rather than black (10% of presentations). No numerosity judgments were required. Participants performed above 90% correct.

The displayed numerosity varied systematically within an fMRI scan (Fig. 1B, top inset). This stimulus elicited remarkably different response profiles at different recording sites (Fig. 1B), despite having similar hemodynamic response functions (fig. S6). We summarized these fMRI signals using numerosity-tuned neural models (Fig. 1C and fig. S4). These describe Gaussian functions in logarithmic numerosity space, following behavioral (4), computational (16), neuroimaging (6), and neurophysiological (4, 5) results (fig. S5). The models have two parameters: preferred numerosity and tuning width (the numerosity range to which the population responds). This analysis is analogous to conventional population receptive field analysis in the visual cortex (17). These models explain much of the signal variance (R^2), summarizing fMRI responses with two parameters. They capture similar amounts

of variance for both example response profiles in Fig. 1B, explaining time course differences by different numerosity tunings (Fig. 1C).

A specific region in the posterior parietal cortex was highlighted, where the models captured much response variance in all stimulus conditions (Fig. 2A and fig. S7). This region’s position was consistent between the eight participants, in the posterior superior parietal lobule, centered at mean (SD) Montreal Neurological Institute x,y,z coordinates of 23 (4), -60 (7), 60 (7) (18) and closely matches previous reports of a region responding strongly to numerosity manipulations (6, 12–14).

Projecting each recording site’s preferred numerosity onto the unfolded cortical surface revealed an orderly topographic map (Fig. 2B). Medial and lateral regions preferred low and high numerosities, respectively. The topographic

Fig. 3. Comparison of numerosity preferences across recording points in different stimulus conditions, averaged across participants. (A) Because numerosity preferences are topographically organized in all stimulus conditions, they are always correlated. (B) However, preferences change with stimulus conditions, with preference increasing particularly in the constant circumference condition. t , t statistic.

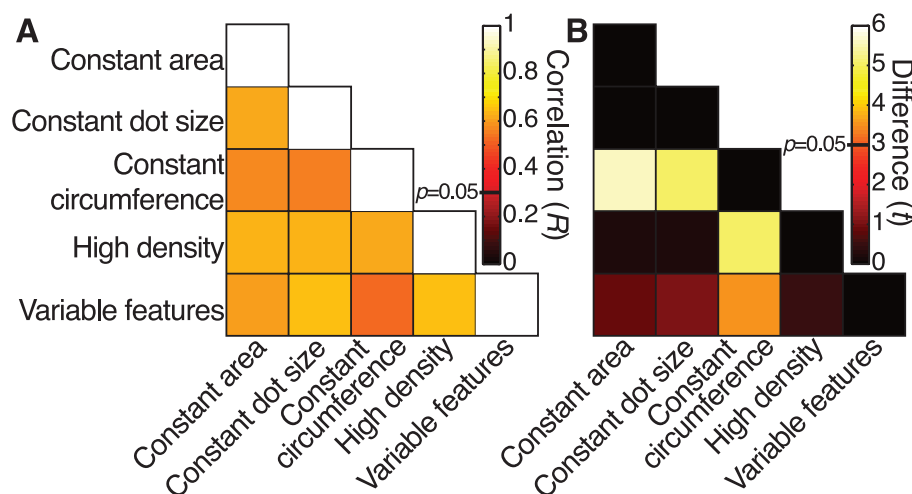
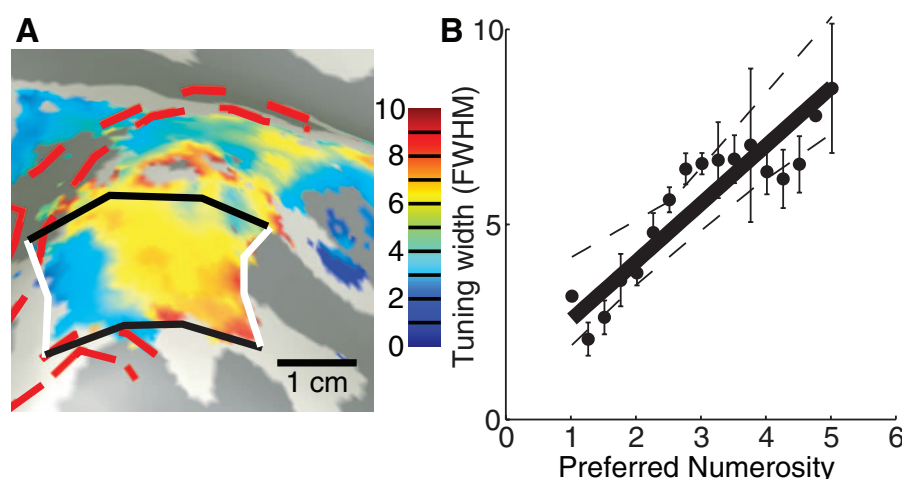


Fig. 4. The progression of population tuning width (see Fig. 1C) across the cortical surface (A) and with preferred numerosity (B) for one representative participant. Dots represent mean tuning widths in each preferred numerosity bin, and error bars represent standard errors. Dashed lines represent 95% confidence intervals of the fit (solid line) to the bin means. Tuning width increases with preferred numerosity for all participants (fig. S13B).



progression and its direction were consistent between participants and stimulus conditions (fig. S8). Numerosity selectivity was also present in the left hemisphere (fig. S9) and in neighboring regions of the right hemisphere, but with lower variance explained and less clear, less consistent topographic structure. To quantify the numerosity organization, we sorted recording sites within this region by their distance from the borders representing lowest and highest numerosities (white lines in Fig. 2B). We then plotted preferred numerosity against cortical distance for individual stimulus conditions and their average (Fig. 2C and fig. S10).

Numerosity preference was organized topographically in all stimulus conditions, so numerosity preference is significantly correlated between conditions (Fig. 3A and fig. S11A). However, absolute numerosity preference varied with stimulus condition (Fig. 3B and fig. S11B), which is consistent with results from single macaque neurons (5). In particular, the constant circumference condition differs from other conditions. It has very different dot sizes from other conditions (Fig. 1A and fig. S2), and we propose that dot size interacts with numerosity preference, be-

cause line length-selective neurons are found with numerosity-selective neurons in the macaque posterior parietal lobe (19).

The rate of numerosity preference change with distance increased with numerosity; i.e., the cortical magnification factor decreases (Fig. 2C). Thus, more cortical surface area represents lower than higher numerosities (fig. S12). Similarly, more macaque posterior parietal neurons prefer low than high numerosities (5). Such over-represented parts of other topographic maps also show more precise response selectivity than elsewhere in the map; i.e., tuning width is smaller. Tuning widths changed across the topographic map along with preferred numerosity (Fig. 4A and fig. S13A). Population tuning width increased with preferred numerosity (Fig. 4B and fig. S13B), in line with single macaque neuron (4, 5), neuroimaging (6), and behavioral results (6–8). However, population tuning widths are larger than macaque single-neuron tuning widths (fig. S14). This may arise from differences in neural population size (~400,000 neurons in our recording points), the scatter of response preferences at a single cortical location, hemodynamic properties, interpolation steps in fMRI

analyses, task differences, and/or species differences (17).

Neuroimaging studies consistently show that this part of the parietal cortex responds to numerosity manipulations (6, 12–14), and parietal lesions can cause number-processing deficits (20). Macaque neurophysiology demonstrates numerosity tuning in single neurons in a similar parietal region (5), and human neural adaptation properties suggest that numerosity-tuned populations exist in the same area, with tuning widths increasing with preferred numerosity (6). We extended these observations by directly measuring numerosity tuning in the human cortex and describing a topographic organization of numerosity, a numerosity cortical magnification factor, and a relationship between preferred numerosity and numerosity tuning width. Based on similar behavioral performance and cortical location of numerosity-selective populations in humans and macaques, we expect similar topographic organization in macaques. The spatial scale of the topographic organization is several centimeters. Consequently, methodological limitations of single-neuron recordings may have prevented its identification; i.e., at single-neuron resolution, topography may

be obscured by the scatter of response properties, broad single-neuron tuning, neurons with other response properties, and an unknown direction of topography change. However, both methodologies are complementary, and our measurements are consistent with neurophysiology. Both support numerosity tuning, albeit at different scales, in similar parts of the brain, with more neurons tuned to smaller numerosities and increases in tuning width with preferred numerosity. These properties are analogous to organization properties of the sensory and motor cortices and may underlie the decreased precision at higher numerosities that is commonly seen in human and animal behavior (4, 6, 8, 12–14).

Our numerosity-selective responses cannot be explained by other visual attributes of the stimulus. First, tuning and topographic structure were found using stimuli controlled for low-level features. Second, responses in visual field maps such as V1 cannot be captured by the numerosity model but follow stimulus contrast energy (fig. S15). Third, parietal visual field map borders (21) did not correspond to numerosity map borders and their relative positions varied considerably between participants (fig. S16). In macaques, over 80% of single neurons here show no numerosity selectivity (5, 19), so independent representations of numerosity and visual space may exist in one cortical region, represented by different neurons. Alternatively, these populations have large visual receptive fields and may be tuned to numerosity presented anywhere within this receptive field. Interactions between overlapping numerosity and visuospatial representations may underlie the cognitive spatial “number line” (11, 22). However, we find no consistent relationship between numerosity and visuospatial responses.

What is the nature of the numerosity representation? We found no number-tuned responses for Arabic numerals (fig. S17), suggesting that neurons here do not respond to symbolic number representations. We propose that current biologically plausible computational models of numerosity processing, driven by visual features, can produce the numerosity selectivity we see (16, 23). Some models suggest that (as we find) numerosity selectivity depends on stimulus features, such as dot size (23). Computational models of nu-

merosity extraction may thus explain these differences in numerosity tuning, consistent with behavioral results (7, 23).

Numerosity processing and its cortical organization may be fundamental to human abilities in mathematics and economics. Although numerosity judgments and complex mathematical abilities rely on different processes, individual differences in these abilities are correlated (24). Macaques and young children can perform simple, approximate addition and subtraction (25, 26). In macaques, the parietal and prefrontal cortices contain neurons responding specifically during simple mathematical tasks, together with numerosity-selective neurons (27). Associations between visual numerosity and symbolic number representations develop early in life (10). Numerosity, number, and size are fundamental to our understanding of magnitude and quantity and underlie higher-level concepts of value (22).

Our results demonstrate that topographic representations, common in the sensory and motor cortices, can emerge within the brain to represent abstract features such as numerosity. Similarities in cortical organization suggest that the computational benefits of topographic representations, for example efficiency in wiring (28, 29), apply to higher-order cognitive functions and sensory-motor functions alike. As such, topographic organization may be common in higher cognitive functions. On the other hand, topographic organization supports the view that numerosity perception resembles a primary sense (2, 3). These views are not mutually exclusive, but both challenge the established distinction between primary topographic representations and abstracted representations of higher cognitive functions.

References and Notes

1. E. M. Brannon, H. S. Terrace, *Science* **282**, 746–749 (1998).
2. D. Burr, J. Ross, *Curr. Biol.* **18**, 425–428 (2008).
3. S. Dehaene, *The Number Sense: How the Mind Creates Mathematics* (Oxford Univ. Press, New York, 1997).
4. A. Nieder, E. K. Miller, *Neuron* **37**, 149–157 (2003).
5. A. Nieder, E. K. Miller, *Proc. Natl. Acad. Sci. U.S.A.* **101**, 7457–7462 (2004).
6. M. Piazza, V. Izard, P. Pinel, D. Le Bihan, S. Dehaene, *Neuron* **44**, 547–555 (2004).
7. M. Tokita, A. Ishiguchi, *Atten. Percept. Psychophys.* **72**, 1839–1853 (2010).

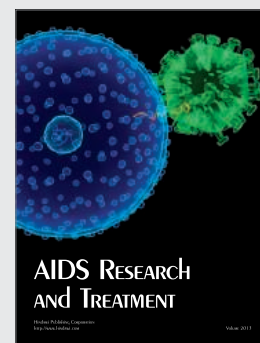
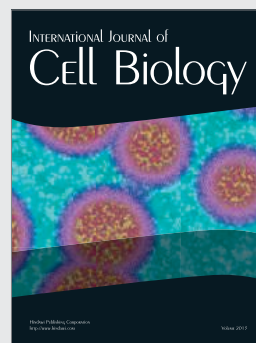
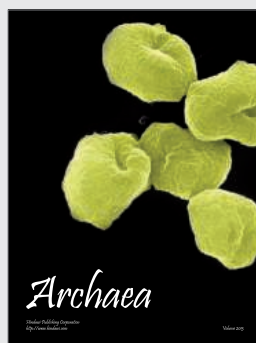
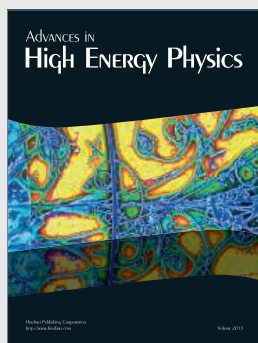
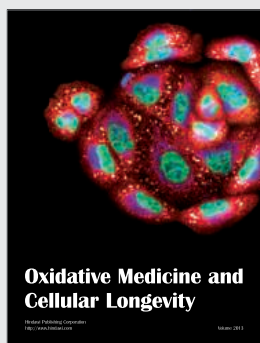
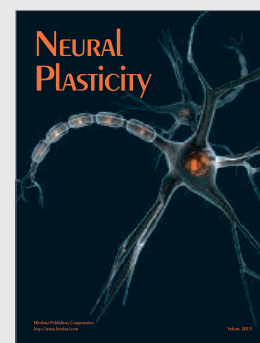
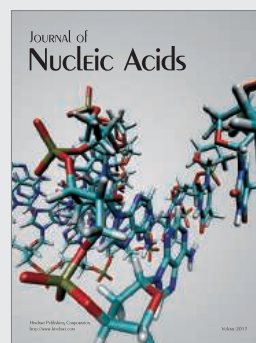
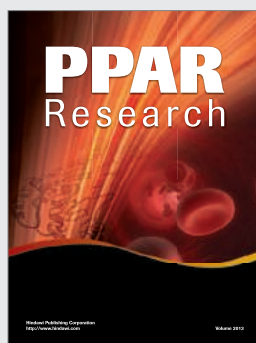
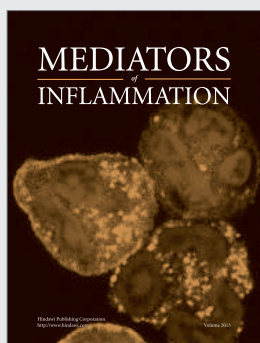
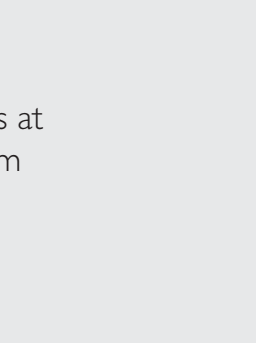
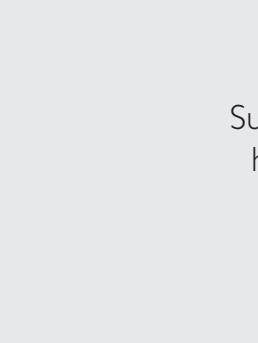
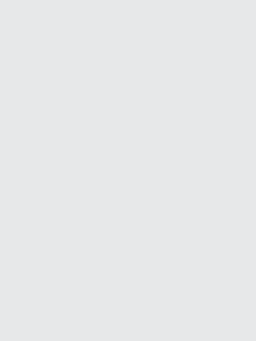
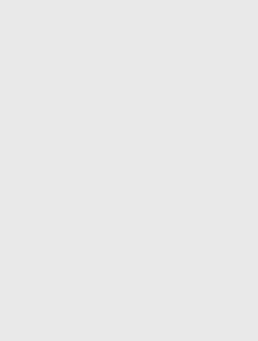
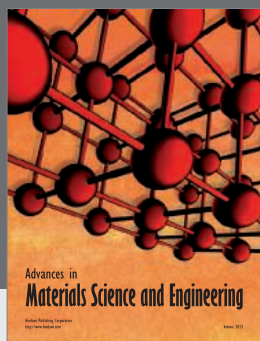
8. J. Whalen, C. R. Gallistel, R. Gelman, *Psychol. Sci.* **10**, 130–137 (1999).
9. I. J. Saltzman, W. R. Garner, *J. Psychol.* **25**, 227–241 (1948).
10. J. F. Cantlon *et al.*, *J. Cogn. Neurosci.* **21**, 2217–2229 (2009).
11. S. Dehaene, V. Izard, E. Spelke, P. Pica, *Science* **320**, 1217–1220 (2008).
12. S. Dehaene, E. Spelke, P. Pinel, R. Stanescu, S. Tsivkin, *Science* **284**, 970–974 (1999).
13. E. Eger *et al.*, *Curr. Biol.* **19**, 1608–1615 (2009).
14. P. Pinel *et al.*, *Neuroreport* **10**, 1473–1479 (1999).
15. A. Nieder, D. J. Freedman, E. K. Miller, *Science* **297**, 1708–1711 (2002).
16. S. Dehaene, J. P. Changeux, *J. Cogn. Neurosci.* **5**, 390–407 (1993).
17. S. O. Dumoulin, B. A. Wandell, *Neuroimage* **39**, 647–660 (2008).
18. D. L. Collins, P. Neelin, T. M. Peters, A. C. Evans, *J. Comput. Assist. Tomogr.* **18**, 192–205 (1994).
19. O. Tudusciuc, A. Nieder, *Proc. Natl. Acad. Sci. U.S.A.* **104**, 14513–14518 (2007).
20. S. Dehaene, L. Cohen, *Neuropsychologia* **29**, 1045–1074 (1991).
21. J. D. Swisher, M. A. Halko, L. B. Merabet, S. A. McMains, D. C. Somers, *J. Neurosci.* **27**, 5326–5337 (2007).
22. V. Walsh, *Trends Cogn. Sci.* **7**, 483–488 (2003).
23. S. C. Dakin, M. S. Tibber, J. A. Greenwood, F. A. Kingdom, M. J. Morgan, *Proc. Natl. Acad. Sci. U.S.A.* **108**, 19552–19557 (2011).
24. J. Halberda, M. M. Mazocco, L. Feigenson, *Nature* **455**, 665–668 (2008).
25. J. F. Cantlon, E. M. Brannon, *PLoS Biol.* **5**, e328 (2007).
26. P. Starkey, *Cognition* **43**, 93–126 (1992).
27. S. Bongard, A. Nieder, *Proc. Natl. Acad. Sci. U.S.A.* **107**, 2277–2282 (2010).
28. B. L. Chen, D. H. Hall, D. B. Chklovskii, *Proc. Natl. Acad. Sci. U.S.A.* **103**, 4723–4728 (2006).
29. S. Ramón y Cajal, P. Pasik, T. Pasik, *Texture of the Nervous System of Man and the Vertebrates* (Springer, New York, 1999).
30. J. Winawer, H. Horiguchi, R. A. Sayres, K. Amano, B. A. Wandell, *J. Vis.* **10**, 1 (2010).

Acknowledgments: Processed data reported in the paper are presented in full in the supplementary materials. Raw data and custom analysis code are available on request from the authors. This work was supported by Nederlandse Organisatie voor Wetenschappelijk Onderzoek Vidi grant 452.08.008. We thank J. W. Brascamp for critical comments on the manuscript.

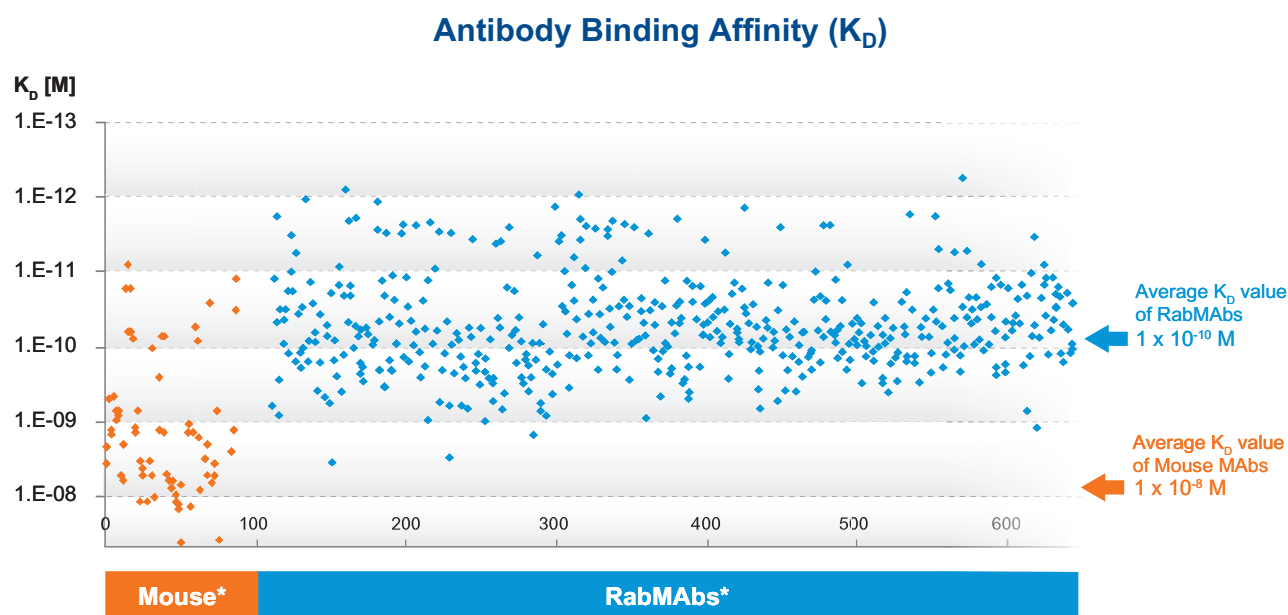
Supplementary Materials

www.sciencemag.org/cgi/content/full/341/6150/1123/DC1
Materials and Methods
Figs. S1 to S17
References (31–65)

11 April 2013; accepted 8 August 2013
10.1126/science.1239052



High quality Rabbit Monoclonal Antibodies with high affinity



Antibody kinetic analysis: Binding affinity constant (K_D)

* Partial literature survey

** In-house K_D measurements



We have systematically measured the K_D (the equilibrium dissociation constant between the antibody and its antigen), in over 800 **Rabbit Monoclonal Antibodies (RabMAbs)**. Based on the comparison with published literature values for mouse monoclonal antibodies, RabMAbs appear to be on average 1-2 orders of magnitude higher affinity.

Discover more at abcam.com/KD



RabMAbs[®]

Make ends meet.



Gibson Assembly[®] Cloning Kit

New England Biolabs has revolutionized your laboratory's standard cloning methodology. The Gibson Assembly Cloning Kit combines the power of the Gibson Assembly Master Mix with NEB 5-alpha Competent *E. coli*, enabling fragment assembly and transformation in just under two hours. Save time, without sacrificing efficiency.

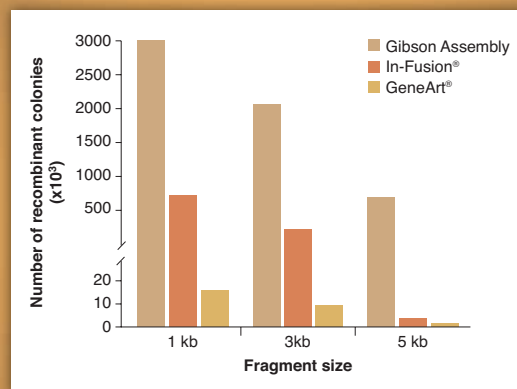
Making ends meet is now quicker and easier than ever before, with the Gibson Assembly Cloning Kit from NEB.

NEBuilder[™]
for Gibson Assembly

Visit NEBGibson.com to view the latest tutorials and to try our primer design tool.

IN-FUSION[®] is a registered trademark of Clontech Laboratories, Inc.
GENEART[®] is a registered trademark of Life Technologies, Inc.
GIBSON ASSEMBLY[®] is a registered trademark of Synthetic Genomics, Inc.

Gibson Assembly Cloning Kit provides robust transformation efficiencies



Assembly reactions containing 25 ng of linear pUC19 vector and 0.04 pmol of each fragment were performed following individual suppliers' recommended protocols and using the competent cells provided with the kit. The total number of recombinant colonies was calculated per 25 ng of linear pUC19 vector added to the assembly reaction.

SGIDNA

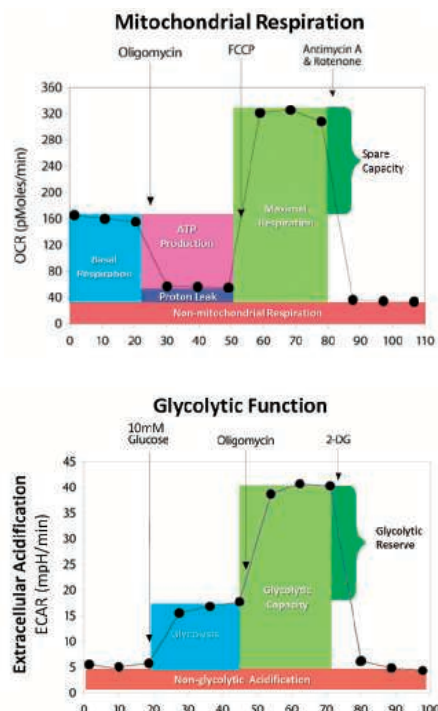
Some components of this product are manufactured by New England Biolabs, Inc. under license from Synthetic Genomics, Inc.

“ WE’RE BRINGING A NEW PERSPECTIVE TO
cancer metabolism research

FIRST WE MADE IT POSSIBLE – NOW WE’VE MADE IT EASY.

XF technology provides the easiest and most comprehensive assessment of cancer cell metabolism, measuring glucose and glutamine metabolism, and fatty acid oxidation of cancer cells in a microplate, in real-time! ”

— David Ferrick, PhD,
CSO, Seahorse Bioscience



The Seahorse XF^e Extracellular Flux Analyzer

Measurements of cellular glycolysis are essential to understanding cancer, immune response, stem cell differentiation, aging, and cardiovascular and neurodegenerative diseases. The XF^e Analyzer and XF Glycolysis Stress Test Kit make it easy to measure the three key parameters of cellular glycolysis in a microplate: glycolysis, glycolytic capacity, and glycolytic reserve, revealing critical information not evident in mitochondrial respiration measurements alone.



See what's possible.

Scan this QR code to view videos and see what the XF Analyzer can achieve.
Visit www.seahorsebio.com/science for more information!

Seahorse Bioscience



Confidence. Inspired by Results.

Alan Alfano
Cancer Researcher,
University of Maryland
School of Medicine,
Baltimore, MD

"In cancer research, achieving uniform results with transfection is often a big hurdle. **X-tremeGENE is by far the best transfection reagent I've ever used.** It's nice to know that with all the potential issues I might encounter in my research, transfection isn't one of them."

X-tremeGENE Reagents. Transfect with confidence.



See more of Alan's story at
www.x-tremegene.roche.com

For life science research only.
Not for use in diagnostic procedures.

X-TREMEGENE is a trademark of Roche.

Roche Diagnostics Corporation
Roche Applied Science
Indianapolis, Indiana

© 2013 Roche Diagnostics.
All rights reserved.





INTERNATIONAL SCIENCE & ENGINEERING VISUALIZATION CHALLENGE

Deadline Approaching

**ENTRY DEADLINE:
SEPTEMBER 30, 2013**

SCIENCE & ENGINEERING'S
MOST POWERFUL
STATEMENTS ARE NOT
MADE FROM WORDS ALONE



You are invited to submit an entry to this year's International Science & Engineering Visualization Challenge, cosponsored by the National Science Foundation and AAA's journal Science.

Entry categories include: Photography, Illustration, Posters and Graphics, Games & Apps, and Video.

Winning entries will be published in a special section of a February 2014 print issue of Science and ScienceMag.org, and NSF's web site.

ENTRY DEADLINE: SEPTEMBER 30, 2013

For entry forms, rules, and more information, go to:

www.nsf.gov/news/scivis

Award Categories

- Photography
- Illustration
- Posters & Graphics
- Video
- Games & Apps



STAY INFORMED! STAY CONNECTED!

Get more from your
AAAS membership



Are you currently registered to receive e-mails from AAAS and *Science*? E-mail is the primary way that AAAS communicates with our members about AAAS programs, new member benefits, invitations to special events, and, of course, the latest news and research being published in *Science*.

Sign up today to ensure that you are getting the most out of your membership and *Science* subscription.* To get started visit: promo.aaas.org/stayconnected You'll need your AAAS Member number. Find it above your name on your *Science* mailing label.

Don't miss a thing. Sign up for e-mail communications from AAAS today!



*AAAS follows CAN-SPAM and European Safe Harbor guidelines for protecting your privacy. We will never sell your e-mail address and you can opt-out of receiving e-mails at any time.

P-1000 Next Generation Micropipette Puller



The latest in micropipette pulling technology!

FEATURES

- Color touch-screen interface
- Safe heat mode to protect and extend filament life
- Pipette Cookbook program directory
- Line repeat mode simplifies programming
- Glossary with micropipette and puller terminology
- Copy & Paste function for writing new programs
- Two symmetrical pipettes with each pull
- Memory storage for up to 100 programs

SUTTER INSTRUMENT

PHONE: 415.883.0128 | FAX: 415.883.0572
EMAIL: INFO@SUTTER.COM | WWW.SUTTER.COM

Grad Students:

Win \$5,000

for scientific achievement

Inaugural ASCB Kaluza Prize supported by Beckman Coulter

Only ASCB members eligible • Membership is just **\$42**. Join now at www.ascb.org

Details/apply by September 30 at
www.ascb.org/Kaluza.cfm



Reminder: Join us at the ASCB 2013 Annual Meeting, New Orleans, Dec. 14-18
Late abstract submission deadline is **October 16**

New accessory:
Eppendorf
ThermoTop®



Multiple Talents

Eppendorf ThermoMixer™ and Eppendorf ThermoStat™

The new generation of Eppendorf Temperature Control and Mixing Instruments offer you more than what meets the eye.

Not only do they provide the versatility and accurate temperature control you come to expect, they now also offer you superior mixing performance, outstanding ergonomic operation and a unique ThermoTop.

- > 2D Mix-Control: perfect mixing results in all vessel formats
- > Eppendorf QuickRelease™: ergonomic block exchange in just 2 seconds
- > Intuitive operation: pre-optimized program and temperature keys
- > Eppendorf ThermoTop prevents condensate formation for more accurate results.



www.eppendorf.com/thermomixer-c

Eppendorf®, the Eppendorf logo and Eppendorf ThermoTop® are registered Trademarks of Eppendorf AG, Germany.
Eppendorf ThermoMixer™, Eppendorf SmartBlocks™, Eppendorf ThermoStat™ and Eppendorf QuickRelease™ are Trademarks of Eppendorf AG.
All rights reserved, including images and graphics. Copyright © 2013 by Eppendorf AG.

THERMAL PLATE SEALER

The MicroSeal is a manual microplate heat sealer designed to be compact, easy-to-use, and offer great performance. Of the various methods of sealing microplates, heat sealing has become the preferred option for many labs as it creates an air tight and chemically resistant seal without the complications of adhesives being applied to a plate. Incorporating a unique ergonomic pull down mechanism makes single action heat sealing of a wide range of plates on the MicroSeal quick and simple. Using a preset temperature of 170°C—ideal for most common sealing applications—and dual LED status display of power and heating, the MicroSeal is very safe and easy-to-use. A built-in thermostat prevents overheating of plates. With its small footprint and ability to handle a wide range of plates the MicroSeal is the obvious choice for laboratories looking for an affordable manual thermal plate sealer.

Porvair Sciences

For info: +44-(0)-1372-824290 | www.porvair-sciences.com



STORAGE TUBES

The Octygen 0.50 mL screw cap tube sets a new standard for low-temperature sample storage. In low-temperature storage facilities the cost of freezer space is an important cost of operation. The ultracompact design of the Octygen tubes—at just 25.6 mm tall to deliver 475 µL working volume—uses only 60% of the space that competitive 0.50 mL 96-well format screw cap tubes use to store the same volume. To further optimize use of valuable storage space, 96 individual 0.50 mL Octygen tubes can be stored in an automation-compatible rack. The unique design of the Octygen tube means that a Revco -80°C freezer can store 120,960 0.50 mL Octygen tubes compared with only 80,640 0.50 mL tubes of a competitive design. Designed for both manual and automated low-temperature storage applications, the external thread design of Octygen tubes facilitates fast and simple sample handling.

Micronic

For info: +31-320-277070 | www.micronic.com

MULTICHANNEL PIPETTES

The manual Rainin Pipet-Lite XLS+ and electronic Rainin E4 XLS+ offer users durable, lightweight liquid ends and new mechanical designs that all but eliminate hand strain while ensuring the highest channel-to-channel consistency. This combination of improved ergonomic comfort and exceptional performance helps pipette operators work more comfortably and reduce the risk of error and potentially expensive rework. Experiment costs go down as throughput accuracy increases. The Rainin XLS+ multichannel pipettes represent an intelligent advance in both performance and ergonomics. Reduced weight and lower pipetting/tip-ejection forces—combined with improved balance—reduce operator fatigue during intensive 96-well plate work. Enhanced reliability ensures data integrity. And operators concerned about cross-contamination will appreciate XLS+'s reduced stiction (piston stickiness), which helps to eliminate splash-up. Capitalizing on recent advances in molding technology, Rainin has achieved an optimal balance between lightness and performance—two goals that often run counter to one another.

Mettler Toledo

For info: 800-472-4646 | www.mt.com/rainin-mc

ELECTRONIC PIPETTE CONTROLLER

Replacing the existing pipette controller model, the Easypet 3 gives greater accuracy by controlling the speed conveniently and intuitively with the use of the operating buttons. The new Easypet 3 boasts decreased battery charging time to three hours, allowing for increased cordless operation time. With its lightweight ergonomic design Easypet 3 enables stress-free pipetting. Easypet 3 promotes reliability, ease of use, and simplicity. Operation buttons are ergonomically shaped, making aspirating and dispensing of liquids easy. Increased or reduced pressure on the buttons regulates speed for precise measurements. Vibrant backlit LEDs highlight the battery status contributing to the user's peace of mind. Easypet 3 delivers efficient performance through a high-powered motor speeding up the pipetting process and can be used with any type of pipette from volumes of 0.1 mL to 100 mL. Easypet 3 is also able to be operated while recharging, ensuring that the workflow is not interrupted.

Eppendorf

For info: 800-645-3050 | www.eppendorf.com/easypet

HEATING BLOCK

New versions of the DrySyn Maxi and DrySyn Super Maxi for labs tasked with larger scale reactions (2,000 mL to 5,000 mL) are now available. Constructed in solid anodised aluminium, both the DrySyn Maxi and DrySyn Super Maxi deliver outstanding thermal and magnetic transfer efficiency and have durability suitable for use in any laboratory environment. Design improvements in the latest generation of these products has resulted in improved heat transfer characteristics up to 300°C, faster heating and cooling, and a smaller footprint. Affordably priced, the DrySyn Maxi single position heating block system is designed to accommodate 2,000 mL or 3,000 mL flasks. For 4,000 mL and 5,000 mL flasks the DrySyn Super Maxi is the heating block of choice. Used in combination with a standard hotplate stirrer, DrySyn Maxi and Super Maxi units are proven to outperform the heat-conducting properties of oil baths.

Asynt

For info: +44-(0)-1638-781709 | www.asynt.com

Electronically submit your new product description or product literature information! Go to www.sciencemag.org/products/newproducts.dtl for more information.

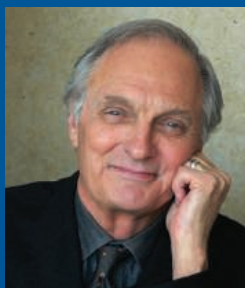
Newly offered instrumentation, apparatus, and laboratory materials of interest to researchers in all disciplines in academic, industrial, and governmental organizations are featured in this space. Emphasis is given to purpose, chief characteristics, and availability of products and materials. Endorsement by Science or AAAS of any products or materials mentioned is not implied. Additional information may be obtained from the manufacturer or supplier.

AAAS|2014 ANNUAL MEETING

13-17 FEBRUARY • CHICAGO

MEETING GLOBAL CHALLENGES:
DISCOVERY AND INNOVATION

Plenary Speakers



Alan Alda

Visiting Professor of Journalism
Stony Brook University

*Getting Beyond a Blind Date
with Science*



Steven Chu

Professor of Physics and Molecular
and Cellular Physiology
Stanford University

*How Discovery and Innovation
Can Meet Our Energy Challenge*



Susan Lindquist

Professor of Biology
Massachusetts Institute
of Technology

*From Yeast Cells to Patient Neurons:
A Powerful Discovery Platform for
Parkinson's and Alzheimer's Diseases*



John A. Rogers

Swanlund Chair and Professor of
Materials Science and Engineering
University of Illinois, Urbana-
Champaign

*Stretchy Electronics that Dissolve
in Your Body*

Registration and housing are now open.
www.aaas.org/meetings



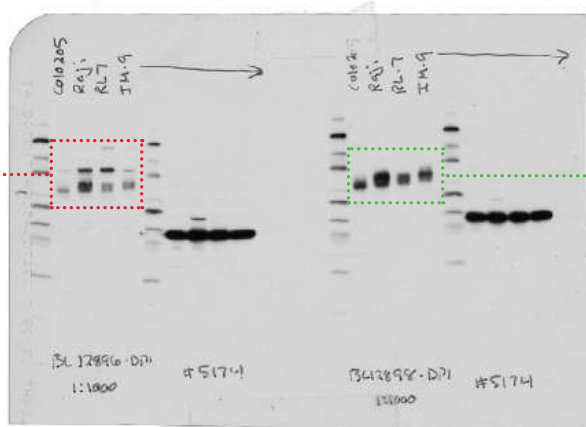
You've carefully
designed your
experiment.

Taylor Ngo started at CST 8
years ago and is currently in
the Molecular Biology group.

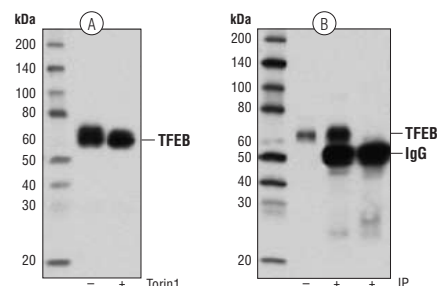
Does your antibody measure up?

We validate all our antibodies in-house. If it's not specific, it doesn't ship.

REJECTED
Extra Band
Weak Signal



**CST
APPROVED**
Clean Band
Strong Signal



TFEB Antibody #4240: (A) WB analysis of Raji cell extracts, untreated (-) or Torin1-treated, using #4240 (Torin1 treatment induces dephosphorylation). (B) IP of TFEB from COLO 205 cells using #4240 (lane 2) or Normal Rabbit IgG #2729 (lane 3). Lane 1 is 10% input.

WB analysis of various cell extracts using two development samples at 1:1000 dilution. GAPDH (D16H11) XP® Rabbit mAb #5174 was used as a loading control.

Please visit our website to request a copy of our new white paper – *A Guide to Successful Western Blotting*.

www.cellsignal.com/successfulWB

© 2013 Cell Signaling Technology, Inc. Cell Signaling Technology® and XP® are trademarks of Cell Signaling Technology, Inc.



Cell Signaling
TECHNOLOGY®



Science Careers Advertising

For full advertising details, go to ScienceCareers.org and click For Employers, or call one of our representatives.

Tracy Holmes
Worldwide Associate Director
Science Careers
Phone: +44 (0) 1223 326525

THE AMERICAS

E-mail: advertise@sciencecareers.org
Fax: 202-289-6742

Tina Burks
East Coast/West Coast/South America
Phone: 202-326-6577

Marci Gallun
Midwest/Canada
Phone: 202-326-6582

Candice Nulsen
Corporate
Phone: 202-256-1528

Online Job Posting Questions
Phone: 202-312-6375

EUROPE / INDIA / AUSTRALIA / NEW ZEALAND / REST OF WORLD

E-mail: ads@science-int.co.uk
Fax: +44 (0) 1223 326532

Axel Gesatzki
Phone: +44 (0)1223 326529

Sarah Lelarge
Phone: +44 (0) 1223 326527

Kelly Grace
Phone: +44 (0) 1223 326528

JAPAN

Yuri Kobayashi
Phone: +81-(0)90-9110-1719
E-mail: ykobayas@aaas.org

CHINA / KOREA / SINGAPORE / TAIWAN / THAILAND

Ruolei Wu
Phone: +86-1367-1015-294
E-mail: rwu@aaas.org

All ads submitted for publication must comply with applicable U.S. and non-U.S. laws. Science reserves the right to refuse any advertisement at its sole discretion for any reason, including without limitation for offensive language or inappropriate content, and all advertising is subject to publisher approval. Science encourages our readers to alert us to any ads that they feel may be discriminatory or offensive.

Science Careers

From the journal *Science*



ScienceCareers.org



Why not change the world?

Two Faculty Positions at Rensselaer Polytechnic Institute

Rensselaer Polytechnic Institute invites applications and nominations for two faculty positions in the broad area of environment and ecology. The positions will each be expected to engage in a new strategic partnership recently established between Rensselaer and IBM called the Jefferson Project at Lake George, a new endeavor to develop a global model for sustained ecosystem understanding and protection focusing on Lake George, a world-class natural resource now threatened with permanent degradation from a range of environmental stressors. An unprecedented array of new tools will fuse monitoring, modeling, simulation, forecasting, and protection of Lake George including a mesocosm facility, high performance computing and visualization platform, and cyberphysical system platform (<http://tiny.cc/qn5s1w>).

The positions will also have deep engagement with Rensselaer's Darrin Fresh Water Institute (DFWI) in Bolton Landing, NY (<http://www.rpi.edu/dept/DFWI/index.html>), a multidisciplinary environmental research and education center dedicated to understanding the structure and function of aquatic, terrestrial, and atmospheric systems. The primary research focus is on the ecological consequences of environmental perturbations due to human activities in the Northeastern United States. For nearly four decades, the DFWI has maintained a consistent record of success in developing and implementing a range of programs in basic and applied research as well as graduate and undergraduate education.

Preference for both positions is any area of environmental or ecological sciences, which will enhance the research, educational, and outreach activities of Rensselaer and the DFWI. **Rensselaer Polytechnic Institute, 110 8th Street, Troy, NY 12180.**

David M. Darrin '40 Senior Endowed Chair

We invite applications and nominations for a distinguished scientist, with international reputation, well-established research and teaching record, and demonstrated ability to generate external funding for the David M. Darrin '40 Senior Endowed Chair. The Darrin Chair will be expected to play a critical leading role in the Jefferson Project, and will be charged to better integrate environmental research and educational programs at the Rensselaer main campus in Troy, NY and the DFWI on Lake George. The successful candidate will also be expected to teach graduate and/or undergraduate courses as assigned within their home department (expected to be either Biology or Earth & Environmental Sciences).

The successful candidate must have an earned Ph.D. (or a foreign degree equivalent) in a science or engineering field, and a distinguished record of academic and professional leadership that are commensurate with a tenured faculty appointment at the level of Full Professor. Candidates must be eligible for tenure and demonstrate having achieved at least seven (7) years of professional scientific experience: community leadership; a nationally or internationally-recognized record of excellence in scholarship; and a sustained level of high quality educational activities.

Nominations and applications must be sent as a single PDF document containing curriculum vitae, a statement of research accomplishments and goals, and a brief description of teaching interests to biology-chair@rpi.edu. Questions may be directed to Dr. Susan P. Gilbert (sgilbert@rpi.edu/518-276-4415) and/or Dr. Frank Spear (spearf@rpi.edu/518-276-6103), Co-Chairs, Search Committee and/or Dr. Sandra Nierzwicki-Bauer, Director of the Rensselaer Darrin Fresh Water Institute (nierzs@rpi.edu/518-644-3541).

Consideration of candidates will begin upon receipt of applications and will continue until the position is filled.

Department of Biology Faculty Search Associate Director of the Darrin Fresh Water Institute

The Department of Biology at Rensselaer Polytechnic Institute invites applications for an innovative scientist in the broad area of freshwater ecological systems. At minimum applicants must hold a Ph.D. degree, or foreign degree equivalent, in science or engineering with accomplishments in developing and managing research programs that are commensurate with a tenured faculty appointment at the level of Associate or Full Professor. Candidates at the Associate Professor level must demonstrate through at least three (3) years of professional scientific experience that they have an emerging national and/or internationally recognized research program, and established record of educating students. To be considered as a Full Professor, candidate must be eligible for tenure and demonstrate having achieved at least seven (7) years of professional scientific experience: community leadership; a nationally or internationally-recognized record of excellence in scholarship; and a sustained level of high quality educational activities.

The successful candidate is expected to become the Associate Director of the DFWI and be an active participant in both the Department of Biology and the Darrin Fresh Water Institute (DFWI). Duties will include teaching at the graduate and/or undergraduate level in the Department of Biology.

Applications must be sent as a single PDF document containing curriculum vitae, a statement of research accomplishments and vision, and a brief description of teaching interests to biology-chair@rpi.edu. For additional information, please contact: Dr. Susan P. Gilbert, Head, Department of Biology (sgilbert@rpi.edu/581-276-4415) or Dr. Sandra Nierzwicki-Bauer, Director Rensselaer Darrin Fresh Water Institute, Email: Nierzs@rpi.edu/ Phone: 518-644-3541.

Application review will be ongoing with an application deadline of November 1, 2013.



Rensselaer

We welcome candidates who will bring diverse intellectual, geographical, gender and ethnic perspectives to Rensselaer's work and campus communities. Rensselaer Polytechnic Institute is an Affirmative Action/Equal Opportunity Employer.



Creation?
Innovation?
Ambition?

The KU Leuven Group Biomedical Sciences invites applications for several Senior academic staff and tenured academic positions (m/f):

- Neuropathology and neurobiology of neurodegenerative disorders
- Molecular pathology
- Viral vector technology
- Hypertension and cardiovascular epidemiology
- Translational metabolic research
- Sexual psychology, psychophysiology and psychopathology
- Musculoskeletal rehabilitation
- Stem cell biology with specific focus on molecular control of stem cell pluripotency versus differentiation
- Regenerative medicine with focus on endogenous tissue responses after cell therapy or transplantation
- Preclinical multimodal imaging
- Quantitative molecular image processing
- Fundamental/translational research in oncology
- Implants to study, manipulate and/or restore the nervous system
- Pharmacometrics
- Biomedical statistics and statistical bio-informatics
- Autoimmunity and mucosal immunology
- Mucosal integrity
- Health economics
- Physical education pedagogy
- Microbiological bioinformatics
- Crystallography and modelling of multi-enzyme complexes in virology
- Synthetic biology
- Bio-informatics of cancer genetics
- Neuroplasticity and neuromotor rehabilitation
- Movement control and neuroplasticity from a lifespan perspective
- General practice
- Chemical biology in cellular and molecular medicine
- Motor control
- Systems biology in cellular and molecular medicine
- Radiopharmacy

For more information about these vacancies: <http://gbiomed.kuleuven.be/career>



Discover yourself, start with your job.

KU LEUVEN

The University of Leuven pursues a policy of equal opportunity and diversity.

www.kuleuven.be/jobsite



SEVERAL Tenure Track or Tenured PROFESSOR Positions

Aalto University School of Electrical Engineering seeks experts especially in the following fields:

- **Radio science and engineering**, especially microwave monitoring and observations of environment and climate change
- **Micro- and nanosciences**, especially nanofabrication and optoelectronics
- **Communication and networking technology**, especially network and cyber security, techno-econo-social and policy aspects of Internet, mathematical modeling and optimization of communications networks, and emerging new technologies in communications

The positions are open at all levels from assistant professor to full tenured professor. Applicants must have a doctoral degree in a relevant field. For assistant and associate professor levels evaluation focuses on merits and potential for excellence, for full professors we look for demonstrated excellence in research and teaching. We especially encourage applications from young professionals. Relevant industrial experience is appreciated.

Application deadline is September 30, 2013. For further information and application details, please visit at: www.elec.aalto.fi/tenuretrack

Aalto University is a new university with over a century of experience. Created from a high-profile merger between three leading universities in Finland – the Helsinki School of Economics, Helsinki University of Technology and the University of Art and Design Helsinki – Aalto University opens up new possibilities for strong multidisciplinary education and research. The university has 20 000 students and a staff of 5 000 including 350 professors.

aalto.fi

RESEARCH PROFESSOR AND DIRECTOR OF RESEARCH Department of Anesthesiology

We invite scientists with outstanding research accomplishments to apply for a tenure track position as Director of Research in the Department of Anesthesiology. Research facilities and resources will be provided commensurate with the accomplishments and research goals of the successful candidate; the position is supported in part by the Distinguished Research Professor Chair. A record of significant peer reviewed publications and external funding is essential. Responsibilities include leading a vigorous research program, as well as the development of research activities and mentoring of research faculty, residents and students. With the major expansion of research at Weill Cornell (<http://weill.cornell.edu/campaign/research/priority.html>), collaborative interactions with investigators in other departments are encouraged. Research areas relevant to anesthesiology will be considered with a focus on neuroscience including pain mechanisms and therapy, neuropharmacology and neurophysiology. Interested candidates should send their curriculum vitae, names of three references, and research plan to Hugh Hemmings M.D. Ph.D., Chair at anes-search@med.cornell.edu.

EOE/M/F/D/V



Weill Cornell Medical College

utmb Health

CHAIR, DEPARTMENT OF BIOCHEMISTRY AND MOLECULAR BIOLOGY

The University of Texas Medical Branch invites applications for the position of **Biochemistry and Molecular Biology**. The new chair will report directly to the Executive Vice President and Provost, Dean of the School of Medicine.

A central element of UTMB's future is building its research enterprise such that it's prepared for the new opportunities that translational science offers, and the Department of Biochemistry and Molecular Biology is a principal focus of that effort. The Department has been highly ranked for NIH funding with strengths in structural biology, effects of oxidative stress, epigenetics, and DNA repair. Research space and equipment for the Department is excellent.

The Chair of Biochemistry and Molecular Biology will have the opportunity to significantly reinvent the Department with new faculty recruitments over the next five years, and is expected to shape the Department for national recognition in part by taking advantage of the school's broader growth strategies and of the many opportunities for collaborative efforts with other units. The Chair must be a passionate advocate for the Departments' students and trainees. He/she will be a major institutional leader, working with the Dean/Provost's office in setting academic directions for UTMB, and promoting the school's accomplishments with external stakeholders. As the Chair of one of the School of Medicine's most critical Departments, the Chair is necessarily both advocate for his/her faculty as well as an important steward and leader for the organization in all its missions.

Interested candidates will be a nationally recognized scientist holding an Ph.D. or M.D./Ph.D. and will have academic credentials appropriate for appointment at the rank of full professor and the leadership skills to guide an important university asset through a transformational period.

The Academic Health Center Practice of Korn/Ferry International is assisting The University of Texas Medical Branch with this important search. Please forward, as soon as possible, your application or nominations of appropriate candidates to: **Warren E. Ross, M.D., c/o M. Sarah Taylor, Senior Associate, Email: sarah.taylor@kornferry.com, Korn/Ferry International, 1835 Market Street, Suite 2000, Philadelphia, PA 19103.**

The University of Texas Medical Branch is an equal opportunity employer committed to excellence through diversity, and strongly encourages applications from women, minorities, and other under-represented groups.



KORN/FERRY INTERNATIONAL



FACULTY POSITION Department of Molecular Biology Massachusetts General Hospital Department of Genetics Harvard Medical School

The Department of Molecular Biology at the Massachusetts General Hospital (MGH) and the Department of Genetics at Harvard Medical School (HMS) invite applications for a joint appointment at the level of Assistant Professor. The laboratory will be located in the Department of Molecular Biology at MGH (<http://molbio.mgh.harvard.edu>), a major research center in the Boston area and a teaching affiliate of Harvard Medical School. The faculty appointment will be in the HMS Department of Genetics (<http://genetics.med.harvard.edu>). The following HMS faculty members have labs in the MGH Department of Molecular Biology:

David Altshuler	Deborah Hung	Marjorie Oettinger
Frederick Ausubel	Joshua Kaplan	Gary Ruvkun
Joseph Avruch	Robert Kingston, Chair	Jen Sheen
Michael Blower	Jeannie Lee	Jack Szostak
	Vamsi Mootha	

Applicants should apply via electronic submission by **November 1, 2013** at: <http://molbio.mgh.harvard.edu/facultysearch/>

Please submit a curriculum vitae, statement of research plans, up to three relevant publications, and contact information for three references.

Harvard University and the Massachusetts General Hospital are Equal Opportunity/Affirmative Action Employers. Applications from women and minorities are encouraged.



HD Biosciences Co. Ltd., is a leading biology focused preclinical drug discovery CRO based in Shanghai, China. The company offers comprehensive drug discovery services, from Target to Hit, Hit to Lead, Lead Optimization to IND, in both small molecules and biologics. The company's strategic clients include seven of world top ten pharmaceutical companies. The outstanding track records in the services and capabilities to provide inputs to our clients have helped company to earn great reputation in the industry.

As part of growing R&D business, we are recruiting to fill several key positions. We are searching for qualified, self-motivated and experienced individuals with strong capability and track record in the following areas:

- ❖ VP/Senior Director/Director/Principal Scientist/Senior Scientists, Molecular Biology, Cell Biology, Biochemistry
- ❖ VP/Director/Director/Principal Scientist, *In vivo* Pharmacology
- ❖ Senior Director/Director/Principal Scientist, discovery biology in enzyme, receptor, transporter and ion channel
- ❖ Senior Director/Director/Principal Scientist/Senior Scientist, in Neuroscience, Oncology, Immunology, Metabolic Diseases
- ❖ Senior Director/Director/Principal Scientist, toxicology
- ❖ Senior Director/Director/Principal Scientist, DMPK
- ❖ Director/Principal Scientist/Senior Scientist, Biologics and Antibody Discovery/Development

We provide excellent career development opportunities, competitive compensation package and employee stock option plan to qualified employees. We are proud to be an Equal Opportunity Employer. To learn more about HDB or view a completed list of job openings and apply online, please visit us at: <http://www.hdbiosciences.com>, or submit a copy of curriculum vitae to recruiting@hdbiosciences.com.

HD Biosciences Co., Ltd. Phone: +86-21-51163700

590 Ruiqing Road, Zhangjiang East Campus, Pudong, Shanghai 201201, P. R. China

Email: recruiting@hdbiosciences.com

ASSISTANT PROFESSORS

Department of Biological Sciences

The Department of Biological Sciences at The University of Alabama is seeking two new tenure-track faculty members at the rank of Assistant Professor in (1) **Computational Biology**, and (2) **Microbiology/Microbial Biology**.

Tenure-Track Position in Computational Biology

All areas of computational biology and bioinformatics will be considered. Applications from candidates with a demonstrated record of developing and/or applying computational approaches to study biological questions in areas including comparative genomics and transcriptomics, evolutionary genomics, phylogenomics, computational ecology/ecoinformatics, cell and molecular biology, and systems biology are especially encouraged to apply.

Tenure-Track Position in Microbiology/Microbial Biology

All areas of microbiology/microbial biology will be considered. Applicants conducting research in microbe-microbe, microbe-environment, and/or microbe-host interactions using genomics, proteomics, and/or transcriptomics approaches are encouraged to apply.

Candidates must have a Ph.D. degree in the Biological Sciences or related field, postdoctoral experience, evidence of the ability to establish an extramurally funded research program and mentor students. The successful applicants will be expected to develop an active research program, develop new courses in his/her area of expertise and participate in the teaching of existing undergraduate and graduate courses. Faculty in the Biological Sciences Department have diverse research interests and have interdisciplinary collaborations with UA faculty in the Departments of Chemistry, Chemical and Biological Engineering, Geography, Geological Sciences, and Metallurgical and Materials Engineering.

Applicants may contact Dr. Juan Lopez-Bautista the chair of the computational biology search committee, at jlopez@ua.edu, or Dr. Robert Findlay, the chair of the Microbiology/Microbial Biology Search Committee at rfindlay@ua.as.edu if additional information is desired.

To apply, go to <https://facultyjobs.ua.edu>, complete the online application (Job #) or (Job #), and upload (1) an application letter with a list of three to five references (including contact information); (2) CV; (3) statement of research interests and goals; and (4) statement of teaching interests and philosophy. Consideration of applications will begin September 1, 2013, and continue until the positions are filled. Prior to the hiring, the final candidate(s) will be required to pass a pre-employment background investigation. Anticipated start date is August 16, 2014, although candidates seeking a January 1, 2014 as start date will be considered.

Additional information on the Department of Biological Sciences and the available positions can be found on our website at <http://bsc.ua.edu>.

The University of Alabama is an Equal Opportunity/Equal Access Employer and actively seeks diversity among its employees. Women and minorities are encouraged to apply.

touching lives
THE UNIVERSITY OF ALABAMA



JAMSTEC

<http://www.jamstec.go.jp/e/>

Scientist/Engineer/Postdoctoral Researcher for Comprehensive Studies on the Evolution of Life and the History of the Earth

The Japan Agency for Marine Science and Technology (JAMSTEC) is recruiting 10 full time fixed term contract positions for pursuing research on "Comprehensive Studies on the Evolution of Life and the History of the Earth", in the position of Scientist, Engineer or Postdoctoral Researcher.

Details of the ongoing research in JAMSTEC regarding exploring the unknown biosphere and investigating biotic evolution since the origin of life are available at;

<http://www.jamstec.go.jp/e/about/research/biogeosciences.html>

<Relevant Research Fields>

Applied microbiology, Applied genomics, Genetic engineering, Protein engineering, Environmental microbiology, Microbial ecology, Geobiology, Marine biology and ecology, Bioinformatics, Microbial physiology, Biochemistry, Bioengineering, Molecular biology and ecology, Biogeochemistry, Environmental chemistry, Astrobiology, Life and biosphere search and detection, Biomimetics, Soft Matter Science, Nanotechnology, Nanobiotechnology, Materials science, Biophysics, Physical chemistry, Natural product, Colloid/Interface science, Polymer chemistry, Marine Geology, Geochemistry, Paleontology, Biogeosciences, Phylogenetic systematics, Deep-sea biology/bionomics and Synthetic biology.

The successful candidates are expected to join us from April 1st, 2014 at either Yokosuka or Yokohama, Japan.

Required documents must be sent to JAMSTEC by **POST** before/ on **September 24th, 2013**.

For further information, please visit our website;

http://www.jamstec.go.jp/e/about/recruit/biogeos_20130924.html

Scientist/Engineer/Postdoctoral Researcher for Understanding and Prediction of Global Climate/Environment Change

The Japan Agency for Marine-Earth Science and Technology (JAMSTEC) is recruiting 25 full time fixed term contract positions for pursuing research on "Understanding and Prediction of Global Climate/Environment Change", in the position of Scientist, Engineer or Postdoctoral Researcher.

Details of the ongoing research in JAMSTEC regarding climate/environment changes are available at;

<http://www.jamstec.go.jp/rigc/e/>

<Relevant Research Fields>

General Earth and Planetary Sciences including Physical Oceanography, Chemical Oceanography, Marine Biology, Meteorology, Atmospheric Chemistry, Dynamic Meteorology, Vegetation Science, Astronomy and Computer Science. Studies of Solid Earth Science are not directly relevant field.

The successful candidates are expected to join us from April 1st, 2014 at either Yokosuka or Yokohama, Japan.

Required documents must be sent to JAMSTEC by **POST** before/ on **October 4th, 2013**.

For further information, please visit our website;

http://www.jamstec.go.jp/e/about/recruit/rigc_20131004.html



Faculty Position- Lung Cancer Research Program Co-Leader and SPORE Principle Investigator University of Pittsburgh Cancer Institute & University of Pittsburgh School of Medicine



The University of Pittsburgh Cancer Institute (UPCI) with the University of Pittsburgh is seeking applications for a faculty position at the level of Associate Professor or Professor. Candidates who have a PhD, MD, or equivalent are being recruited to lead lung cancer laboratory research at UPCI, serve as Co-Leader for the UPCI Lung and Thoracic Malignancies Program and serve as Principle Investigator for the Lung Specialized Program in Research Excellence (SPORE). The incumbent will have primary appointments in a Department at the University of Pittsburgh, School of Medicine (UPSOM) that will reflect to their research area of expertise.

The incumbent will have a demonstrated track record of leadership, excellent communication skills, and publications in high-impact journals, and will be expected to sustain an outstanding, extramurally supported lung cancer research program. Candidates at the Associate Professor level or higher, with a proven track record in cutting edge basic and translational research and a strong track record of NIH funding, are encouraged to apply. Salary and benefits will be commensurate with experience.

Founded in 1985, the University of Pittsburgh Cancer Institute has consistently been ranked among the top NCI-funded cancer centers and is the only NCI-designated Comprehensive Cancer Center in western Pennsylvania. In collaboration with the UPMC CancerCenter, UPCI offers a highly interactive environment to its community of basic, translational and clinical investigators and provides state-of-the-art shared resources for tissue imaging, high-throughput drug discovery, 'omics' technologies and pre-clinical and clinical in vivo imaging. With more than 400 research faculty members specializing in disciplines ranging from basic cancer research, cancer prevention and early detection, novel therapy drug discovery and development, to survivorship, and end of life care, UPCI maintains a broad strategic vision and comprehensive approach to understanding and treating cancer.

Interested candidates should send a curriculum vitae, brief description of research interests and contact information for three references to: **UPCI Search Committee, C/O Dr. Mark Socinski, 5150 Centre Avenue, Suite 556, Pittsburgh, PA 15232. Email: socinskima@upmc.edu.** If using E-mail, please include 'Lung Cancer Faculty Candidate' in the subject line.

The University of Pittsburgh is an Affirmative Action, Equal Opportunity Employer.



AAAS is here – helping scientists achieve career success.

Every month, over 400,000 students and scientists visit ScienceCareers.org in search of the information, advice, and opportunities they need to take the next step in their careers.

A complete career resource, free to the public, *Science Careers* offers a suite of tools and services developed specifically for scientists. With hundreds of career development articles, webinars and downloadable booklets filled with practical advice, a community forum providing answers to career questions, and thousands of job listings in academia, government, and industry, *Science Careers* has helped countless individuals prepare themselves for successful careers.

As a AAAS member, your dues help AAAS make this service freely available to the scientific community. If you're not a member, join us. Together we can make a difference.

To learn more, visit
aaas.org/plusyou/sciencecareers



Memorial Sloan-Kettering
Cancer Center
The Best Cancer Care. Anywhere.

TENURE TRACK FACULTY POSITIONS Cancer Biology

Applications are invited for tenure-track faculty positions in the Cancer Biology and Genetics Program of the Sloan-Kettering Institute, Memorial Sloan-Kettering Cancer Center (www.ski.edu). Successful candidates will carry out independent research on the genesis, progression, prognosis, prevention and treatment of cancer that synergizes with ongoing efforts at the Center. Areas of special interest include, but are not limited to: cancer genetics, cancer stem cells, metastasis, tumor microenvironment, inflammation and cancer, and animal models of cancer.

New faculty members will join an interactive, interdisciplinary community of scientists and clinicians at the Center, which offers an outstanding basic and translational research environment within expanded state-of-the-art research facilities. Faculty will be eligible to hold graduate school appointments in the Gerstner Sloan-Kettering Graduate School of Biomedical Sciences, the Weill Cornell Graduate School of Medical Sciences of Cornell University, as well as the Tri-Institutional MD/PhD Training Program.

CANCER BIOLOGY & GENETICS FACULTY

Robert Benezra, PhD
Chromosome Instability and Cancer

Kitai Kim, PhD
Induced Pluripotent Stem Cells

Johanna Joyce, PhD
Tumor Microenvironment

Scott Lowe, PhD
Tumor Suppressor Genes

Joan Massague, PhD (Chairman)
Cell Signaling and Metastasis

Christine Mayr, MD, PhD
mRNA Control Mechanisms

Kenneth Offit, MD
Cancer Genetics

Craig Thompson, MD
Cancer Metabolism

Andrea Ventura, MD, PhD
microRNAs in Development and Cancer

Hans-Guido Wendel, MD
Genetic Basis for Drug Resistance

Richard White, MD, PhD
Modeling Metastasis in Zebrafish

The deadline for applications is **November 1, 2013**. Interested candidates should visit <http://facultysearch.ski.edu> to access the on-line faculty application. Please visit the site as soon as possible, as it contains important information on the required application materials, including deadlines for submission of letters of reference. Inquiries may be sent to Dwana.Agosto@mskcc.org.

facultysearch.ski.edu

MSKCC is an equal opportunity and affirmative action employer committed to diversity and inclusion in all aspects of recruiting and employment. All qualified individuals are encouraged to apply and will receive consideration without regard to race, color, gender, gender identity or expression, sexual orientation, age, religion, creed, disability, veteran status or any other factor which cannot lawfully be used as a basis for an employment decision.



ÉCOLE POLYTECHNIQUE
FÉDÉRALE DE LAUSANNE

EPFL's School ENAC (Architecture, Civil and Environmental Engineering) seeks to fill a Faculty position in Ecohydraulics. While ordinarily a Tenure-Track Assistant Professor is expected to be hired, in exceptional cases appointments as Associate Professor or Full Professor are possible.

Topics of interest include: theoretical, laboratory and field studies on the sustainable use of water resources in alpine environments; ecologically sustainable flow releases; stochastic dynamics of hydraulic phenomena and stream ecology; streamflow variability and its impact on biota (like e.g. on benthic macroinvertebrates or biofilms and/or on root distributions of riparian vegetation); spatial controls on freshwater fish biodiversity; patterns of riparian vegetation biodiversity; biodiversity in river networks; basin-scale transport phenomena; metacommunity modeling in river network ecological corridors; fluvial morphology and habitat suitability modifications; large-scale water resources management and ecosystem services including social, political and economic aspects.

Expertise at the interface of ecology, hydraulics and fluid mechanics is sought. We shall look broadly in the area of fluvial geomorphodynamics and fluvial ecohydrology with a focus on observational and experimental techniques including recent advances in sensor technology and instrumentation and/or innovative theoretical approaches.

Successful candidates are expected to initiate independent research programs and be committed to excellence in research and to undergraduate / graduate teaching

EPFL offers internationally competitive salaries and benefits. Significant financial resources and well-developed research infrastructure will be available.

Faculty Position in Ecohydraulics at Ecole polytechnique fédérale de Lausanne (EPFL)

Research activities will be based on campus EPFL-Wallis-Valais in Sion, and teaching activities in Lausanne.

The following documents are requested in PDF format: motivation letter, curriculum vitae, publications list, concise statement of research and teaching interests as well as the names and addresses (including e-mail) of at least five referees.

Applications should be submitted electronically to :

<http://enac.epfl.ch/page-2114.html>

by **November 1, 2013**, when the formal screening of applications will begin.

Enquiries may be made to:

Professor Andrea Rinaldo

**Director of the Institute of Environmental Engineering
School of Architecture, Civil and Environmental
Engineering**

Ecole Polytechnique Fédérale de Lausanne

CH-1015 Lausanne, Switzerland

andrea.rinaldo@epfl.ch

Ph. +41 (21) 693 80 34 / 37 25

Additional information about EPFL is available at:

<http://www.epfl.ch> ; <http://www.enac.epfl.ch>

Ecole polytechnique fédérale de Lausanne is an equal opportunity employer. Women candidates are particularly encouraged to apply.



The **Georgia Institute of Technology** is one of the top ranked educational/research institutions in the country and is rated as one of the best places to work. Georgia Tech aims to meet several grand challenges in the life sciences based upon current strengths and areas of growth, including Environment & Health, Biomedical Therapies, and Complex Biological Systems. Research in these interdisciplinary fields at Georgia Tech benefits from strong interactions between biologists and faculty of diverse disciplines including engineering, computing, policy, and other sciences. As part of substantial expansion in the biological sciences, the **School of Biology** is seeking applications for multiple tenure-track positions from candidates whose research would thrive in this community.

Assistant or Associate Professors in Biology. We welcome applications from candidates in all research areas relevant to activities in the School of Biology (<http://www.biology.gatech.edu/research/>), including those working in synthetic & chemical biology, predictive health, or the genomics of health & behavior. Endowed Full Professor in Experimental Integrative or Structural Biology. We are seeking an outstanding senior investigator in the molecular biosciences. Fields of interest include the temporal, structural and spatial understanding of cellular biochemistry, the dynamics of cellular organization and function, and protein interactions.

Endowed Full Professor in Experimental Integrative or Structural Biology. We are seeking an outstanding senior investigator in the molecular biosciences. Fields of interest include the temporal, structural and spatial understanding of cellular biochemistry, the dynamics of cellular organization and function, and protein interactions.

Candidates should submit an application online at <http://searches.biology.gatech.edu>, including a letter of application, curriculum vitae, statement of research interests and plans, and contact information for three references. Review of applications begins **October 1, 2013** and will continue until positions are filled.

Georgia Tech is a unit of the University System of Georgia and an Affirmative Action/Equal Opportunity Employer and requires compliance with the Immigration Control Reform Act of 1986.

GEORGIA INSTITUTE OF TECHNOLOGY



Tenure Track Faculty Position Assistant Professor

The Department of Biochemistry and the Ion Channel Research Unit (ICRU) at Duke University Medical Center invite applications for a tenure track faculty position at the Assistant Professor level in the Department of Biochemistry.

The candidate should have a laboratory research program in an area of membrane excitability and/or ion channel structure/function and/or ion channel physiology. Among the broad research areas relevant to this search are programs employing cutting-edge molecular and biochemical approaches that focus on channelopathies, neuropsychiatric disorders and neuronal function, cardiac arrhythmias, peripheral nociception, optogenetics, and development.

The laboratory space will be localized within the ICRU, a multi-departmental and interdisciplinary group of investigators organized around membrane excitability. Opportunities to interact with and build upon programs relevant to membrane excitability include those in neuroscience, cardiac electrophysiology, structural biology, hormone signaling, renal physiology, and development.

High priority will be placed on creativity in laboratory research, potential for independent funding, and dedication to excellence in teaching. A generous start up package will be provided.

Interested individuals should submit a CV, statement of research interest, and request that three letters of references to be sent as PDF files directly to: icru@mc.duke.edu.

The deadline for receipt of applications is **November 1, 2013**.

Duke University Medical Center is an Equal Opportunity/Affirmative Action Employer.

2013 Annual p Employers Survey

Special Career Feature: October 25, 2013

Reserve your ad by October 8 to guarantee space.*

*Ads accepted until October 21 if space is still available.

Who is No. 1 this year?

Science publishes its 12th annual Top Employers Survey on October 25, 2013. *Science* has a long history of providing a forum for scientists to express their opinions about the biotech and pharma industry. For 2013, we gathered the responses from 3,600 scientists who had plenty to say about the industry.

Advertise in this issue to reach both ACTIVE and PASSIVE job seekers. Here's how:

1. Scientists in the biotech/pharma community eagerly anticipate the results of this survey every year. By announcing your openings in this special feature, your reach goes beyond active job seekers to those involved in the field, targeting elusive passive job seekers at the same time.
2. Your association with this issue tells prospective recruits that you are among the best. You have a unique opportunity to brand your company as a leader. Reach the scientists that your competitors are reaching and promote your advantages.

Start building your pipeline today with *Science*.

Over
84,000
Science print readers work
in industry—reach these
passive job seekers!**

To book your ad:

E-mail: advertise@sciencecareers.org

Or telephone us:

US/Canada/South America:
202-326-6582

**Europe/India/Australia/New Zealand/
Rest of World: +44 (0) 1223 326500**

Japan: +81-(0)90-9110-1719

**China/Korea/Singapore/Taiwan/
Thailand: +86-1367-1015-294**

For recruitment in science, there's only one **Science**

Science Careers

From the journal *Science*

ScienceCareers.org

** Publisher's Own Data, August 2012
Produced by the *Science*/AAAS Custom Publishing Office

NATIONAL RESEARCH COUNCIL OF THE NATIONAL ACADEMIES Research Associateship Programs

Graduate, Postdoctoral and Senior Research Awards offered for research at US Federal Laboratories and affiliated institutions

Opportunities for graduate, postdoctoral and senior research in all areas of science and engineering

- Awards for independent research at over 100 participating laboratory locations
- 12-month awards renewable for up to 3 years
- Annual stipend \$42,000 to \$80,000 - higher for senior researchers; graduate entry level stipend begins at \$30,000
- Relocation, professional travel, health insurance
- Annual application deadlines Feb. 1, May 1, Aug. 1, Nov. 1
- Open to US and non-US citizens

Detailed program information, including instructions on how to apply online, is available on the NRC Web site at :
www.nationalacademies.org/rap

Applicants must contact Adviser(s) at the lab(s) prior to application deadline to discuss research interests and funding opportunities

Questions should be directed to the :
National Research Council Fellowships Office
TEL: (202) 334-2760
E-MAIL: rap@nas.edu

Qualified applicants will be reviewed without regard to race, religion, color, age, sex or national origin.

THE NATIONAL ACADEMIES
Advisers to the Nation on Science, Engineering, and Medicine



STANFORD UNIVERSITY Stanford Institute for Chemical Biology

The Stanford Institute for Chemical Biology is an independent institute at Stanford University, formed in partnership with the Schools of Medicine, Humanities and Sciences, and Engineering. The Institute is seeking applicants for a tenure-track faculty position at the junior level (Assistant or untenured Associate Professor). Candidates are expected to have earned a Ph.D. or M.D. degree in any discipline of science, engineering or medicine. We will consider candidates knowledgeable in the general area of chemical biology. All areas encompassed by the field of chemical biology are acceptable. In general, we give higher priority to the overall originality and promise of the candidate's work than to the sub-area of specialization.

The successful candidate will have his/her primary appointment in a department within the School of Medicine, Humanities and Sciences, or Engineering. He/she will be expected to teach and/or perform clinical service within this department in a manner that is consistent with standard practices for tenure-track faculty within that department. The candidate will also be expected to develop a world-class research program in chemical biology. Candidates should be seeking a stimulating interdisciplinary environment in which to pursue teaching and research. We anticipate that the faculty member will develop interactions with faculty not only in his/her home department but also in other departments and Schools at Stanford and at the Stanford Synchrotron Radiation Laboratory.

Applications should be addressed to Professor James K. Chen, Search Committee Chair and include a curriculum vitae, a description of future research plans, and a teaching statement. These materials should be submitted electronically as a single PDF to sicbsearch@stanford.edu by **November 1, 2013** to ensure full consideration. Applicants should also have three reference letters submitted to sicbsearch@stanford.edu by the application deadline.

Stanford University is an Equal Opportunity Employer and is committed to increasing the diversity of its faculty. It welcomes nominations of and applications from women and minority groups, as well as others who would bring additional dimensions to the university's research, teaching, and clinical missions.



SCHOOL OF BIOLOGICAL SCIENCES UNIVERSITY of CALIFORNIA • IRVINE

DEAN, SCHOOL OF BIOLOGICAL SCIENCES

The University of California, Irvine invites applications and nominations for the position of Dean, School of Biological Sciences. The university seeks an independent thinker who is decisive while fair and strategically focused and possesses the skills to navigate within a complex and multi-constituent organization. The successful candidate has a keen intellectual capacity and creativity, and is an open and persuasive communicator who leads from values; a candidate with energy and vision to head and continue the mission of the school. Key selection criteria will include:

- Demonstrated leadership in promoting the latest intellectual advances in the Biological Sciences
- Experience and demonstrated success with external relations/development - Demonstrated skill/ability to work effectively with the business community and other constituents in resource development and advancement of the School
- Faculty leadership and team building - Proven ability to inspire consensus and develop a culture that is mutually supportive, goal-directed and ambitious. Ability to attract and recruit a diverse world-class faculty
- A strong commitment to the growth and development of exceptional undergraduate and graduate academic programs
- Administrative management - Demonstrated success as an administrator, including staff development, facility/resource management and fiscal leadership

The School of Biological Sciences is one of twelve schools in the University of California, Irvine, a top-ranked public university committed to rigorous academics, cutting-edge research, excellence in undergraduate and graduate teaching, and community engagement. The School represents a premier center for biological education and research with four highly-ranked departments: Developmental and Cell Biology, Ecology and Evolutionary Biology, Molecular Biology and Biochemistry, and Neurobiology and Behavior. Further information about the school can be found at: <http://www.bio.uci.edu/>

In 2012, UC Irvine was ranked #1 in *Times Higher Education* among U.S. colleges and universities 50 years old or younger. With 28,000 undergraduate and graduate students, 1,100 regular ranks faculty and 9,400 staff, UC Irvine is among the most dynamic campuses in the University of California system. Orange County's second-largest employer, UC Irvine generates an annual economic impact on the county of \$4.3 billion. It is located on a 1,500 acre site three miles from the Pacific Ocean.

Candidates for this position should have a strong academic record that would justify a senior rank appointment in one of our four departments and a sustained record of peer reviewed extramural funding and an international reputation in a biological sciences discipline.

Applicants will have until **October 15, 2013** to apply. Applications should include a curriculum vitae, names of three or more references, and a cover letter including a statement of relevant experience and vision for the biological sciences. We encourage electronic application submission; please click this link for more information: <http://www.provost.uci.edu>, OR email applications or nominations to: biosearch@uci.edu

UCI is an Equal Opportunity Employer committed to excellence through diversity and strongly encourages applications from women, minorities, and other under-represented groups.

For your career in science, there's only one

Science

Introducing myIDP: A career plan customized for you, by you.

- The first and only online app that helps scientists prepare their very own individual development plan.
- Recommended by leading professional societies and the NIH.
- Developed by scientists at FASEB, UCSF, and the Medical College of Wisconsin in collaboration with AAAS and Science Careers, with support from the Burroughs Wellcome Fund.



Visit the website and
start planning today!
myIDP.sciencecareers.org



In partnership with:



FASEB
Federation of American Societies
for Experimental Biology



University of California
San Francisco



The University of Idaho seeks to expand our expertise in systems biology by hiring a cluster of three faculty in the Departments of Mathematics, Statistics and Physics. These tenure track faculty positions are academic year (9-month) appointments at the rank of **Assistant Professor** that commence in August 2014.

The University has a strong commitment to interdisciplinary studies, particularly evolutionary and computational biology. Through the Institute for Bioinformatics and Evolutionary Studies (<http://www.ibest.uidaho.edu/>) the University has invested in high-level genomics, computing, imaging, and mass spectrometry facilities to support research in these areas. We seek motivated faculty who have demonstrated that they can work across disciplines and can collaborate broadly. Applicants must have a demonstrated interest in complex systems.

All applicants must have a doctoral degree (or equivalent) and a commitment to teaching at the undergraduate and graduate levels. Applicants must also have an excellent record of research productivity, engagement in interdisciplinary studies, and demonstrate the potential for developing a creative independent research program.

We seek faculty members who will create a climate that embraces excellence and diversity, with a strong commitment to teaching and mentoring that will enhance the work of the department and attract and retain students of all races, nationalities, and genders.

Applicants should apply online at www.uidaho.edu/human-resources. At least three letters of recommendation are required and may be sent electronically as separate PDF files to math@uidaho.edu for mathematics position, stat@uidaho.edu for statistics position, physics@uidaho.edu for physics position. Applications will be reviewed starting **November 1, 2013**. Applications will be accepted until the position is filled.

Science Careers is the forum
that answers questions.



Science Careers is dedicated to opening new doors and providing timely answers to the career questions that matter to you.

Science Careers Forum:

- » Relevant Career Topics
- » Timely Advice and Answers
- » Community, Connections, and More!

Your Future Awaits.



From the journal Science AAAS

Visit the forum and join
the conversation today!

ScienceCareers.org

WOMEN IN SCIENCE

forging
new pathways in
green
science



Read inspiring stories
of women working in
“Green Science”
who are blending
a unique combination of
enthusiasm for science
and concern for others
to make the world
a better place.

Download this
free booklet
[ScienceCareers.org/
LOrealWiS](http://ScienceCareers.org/LOrealWiS)



This booklet is brought to you by the
AAAS/Science Business Office
in partnership with the
L'Oréal Foundation

Institut national de recherche scientifique (INRS) is a graduate and post-graduate research and training university. One of Canada's leading research universities in terms of grants per professor, INRS brings together some 150 professors and close to 700 students and post-doctoral fellows in its centers in Montreal, Quebec City, Laval, and Varennes. Conducting fundamental research essential to the advancement of science in Quebec as well as internationally, INRS research teams also play a critical role in developing concrete solutions to problems facing our society.

The INRS–Institut Armand-Frappier Centre seeks to fill four tenure-track positions of:

PROFESSOR-RESEARCHER

- **HOST-PATHOGEN INTERACTIONS** (DS 13-06)
- **IMMUNOLOGY** (DS 13-07)
- **MICROBIOLOGY** (DS 13-08)
- **EPIDEMIOLOGY** (DS 13-10)

The detailed position announcements, eligibility requirements and the application process are available at the INRS website at the following link:

www.inrs.ca/english/english/career-opportunities

INRS is committed to equity in employment and diversity.



INRS

Université d'avant-garde

WWW.INRS.CA



Memorial Sloan-Kettering
Cancer Center

The Best Cancer Care. Anywhere.

FACULTY POSITIONS

Immunology

Sloan-Kettering Institute

The Immunology Program at the Sloan-Kettering Institute (www.ski.edu) is seeking innovative investigators for tenure-track positions at the Assistant, Associate, and Member levels who wish to address basic problems in immunology with possible relevance to cancer. Applicants should have a doctoral-level degree and the potential to develop a strong independent research program or a proven record of research accomplishments, depending on the level of appointment. Qualified applicants with an M.D. degree may be offered a joint appointment in an appropriate department in Memorial Hospital. Candidates will join a faculty with a broad range of research interests, including innate immunity, tumor immunology, B, T and NK cell development and function, regulation of immune responses, and infectious disease. New faculty members will join an interactive, interdisciplinary community of scientists and clinicians at the Center, which offers an outstanding basic and translational research environment within expanded state-of-the-art research facilities. Faculty will be eligible to hold graduate school appointments in the Gerstner Sloan-Kettering Graduate School of Biomedical Sciences, the Weill Cornell Graduate School of Medical Sciences of Cornell University, as well as the Tri-Institutional MD/PhD Training Program.

The Sloan-Kettering Institute offers a highly interactive, supportive and exciting research environment with programs in Immunology, Cancer Biology & Genetics, Cell Biology, Molecular Pharmacology & Chemistry, Molecular Biology, Developmental Biology, Computational Biology and Structural Biology, as well as unparalleled clinical programs in cancer research, treatment, and prevention.

The deadline for applications is **November 1, 2013**. Interested candidates should visit <http://facultysearch.ski.edu> to access the on-line faculty application. Please visit the site as soon as possible, as it contains important information on the required application materials, including deadlines for submission of letters of reference.

Inquiries may be sent to **Dwana Agost** at agostod@mskcc.org or **Dr. Alexander Rudensky**, Chair, Immunology Program at rudenska@mskcc.org.

facultysearch.ski.edu

MSKCC is an equal opportunity and affirmative action employer committed to diversity and inclusion in all aspects of recruiting and employment. All qualified individuals are encouraged to apply and will receive consideration without regard to race, color, gender, gender identity or expression, sexual orientation, national origin, age, religion, creed, disability, veteran status or any other factor which cannot lawfully be used as a basis for an employment decision.

Carnegie Mellon University

FACULTY POSITION in the Area of Host-Microbe Interactions

The Department of Biological Sciences at Carnegie Mellon University seeks applicants for a tenure-track faculty position who work at the interface between mammalian hosts and microorganisms that can colonize or cause infection. Research topics of interest include but are not limited to mucosal defenses, pathogen effectors, innate immunity, and the role of commensal flora in host defense mechanisms. We seek candidates for an **ASSISTANT** or **ASSOCIATE PROFESSOR** position.

Candidates should have a Ph.D. or equivalent degree with postdoctoral training. The Department of Biological Sciences is a research-intensive environment, and our faculty members are expected both to develop high quality research programs and to participate in our graduate and undergraduate teaching mission. We are especially interested in candidates who can leverage our department's strengths in imaging, computational biology, molecular genetics, and cell biology, and contribute to our collaborative culture. The new Disruptive Health Technology Institute, hosted in the College of Engineering, enables translational applications of new findings in infection biology. Pittsburgh has strong interactive Immunology and Microbiology communities at the University of Pittsburgh and Allegheny Genome Sciences Center.

Applications must be received by December 1, 2013. The application package should include a cover letter that outlines interest in and qualifications for the position, curriculum vitae, statements of research interests (three pages or less), a statement of teaching goals (one page or less), and names and contact information for three references. **Website:** <https://apps.bio.cmu.edu/facultySearch/view/14>.

Address correspondence to: **Aaron Mitchell, Search Committee Chair, Department of Biological Sciences, Carnegie Mellon University, 4400 Fifth Avenue, Pittsburgh, PA 15213; e-mail** apml@cmu.edu.

BIOLOGICAL CHEMISTRY Dartmouth College

The Department of Chemistry at Dartmouth College is seeking an outstanding applicant for an open rank (tenured or tenure-track) faculty position in Biological Chemistry, broadly defined, starting July 2014. We particularly seek candidates who will help lead, initiate, and participate in collaborative research projects both within Chemistry and involving other Dartmouth researchers, including those at Dartmouth's Geisel School of Medicine, Norris Cotton Cancer Center, and Thayer School of Engineering. Teaching responsibilities will include biochemistry and advanced/graduate courses in biological chemistry. The department (**website:** <http://www.dartmouth.edu/~chem/>) is home to 16 tenured and tenure-track faculty with strong Ph.D. and M.S. programs and affiliated with Dartmouth's M.D.-Ph.D. program. Dartmouth College, a member of the Ivy League, is located in Hanover, New Hampshire (on the Vermont border). Dartmouth has a beautiful, historic campus, located in a scenic area on the Connecticut River. Recreational opportunities abound in all four seasons.

Applicants should submit a cover letter, curriculum vitae, a description of research (funding and future plans), and a statement of teaching interests. Senior candidates should provide the names of three references, while tenure-track candidates should arrange for at least three reference letters to be sent. All communications will be treated confidentially. Application materials and reference letters should be submitted to **website:** <https://secure.interfolio.com/apply/22014>; inquiries may be addressed to **e-mail:** chemistry@dartmouth.edu. Applications received by October 1 will receive first consideration. *With an even distribution of male and female students and over a quarter of the undergraduate student population members of minority groups, Dartmouth is committed to diversity and encourages applications from women and minorities.*



ASSISTANT PROFESSOR for Chemistry

The Department of Chemistry at Boston University invites applications from outstanding candidates for a tenure-track position at the Assistant Professor level in the field of Organic Chemistry, beginning July 2014 (pending final budgetary approval). Of particular interest is the general area of synthetic organic chemistry including asymmetric synthesis and applications in natural product/bioactive molecule synthesis. The successful applicant will benefit from the department's supportive and collegial environment, which includes faculty possessing a wide range of complementary expertise including biochemistry and synthetic organic chemistry. The candidate will also interact closely with the Chemistry Department's Center for Chemical Methodology and Library Development (CMLD-BU, **website:** <http://cmlb.bu.edu>) and related initiatives. Undergraduate teaching responsibilities will be in the areas of organic chemistry, with the opportunity to develop graduate courses in the candidate's area of expertise.

Applicants should apply by submitting a letter of interest, including teaching and research objectives, current curriculum vitae, and three letters of reference to **website:** <https://academicjobsonline.org/ajo/jobs/2969>.

The deadline for applications is October 1. *Boston University is an Affirmative Action/Equal Opportunity Employer.*

ASSISTANT PROFESSOR, ECOLOGIST Tenure-track

The Department of Zoology at Oklahoma State University (**website:** <http://zoology.okstate.edu>) invites applications for an Assistant Professor in ecology. We seek applicants whose research integrates ecology with the study of animal development, behavior, biodiversity, or ecosystems. Applicants should have a Ph.D., postdoctoral experience, teaching experience, and success in obtaining extramural funding. Responsibilities include establishing an extramurally funded research program, mentoring M.S. and Ph.D. students, and teaching at the undergraduate and graduate levels. To apply (1) send a single PDF file composed of a cover letter, curriculum vitae, and statements of research interests and teaching philosophy, and (2) arrange to have three letters of recommendation sent to the search committee chair, **Dr. Andrew Dzialowski**, at **e-mail:** zoologysearch@okstate.edu. Application review begins October 7, 2013, with employment beginning August 16, 2014. Filling of this position is contingent upon funding availability. *Oklahoma State University is an Affirmative Action/Equal Employment Opportunity/E:Verify Employer committed to diversity. OSU-Stillwater is a tobacco-free campus.*

FACULTY POSITION in Biochemistry

The University of Wisconsin (UW) Oshkosh seeks a tenure-track **ASSISTANT PROFESSOR** beginning September 1, 2014. Requirements: Ph.D. in biochemistry or related field, ability (or potential) to teach effectively at undergraduate level and establish an active research program in biochemistry. Responsibilities: teach undergraduate biochemistry, general chemistry, labs in organic chemistry, advise chemistry majors, establish an active research program, and pursue extramural funding. Submit: letter of application, curriculum vitae, three current confidential letters of recommendation, transcripts (photocopies accepted initially), research plans, and a one-page statement of teaching philosophy to: **Dr. Jennifer Mihalick, Chair, Department of Chemistry, University of Wisconsin Oshkosh, Oshkosh, WI 54901-8654**. Electronic submissions will be accepted at **e-mail:** chemhire@uwosh.edu.

UW Oshkosh values diversity and is an Affirmative Action/Equal Opportunity Employer Institution. Employment will require a criminal background check. Application deadline is October 11, 2013.

UNIVERSITY OF ILLINOIS at Chicago

Department of Chemistry invites applications for a tenure-track **ASSISTANT PROFESSOR** in the area of bioanalytical chemistry. Areas of greatest interest are cutting-edge analysis methods at the intersection of analytical chemistry with biology, biochemistry, structural biology, biophysics, chemical biology, and/or biological imaging. The successful candidate will be expected to carry out a full and innovative program of experimental research and to teach graduate and undergraduate courses in analytical chemistry and biochemistry. Ph.D. is required. Women and minority candidates are strongly encouraged to apply. Please submit an online application (include the names and e-mail addresses of three references), and upload a cover letter, curriculum vitae, list of publications, summary of past research, plans for future research, and statement of teaching philosophy at **website:** <https://jobs.uic.edu> (Click on the Job Board, then our posting) by October 7, 2013. Final authorization of the position is subject to availability of state funding.

University of Chicago at Illinois is an Affirmative Action/Equal Opportunity Employer.

POSTDOCTORAL RESEARCH ASSOCIATE

A Postdoctoral Research Associate position at the Eppley Cancer Institute, University of Nebraska Medical Center (UNMC). Excellent opportunity to join a well-funded, multidisciplinary research group to study cancer metabolism in the context of tumor microenvironment, with special emphasis on pancreatic cancer.

We are looking for highly motivated candidates possessing an M.D. or Ph.D. in the field of Biochemistry/Molecular Biology/Cancer Biology/Biotechnology or a related field with expertise in molecular biology, cell-based assays, and animal studies.

Apply online to position 2013-072 at **website:** <http://jobs.unmc.edu>. Upload curriculum vitae, a description of research accomplishments, and names of three references.

UNMC is an Equal Opportunity/Affirmative Action Employer.

Stop
searching
for a job;
start your
career today.

Science Careers

From the journal *Science*



www.ScienceCareers.org

Find your future here.

www.ScienceCareers.org